Optimization of organic solar cells for innovative indoor applications

Ruoxue He

Thèse de doctorat

Université de Limoges
ED 653 - Sciences et Ingénierie (SI)
Institut de recherche XLIM, CNRS UMR 7252

Thèse pour obtenir le garde de Docteur de l'Université de Limoges

en Science et Ingénierie pour l'Information

Présentée et soutenue par

Ruoxue HE

le 17 Décembre 2024

Optimisation de cellules solaires organiques pour applications indoor innovantes

Thèse dirigée par **Bernard Ratier** et **Johann Bouclé**

JURY:

Président du jury

M. Philippe Leclère, Professeur, Laboratoire LPNE, Université de Mons

Rapporteurs

M. Clément Cabanetos, Directeur de Recherche CNRS, Laboratoire Moltech-Anjou, Université d'Angers
M. Guillaume Wantz, Professeur, Laboratoire IMS, Bordeaux INP/Université de Bordeaux

Examinateurs

M. Nicolas Leclerc, Directeur de Recherche CNRS, Laboratoire ICPEES, Université de Strasbourg
M. Pierre Audebert, Professeur, Laboratoire PPSM, Université de Paris-Saclay/ENS
M. Bernard Ratier, Professeur, Laboratoire XLIM, Université de Limoges
M. Johann Bouclé, Maître de Conférence, Laboratoire XLIM, Université de Limoges

To my family

Nothing in life is to be feared, it is only to be understood.
Marie Curie

Acknowledgments

I would like to express my sincerest gratitude to all those who have supported me during my thesis.

First of all, I would like to express my deepest gratitude to my supervisors for their invaluable guidance, support, discussions, and encouragement throughout this journey. Prof. Dr. Bernard Ratier and Dr. Johann Bouclé, your expertise, patience, and guidance were essential to the completion of this thesis, and I am very grateful for the opportunity to learn from you.

I would also like to express my sincere thanks to the members of the jury: Prof. Dr. Clément Cabanetos, Prof. Dr. Guillaume Wantz, Prof. Dr. Philippe Leclère, Dr. Nicolas Leclerc, and Prof. Dr. Pierre Audebert, for their time, insightful evaluations, and constructive feedback on this thesis. In particular, I am very grateful to Dr. Nicolas Leclerc and Prof. Dr. Pierre Audebert for providing crucial materials that made this research possible and to Prof. Dr. Philippe Leclère for his guidance in the AFM experiments at the Laboratoire de Physique des Nanomatériaux et Énergie (LPNE), as well as PhD student Pierre Nickmilder for his help with the AFM experiments.

I would like to thank the National Research Agency under the Investments for the Future program, with the reference ANR-18-EURE-0017 TACTIC, for their financial support that enabled my international mobility to the LPNE laboratory in Belgium. This opportunity has greatly contributed to the advancement of my research, and I am truly thankful for the support that made it possible.

I would like to extend my sincere gratitude to Dr. Sylvain Vedraine, Dr. Rémi Antony, Dr. Bruno Lucas, and Dr. Thierry Trigaud, all permanent members of the ELITE team of the XLIM Research Institute. I would also like to thank Nicolas Parou and Lionel Rechignat from the technical group for their invaluable help with the equipment used in this study, as well as Marie-Laure Guillat from the secretariat for her help and administrative support.

I would also like to give a heartfelt thank you to my wonderful labmates for the meaningful exchanges and the moments we shared working together: Issoufou Ibrahim Zamkoye, Ceren Yildirim, Daniel Ribeiro Dos Santos, Quang-Huy Do, Camille Frouin, Vishal Viswakarman, and other members of RF-ELITE have been an absolute pleasure, they have become much more than just colleagues. I am also fortunate to have met Baptiste Moeglen-Paget, Colman Buckley, Manal Ait-Assou, and Clara Abbouab, who have made XLIM an even better place. The daily support and friendship of all of you have been invaluable, and I am deeply grateful for your presence throughout this journey.

Thank you to all the members of the Sigma DocX Association 2023 class for your dedication to the life of the laboratory and for promoting the role of PhD students through the events organized. It was a valuable experience for me to serve as secretary, and I am grateful for the opportunity to contribute to such a dynamic group.

Finally, I would like to extend a heartfelt thank you to my family and friends. To my parents, thank you for your unconditional support and for always being there to lift me. To my husband, Xin Li, thank you for your unwavering love and companionship. To my friends outside of academia, thank you for always being a source of positivity and balance in my life.

Merci!

感谢!

Rights

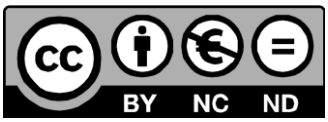

Table of Contents

List of Abbreviations

AFM	Atomic force microscopy
a-Si	Amorphous silicon
AsF_5	Arsenic pentafluoride
BHJ	Bulk heterojunction
BIPV	Building-integrated photovoltaic
BDT	Benzodithiophene
CB	Chlorobenzene
CF	Chloroform
CdTe	Cadmium telluride
CIGS	Copper indium gallium selenide
CFL	Compact fluorescent lamp
CT	Charge transfer
CS	Charge separation
DCM	Dichloromethane
DSSC	Dye-sensitized solar cell
D/A	Donor-acceptor
DOS	Density of state
E_g	Optical bandgap
EQE	External quantum efficiency
ETL	Electron transport layer
E_{Loss}	Energy loss
FA	Fullerene acceptor
FF	Fill factor
GaAs	Gallium arsenide
HOMO	Highest occupied molecular orbital
HTL	Hole transport layer
HCl	Hydrochloric acid
IEC	International Electrotechnical Commission
IOPVs	Indoor organic photovoltaics
IoT	Internet-of-things
IPV	Indoor photovoltaic
I_{SC}	Short-circuit current

ISTC	Indoor Standard Test Condition
J_{SC}	Short-circuit current density
LED	Light-emitting diode
LUMO	Lowest unoccupied molecular orbital
L_D	Exciton diffusion length
mono-Si	Monocrystalline silicon
MPP	Maximum power point
Mw	Molecular weight
NFA	Non fullerene acceptor
NIR	Near-infrared
OLED	Organic light-emitting diode
o-DCB	Ortho-dichlorobenzene
OPV	Organic photovoltaic
OSCs	Organic solar cells
PCE	Power conversion efficiency
PEN	Polyethylene naphthalate
PET	Polyethylene terephthalate
poly-Si	Polycrystalline silicon
PL	Photoluminescence spectroscopy
PSC	Perovskite solar cell
P_{MAX}	Maximum power output
P_{in}	Power density of incident light
PTFE	Polytetrafluoroethylene
QNM	Quantitative Nanomechanics
R2R	Roll-to-roll
R_S	Series resistance
R_{SH}	Shunt resistance
RMS	Root mean square
SCLC	Space charge limited current
SVA	Solvent vapor annealing
STC	Standard Test Condition
sMIM	Scanning microwave impedance microscopy
UV	Ultraviolet
V_{OC}	Open-circuit voltage

List of Figures

List of Tables

List of materials

Alq3	Tris-(8-hydroxyquinoline) aluminum
APO	6-methoxynicotinamide hydrochloride
BTR	Benzodithiophene-terthiophene-rhodamine
D18 (PCE18)	Poly[(2,6-(4,8-bis(5-(2-ethylhexyl-3-fluoro)thiophen-2-yl)-benzo[1,2-b:4,5-b']dithiophene))-alt-5,5'-(5,8-bis(4-(2-butyloctyl)thiophen-2-yl)dithieno[3',2':3,4;2'',3'':5,6]benzo[1,2-c][1,2,5]thiadiazole)]
Di-PDI	2,2′,9,9′-Tetrakis(1-pentylhexyl)-[5,5′-bianthra[2,1,9-def:6,5,10-d′ e′ f′]diisoquinoline]-1,1′,3,3′,8,8′,10,10′(2H,2′H,9H,9′H)-octone
DMP	2,9-dimethyl-1,10-phenanthroline
NT	Naphtho[1,2-c: 5,6-c']bis([1,2,5]thiadiazole
NBT	Naphtho[2,3-c][1,2,5]thiadiazole
NITZ	N-(2-(6-chlorotetrazin-3-yloxy)ethyl)-naphthalimide
P3HT	Poly(3-hexylthiophene-2,5-diyl)
PBDB-T (PCE12)	Poly[(2,6-(4,8-bis(5-(2-ethylhexyl)thiophen-2-yl)-benzo[1,2-b:4,5-b']dithiophene))-alt-(5,5-(1',3'-di-2-thienyl-5',7'-bis(2-ethylhexyl)benzo[1',2'-c:4',5'-c']dithiophene-4,8-dione)]
PCBM ($PC_{61}BM$)	[6,6]-phenyl-C61 butyric acid methyl ester
$PC_{71}BM$	[6,6]-phenyl-C71 butyric acid methyl ester
PM6 (PBDB-TF)	Poly[(2,6-(4,8-bis(5-(2-ethylhexyl-3-fluoro)thiophen-2-yl)benzo[1,2-b:4,5-b']dithiophene))-alt-(5,5-(1',3'-di-2-thienyl-5',7'bis(2-ethylhexyl)benzo[1',2'-c:4',5'-c']dithiophene-4,8-dione)]
PMMA	Polymethyl methacrylate
PTB7-Th	Poly[4,8-bis(5-(2-ethylhexyl)thiophen-2-yl)benzo[1,2-b;4,5-b']dithiophene-2,6-diyl-alt-(4-(2-ethylhexyl)-3-fluorothieno[3,4-b]thiophene-)-2-carboxylate-2-6-diyl]
PF2	Di-fluorinated copolymer
PS	Polystyrene
ITIC	3,9-bis(2-methylene-(3-(1,1-dicyanomethylene)-indanone))5,5,11,11-tetrakis(4-hexylphenyl)-dithieno[2,3-d:2',3'-d']-sindaceno[1,2-b:5,6-b']dithiophene
TDPH	2,5,8-tris(3,5-diethyl-pyrazolyl)-heptazine
Y6 (BTP-4F)	2,2'-((2Z,2'Z)-((12,13-bis(2-ethylhexyl)-3,9-diundecyl-12,13-dihydro-[1,2,5]thiadiazolo[3,4-e]thieno[2",3'':4',5']thieno[2',3':4,5]pyrrolo[3,2-g]thieno[2',3':4,5]thieno[3,2-b]indole-2,10-

	diyl)bis(methanylylidene))bis(5,6-difluoro-3-oxo-2,3-dihydro-1H-indene-2,1-diylidene))dimalononitrile
2PACz	2-(9H-carbazol-9-yl) phosphonic acid
2,4-diF-Hep	2,4-difluoro-Heptazine
2,4-DM-Hep	2,4-dimethyl-Heptazine

Introduction

The increasing demand for low-power Internet of Things (IoT) devices for indoor applications is driving significant advances in the electronics and semiconductor industries, particularly in the design and development of ultra-low-power IoT systems (Figure 1). This surge in demand is also stimulating the growth of high-performance indoor photovoltaic (IPV) systems[1]. Solar energy's inherent sustainability aligns with global environmental goals, offering substantial cost savings and reducing the carbon footprint of IoT systems. Organic solar cells (OSCs) are emerging as an up-and-coming solution for powering IoT devices due to their sustainability, flexibility, and autonomy in various industrial and sectoral applications[2,3]. Indoor IoT devices serve multiple purposes, including home automation, industrial process control, retail analytics, and intelligent building management. Given the predominance of indoor IoT deployments, integrating OSCs with these devices to harness ambient light offers significant potential to enhance environmental sustainability and minimize reliance on traditional power sources, thereby eliminating the need for frequent battery replacement or external power supplies.

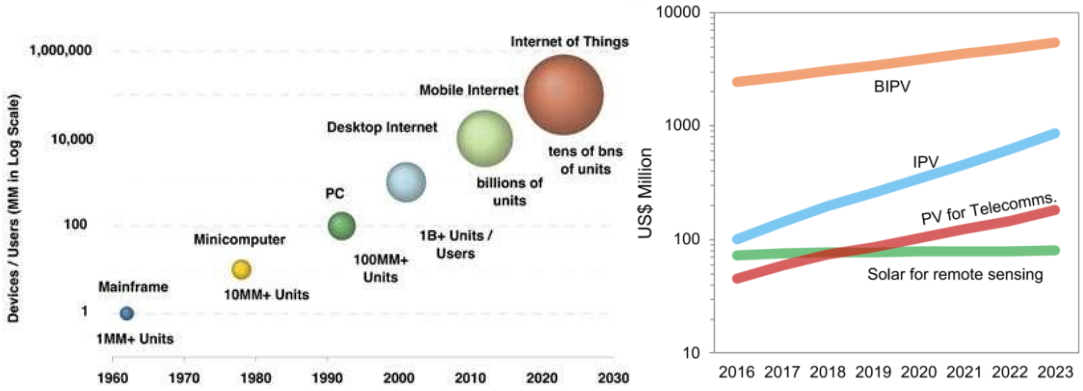

Figure 1. Growth of IoT Devices and the Expanding Market for Photovoltaic Applications (BIPV, IPV, and PV for Telecom and Remote Sensing)[1].

Unlike conventional solar cells made from inorganic materials such as silicon, OSCs offer several advantages for indoor applications. These include high tunability, excellent light absorption, sustainability, flexibility, low-cost production, semi-transparency, and efficient light-harvesting capabilities. Their flexible and lightweight nature facilitates integration into various indoor environments without compromising aesthetics or functionality. The high tunability of OSCs allows the molecular optical properties to be easily tuned to match the indoor light emission spectrum. Furthermore, the lifetime of OSCs in indoor environments is considerably extended compared to their outdoor counterparts due to reduced exposure to harsh environmental conditions such as UV radiation, humidity, and temperature fluctuations.

Despite significant advancements in organic photovoltaic (OPV) performance under outdoor conditions over the last decade, innovative approaches are still required to improve their power conversion efficiency for indoor applications. Indoor organic photovoltaics (OPVs) face unique challenges that hinder their performance, such as spectral mismatch between conventional solar cell materials and indoor light sources, low-intensity lighting typical of indoor environments (100-1000 lux), and increased sensitivity to low-light conditions. Furthermore, achieving high open-circuit voltage (V_{OC}) and maximizing short-circuit current density (J_{SC}) under low-light conditions remain key obstacles. Recent developments have demonstrated that OPVs can achieve impressive indoor power conversion efficiencies (PCEs) exceeding

36% under 1000 lux light-emitting diode (LED) illumination by using non-fullerene acceptors (NFAs) optimized for the visible light spectrum[4]. The efficiency of OPV devices is influenced by various factors, including the selection of donor and acceptor materials, their optoelectronic properties, the nanoscale morphology of the photoactive blends, the thickness of the photoactive layer, the blend ratio, the use of additives, the choice of solvent, and the processing conditions. Optimizing these parameters is crucial in improving OPV technologies' performance and practicality for indoor environments. Our research will explore several strategies to develop photoactive layer materials that specifically absorb in the blue region (about 400-500 nm) of artificial light sources, such as white LEDs. Conventional OPV materials are primarily optimized for outdoor sunlight and typically exhibit poor absorption in the blue range. This limitation reduces the efficiency of charge generation under indoor lighting conditions, where the blue light of LEDs is particularly prominent. To address this issue, our work focuses on creating new photoactive materials that are more sensitive to blue wavelengths, thereby improving charge carrier generation and overall device performance in indoor environments.

The manuscript consists of five chapters that cover these challenges in-depth and present innovative solutions to advance the field of IOPVs:

The first chapter provides a comprehensive bibliographical study of OSCs for indoor applications. It presents an overview and analysis of the state-of-the-art OSCs for indoor applications. It examines light sources for IPVs, the working principles of OPVs, essential characteristic parameters, and different architectures. In addition, recent progress in developing donor and NFA materials for indoor applications will be discussed.

In the second chapter, we delve into the comprehensive process of fabricating OPV devices at the laboratory scale and characterizing their optoelectronic properties. This study was conducted at XLIM, under the supervision of Bernard Ratier and Johann Bouclé, in collaboration with the Laboratoire de Physique des Nanomatériaux et Énergie (LPNE) in Belgium, led by Philippe Leclère. The focus is on evaluating the performance of OPV devices through a series of advanced characterization techniques that explore the morphological, optical, and electrical properties of OSCs. Notably, a dedicated setup for indoor J-V characterization is presented, emphasizing the importance of this analysis in evaluating device performance under indoor lighting conditions.

The third chapter introduces and explores a new platform of electron acceptor compounds based on heptazines as NFAs for indoor applications[5-7]. Heptazines are indeed good candidates as NFA for indoor organic photovoltaics due to their particular electronic properties and their electronic gap, which can be modulated in the blue region of the light spectrum[8]. In particular, they have a very high nitrogen/carbon atomic ratio, which gives them a highly electro-deficient character. Their integration into OPV components can also allow the development of more efficient devices for energy harvesting under indoor lighting, potentially semi-transparent, and targeting high operating voltages (of the order of Volt) required for most IoT applications without having to make a series association of cells and therefore considerably simplify the energy harvesting module. This project is thus part of a close collaboration with Prof. Pierre Audebert at the Laboratory of Photo-physique et Photo-chimie Supramoléculaire et Macromoléculaires (PPSM – Université Paris-Saclay, ENS Paris-Saclay, CNRS) and at XLIM, who is the originator of an original synthesis method for heptazine derivatives of interest for optoelectronics and photocatalysis[9]. Initially, several non-optimized derivatives were considered for this application, and later, new derivatives with electronic gaps closer to the

blue region were targeted: TDPH, 2,4-diF-heptazine, and 2,4-dimethyl-heptazine. We use different donor material to process D/A blends with these heptazines, to measure their optical and electrical properties, and to characterize their JV characteristics and external quantum efficiency (EQE).

The fourth chapter investigates an active layer blend based on PF2, a fluorinated polymer donor, and ITIC, a small-molecule NFA, with a focus on optimizing their performance for IPV applications. PF2 demonstrates impressive light-harvesting capabilities with an absorption spectrum ranging from 400 to 750 nm, well-matched to the emission spectra of indoor artificial light sources (400-730 nm)[10,11]. This chapter examines various aspects of the PF2:ITIC blend for indoor photovoltaic energy conversion, including optimization of the blend ratios, solvent selection, and active layer thickness. These parameters are systematically varied and studied to achieve the best possible PV performance under indoor LED lighting conditions.

In the final chapter of this thesis, we shift focus to explore a different aspect of the OPV technology, specifically their performance under outdoor conditions and the challenges posed by UV-induced degradation[12]. We explore a novel approach which aims at improving the stability of OSCs through the integration of S-tetrazine (NITZ) molecules with hemicellulose for luminescent downshifting (or LDS) applications[13]. One of the critical challenges for OSCs in outdoor environments is their high sensitivity to ultraviolet (UV) light, which accelerates degradation and reduces device lifetime. The LDS strategy, which involves absorbing UV light and re-emitting it as visible light, is proposed as a potential solution to mitigate the negative effects of UV exposure and improve the long-term stability and performance of OSCs.

Chapter I. OPVs: The shift from outdoor to indoor applications

I.1. Historic of OPVs

Electrification with renewable energy can substantially reduce CO_2 emissions, which is an urgent requirement for the sustainable development of humanity on earth. Renewable power sources, increasingly cost-competitive compared to fossil fuels, also offer health and socio-economic benefits. To meet climate goals, the share of renewable energy in global energy consumption must increase from 19% in 2017 to 65% by 2050, with PV systems contributing significantly. Solar energy, in particular, is a mature, scalable technology capable of meeting the rising global electricity demand. OPVs present a promising technology in this transition, with applications spanning both outdoor and indoor environments. OPVs utilize the properties of semiconducting materials to convert light into electricity. The semiconducting nature of π-conjugated organic materials was first demonstrated by H. Shirakawa, along with collaborators Alan MacDiarmid and Alan Heeger, in 1977 through their studies on polyacetylene[14]. They were able to enhance the conductivity of polyacetylene to levels comparable to many metals when doped with controlled amounts of halogens and arsenic pentafluoride (AsF_5). Despite polyacetylene itself being too unstable and difficult to work with for commercial applications, this discovery paved the way for the development of a wide range of conducting polymers, including those used in OPVs. This pioneering work led to Shirakawa, MacDiarmid, and Heeger being awarded the Nobel Prize in Chemistry in 2000. In 1986, Tang et al. introduced the first OPV device based on a planar architecture, achieving a PCE of around 1%[15]. This low efficiency was attributed to the limited donor-acceptor interfaces in the bilayer configuration, which hindered the efficient dissociation of tightly bound excitons of organic semiconductors. This limitation in OPVs persisted until 1995, when Yu et al. developed a bulk heterojunction (BHJ) design using MEH-PPV as the donor and C_{60} as the acceptor[16]. The BHJ design featured a bi-continuous network of donor and acceptor materials, significantly enhancing the donor-acceptor interface, exciton dissociation, and charge generation. Based on this approach, OPV research has continuously evolved with the synthesis of new organic materials, electrode interface layers, and advanced device configurations, driving the PCE from 2.8% to 19.2% over the past two decades, as shown in Figure 2[17].

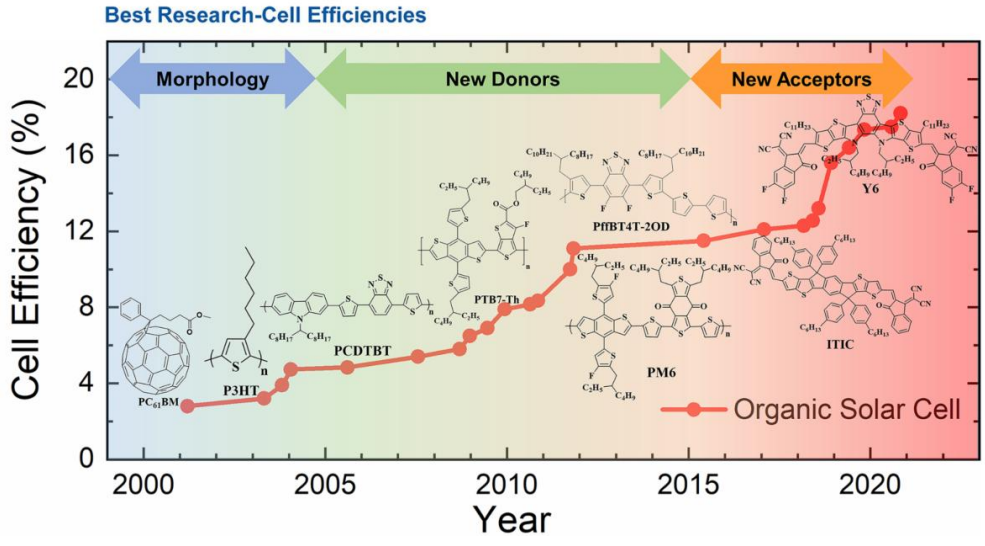

Figure 2. OPVs have advanced steadily through three critical stages of photoactive material development: morphology, new donors, and new acceptors[17].

In the early stages of OPV research, significant progress was achieved by optimizing the morphology of BHJ layers and developing fullerene acceptors (FAs) such as C_{60} derivative [6,6]-phenyl-C61 butyric acid methyl ester (PCBM or $PC_{61}BM$)[18]. These BHJ layers typically consisted of a blend of poly(3-hexylthiophene) (P3HT) and FAs. Although P3HT demonstrated the commercial potential of polymer solar cells, it also presented several challenges, in particular, its wide bandgap, which limited the absorption of the solar spectrum. To overcome this problem, researchers have concentrated on the design and synthesis of low-bandgap donor materials that better match solar radiation. These materials include conjugated polymers, copolymers, and small molecules with enhanced light-absorbing properties to pair effectively with FAs such as PCBM and its derivatives such as [6,6]-phenyl-C_{71} butyric acid methyl ester ($PC_{71}BM$), bisPCBM, ICBA, and others. These new donors exhibited improved charge-transporting properties due to a two-dimensional charge-transporting network. For example, PCPDTBT, with an optical energy gap of approximately 1.46 eV, showed absorption and photoconductive response spanning from 300 to 850 nm. When blended with $PC_{71}BM$, this material achieved a PCE of 3.2%[19]. With the optimization of BHJ morphology through the incorporation of alkane dithiols as additives, the devices achieved a PCE of 5.5%[20]. Following this, materials such as PTB7[21], PTB7-Th[22,23] (which has a lower highest occupied molecular orbital (HOMO) than PTB7), PBDB-T[24], and PffBT4T-2OD[25] were developed. When blended with $PC_{71}BM$, these materials achieved PCE of 7.4%, 10.31%, 7.45%, and 10.4%, respectively. These advancements, together with the enhanced electron-withdrawing and electron-transporting properties of FAs, have led to the fabrication of devices with PCEs exceeding 11%[26]. Despite the considerable attention that FAs have received in the field of BHJ OSCs, they have several inherent limitations: limited tunability of energy levels, weak absorption, and high synthesis costs, especially for high-performance acceptors like $PC_{71}BM$. These limitations have driven the exploration of NFAs to improve the performance of OSCs. In 2015, a remarkable NFA, ITIC, was reported[27], opening the third stage of OSC developments. ITIC has strong and broad absorption, the lowest unoccupied molecular orbital (LUMO) energy levels, good electron transport ability, and excellent miscibility with polymer donors. This research unlocked the potential of A-D-A type NFAs as alternatives to FAs in OSCs. Then, the development of ITIC derivatives has significantly improved the PCE of OSCs, increasing from 6.8%[27] to 14%[28] within a few years. In addition to the A-D-A structured NFAs, another notable NFA known as Y6 has been introduced[29] by using a fused-ring benzothiadiazole core unit (see Figure 2). Y6 features an A-D-A'-D-A structure, which enhances the intramolecular electron push-pull effect within the molecule. This structural modification aims to optimize the electronic properties of the NFA, making it more efficient at absorbing light and separating charges in organic photovoltaic devices. OPVs made from Y6 in both conventional and inverted architectures have exhibited a high efficiency of 15.7%[29]. In 2020, a new wide-bandgap copolymer donor, D18, was developed, which showed electron-withdrawing solid capability and good hole mobility. D18:Y6 solar cells demonstrate a PCE of 18.22%[30]. To further improve the performance, ternary blends of three components are particularly interesting because they enable complementary absorption and energy level alignment, leading to improved light-harvesting efficiency and charge separation[31,32]. Nowadays, state-of-the-art OSCs have achieved PCEs of 19.2% using a single-junction ternary donor-acceptor morphology by incorporating D18 into the PM6:L8-BO blends[33]. As the efficiency of OPVs continues to increase, reaching levels comparable to traditional silicon cells (with a state-of-the-art single crystal PCE of 26.1%), OPVs are also mechanically flexible[34,35] and lightweight, making them highly advantageous for integration into curved, portable, or wearable electronic devices. Additionally, the scalability of OPV is being enhanced by emerging printing technologies such

as roll-to-roll (R2R) printing[36,37], slot-die coating[38], and inkjet printing[39,40], which offer high throughput and the potential for low-cost manufacturing, large-scale production (Figure 3). Despite these advantages, outdoor deployment of OPV presents both opportunities and challenges. While their lifetime in actual outdoor conditions has been significantly improved, with operational stability now reaching several years under favorable conditions[41] and accelerated stability testing having extrapolated OPV service lives of up to 30 years[42], further enhancements in packaging and material stability are needed to extend OPV lifetime, especially in harsher environments. By leveraging these unique advantages, OPVs offer a promising approach to integrating renewable energy solutions into everyday life, supporting the development of IoT networks and other energy-saving technologies, from portable electronics to building-integrated photovoltaics, particularly well-suited for indoor environments.

a) Multi-color,
Semi-transparent OPV, XLIM

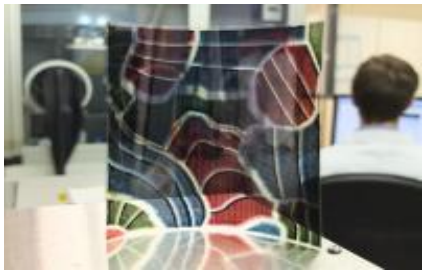

b) OPV module,
Dracula Technologies

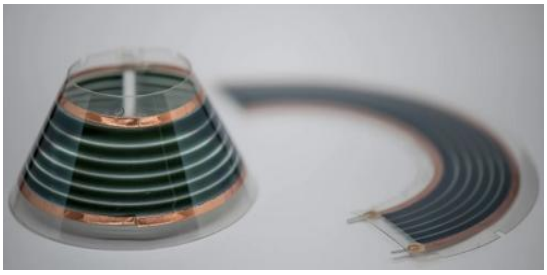

c) R2R OPV manufacturing,
infinityPV

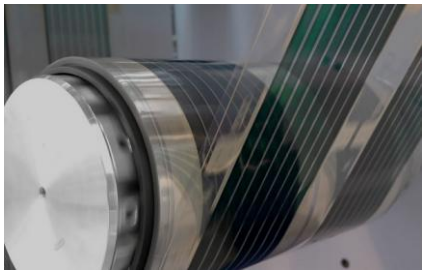

d) OPV covered polytunnel

Figure 3. Examples of OPV devices: a) multi-color transparent OPV made at XLIM in collaboration with CEA and Disasolar. b)OPV module by Dracula Technologies[43]. c) Roll-to-roll (R2R) OPV manufacturing from infinityPV[44]. d) Photo of experimental OPV-covered polytunnel greenhouse[45].

I.2. Indoor applications

In the rapidly expanding market of IoT smart devices, such as fire alarms, smart locks, RFID tags, and IoT sensors, IPV based on OPV technology is emerging as a promising and environmentally friendly, self-sufficient power solution. Considering the challenges OPVs face in outdoor conditions, such as degradation at 1 sun intensity and limited lifetime, their potential for indoor applications is more attractive. Artificial light is typically 1,000 times less intense than sunlight, which significantly reduces the degradation factor. Moreover, the tunability of OPVs enables them to be optimized to match the emission spectra of artificial lighting such as LEDs. At the same time, the growth of IoT devices often requires distributed power solutions in hard-

to-reach places, creating a strong demand for durable, low-maintenance energy sources. Conventional disposable batteries are not only impractical due to frequent replacement but also pose environmental issues due to their non-rechargeable nature. OPVs offer a sustainable alternative by proposing to convert wasted indoor energy into usable electricity, either as a replacement for conventional batteries or by extending battery life when integrated with rechargeable systems. This shift both reduces the environmental footprint and lowers the operating costs of IoT networks, enhancing their business potential and overall usefulness. Additionally, with the rise of smart wearable devices and the growing emphasis on health and fitness among young people, OPV-powered devices can further benefit these emerging industries.

A key function of a PV harvester is the ability to provide enough energy and power to operate a specific IoT node, with requirements varying by application, electronics technology, wireless communication protocol, and configuration of the energy harvesting system[46-48]. Typical power consumption for personal and household devices, as well as mainstream wireless communication protocols, ranges from µW to W. Indoor ambient light harvesters with small area PV modules (cm²) typically operate at peak power consumption ranging from 10nW to 10mW, ideal for low-power electronic devices. Figure 4[47] highlights that current technological advancements enable personal devices, household appliances, and multiple wireless technologies to operate with average power consumption lower than that supplied by an IPV module, enabling sustained IoT nodes within buildings. However, devices like mice, smartwatches, standard Bluetooth, and SigFox systems, which consume between 10–100 mW on average, may require small outdoor solar panels for adequate power supply. Technologies needing more than 100 mW, such as smartphones, Wi-Fi, and 5G small cells, would necessitate larger solar panels for autonomous operation[47,49].

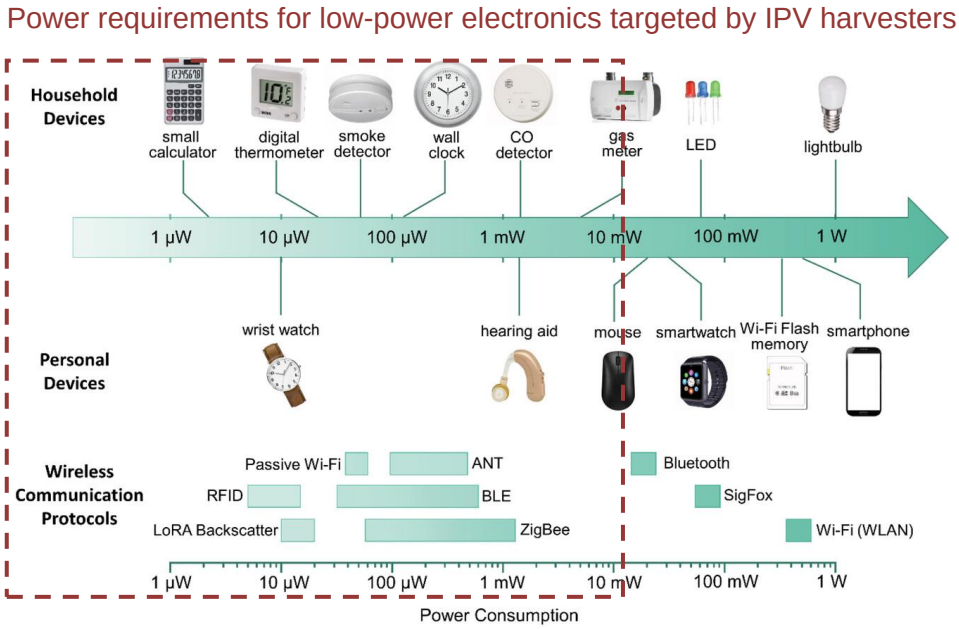

Figure 4. Power requirements associated with typical home and personal devices and popular wireless communication protocols.

The scientific interest in IPV has surged over the last two decades, as evidenced by the rapid increase in scientific publications on this topic. Figure 5a provides a visual representation of the main areas of focus in these publications over the last 15 years. The majority of the research has concentrated on the development of IPV devices, including materials,

architectures, and design of IPV. Meanwhile, studies have been conducted on the integration of cells onto indoor devices, such as power management circuits, schemes, and elements: indoor applications, indoor lighting conditions, and simulation studies on IPV and characterization and setups. The IPVs market has experienced remarkable growth in the past twenty years, fueled by advancements in the development, commercialization, and cost reduction of low-power electronic devices used in the IoT. The IPV market was valued at USD 850 million in 2023[1] and is estimated to reach USD 1.5 billion by 2030[50], with further expansion expected in subsequent years. By 2030, the market value of IoT-connected devices is forecasted to surpass USD 30 billion per year, with the wireless sensor segment alone anticipated to achieve USD 8 billion (Figure 5b) [50].

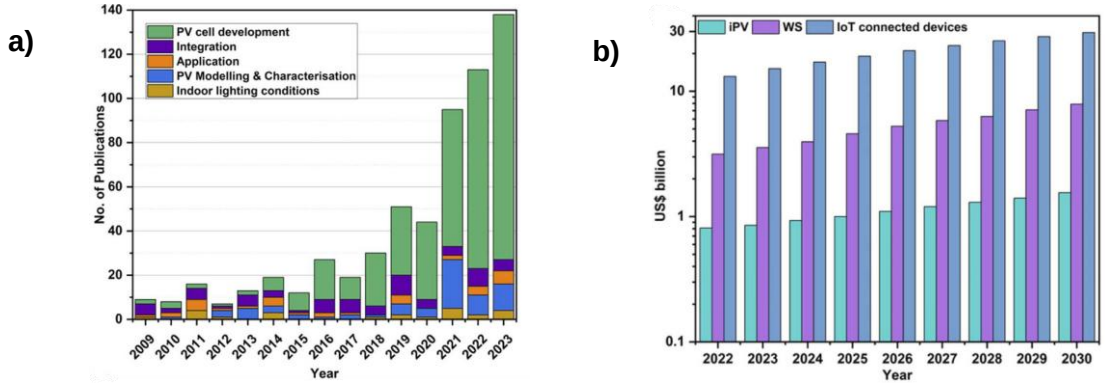

Figure 5. The influence of IPVs in both literature and markets. a) Number of publications on IPVs, with an annual breakdown by focus area. b) Estimated market growth of IPV and WS (wireless sensor) in billions of dollars and the number of IoT-connected devices[1].

I.3. Indoor light sources for PVs

IPV systems rely heavily on indoor lighting as their primary energy source, highlighting the critical need to understand the spectral characteristics of different light sources to optimize IPV device performance. Familiar indoor artificial light sources include compact fluorescent lamps (CFLs), halogen lamps, and various types of white LEDs, such as cold and warm variants. CFLs and white LEDs emit light predominantly in the visible spectrum, typically ranging from approximately 400 nm to 750 nm, as shown in Figure 6a[48]. LEDs emit light in a broader and more consistent spectrum than CFLs. In particular, CFLs have distinct peaks at 420 nm, 480 nm, 550 nm, 600 nm, and 630 nm. Cold white LEDs show peaks around 440 nm and 550 nm, while warm white LEDs show peaks around 450 nm and 600 nm (Figure 6b). In contrast, halogen lamps emit light over a broader range of wavelengths from around 300 nm to 900 nm, characterized by a less defined emission profile. These light sources have different spectral distributions, with luminous intensities typically ranging from 50 lux to 2000 lux. Most indoor environments require illumination levels below 1000 lux, as shown in Figure 6c.

The standard AM 1.5 global solar spectrum, with an intensity of 100 mW/cm², contrasts sharply with typical indoor lighting levels, which are generally less than 1 mW/cm², representing an intensity 100 to 1000 times lower intensity than AM 1.5G. For outdoor conditions, the International Electrotechnical Commission (IEC) has long-established protocols for measuring photovoltaic current-voltage characteristics, illustrated by IEC 60904-1 since the 1980s. The Standard Test Condition (STC) defines the electrical performance of PV cells and modules, assuming 1000 W/m² (100 mW/cm²) solar irradiance, AM1.5 spectrum, and a cell temperature of 25°C. Conversely, IPV technologies have recently received focused attention. The IEC introduced the technical specification 'Nano-enabled photovoltaics - Device evaluation method

for indoor light' (IEC TS 62607-7-2) in 2023[51]. This specification requires measurements at three different light levels (50 lux, 200 lux, and 1000 lux) to ensure the linearity characteristics of IPV devices. It serves as a critical resource for establishing standardized guidelines and defining optimal testing parameters for IPV systems, facilitating consistent measurements and meaningful comparisons across various technologies and architectures of IPV devices under standardized Indoor Standard Test Conditions (ISTC)[49]. Further details on this topic are discussed in Chapter II.5.2.

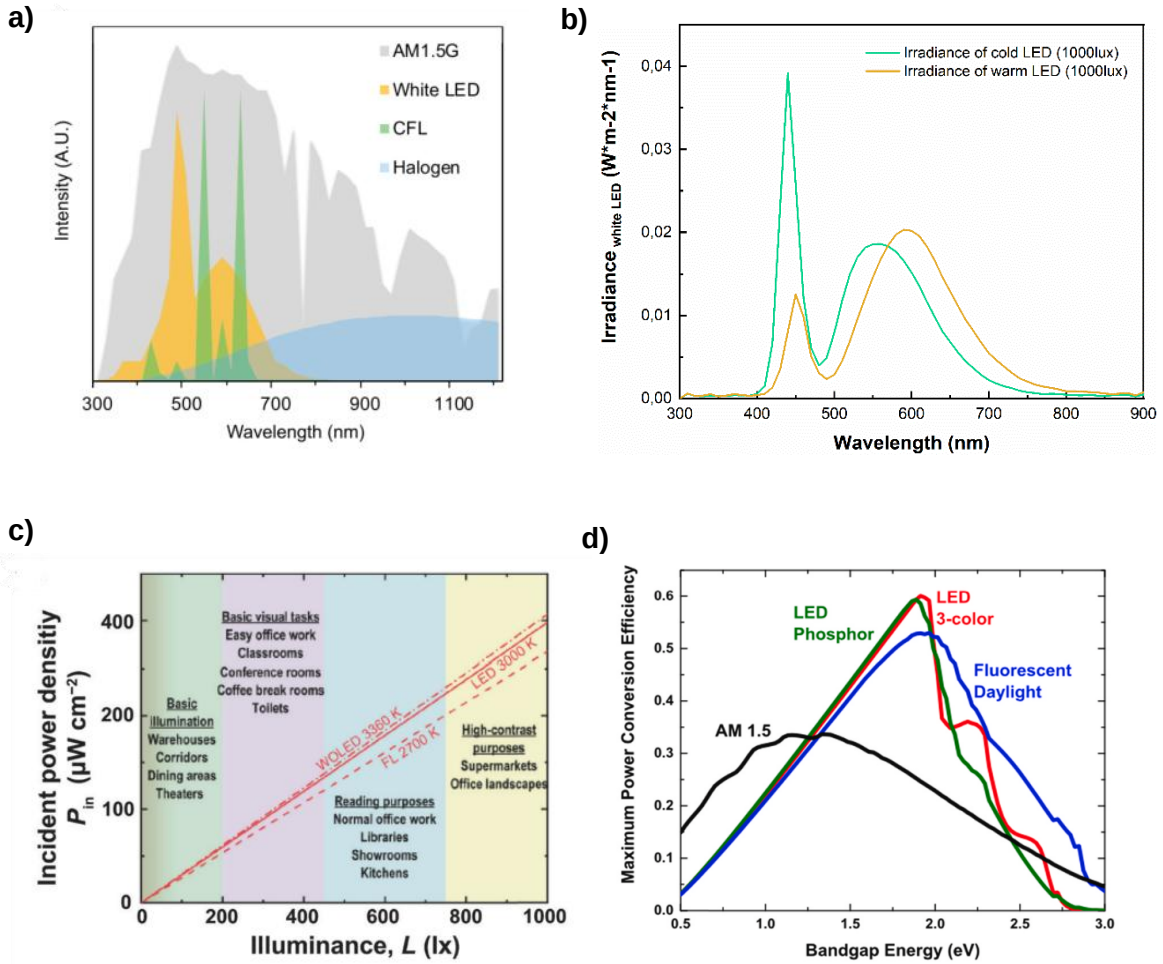

Figure 6. a) Normalized emission spectra of different light sources and standard AM 1.5.[48] b) Comparison of emission spectra for cold and warm LEDs. c) Under the same illuminance, different light sources have different power inputs (Pin), depending on the specific light source, color rendering, and the sensitivity of the human eye.[52] d)Theoretical maximum PCE is calculated by limiting the Shockley-Queisser using the ideal bandgap energy E_g under different light sources.

Due to significant differences in emission spectra and intensity between indoor and outdoor conditions, the requirements for photoactive materials in IPV systems differ from those used in outdoor solar cells. The theoretical maximum PCE of single-junction PV devices can be calculated using the Shockley-Queisser method, as shown in Figure 6d[53]. This calculation assumes that all photons above the material's band gap are absorbed and carriers are thoroughly extracted. For indoor LED lighting, the ideal bandgap energy is approximately 1.9-2.0 eV, resulting in a maximum theoretical PCE approaching 60%. This bandgap energy is well matched to the spectral characteristics of typical indoor lighting, emphasizing the need for photoactive materials with medium to large bandgaps and narrow visible absorption spectra within the visible range to capture photons from artificial light sources effectively. In contrast,

under standard AM 1.5 conditions (outdoor sunlight spectrum), the ideal bandgap narrows to about 1.3 to 1.4 eV, resulting in a maximum theoretical PCE of about 33%. These differences highlight that materials for indoor applications must have medium to large bandgaps and narrow absorption spectra in the visible range to capture photons emitted by indoor lighting effectively. In contrast, outdoor solar cells require smaller band gaps and broader absorption spectra to capture a wider solar spectrum, even though this may lead to a reduction in the open-circuit voltage (V_{OC}).

In addition to material selection, differences between indoor and outdoor conditions can also affect the electrical characteristics of PV devices, especially those related to the resistance element of the equivalent circuit model. The series resistance (R_s) and shunt resistance (R_{SH}) play a crucial role in determining performance. Indoor environments with lower light intensities can tolerate slightly higher R_s values because the reduced current lessens the negative effects of resistive losses. On the other hand, R_{SH}, which represents the leakage paths within the cell, must be kept high for efficient operation in both environments, especially in low-light conditions where the current is already small and its impact is more obvious. Therefore, optimizing these resistances is critical to ensure the efficient operation of PVs in both indoor and outdoor environments.

I.4. Technologies for IPV

There is a diverse range of PV technologies designed for implementing the PV effect in indoor applications, which can be categorized into three generations based on technological evolution and materials, as shown in Figure 7.

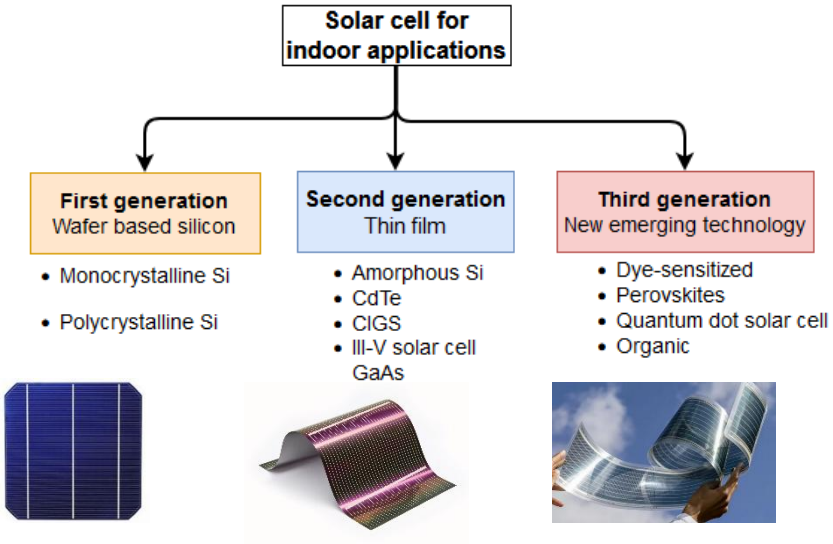

Figure 7. Three generations of solar cell technologies for indoor applications

Table 1. Maximum PCEs of different generation PV technologies under solar illumination (AM1.5G solar spectrum) and typical indoor illumination conditions.[54]

IPV Technologies	1-Sun Efficiency (STC)	Light Sources	Intensity (lux)	Indoor PCE_{MAX} (%)	Ref
First generation					
mono-Si	26.1	LED	890	9.65	[55]
poly-Si	23.3	LED	1000	4	[56]

Second generation					
a-Si	9.97	LED	1000	17.68	[57]
a-Si:H (with high-gap triple-layers)	6.66	w-LED	1000	29.9	[58]
$Al_{0.2}Ga_{0.8}As$	13.6	LED	580	21.1	[59]
GaInP		c-LED	500	39.9	[60]
Third generation					
DSSC	13	CFL	1000	35.6	[61]
Perovskite ($FAPbI_3$ with passivator APO at RT)	24.73	LED	1000	41.71	[62]
Perovskite ($FAPbI_3$ with passivator APO at 198K)	24.73	LED	1000	45.51	[62]
OPV (2PACz/PM6:Y6:2PACz)	16.5	LED	1000	36.5	[4]

The first generation of solar cells is based on inorganic materials, primarily silicon, including monocrystalline silicon (mono-Si) and polycrystalline silicon (poly-Si), which dominate the solar market. In 2022, monocrystalline silicon accounted for 96% of PV shipments, a substantial increase from 36% reported in 2015[63]. These technologies were initially developed and optimized for outdoor energy harvesting but have also been characterized under low illumination conditions for indoor applications. Mono-Si stands out with a record solar efficiency of 26.1% under standard conditions (1 sun) [56], owing to its broad absorption spectra. However, its efficiency under ambient indoor lighting is around 9.65% at 890lx[55], influenced by its narrow bandgap of around 1.1 eV, susceptibility to Shockley-Read-Hall recombination at low light intensities, and lower shunt resistance in tested devices[59]. In comparison, polycrystalline silicon achieves a solar efficiency of 23.3% under 1-sun and about 4% under LED illumination at 1000 lux conditions[56]. Despite their efficiency achievements, the high manufacturing costs associated with silicon-based PVs and their limitations under indoor lighting conditions remain notable limitations for these technologies in IPV applications.

The second generation of indoor photovoltaic cells represents a shift from traditional silicon-based technologies to embrace a range of thin-film alternatives, prominently including amorphous silicon (a-Si). Alongside these advancements, significant research has focused on exploring other inorganic materials such as cadmium telluride (CdTe), copper indium gallium selenide (CIGS), and III-V group materials such as gallium arsenide (GaAs). These materials offer distinct advantages over first-generation crystalline silicon cells, including flexibility, lightweight construction, and improved performance. In particular, III-V semiconductors offer high and adjustable bandgap energies that are well-matched to the spectral characteristics of indoor lighting, making them promising candidates for indoor solar cells. Among III-V semiconductors, GaAs-based solar cells have demonstrated remarkable efficiencies, with Teran and colleagues achieving up to 21.1% conversion efficiency using $Al_{0.2}Ga_{0.8}As$ solar cells under LED illumination at 580 lux[59]., surpassing the performance of silicon PV technologies. In addition to III-V materials, other inorganic semiconductors such as gallium indium phosphide solar cells have also been investigated for indoor applications, with a band gap of 1.89 eV showing a record efficiency of 39.9% under 500 lx cold white LED light, as illustrated in Table 1.

The challenges posed by the high manufacturing costs and low indoor performance of first- and second-generation solar cells under indoor conditions have led to a shift in photovoltaics towards the exploration of third-generation technologies. Among these, dye-sensitized solar cells (DSSCs), perovskite solar cells (PSCs), quantum dot solar cells, and OPVs stand out as compelling alternatives due to their cost-effectiveness, lightweight nature, and remarkable

tunable absorption properties. Since 2019, the optimization and development of IPVs have mainly focused on these emerging PV technologies, with OPVs leading the way over the other types (Figure 8a).

DSSCs have achieved a peak efficiency of 13% under 1-sun at STC. Although their outdoor performance is relatively modest compared to other emerging PV technologies, DSSCs continue to be a focus of research due to their many advantages: the use of environmentally friendly photoactive materials, a simple manufacturing process, and suitability for indoor light environments. Significant improvements in DSSC performance for indoor conditions have been achieved through material innovations, in particular, the development of new dyes and co-sensitizers. Recently, DSSCs have exhibited an outstanding PCE of nearly 35.6% under 1000 lux FL light[61], with a high V_{OC} of 0.9 V and an FF of about 83%, using a device engineering strategy that suppressed charge recombination in a co-sensitized D35:XY1 with a bandgap of 1.8 eV. This was achieved by using Cu(II)/Cu(I) electrolytes with a 2,9-dimethyl-1,10-phenanthroline (DMP) ligand as an additive. A notable challenge, however, is the need to avoid the use of certain materials, in particular platinum and ruthenium, as electrodes due to their non-preference for commercialization.

PSC represents the latest scientific and technological development in the PV community. PSCs offer compelling properties, including a high absorption coefficient, long carrier lifetime, low recombination rate, high defect tolerance, and excellent PCE under STC. These advantages stem from their distinctive crystal structure, which is characterized by a three-dimensional arrangement of metal cations typically forming a metal halide octahedron surrounded by anions. The general chemical formula for perovskite materials is ABX_3, where the A site can be occupied by single cations such as methylammonium (MA), formamidinium (FA), cesium (Cs), or a combination of Cs-FA-MA triple cations. The B site is typically occupied by lead (Pb), while the X site is filled by halide or mixed halide ions. Notably, PSCs exhibit exceptional performance under indoor conditions due to their ability to tune the bandgap through halide substitution. In 2019, Cheng and his group demonstrated the importance and potential of mixed halide ions (I/Br/Cl triple-anion perovskite) in achieving not only a tuned bandgap but also suppressed trap states under 1000lux fluorescent light. Using an indoor bandgap of 1.8 eV and an ultra-low trap-state density, they achieved a record-high PCE of 36.2% and a remarkably high V_{OC} of 1.028V[64]. Other strategies, such as suppressing interfacial carrier recombination and stabilizing the perovskite layer by passivating defects in the internal PSCs, were also used to improve efficiency. In 2021, Chong and his group achieved an outdoor efficiency of over 21% and an indoor efficiency (at FL 1000 lux) of over 40.2% by incorporating tomato lycopene as a surface modification layer on the perovskite absorber. This modification prevents moisture and oxygen erosion, thereby improving both intrinsic and environmental stability[65]. Recently, Wang et al. employed a coordinated passivation strategy, using a multifunctional organic additive, 6-methoxynicotinamide hydrochloride (APO), to enhance the carrier dynamics of perovskite films under dual extreme conditions of low temperature and low light. This refined passivation effectively suppressed energy loss induced by intrinsic defects within the perovskite under these challenging conditions. As a result, the optimized solar cells achieved an impressive efficiency of 41.71% under low light at room temperature and an even higher efficiency of 45.51% under combined low temperature and low light conditions [62]. The superior performance of perovskite solar cells under these extreme conditions is promising for the application of IPVs in regions with harsh climates, such as polar regions and outer space. While perovskite solar cells have shown great promise, they still face

significant challenges, including issues of stability, toxicity (due to lead content), and scalability. Researchers and engineers are actively working to overcome these challenges.

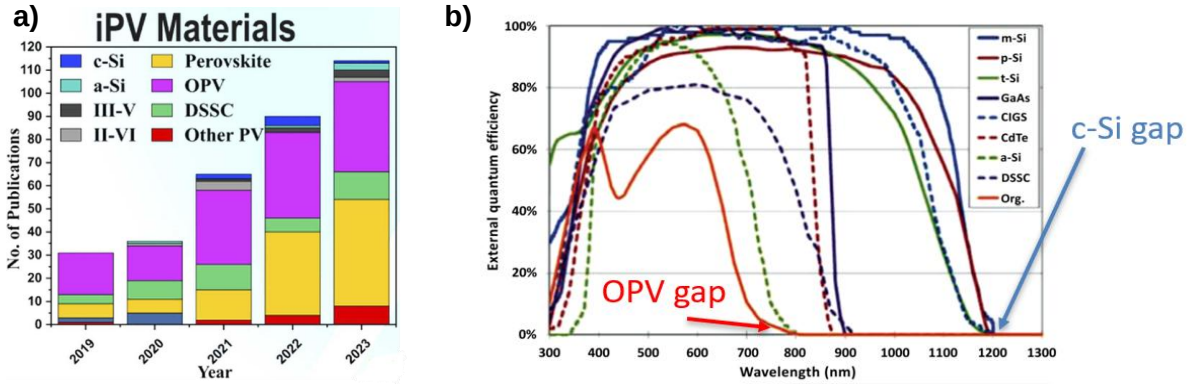

Figure 8. a) Publication on IPV cell development divided by class of materials. b) EQE spectra for various PV technologies.

Organic materials have gained considerable attention as an alternative to inorganic materials for solar cells due to their versatile properties, including tunable optical properties, potential for transparency, flexibility, lightweight, and low-cost manufacturing. These advantages, combined with solution-processability, enable scalable production techniques such as inkjet printing, slot-die coating, and roll-to-roll processing. In addition, the EQE spectra in Figure 8b highlight the bandgaps of various photovoltaic technologies, including OPVs and c-Si. The OPV gap is shown to be well-aligned with the indoor light spectrum, particularly in the 400 to 700 nm range, which is dominated by artificial light sources like LEDs and fluorescent lighting. As a result, OSCs are increasingly recognized for their adaptability to a wide range of applications, from portable power solutions to building-integrated photovoltaic (BIPV) systems. To date, several companies, such as Dracula Technologies[43] in France, Epishine[66] in Sweden, and Ribes Tech[67] in Italy, have already commercialized OPV devices that are actively used in IoT applications. With their scalability well-established, OPVs are poised to play a significant role in the future of sustainable energy solutions[68].

Unlike inorganic semiconductors, which have high dielectric constants facilitating the immediate generation of free charge carriers upon light absorption, organic semiconductors typically produce exciton-bound electron-hole pairs, with Coulombic attraction, around 0.5 eV, due to their lower dielectric constants. This binding energy significantly exceeds the thermal energy available at room temperature, so additional energy is required to dissociate these excitonic pairs to generate charge carriers effectively. To overcome this problem, the active layer of an OSC is engineered with electron donor materials coupled to electron acceptor materials with suitable energy levels. At the donor-acceptor (D/A) interface, the energetic mismatch of the molecular orbitals provides sufficient driving force to split these tightly bound excitons. The development of novel OPV materials, innovative device structure engineering, and advanced interfacial engineering have driven recent advancements in OPV technology. Despite their limitations, OPVs have attracted considerable attention in the IPV field and have shown significant improvements in performance over the years. In particular, Kim and his team have reported a breakthrough PCE of up to 36.5% under 1000lux LED illumination using a strategy that employs a 2-(9H-carbazol-9-yl) phosphonic acid (2PACz) as both the HTL layer and the additive with a photoactive layer of PM6:Y6 (where PM6 is a donor polymer, and Y6 is a NFA, described in detail in Chapter III.1)[4]. The use of 2PACz induces spontaneous vertical

phase separation in the photoreactive layers, creating a vertical component distribution that significantly improves the carrier yield-mobility product. This enhancement effectively suppresses trap-assisted recombination and reduces leakage current in IOPVs. In addition, treating ITO with 2PACz, which contains phosphonic acid groups, results in a significant increase in work function due to a vacuum-level shift. This shift ensures efficient energy-level alignment, thereby improving charge selection at the hole-selective interface.

OPVs are being developed not only on glass but also on flexible substrates such as polyethylene terephthalate (PET)[36,69] and polyethylene naphthalate (PEN). PET is particularly favored due to its transparency, low cost, lightweight nature, excellent flexibility, and compatibility with the large-scale roll-to-roll deposition process. To date, flexible IOPVs using PET have achieved efficiencies of up to 29% under 1000 lux LED illumination. This performance has been achieved by using an active layer composed of a commercial low bandgap copolymer donor and a fullerene derivative acceptor[36].

I.5. How does OPV work?

The working principle of OPVs is to convert light energy into electrical energy through a series of key steps, as shown in Figure 9a. At the core of OPV operation are organic semiconductors, such as polymers and small molecules, which are characterized by π-conjugated systems. These systems consist of alternating single C-C bonds and double C=C bonds, enabling the delocalization of π electrons along the polymer or small molecule chain via π (Pz) orbitals. This delocalization promotes electrical conductivity, a key property for generating electric current in OPV devices. The photoactive layer of an OPV usually consists of two main components: donor material and acceptor material. Donor materials, such as conjugated polymers and small molecules, possess electron-donating properties, whereas acceptor materials, including FAs and NFAs, possess electron-accepting and electron-transporting properties. Together, the donor material and the acceptor material form a blend that supports the separation of photogenerated excitons (bound electron-hole pairs) into free charge carriers that can be extracted to generate an electric current. This process involves four basic steps: light absorption, exciton diffusion, exciton dissociation, and charge transport and collection.

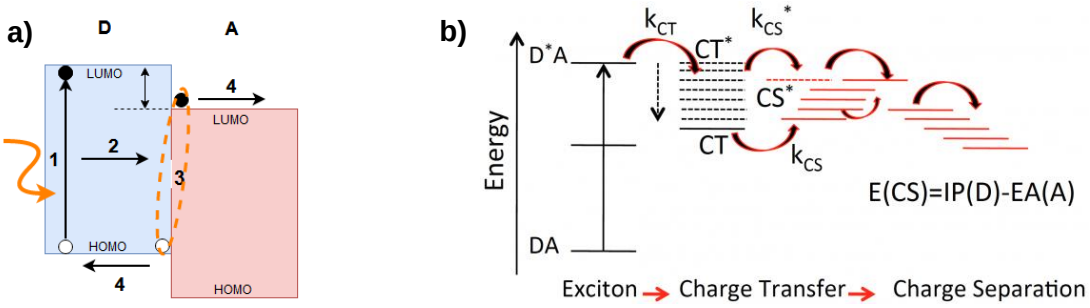

Figure 9. a) Photocurrent generation process (1) light absorption and excitation creation, (2) diffusion of the excitation to the D/A interface, (3) exciton dissociation into free charge carriers (CT-state), (4) charge extraction. b) An electronic state diagram shows the excitonic state, CT state, and CS state.

Light absorption and excitation creation

When an organic material absorbs photons from light, an electron is excited from the HOMO to the LUMO, forming an exciton. Excitons are essentially electron-hole pairs bound by Coulombic interaction. The exciton binding energy is generally quite strong in organic materials

(in the order of 0.3-1 eV), resulting from a low dielectric permittivity, leading to short-lived excitons that rapidly recombine.

Diffusion of the exciton to the D/A interface:

For the exciton to generate a photocurrent, it must diffuse to an interface between the donor and the acceptor materials within its short lifetime. The exciton diffusion length (L_D) is typically in the range from 10 to 20 nm, which represents the average distance an exciton can travel within materials before geminate recombination occurs. If the exciton does not reach the D/A interface within this diffusion length, it will recombine and lose its energy as heat. Therefore, efficient OPV design requires careful control of morphology to ensure that the donor and acceptor phases are finely intermixed so that excitons can efficiently reach the interface.

Exciton dissociation into free charge carriers

Once the exciton reaches the D/A interface, it dissociates into a free electron and a free hole due to the energy offset between the LUMO of the donor and the LUMO of the acceptor materials. This process creates a charge-transfer (CT) state (Figure 9b), where the electron and hole are still bound due to Coulombic attraction but are located on neighboring molecules. If the separation between electrons and holes exceeds the Coulomb trapping radius, the CT state transforms into a charge-separated (CS) state, where electrons and holes are free carriers and can migrate independently.

Charge transport and extraction

In the last step, the free electrons and holes travel through their respective transport layers: the electron transport layer (ETL) and the hole transport layer (HTL). The electron migrates toward the cathode, and the hole migrates toward the anode. These charge carriers are then collected at their respective electrodes, generating an electrical current.

The mechanisms responsible for driving charge transport and collecting at electrodes involve several key factors:

Work function difference between electrodes: The difference in work function between the cathode and anode creates a built-in electric field throughout the device. This field helps separate the excitons and drives the transport of electrons and holes toward their respective electrodes. The cathode with a lower work function preferentially collects electrons, while the anode with a higher work function attracts holes, thus facilitating efficient charge extraction.

Diffusion of charge carriers: In areas of high carrier concentration (usually near the donor/acceptor interface), charge carriers diffuse to areas of lower concentration near the electrode. This diffusion process is critical, especially when no external bias is applied, because it keeps the current flowing even under open-circuit conditions but at a lower efficiency.

Electric field-induced drift: When an external bias is applied (for example, under operating conditions in the short circuit or forward bias region), an additional electric field is generated across the device. This field enhances the drift of charge carriers toward their respective electrodes, significantly improving the efficiency of charge extraction under operating conditions.

These factors also explain the behavior seen in the current-voltage (J-V) curve, as shown in Figure 10. The underlying mechanisms of IOPVs are similar to those of outdoor (AM 1.5G) OPVs, and the key difference lies in the different light environments. IOPVs must be optimized

to capture low-intensity light with a narrow emission spectrum, while outdoor OPVs are designed to absorb the broader, more intense solar spectrum.

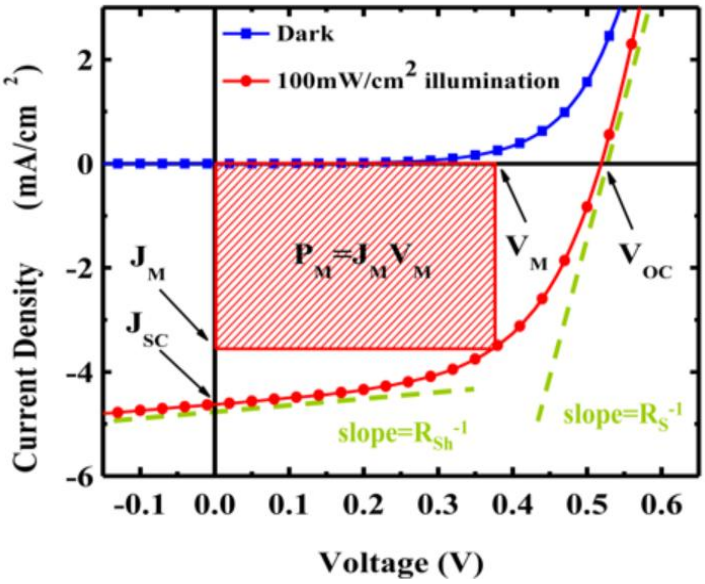

Figure 10. Typical J-V curve of an OSC device in dark and under 100mW/cm^2 illumination [70].

In the short-circuit region (zero applied voltage), charge extraction is mainly driven by the built-in electric field and diffusion, resulting in high photocurrent. As the applied voltage increases toward the open-circuit region, the internal electric field begins to hinder charge extraction, thereby reducing the current output. In the power generation region (between open-circuit and short-circuit conditions), diffusion and drift work together to extract maximum power, which is reflected in the maximum power point (MPP) of the JV curve.

The behavior of solar cells can be represented by an ideal single-diode equivalent circuit model, which simplifies the complex physical processes occurring inside the cell. As shown in Figure 11, the equivalent circuit of an OSC consists of four main components: a photocurrent source, a diode, R_S, and R_{SH}[71].

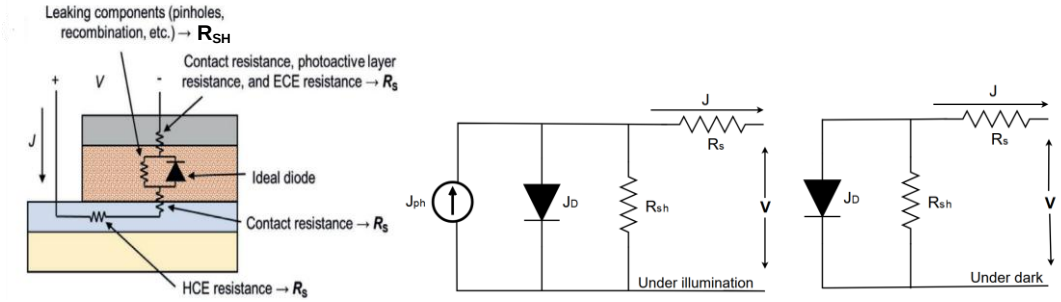

Figure 11. a) Realistic OPV with parasitic resistance[72]. b) Equivalent circuit model of an OSC under illumination and dark conditions.

The J-V characteristics of the OPV reveal that the total current is the sum of the dark current and the photogenerated current. As shown in Figure 11b, the solar cell under illumination is modeled by a photocurrent source in parallel with a diode, representing the behavior of the p-n junction in the OPV. The photocurrent source, which is directly proportional to light intensity, reflects the generation of current within the device as photons are absorbed by the active layer, creating electron-hole pairs. In an ideal solar cell, these two components alone would be

sufficient to model the device. However, actual solar cells are not ideal. Electrical losses, such as recombination processes in the absorber layer or at the interfaces between different layers, must also be taken into account. These losses are accounted for by including R_S and R_{SH}.

With the equivalent circuit components defined, the resulting current-voltage (J-V) characteristics can be modeled using the Shockley diode equation, as shown in Eq. 1:

$$I_{SC} = I_0 \left[\exp\left(\frac{qV}{nkT}\right) - 1\right] - I_{ph} \quad \text{(Equation 1)}$$

where k is Boltzmann's constant (1.380649 x 10^{-23} $J.K^{-1}$), n is the diode ideality factor, T is the absolute temperature, I_{SC} is the photogenerated current of the solar cell, I_0 is the dark saturation current of the diode, and I_{ph} is the current generated by light.

J-V measurement is a fundamental technique used to evaluate the performance of solar cells. In this method, a source meter is used to apply a controlled voltage bias across the device, and the resulting current flow is measured. There are two primary J-V measurements: the dark J-V curve and the light J-V curve, as shown in Figure 10. In dark conditions, the behavior resembles that of a typical diode, where recombination losses dominate the current. Under illumination, the photocurrent shifts the entire curve downward, generating a measurable J_{SC}, V_{OC}, fill factor (FF), power conversion efficiency (PCE), R_{SH}, R_S.

Open-circuit voltage (V_{OC})

The V_{OC} represents the maximum voltage that a solar cell can generate under open-circuit conditions, where the current density is zero. It is related to the difference between the HOMO of the donor material and the LUMO of the acceptor material in OSCs. Still, it is also governed by charge recombination mechanisms in the device. A key factor in maximizing V_{OC} is to limit the density of states (DOS) in the gap between the acceptor LUMO and the donor HOMO (Figure 12a)[73]. The higher the DOS under the gap, the greater the compound losses, which slows down the rise of V_{OC}. The more states available within the gap, the greater the probability that electrons and holes can recombine, thus reducing the voltage. In general, the V_{OC} is determined by the separation between the electron and hole quasi-Fermi levels, expressed as in Eq. 2:

$$Voc = \frac{1}{q}.(E_{Fn} - E_{Fp}) \quad \text{(Equation 2)}$$

where q is the elementary charge, E_{Fn} is the electron quasi-Fermi energy level, and E_{Fp} is the hole quasi-Fermi energy level. These energy levels are directly related to the DOS, which is influenced by the intensity of the light illumination.

Minimizing the loss of V_{OC} and increasing the V_{OC} in dim light are necessary to achieve a high PCE. However, when the illumination changes from 1-sun conditions to indoor lighting, the V_{OC} of devices will inevitably decrease due to the significantly reduced intensity of indoor light sources. As shown in Figure 12b, the E_{Fn} is shifted downward, and the E_{Fp} is shifted upward under indoor illumination. This explains why the reduction in illumination intensity leads to a decrease in V_{OC}.

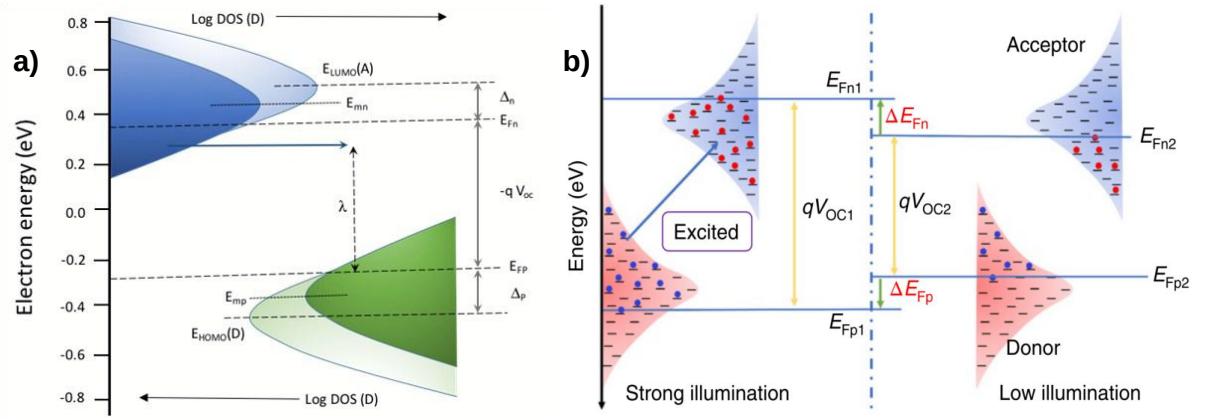

Figure 12. a) Diagram showing the Gaussian DOS for the acceptor HOMO and donor LUMO (line), and the occupied (for LUMO) or unoccupied (for HOMO) states (shaded area) populated by thermalized carriers. These states arise from the kinetic balance between photogeneration and recombination fluxes. The recombination event (horizontal solid arrow) is indicated for a given value of the reorganization energy λ[73]. b)The quasi-Fermi levels and density of states of donors and acceptors under strong and low illumination[74].

V_{OC} can also be derived using the Shockley diode equation (Eq. 1) under illumination, where the net current in the solar cell is set to zero. The following Eq. 3 then gives the relationship between V_{OC} and the photocurrent:

$$V_{OC} = \frac{nkT}{q}.\ln\left(\frac{J_{SC}}{J_0} + 1\right) \qquad \text{(Equation 3)}$$

where J_{SC} is the short-circuit current density and J_0 is the saturation current density. In the case of short-circuit condition (where V = 0), the J_{SC} is equal to the J_{ph} under indoor lighting, the incident light intensity is lower, resulting in a significant decrease in J_{SC}, thus limiting the V_{OC} and the overall PCE of the device.

Short-circuit current density (J_{SC})

J_{SC} represents the maximum current that a solar cell can generate under short-circuit conditions, where the voltage across the solar cell is zero and is directly proportional to the concentration of photogenerated charge carriers in the photoactive material and their mobility. When a solar cell is short-circuited, the external load resistance is reduced to zero, allowing the generated carriers to flow through the circuit without encountering any resistance. As a result, the current density reaches its maximum value, which is determined by the intensity of incident light and the efficiency of the carrier generation and collection within the solar cell. However, under indoor lighting conditions, the photogenerated carrier density is significantly lower than that under 1-sun conditions.

Under illumination conditions, the circuit model can be expressed analytically by applying the Shockley diode equation to derive the Eq. 4 for J_{SC} :

$$J_{SC} = J_{Ph} - J_0\left[\exp\left(\frac{q(V-JR_S)}{nkT}\right) - 1\right] - \frac{V-JR_S}{R_{sh}} \qquad \text{(Equation 4)}$$

where J_{ph} is the light-induced current density.

Fill factor (FF)

The FF is defined as the ratio of the maximum obtainable power (P_{MAX}) to the product of J_{SC} and V_{OC}, as shown in Eq. 5:

$$FF = \frac{P_{MAX}}{J_{SC}.V_{OC}} = \frac{J_{MAX}.V_{MAX}}{J_{SC}.V_{OC}} \quad \text{(Equation 5)}$$

This factor is a measure of the quality of a solar cell and indicates the deviation of the J-V curve from the ideal curve. It represents the ratio of the maximum power obtained to the theoretical power, which can be visualized as the ratio of different rectangular areas within the J-V curve. When the J-V curve more closely resembles a rectangular shape, it reflects a favorable balance between the extraction and recombination of free charge. Under indoor illumination, where light intensity is typically low, fewer photogenerated charges are produced, leading to reduced recombination of non-geminate charge, particularly bimolecular recombination, which can potentially result in a higher FF.[75]

Power conversion efficiency (PCE)

Based on the three PV parameters mentioned above, a mathematical formula has been used to describe the efficiency of a solar cell as Eq. 6:

$$PCE = \frac{P_{out}}{P_{in}} = \frac{J_{SC}.V_{OC}.FF}{P_{in}} \quad \text{(Equation 6)}$$

The PCE of a solar cell quantifies its performance and is defined as the ratio of the maximum electrical power output (P_{out}) to the incident light power (P_{in}). It reflects the balance between the absorbed light energy and the electrical power generated by the cell. The maximum P_{out} is derived from the cell's J_{SC}, V_{OC}, and FF. Under outdoor conditions, Pin is normalized to the AM 1.5 spectrum with an irradiance of 100 mW.m^{-2} at 25°C according to the IEC 60904-3-Ed2. For indoor measurements using light sources such as LEDs or fluorescent lamps (FL), the P_{in} is typically much lower than under sunlight, usually in the range of 0.1 to 3 mW.m^{-2}. According to the Shockley-Queisser limit, the theoretical maximum efficiency for a solar cell under ideal conditions is around 33% for 1-sun outdoor conditions. However, under indoor conditions, where the light spectrum is narrower and intensity is lower, the theoretical maximum PCE can be higher, close to 60%, due to the more optimal bandgap alignment and the reduced thermalization losses. Therefore, improving the PCE of single-junction OPV cells for indoor conditions requires optimizing the design of photoactive materials with an optimal bandgap to maximize the use of incident light, as well as fine-tuning the morphology of the active layer to minimize energy losses due to recombination and resistive losses within the device.

Series Resistance (R_S)

R_s represents the resistance encountered by the current as it flows through the conductive materials, the contact resistance at the interface, and the internal resistance within the OPV device. An increase in R_s results in a greater voltage drop across the R_S, reducing the voltage available for external work. This reduction in voltage lowers the FF and, consequently, the overall efficiency of the cell. Ideally, R_s should approach zero ohms per square centimeter (Ω·cm²). As shown in Figure 10, R_s can be estimated from the slope of the J-V curve near the V_{OC}. The J-V curve is almost linear in this region, and the slope of this linear region gives an approximation of R_s.

Under outdoor conditions (100 mW.cm^{-2}, AM 1.5G), the effect of R_s becomes more pronounced due to the higher light intensities, which increase the photocurrent and, thus, the voltage drop across R_s. Conversely, in an indoor environment, where the photocurrent generated is lower, the voltage drop across R_s is relatively reduced, potentially diminishing its impact compared to outdoor conditions, as shown in Figure 13.

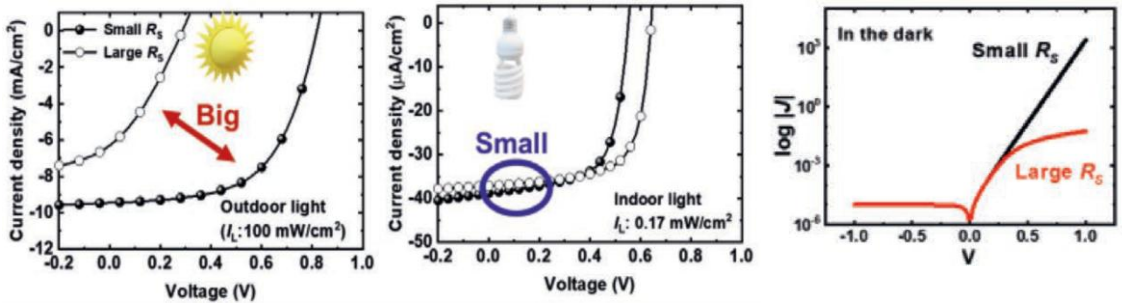

Figure 13. R_s-dependent J-V characteristics under outdoor, indoor light conditions and in the dark[72].

Shunt Resistance (R_{SH})

R_{SH}, also known as R_P, characterizes the extent to which a device is prone to non-ideal current leakage within the photoactive layer. Several factors, including the edges of the cell, the purity and uniformity of the organic active layers, and the presence of defects, traps, pinholes, or impurities, can affect R_{SH}. A high R_{SH} is critical to the performance of the OPV device as it minimizes leakage current, thereby enhancing the V_{OC} and overall device efficiency. Ideally, R_{SH} should be infinitely high to eliminate any leakage current. Under indoor lighting, where photocurrent is reduced due to lower light intensities, minimizing leakage current becomes crucial to achieving high efficiency. In this context, increasing R_{SH} is even more critical than decreasing R_S[76]. Similarly, R_{SH} can be estimated from the slope of the J-V curve near the J_{SC}.

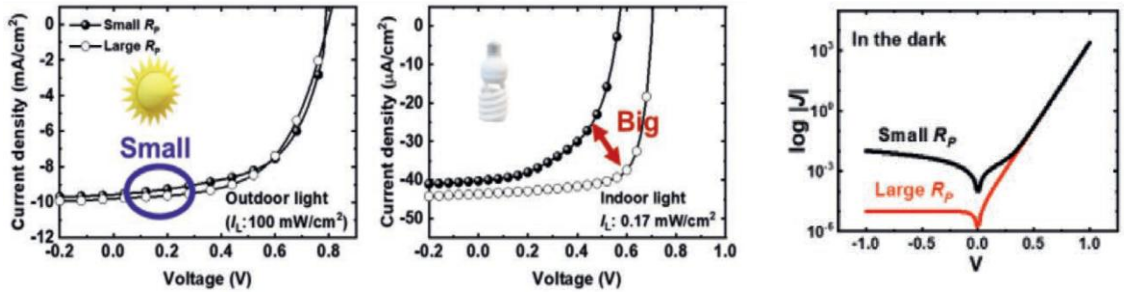

Figure 14. R_{SH}-dependent J-V characteristics under outdoor, indoor light conditions and in the dark[72].

I.6. How to choose OPV materials for room lights

In our research, we will explore various strategies to develop photoactive layer materials suitable for the emission spectrum of artificial light sources, particularly white LEDs. To achieve high photovoltaic performance under indoor lighting conditions, organic photoactive materials should have several interconnected properties according to the following scheme[77]:

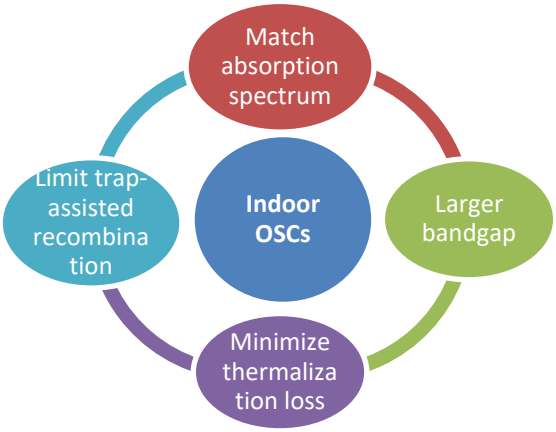

Matching the absorption spectrum to the indoor light response:

Organic photoactive materials should have an absorption spectrum that matches well with the spectrum distribution of indoor light sources, which typically cover a wide range of wavelengths within the visible spectrum (400 to 700 nm), such as LEDs or fluorescent lights. Therefore, the organic materials should efficiently absorb light within this range to maximize photon capture and conversion efficiency while minimizing the thermalization of photogenerated charges. In addition, the materials should have a high absorption coefficient and be able to efficiently absorb photons even at lower light intensities, which is typical of indoor environments.

Utilizing large-bandgap material systems:

As discussed earlier, the ideal bandgap energy for OPV materials under indoor LED illumination is approximately 1.9–2.0 eV, as determined by the Shockley-Queisser limit calculation. This bandgap allows for efficient absorption of visible light, which is the predominant component of indoor lighting.

Minimizing thermalization losses through energy level engineering:

For optimal OPV cell performance, the LUMO level of the donor semiconductor is usually higher than that of the acceptor semiconductor, with an energy shift of typically about 0.3 eV[78]. This offset is generally believed to be sufficient to provide the driving force required for efficient exciton dissociation, a concept that has been well recognized in fullerene-based OSCs. However, with the rapid development of non-fullerene small molecule acceptors, many non-fullerene OSCs have been demonstrated to achieve efficient exciton dissociation even at much smaller energy level offsets[79]. These minimal offsets not only facilitate charge separation but also reduce energy losses (E_{LOSS}), thereby improving photovoltaic performance by minimizing thermalization losses[80].

Limiting trap-assisted recombination:

Under low illumination conditions, as shown in Figure 12b, the reduction in photocurrent limits the ability to fill all trap states within the band gap, thereby limiting the V_{OC}. Trap-assisted recombination becomes more pronounced at low photocurrent levels, providing pathways through which charge carriers can recombine before extraction, resulting in additional V_{OC} losses. In other words, in lower-intensity indoor lighting, minimizing leakage current is critical for high efficiency. Therefore, maximizing the R_{SH} is crucial as it suppresses leakage current and mitigates the impact of trap-assisted recombination, helping to maintain V_{OC}[76].

I.7. OPV device architecture

As IOPVs have gained significant attention over the last decade, considerable efforts have been made to improve the performance of OPV technologies under indoor lighting conditions. In addition to advances in materials, innovations in device architecture and interfacial engineering continue to push the boundaries of what can be achievable with OSCs. Each configuration has its trade-offs, and it is essential to examine the architectural developments in IOPV. A typical OSC consists of several key components, as shown in Figure 15: an active layer, electrodes, an electron transport layer, a hole transport layer, and a substrate.

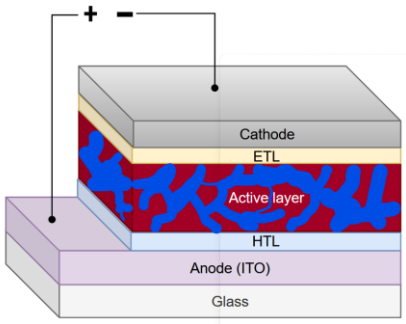

Figure 15. Schematic of an OSC structure

The active layer consists of light-absorbing materials, typically electron donor (p-type) and electron acceptor (n-type) materials. These materials convert light photons into free charges, initiating the generation of electrons and holes.

Electrode layers, known as the anodes and cathodes, collect the electrical current generated by the OSC. They are located at the top and bottom of the OSC and have different functions. In a direct OSC, the anode electrode is often a transparent conductive oxide such as indium tin oxide (ITO) due to its high conductivity and transmittance. The cathode is usually made from metals such as silver and aluminum.

The Electron Transport Layer (ETL) is located between the active layer and the cathode electrode. Its primary function is to facilitate the movement of electrons toward the cathode while blocking holes, leading to selective contacts, which drastically enhance the overall performance of the device. ETL materials, which can be either organic or inorganic, allow efficient electron transport and prevent recombination, thereby increasing cell efficiency. For optimal performance, the ETL should ideally have an appropriate energy level that matches both the electrode and the active layer, as well as high visible transparency and high electron mobility. In indoor conditions, various ETLs have been studied for their effectiveness, including PFN[81], TiOx[81], ZnO[29,82], SnO_2[83], and PDINO[84]. These materials have been selected for their ability to improve charge extraction and transport, contributing to the overall higher efficiency of IOPV devices.

The hole transport layer (HTL) is located between the active layer and the anode electrode and facilitates the movement of photogenerated holes toward the anode while blocking electrons. HTL materials can be organic polymers, small molecules, or inorganic substances such as MoO_3[24]. A widely used organic polymer for HTL in OSCs is poly(3,4-ethylene dioxythiophene): polystyrene sulfonate (PEDOT:PSS)[85] due to its water solubility at low temperatures. With its high hole mobility and work function, PEDOT:PSS helps prevent interfacial hole-electron recombination, further enhancing cell efficiency. Recent advancements in OPVs have achieved impressive PCE using 2-(9 H-carbazol-9-yl)

phosphonic acid (2PACz)[4] as the HTL and as an additive in a PM6:Y6 blend. The incorporation of 2PACz, with its phosphonic acid groups, onto ITO substrates induces a sufficiently large work function shift through a vacuum-level shift, thereby facilitating effective energy-level alignment and enhancing charge selection at the hole-selective interface. The device, fabricated with an ITO/2PACz/PM6:Y6:2PACz/PDINO/Ag architecture, exhibited efficiencies of around 36.5% under 1000 lx LED illumination. In addition, these devices retained 95% of their initial efficiency after 1000 hours of operation in ambient air.

The substrate, usually made of transparent materials such as glass or plastic, allows light to pass through to reach the active layer.

Various structures and strategies have been developed to enhance the photovoltaic conversion efficiency of organic cells. Some of these are included in Table 2:

Table 2. Summary of maximum PCEs of different architecture OPV technologies under solar illumination (AM1.5G solar spectrum) and typical indoor illumination conditions.

OPV	Active layer	Light sources	V_{OC} (V)	J_{SC} (Indoor: μA.cm^{-2} Sun: mA.cm^{-2})	FF (%)	PCE_{MAX} (%)	ref
Bilayer	PM6:IDIC	LED 1000 lux	0.835	103	66.3	19.6	76
		Sun	0.954	12.9	60.6	7.8	76
BHJ	PM6:Y6:2PACz	LED 1000 lux	0.720	146.6	77.0	36.5	4
		Sun	0.842	27.4	71.2	16.5	4
Ternary	PM6:IT-4F:ITIC-Th	LED 500 lux	0.75	74.73	77.1	30.1	86
		Sun	0.89	20.13	64.3	11.5	86

I.7.1. Bilayer

Bilayer OPVs have also been studied for their potential in indoor energy harvesting applications. In a bilayer OPV, the active layer consists of two distinct layers: a layer of electron donor material and a layer of electron acceptor material. These layers are deposited separately as separate layers on top of each other. The interface between the donor and acceptor layers facilitates the separation of excitons into free charges, which can then be collected at the respective electrodes to generate an electrical current. This charge separation is crucial to the efficient operation of the solar cell. In essence, the bilayer OPV structure allows for a more controlled arrangement of the donor and acceptor materials, potentially leading to better charge transport and reduced recombination losses by minimizing trapped charge carriers in isolated domains or non-ideal interfaces where there is direct contact between the donor and the ETL or the acceptor and the HTL. A schematic diagram of the bilayer is shown in Figure 16 below.

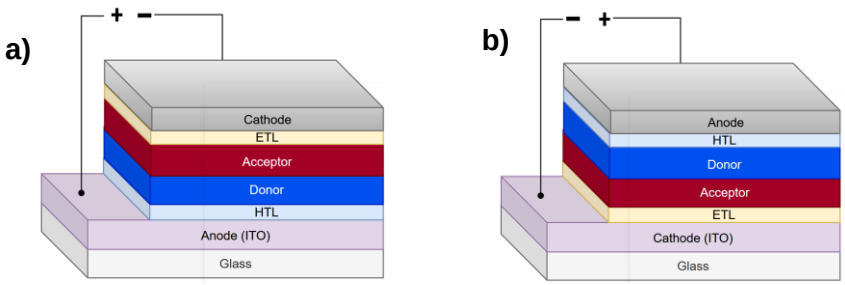

Figure 16. Structure of a bilayer organic solar cell in the traditional n-i-p (a) and inverted p-i-n (b) polarity.

In 2022, Park, S. Y. and his team demonstrated that under 1 Sun, PM6:IDIC BHJ devices exhibit better OPV performance compared to bilayer devices. However, this trend is reversed under indoor lighting conditions, with PM6:IDIC bilayer devices showing a higher P_{MAX} of 62.6 μW cm^{-2} compared to 54.6 μW cm^{-2} for BHJ OPVs under 1000 lux LED. The significant drop in P_{MAX} for BHJ devices under indoor light is primarily due to a significant decrease in V_{OC}. In contrast, the bilayer devices show a much smaller V_{OC} drop and a considerable increase in FF, resulting in a higher P_{MAX} under indoor light. These improvements are attributed to the high R_{SH} provided by the ideal interfacial contacts between the photoactive layer and the charge transport layers (i.e., pure donor layer contacting HTL and pure acceptor layer contacting ETL), as illustrated in Figure 17[76]. The consistently high R_{SH} regardless of light intensity, demonstrates the suitability of bilayer OPVs for various indoor lighting conditions. As mentioned before, in low-light conditions, a high R_{SH} is more important than a low R_S because leakage current has a more significant impact on the performance at low light intensity.

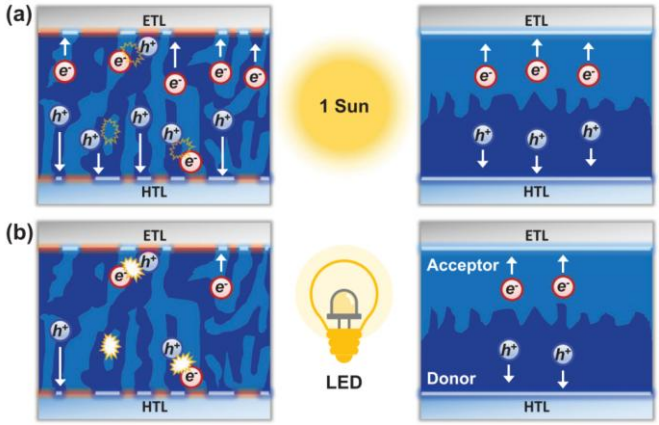

Figure 17. A schematic shows charge transport and recombination in BHJ (left) and bilayer (right) devices under a) 1-sun and b) LED indoor light. Dark blue is the donor layer, and light blue is the acceptor layer. Red highlights indicate undesirable contacts in BHJ devices.[76]

I.7.2. BHJ

Currently, BHJ photoactive layers are the most intensively studied and highest-performing OPV systems since 1995[16]. In BHJ structures, electron donor and acceptor materials are blended to form a bicontinuous network of interpenetrating nanoscale phases. This bicontinuous three-dimensional network increases the interface area between the donor and acceptor. It should also match the dimensionality of the exciton diffusion length L_D, thereby increasing the probability of exciton dissociation at the interface and facilitating efficient charge separation and transport. In terms of the relative arrangement of donor and acceptor materials within the active layer, both conventional and inverted BHJ solar cells have been developed. Optimization of the device architecture has also been shown to have a significant effect on the performance of OPVs. To date, the maximum PCE achieved for BHJ solar cells under indoor conditions is around 36.5%[4] by using 2PACz as both the HTL layer and the additive with the organic mixture of PM6:Y6.

Traditional BHJ solar cell, or direct architecture (Figure 18a): In a traditional BHJ solar cell, the transparent conductive electrode (usually ITO) acts as the anode and is positioned at the bottom. The HTL and active layer follow. Finally, the ETL and the top cathode electrode, such as calcium, are placed at the top of the stack. However, this conventional BHJ architecture suffers from limited device stability due to the air-sensitive nature of the low-work function metal

cathode. Oxygen can penetrate through pinholes and grain boundaries, leading to its degradation.

Inverted BHJ solar cell (Figure 18b): In an inverted BHJ solar cell, the order of the layers is reversed compared to a conventional cell. The transparent conductive electrode, which acts as the cathode, is placed at the bottom, followed by the ETL, the active layer, the HTL, and finally, the anode electrode at the top. This configuration offers advantages such as improved stability and better compatibility with flexible substrates. This efficient device structure has been the subject of numerous publications over the last few decades.

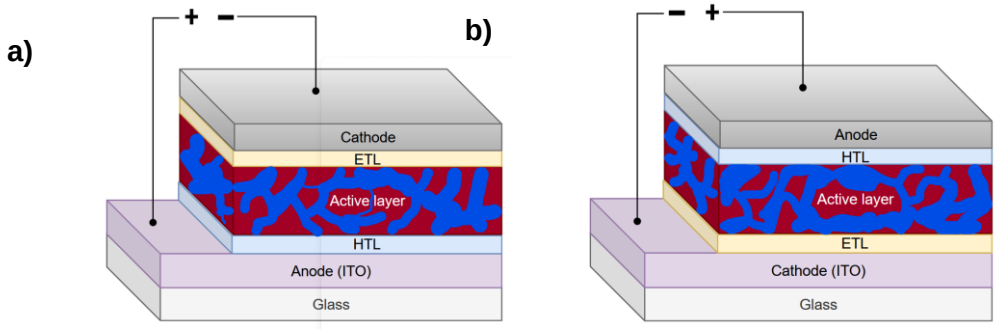

Figure 18. Structure of a BHJ organic solar cell in the traditional (a) and inverted (b) polarity.

The success of BHJ-based OPVs is largely the result of continuous innovations in materials science. Currently, the photoactive materials of OPVs can be roughly divided into four categories: polymer donors, small molecule donors, fullerene acceptors, and non-fullerene acceptors.

I.7.2.1. Polymer donor

In recent years, mid-bandgap polymer donors and fullerene-based acceptors have been reported to achieve PCEs of 4.6-23.1% for IOPVs under indoor lighting conditions [71,87-93]. Figure 19 shows the chemical structures of some polymer donor materials commonly used in IOPVs, and Table 3 shows the PV performance of polymer donors with fullerene-based OPVs for indoor applications. Among these, poly(3-hexylthiophene) (P3HT) has emerged as one of the most important donor materials in the development of OPVs[94-96]. Characterized by its simple molecular structure, P3HT is not only easy and cost-effective to synthesize but also exhibits high absorption in the 400-650 nm range, which is well-matched to the spectral irradiance of indoor LED lighting. In 2011, Steim et al. reported the first IOPV based on P3HT:PCBM, achieving a PCE of 7% under low-light conditions[97].

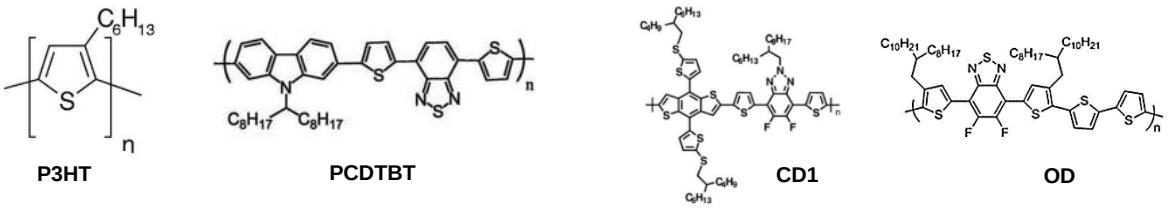

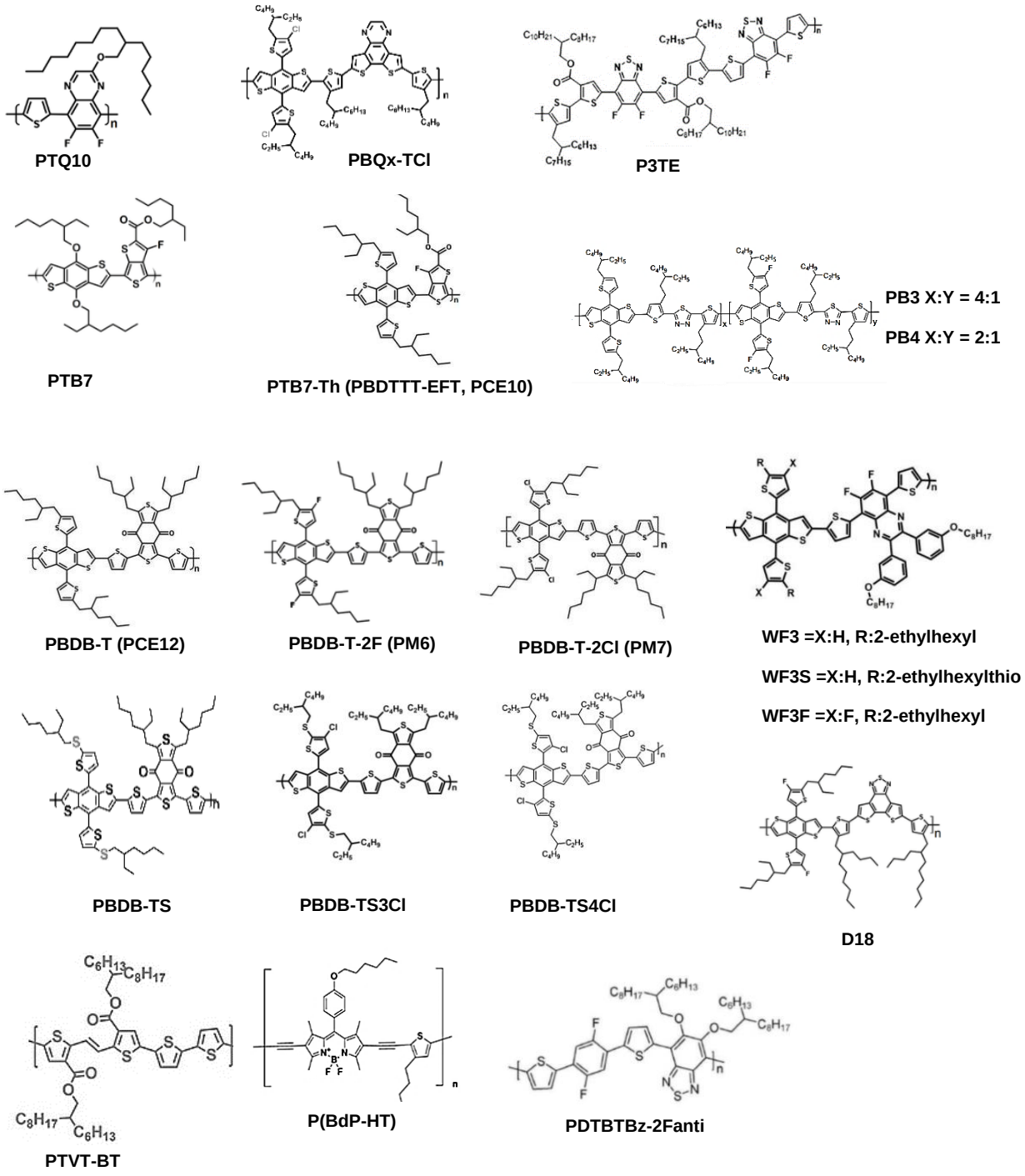

Figure 19. The chemical structure of IOPV polymer donor materials.

Table 3. The PV performance of polymer donors with fullerene-based OPVs for indoor applications.

Active Layer (D:A)	Light Sources	Intensity (lux)	V_{OC} (V)	J_{SC} (μA.cm^{-2})	FF (%)	PCE_{MAX} (%)	P_{out} (μW.cm^{-2})	ref
Polymer donor with FA								
P3HT:PCBM	FL	300	0.41	20.6	56.6	5.8	4.8	88
P3HT:PCBM	LED	500	0.43	62	0.59	8.90	15.67	89
P3HT:ICBA	LED	500	0.73	50	63	13.05	22.97	89
P3HT:ICBA (130nm)	LED	1000	0.662	66.7	60.09	4.6	12.88	90

P3HT:ICBA (230nm)	LED	1000	0.661	75.0	61.91	5.4	15.12	[90]
P3HT:ICBA (210nm)	LED	1000	0.736	81.2	70.12	15	41.9	[91]
P3HT:$PC_{71}BM$	LED	1000	0.498	73.7	71.9	9.4	26.32	[92]
PCDTBT:PCBM	LED	1000	0.79	84	62	14.7	41.16	[93]
PCDTBT:bis-PCBM	LED	1000	0.90	77.7	55	13.8	38.64	[93]
PCDTBT:$PC_{71}BM$	FL	300	0.72	27.7	69.3	16.6	13.9	[88]
PTB7:PNP	LED	200	0.57	19.0	67	9.5	7.3	[98]
PTB7:$PC_{71}BM$	FL	300	0.61	28.6	69.5	14.6	12.2	[88]
PTB7:$PC_{71}BM$	LED	1000	0.569	87.6	69.3	12.3	34.44	[92]
PTB7-Th:$PC_{71}BM$	LED	500	0.59	66	58	13.20	23.23	[89]
WF3:$PC_{71}BM$	LED	500	0.57	51.46	58.86	10.33	17.56	[71]
WF3S:$PC_{71}BM$	LED	500	0.62	52.73	59.47	11.79	20.04	[71]
WF3F:$PC_{71}BM$	LED	500	0.69	55.42	62.23	14.36	24.41	[71]
OD:$PC_{71}BM$	LED	1000	0.57	125.8	68.33	18.04	50.51	[87]
PDTBTBz-2Fanti:PC71BM	LED	1000	0.817	112.4	70.4	23.1	64.68	[92]
PBDB-T:$PC_{71}BM$	w-LED	1000	0.69	106.4	73.07	17.54	52.97	[75]

With advancements in donor materials for outdoor conditions, significant improvements have also been realized in indoor environments. In 2016, Lee et al. demonstrated IOPVs using PCDTBT and PTB7 donor polymers blended with fullerene-based acceptor materials and compared their performance under low-light illumination using a fluorescent lamp[88]. Devices based on PCDTBT:$PC_{71}BM$ generated a high V_{OC} of 0.72 V and achieved a PCE of 16.6% under 300 lux FL illumination. This high performance of PCDTBT-based devices under indoor conditions aligns well with theoretical models for indoor OPVs. According to Shockley-Queisser analysis, the ideal band gap for efficient harvesting of energy from fluorescent or LEDs is about 1.9 eV. PCDTBT has a band gap of exactly 1.9 eV, making it ideal for indoor light harvesting. On the other hand, PTB7 has a slightly smaller bandgap of 1.8 eV and can absorb more photons from the solar spectrum, but it is not as ideal for harvesting indoor light sources compared to PCDTBT. Therefore, PTB7:$PC_{71}BM$ devices exhibit higher efficiency under standard 1-sun illumination; a lower V_{OC} of 0.61 V under low-light conditions limits their PCE to 14.6%. The PTB7-Th:$PC_{71}BM$ blend is a well-established system in the field of OPV research, capable of achieving PCEs of 13.20% under 500 lux LED illumination[89].

As previously discussed, for indoor conditions, wide bandgaps and appropriate molecular energy levels are required for a higher V_{OC}, which helps to improve OPV efficiency. The bandgap of photovoltaic materials in OPV is related to the energy difference between the HOMO of the acceptor and the LUMO of the donor. Therefore, achieving a deeper HOMO level for the donor is also a viable solution to improve performance. Singh et al. investigated the effect of substituents on the HOMO level and absorption of the donor, thereby affecting device performance. They designed three donor polymers based on benzodithiophene (BDT) with different substituents:alkyl (WF3), alkylthio (WF3S), and fluorine (WF3F). Fluorination has been shown to effectively tune the optoelectronic properties of a polymer by reducing the HOMO level. The fluorine (F) substituent, as in WF3F, can minimize bimolecular recombination, reduce R_S, increase R_{SH}, suppress trap-assisted recombination, achieve higher V_{OC} and promote better morphological properties in the polymer blend. As a result, WF3F has a deeper HOMO of -5.62eV compared to -5.44eV for WF3 and -5.45eV for WF3S. Under LED illumination at 500lx, the WF3F:PC71BM device showed a higher PCE of 17.34% with a V_{OC} of 0.69V compared to a PCE of 12.83% (V_{OC}: 0.57V) for WF3:PC71BM and a PCE of 14.32% (V_{OC}: 0.57V) for WF3S:PC71BM[71].

Recent advancements in the development of novel donor polymers have further improved the PCE of IOPVs. In 2019, You et al. conducted a comparative study on the photovoltaic performance of four different polymer donors: P3HT, PTB7, PDTBTBz-2F_{anti}, and PBDB-T, blended with $PC_{71}BM$ under low-light conditions. The active layers formed from these polymers exhibited different absorption spectra and distinct spectral matches with the emission spectrum of LED light, resulting in different power absorption efficiencies. Among these materials, the wide bandgap polymer PDTBTBz-2F_{anti} showed superior spectral matching with LED light, leading to a remarkable PCE of 23.1% under 1000 lux LED illumination. This exceptional efficiency is attributed to the optimal spectral matching to indoor lighting conditions, which enhances the power absorption ratio. The high V_{OC} of 0.81 V is due to the lower HOMO energy level and larger bandgap of the polymer. Also, the BHJ film of PDTBTBz-2F_{anti} and $PC_{71}BM$ exhibited a crystalline nanofibrillar morphology with excellent face-on π-π stacking, facilitating efficient charge transport and minimal carrier recombination loss under dim indoor lighting conditions[92]. Similarly, the wide bandgap polymer PBDB-T, when blended with $PC_{71}BM$, achieved a PCE of 17.75% under 1000 lux warm LED illumination[75].

I.7.2.2. Small molecule (SM) donor

Novel SM donor materials (Figure 20), which have attracted attention due to their tunable electronic properties, well-defined molecular structures, and relatively simple purification processes compared to polymers, have been successfully hybridized with FAs in IOPVs despite some challenges during their synthesis. Table 4 provides a summary of the PV performance of these SM donor materials when combined with FAs in IOPV devices. These IOPVs achieved PCEs ranging from 8.4% to 28.1% under indoor lighting[98-103]. In 2018, Lee et al. achieved an impressive PCE of 28.1% under 1000 lux FL illumination using the SM donor benzodithiophene-terthiophene-rhodamine (BTR) blend with $PC_{71}BM$ as the active material[99]. This SM donor was selected due to its unique morphology, resulting from the particular arrangement of the alkyl chain and its correspondingly high optical energy band gap of 1.80 eV, which is suitable for indoor light harvesting. Their study also showed that the solvent vapor annealing (SVA) treatment affects the device performance, strongly correlating with the morphology of the active layer. In 2019, Arai et al. compared the SM donors BDT-2T-ID and BDT-1T-ID with the polymer donor PTB7 in OSCs using the FA PNP under 200 lx LED illumination. They demonstrated that the solution-processed small molecule BDT-2T-ID PNP OPVs achieved a high PCE exceeding 16% under white LED illumination. The V_{OC} of the BDT-2T-ID (0.75V) and BDT-1T-ID (0.85V) based devices was higher than that of the PTB7 (0.58V) based devices due to their deep HOMO values of -5.13 and -5.23 eV, respectively. Besides, these SM devices exhibited higher P_{out} of 12.4 and 9.9 μW cm^{-2}, with PCEs of 16.2% and 12.9%, respectively, compared to PTB7-based devices, which had a P_{out} of 7.6 μW cm^{-2} and a PCE of 9.9%[98]. Following the same strategy to achieve low HOMO levels of donors, this group further synthesized two new SM donors using one or two dithieno[3,2b:2',3'-d]pyridin-5(4H)-one (DTP) as the functional molecular core bearing electron-withdrawing fused lactam subunits linked to 1,3-indandione (ID) units, namely 1DTP-ID and 2DTP-ID, with HOMO levels of -5.35 eV and -5.25 eV, respectively[100]. Both 1DTP-ID and 2DTP-ID-based devices showed superior PV performance under warm white LED light, resulting in improved PCEs of 19.3% and 17.8%, respectively.

In 2020, Wang et al. synthesized four new SM donors with donor-acceptor-acceptor (D-A-A')-configurations: CPNT, DCPNT, CPNBT, and DCPNBT. In these molecules, naphtho[1,2-c: 5,6-c']bis([1,2,5]thiadiazole) (NT) or naphtho[2,3-c][1,2,5]thiadiazole (NBT) served as the electron-

deficient core (A), bridging the electron-donating triarylamine donor group (D) and the electron-withdrawing cyano or dicyanovinylene acceptor group (A'). These materials include vacuum deposited OPVs based on CPNT:C70 and DCPNT:C70, which showed the best PCE of 5.9% and 8.3% under AM 1.5G and 12.8% and 12.6%, respectively, under 500 lux TLD-840 FL lamp[101]. In 2021, Su et al. reported two thieno[3,2-b]thiophene (TT)-based donor-π-acceptor-type SM donors, namely DTDCPTT and DTDCPTT-2CN, designed for use in IOPVs. These molecules exhibited intramolecular state charge transfer absorption in the visible light region, high thermal stability, and suitable energy level alignment with C_{70}. In particular, DTDCPTT exhibited more compact crystal packing and uniform distances between adjacent antiparallel dimer pairs, providing advantages for exciton dissociation and carrier transport compared to DTDCPTT-2CN. Vacuum-deposited binary cells using DTDCPTT and DTDCPTT-2CN in conjunction with FA C_{70} achieved power conversion efficiencies (PCE) of 7.81% and 6.00%, respectively, under simulated AM 1.5 G illumination. Impressively, these cells achieved outstanding PCE values of up to 16.89% and 12.35% respectively under 500 lux TLD-840 FL illumination[102]. More recently, Gao et al. focused their efforts on the design and synthesis of new A-π-D-π-A porphyrin-based SM donors for IOSCs, namely, C19-PdP, C19-PtP, and C19-H2P. The metalloporphyrins C19-PdP and C19-PtP, featuring the insertion of noble metals (Pd and Pt) into the porphyrin core, exhibited lower HOMO levels compared to the free base porphyrin C19-H2P. This insertion of noble metals resulted in well-ordered surface morphology, higher charge carrier mobilities, and suppressed charge recombination dynamics. As a consequence, OSC devices based on C19-PdP:PC71BM and C19-PtP:PC71BM exhibited improved PCE of 16.54 and 16.74%, respectively, under 300 lux LED illumination[103].

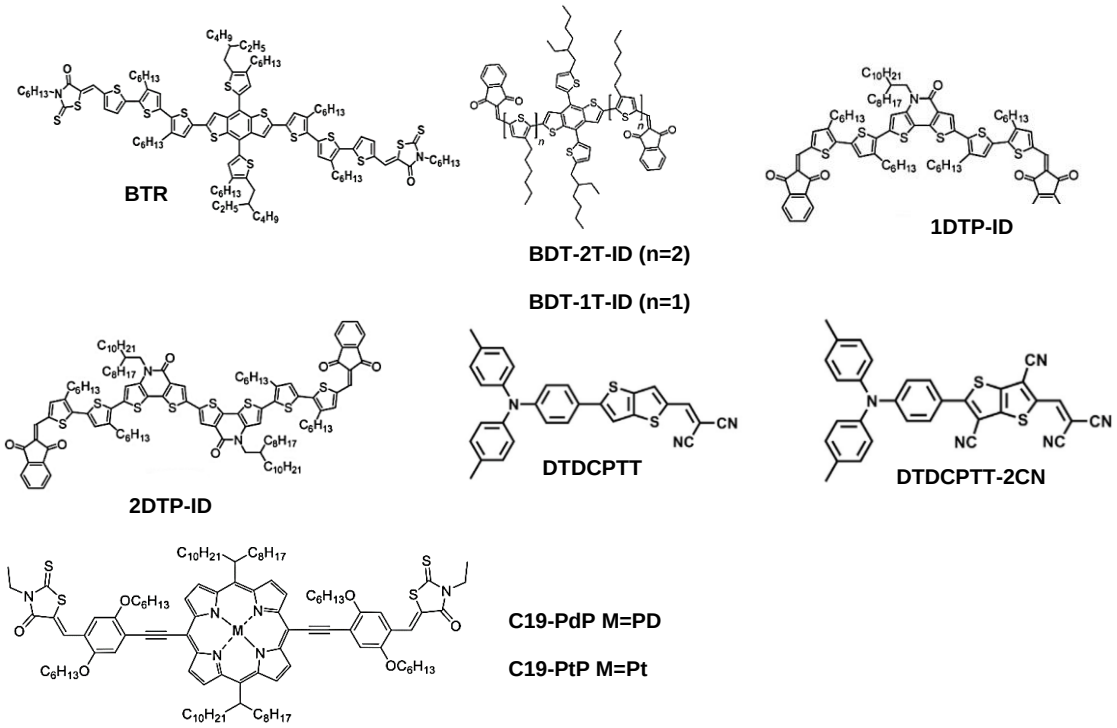

Figure 20. The chemical structure of small-molecule donor for IOPV

Table 4. The PV performance of small donors with fullerene-based OPVs for indoor applications.

Active Layer (D:A)	Light Sources	Intensity (lux)	V_{OC} (V)	J_{SC} ($\mu A.cm^{-2}$)	FF (%)	PCE_{MAX} (%)	P_{out} ($\mu W.cm^{-2}$)	ref
Small Molecule Donor with FA								
BTR:PC71BM	FL	1000	0.791	133.1	75.2	28.1	78.2	99
BDT-2T-ID:PNP	LED	200	0.75	24.2	68	16.0	12.3	98
BDT-1T-ID:PNP	LED	200	0.84	19.2	59	12.4	9.5	98
1DTP-ID:PNP	LED	200	0.67	24.6	68	19.3	11.2	100
2DTP-IDCPNT:PNP	LED	200	0.72	22.8	63	17.8	10.3	100
CPNT:C70	FL	500	0.667	53.5	51.9	12.8	18.57	101
CPNBT:C70	FL	500	0.533	39.5	58.1	8.4	12.18	101
DCPNT:C70	FL	500	0.680	46.6	57.4	12.6	18.13	101
DTDCPTT:C70	FL	1000	0.68	103	67.73	16.35	47.25	102
DTDCPTT-2CN:C70	FL	1000	0.75	99.2	52.20	13.44	39	102
C19-PdP:PC71BM	LED	300	0.72	30.68	66.1	16.36	13.74	103
C19-PtP:PC71BM	LED	300	0.78	29.07	64.7	16.47	13.83	103

I.7.2.3. Fullerene acceptors

As mentioned in the donor section, FAs play an essential role in OPVs by accepting electrons from donors, thereby facilitating the separation of excitons into free charges. FAs are based on carbon cage structures, with well-known examples such as PCBM, $PC_{71}BM$, ICBA, and PNP. Among these, PCBM stands out as one of the most critical fullerene acceptor materials in the history of OPVs due to its good solubility, favorable electron acceptor properties, and compatibility with P3HT materials. The first IOPV was made of P3HT:PCBM with a PCE of 7% under low light conditions in 2011 [97]. In 2017, Yang et al. compared the IPV properties of PCBM and ICBA with P3HT donors. The P3HT:ICBA device exhibited a higher V_{OC} (0.73V) than the V_{OC} (0.43V) of P3HT:PCBM, achieving a high PCE of 13.05% and a high P_{out} of 22.97 μW cm^{-2} under LED illumination at 500 lux. In addition, the P3HT:PCBM device showed a PCE of 8.90% with a P_{out} of 15.67 μW cm^{-2}. They found that using an acceptor with a higher LUMO energy level (-3.74 eV for ICBA compared to -3.90 eV for PCBM) significantly increased the V_{OC}, thereby greatly improving device performance in low light conditions[89]. In 2023, this concept was further refined by Hou et al. using bis-PCBM and PCBM as acceptors. These PCDTBT:bis-PCBM devices achieved a high V_{OC} of up to 0.9 V under 1000 lx indoor light, compared to 0.79 V for devices using PCBM. This improvement was attributed to the high LUMO level of bis-PCBM (-3.83 eV). However, the bis-PCBM devices exhibited a lower PCE of 13.8% compared to 14.7% for the PCBM devices. The lower efficiency was due to the disorder and amorphous properties of the bis-PCBM devices, which led to diminished J_{SC} and FF[93].

$PC_{71}BM$ has better absorption properties than PCBM in the visible region, allowing for increased photon harvesting and potentially higher photocurrent for devices using $PC_{71}BM$ instead of PCBM. As discussed in the small molecule donors section, SM donors have tunable electronic properties, well-defined structures, and relatively simple purification, making them excellent candidates for blending with FAs in IOPVs. Whether polymeric or SM donors are used, the incorporation of FAs as acceptors in the active layer of OSCs provides flexibility in optimizing the optoelectronic properties of the devices under various light conditions.

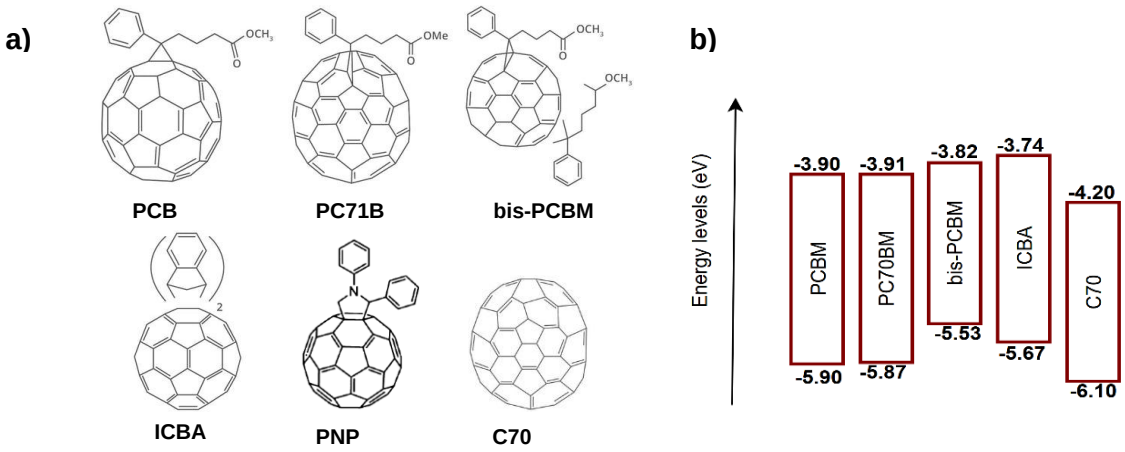

Figure 21. a) The chemical structure of FA materials for IOPV. b) The energy band gap of FA for IOPV.

I.7.2.4. Non-fullerene acceptors

In the field of OPVs, the development of NFAs represents a significant advancement. Unlike traditional FAs, NFAs provide numerous advantages, including better light absorption in the visible range, tunable bandgaps suitable for different artificial light sources by introducing suitable side chains that also provide appropriate solubility and tune the packing structures in the solid state, superior electron mobilities, and customizable frontier orbital energy levels. These properties are invaluable in increasing V_{OC} and minimizing energy losses, especially under the low-intensity lighting conditions typical of indoor environments. As a result, the unique properties of NFAs make them up-and-coming candidates for improving the performance of IOPVs. In this subsection, we will explore the recent studies on various NFA-based OPVs for indoor applications, the performance of which is summarized in Table 5.

Since its first synthesis in 2016, NFA ITIC[24] (Figure 22), with its A-D-A structure, has presented excellent photoelectric properties characterized by broad and strong absorption in the range of 500 to 750 nm. This absorption spectrum matches well with the emission spectrum of LEDs and FLs, making ITIC an up-and-coming candidate for indoor applications. In 2019, Ding and his research group constructed an OPV device based on CD1:ITIC. The device showcased a V_{OC} of 0.78 V, a J_{SC} of 116 µA cm^{-2}, an FF of 68.1%, and a P_{out} of 62 µW cm^{-2}, resulting in a PCE of 17.9% under FL illumination at 1000 lux[104]. Afterward, other NFAs from the ITIC family were developed and used for IPV. Modifications to the ITIC molecule, such as changes to the halogen elements, end groups, and side chains, have allowed the energy levels to be adjusted, the light absorption range to be extended, and the morphology of the active layer to be improved. Examples include IO-4Cl, IT-4F, and IT-M, which were blended with the donor polymer PM6 and characterized under LED conditions. These solar cells achieved impressive PCEs of up to 26.1% for IO-4Cl[74], 15.03% for IT-4F[105], and 22.8% for IT-4M[106]. In 2022, Saeed et al. introduced a novel derivative of ITIC, m-ITIC-O-EH, with modified alkoxy chains. This modification effectively tuned the energy levels (Figure 23a) and reduced charge recombination losses between electrodes, contributing to exceptional IPV performance. Devices based on PBDB-T:m-ITIC-O-EH achieved a PCE of 21.6% under LED at 1000 lux. Moreover, a comparative study was conducted on the photovoltaic performance of devices based on FAs and NFAs under both 1-sun and indoor lighting conditions. The PBDB-T:m-ITIC-O-EH-based device presented superior indoor performance compared to its PBDB-T:PC70BM counterpart, generating three times higher P_{MAX} and demonstrating improved stability, retaining

80% of its initial PCE value after 12 hours of continuous illumination by a halogen lamp (1000 lux)[107].

One of the most promising NFAs for indoor applications is IDIC, which has an A-D-A structure and an ideal bandgap of around 1.6 eV, enabling it to achieve very high EQEs in the 500-700 nm range. The main differences between the ITIC and IDIC families lie in their molecular structures. IDIC typically contains thiophene-containing five-ring fused units as the donor unit. In contrast, ITIC consists of an asymmetric seven-ring fused electron donor unit containing thienothiophene as the core. In 2022, Radford et al. investigated the addition of heteroatom-based rotational blocking groups to IDIC, resulting in IDIC-Br and IDIC-S derivatives. They compared the PV performance of these NFAs mixed with PTQ10 devices. Their results showed that the bromine rotational blocking group could enhance the performance of OSCs under both standard AM1.5G and 1200 lx LED light conditions, resulting in high PCEs of 10.8% and 23%, respectively. IDIC and IDIC-S produced similar PCEs under 1-sun illumination (9.9% and 9.2% respectively). However, IDIC-S delivered lower P_{out} than IDIC-based cells under indoor lighting conditions (PCE of IDIC-based: 20%, PCE of IDIC-S-based: 17%).[108]

Bai et al. designed and synthesized a high-performance NFA named FCC-Cl, optimized for IOPVs with a desirable optical band gap of 1.71 eV. The strategic design of FCC-Cl involved combining a weak electron-donating core with a moderate electron-withdrawing end group, resulting in a wide energy band gap, high absorption coefficient, and enhanced crystallinity. OPVs using the D18:FCC-Cl blend achieved an EQE of up to 85%, and an impressive PCE of 29.4% under 1000 lux LED illumination (2600 K). As well as, PM6:FCC-Cl devices demonstrated high efficiencies of 26.5% under 1000 lux indoor illumination, even with active layer thicknesses up to 300 nm, which is a feature particularly beneficial for large-scale roll-to-roll printing processes[109]. In 2022, Luo et al. reported a series of large-bandgap NFAs based on a derivative of FCC-Cl, achieved by modifying the alkyl side chains with alkylphenyl chains, either partially or entirely. These derivatives, named FCC-Cl-C8, FCC-Cl-4Ph, and FCC-Cl-6Ph, were designed to fine-tune the absorption spectra and energy levels of the NFAs, thereby reducing energy loss. The bulky alkylphenyl side chains also positively influenced the blend film morphology, leading to smaller domain sizes and purer phase separation, which facilitated exciton dissociation and suppressed charge recombination. Among the derivatives, FCC-Cl-4Ph, with partial alkyl and alkylphenyl substitutions, demonstrated the best performance. This derivative successfully blueshifted the absorption of the NFAs while minimizing the adverse morphological effects of the bulky alkylphenyl chains. The well-matched absorption spectrum and improved blend film morphology of the D18:FCC-Cl4Ph enabled a high PCE of over 29% under 3000 K LED at 1000 lux and approximately 27% under 6500 K LED at 1000 lux. Additionally, the stability test showed that the device retained more than 90% of the original PCE after more than 1000 hours of continuous illumination at 500 lux[110].

In addition to the A-D-A structured NFAs, such as the ITIC and IDIC families, another notable NFA, Y6, has been introduced. Y6 features an A-D-A'-D-A structure, which enhances the intramolecular electron push-pull effect within the molecule. This structural modification optimizes the electronic properties of the NFA, making it more efficient at absorbing light and facilitating charge separation in OPV devices. Y6 represents a significant advancement in the field of NFA under 1-sun conditions, offering new opportunities to improve the performance and efficiency of OSCs. Several derivatives have been developed to adapt Y6 to indoor conditions. In 2020, Ma and co-workers reported on a Y6 derivative named Y6-O, in which an alkoxy chain replaces the alkyl chain at the edge of the thiophene units. While the absorption range of Y6 typically extends up to 940 nm, which is excessively red-shifted, the alkoxy

substitution in Y6-O helped to blueshift the absorption of the acceptor by increasing its HOMO and LUMO levels (Figure 23b), making it better aligned with the indoor illumination spectrum. For the energy gap to change, one of the bands (the HOMO or the LUMO) must grow more than the other, as this differential growth adjusts the energy gap. As a result, PM6:Y6-O devices achieved a remarkable PCE of 31% under 1650 lx LED illumination, with an FF of 76%, V_{OC} of 0.84V, and J_{SC} of 0.235 $mAcm^{-2}$, especially when PDINO was used as the ETL.[111] Building on this progress, in 2021, Xu et al. synthesized a new Y6 derivative with chlorinated terminal groups, HD-4Cl. They developed another novel Y6 derivative, HDO-4Cl, in which alkoxy groups were introduced at the edge of the thiophene units instead of alkyl chains in HD-4Cl. The PM6:HD-4Cl-based devices achieved a PCE of 19.9% under warm LED illumination at 1000lx. Meanwhile, the PM6:HDO-4Cl-based devices achieved an optimal PCE of 23.4% under the same conditions. This improvement was attributed to the alkoxy group's ability to reduce electron affinities and increase the bandgap, resulting in a blueshift in the absorption spectrum. In addition, π-linkers with multiple alkoxyl substitutions could act as non-covalent conformational locks, leading to a delocalized LUMO energy level and a planar geometry, which is beneficial to π-π stacking [112]. Consequently, HDO-4Cl emerged as a more promising candidate for indoor lighting applications compared to HD-4Cl[113]. In 2023, Kim et al. developed IOPV devices integrating ultrathin 2PACz as the HTL and 2PACz with PM6:Y6 as the photoactive layer. The spontaneous vertical phase separation of PM6:Y6 photoactive layers with 2PACz resulted in a vertical component distribution, which significantly enhanced the carrier yield-mobility product and effectively suppressed trap-assisted recombination and leakage current in the IOPVs. As a result, the PM6:Y6:2PACz device achieved a record high efficiency of 33.5% under 1000 lx LED illumination, an improvement of approximately 30.8% over the PM6-Y6 device (with a PCE of 25.6%). In addition, the use of phosphonic acid group-based 2PACz-treated ITO induced a sufficiently large work function, resulting in a vacuum level shift. This shift enabled efficient energy level matching and improved charge selection at the hole-selective interface. The champion OPV achieved an outstanding PCE of 36.5% under indoor lighting conditions and retained 95% of its initial efficiency after 1000 hours of operation in ambient air.[4] In addition, Kim et al. reported another strategy to synthesize Y6 derivative acceptors by varying the length and type of the outer side chain. They synthesized four new molecules by modifying the chalcogen-containing heterocycle of the Y6 molecule to thiophene (ThTh) and selenophene (ThSe) and varying the length of the outer side chain using n-hexyl (C6) and n-nonyl (C9) moieties: ThTh-C6, ThTh-C9, ThSe-C6, and ThSe-C9. When paired with PM6 as a donor, the ThTh-containing OPVs exhibited improved J_{SC} and V_{OC} due to their enhanced crystallinity and reduced degree of bimolecular recombination compared to the ThSe systems. In addition, the short side chain resulted in relatively reduced monomolecular recombination and moderated planarity compared to the long chain. The optimum OSCs based on PM6:ThTh-C6 achieved a high PCE of 24.8% under 1000 lx LED illumination.[114]

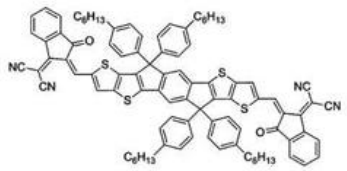

ITIC

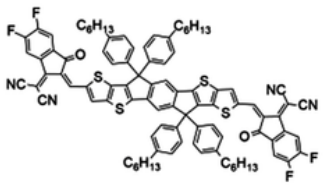

IT-4F

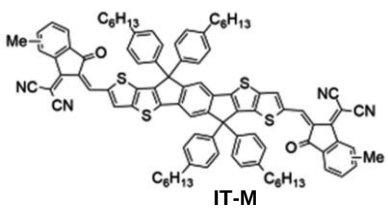

IT-M

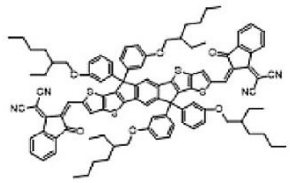

m-ITIC-O-EH

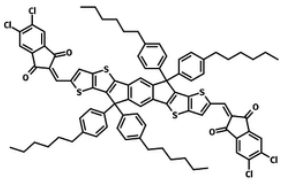

IO-4Cl

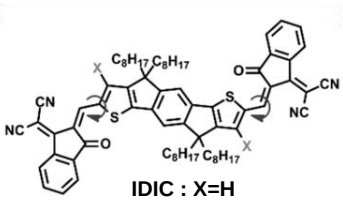

IDIC : X=H
IDIC-Br : X=Br
IDIC-S : X=SHex

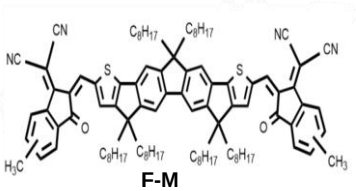

F-M

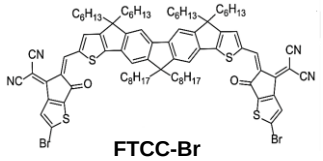

FTCC-Br

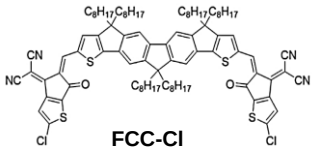

FCC-Cl

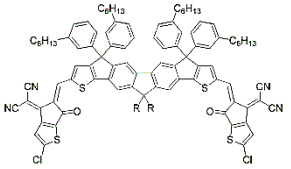

FCC-Cl-4Ph : R=Ra=C_8H_{17}
FCC-Cl-6Ph : R=Rb=

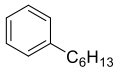

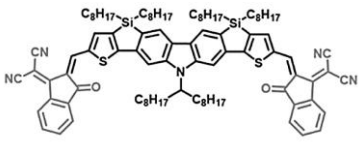

DTSiC-IC

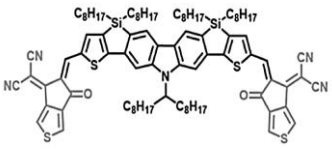

DTSiC-TC

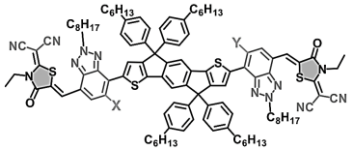

BTA3 : X=Y=H

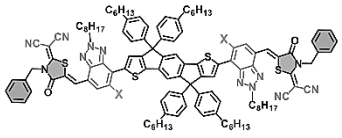

Cl-BTA5 : X=Cl

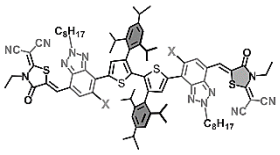

Cl-BTA33 : X=Cl

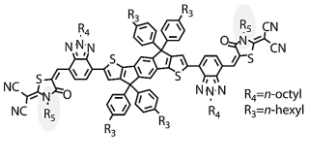

R_5=methyl
R_5=ethyl
R_5=*n*-butyl

DTz-R1
DTz-R3
DTz-R2

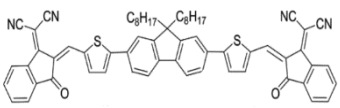

DICTF

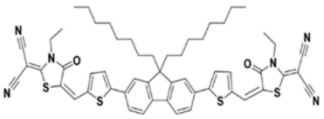

DRCTF

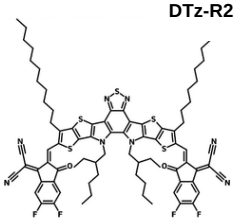

Y6 (BTP-4F)

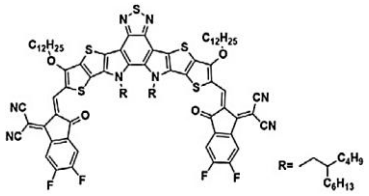

Y6-O

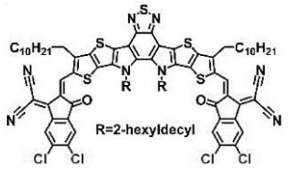

HD-4Cl

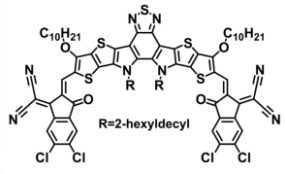

HDO-4Cl

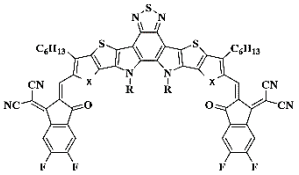

ThTh-C6 : X=S
ThSe-C6: X=Se

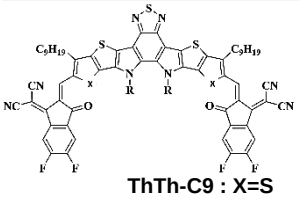

ThTh-C9 : X=S
ThSe-C9: X=Se

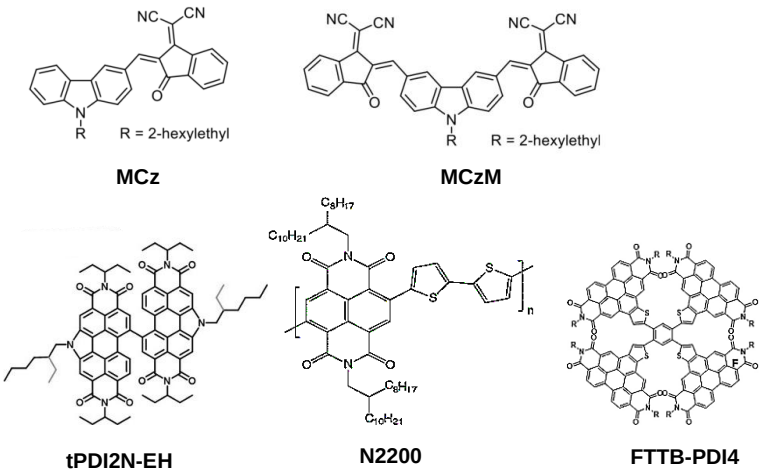

Figure 22. The chemical structure of IOPV NFA materials.

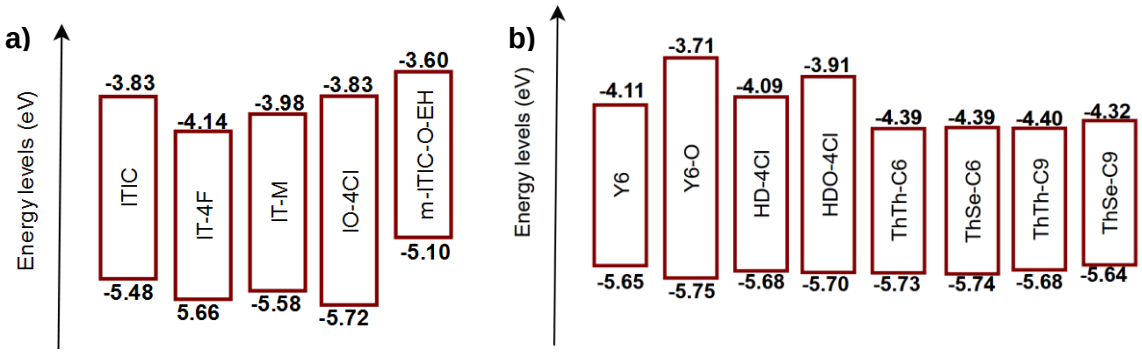

Figure 23. Energy bandgap of ITIC and Y6 families.

Table 5. The PV performance of the non-fullerene-based OSCs under light sources.

Active Layer (D:A)	Light Sources	Intensity (lux)	V_{OC} (V)	J_{SC} ($\mu A.cm^{-2}$)	FF (%)	PCE_{MAX} (%)	P_{out} ($\mu W.cm^{-2}$)	ref
CD1:ITIC	FL	1000	0.78	116	68.1	17.9	62	104
	LED	1000	0.77	107	67.5	15.4	56	104
PM6:IO-4CL	w-LED	1000	1.10	90.6	79.1	26.1	78.8	74
PM6:IT-4F	LED	1000	0.671	94.59	71.48	15.03	45.38	105
PM6:IT-4F	FL	1000	0.621	112.88	62.75	14.74	43.99	115
PCE12:IT-4F	w-LED	1000	0.52	114.5	72.03	13.95	42.13	75
PM6:IT-M	LED	500	0.880	54.2	75.4	22.8	36.02	106
PCE12:m-ITIC-OEH	LED	1000	0.678	163.9	69.8	21.6	60.4	107
PBDB-TS:IT-4F	FL	1000	0.48	125.5	36.2	7.0	22.1	116
PBDB-TS3CL:IT-4F	FL	1000	0.66	123.8	72.8	19.4	60.2	116
PBDB-TS4C:IT-4F	FL	1000	0.66	129.3	74.3	20.7	64.0	116
PBDB-TSCl:IT-4F	FL	1000	0.657	117.92	77.37	20.08	59.94	115
PM6:IDIC	LED	1000	0.777	105	63.4	19.5	54.6	76
PTQ10:IDIC	LED	1200	0.84	120	56	20	55.8	108
PTQ10:IDIC-Br	LED	1200	0.73	150	64	23	68.2	108
PTQ10:IDIC-S	LED	1200	0.76	104	59	17	46.5	108

PM6:Y6	LED	1000	0.667	154.6	66.1	25.4	68.58	[4]
PM6:Y6-O	LED	1650	0.84	245	76	31.01	155.7	[111]
PM6:HD-4Cl	LED	1000	0.690	123.5	72.0	19.9	61.4	[113]
PM6:HDO-4Cl		1000	0.793	120.2	75.7	23.4	72.2	[113]
PM6:THTH-C6	LED	1000	0.67	115.2	73.2	24.8	56.58	[114]
PM6:THTH-C9	LED	1000	0.676	110.9	71.1	23.7	53.36	[114]
PM6:THSE-C6	LED	1000	0.604	111.0	70.1	21.1	46.92	[114]
PM6:THSE-C9	LED	1000	0.647	106.7	71.2	22.3	49.22	[114]
PTQ10:Cl-BTA33	LED	1000	0.989	98.13	76.34	24.28	74.54	[117]
PCE12:BTA3	w-LED	1000	0.99	111.6	70.07	25.61	77.34	[75]
PCE12:BTA3	LED	1000	0.990	98.5	73.6	23.3	71.8	[118]
PCE12:N2200	LED	1000	0.70	89.08	70.46	14.74	40.71	[119]
PCE12:F-M	LED	200	0.74	33	63.4	20.18	15.5	[120]
PTQ10:TPDI2N-EH	LED	2000	1.09	112	51	10.9	60.91	[121]
PM7:BTA3	LED	1000	1.103	38.0	55.5	7.6	23.3	[118]
PM7:DTSIC-IC	w-LED	1000	0.89	91	58.80	16.92	47.62	[122]
PM7:DTSIC-TC			0.87	95	70.86	20.73	58.57	[122]
PM6:BTA3	LED	1000	1.117	65.0	67.1	15.8	48.7	[118]
PB4:FTCC-Br	LED	1000	0.967	119.87	82.00	31.09	95.05	[123]
PB3:FTCC-Br	LED	1000	0.954	119.06	80.72	30.00	91.68	[123]
P3TEA:FTTB-PDI4	LED	1200	1.02	143	67	26.44	96.51	[124]
PBQX-TCL:BTA3	LED	1000	1.10	97.7	80.1	28.5	86.1	[125]
PBQX-TCL:DTZ-R1	LED	500	1.07	47.5	81.1	26.8	41.2	[126]
PBQX-TCL:DTZ-R2	LED	500	1.08	42.3	79.5	23.6	36.3	[126]
PBQX-TCL:DTZ-R3	LED	500	1.08	37.5	76.3	20.1	30.9	[126]
D18:FCC-Cl	LED	1000	0.955	123	79.8	29.4	93.5	[109]
D18:FCC-Cl-C8	LED	1000	0.947	110.0	79.3	28.4	82.36	[110]
D18:FCC-Cl-4PH	LED	1000	0.972	110.5	79.0	29.3	84.97	[110]
D18:FCC-Cl-6PH	LED	1000	0.996	94.2	69.8	22.6	65.54	[110]
D18:Cl-BTA5	LED	1000	1.019	91.11	68.96	21.20	65.08	[127]
PTB7-TH:MCZM	LED	1000	0.88	81.08	66	18.88	52.86	[128]
PTB7-TH:MCZ	LED	1000	0.74	111.95	68	22.14	61.99	[128]
PTVT-BT:BTA3	LED	1000	1.031	106.54	77.04	27.30	84.65	[129]
P(BDP-HT):DCRTF	LED	1000	1.08	66.53	63	17.68	49.50	[130]
P(BDP-HT):DICTF	LED	1000	0.93	88.43	68	21.84	61.15	[130]

I.7.3. Ternary blend active layers

Another strategy to improve OPV performance is the ternary blend approach. In this configuration, three different materials are incorporated into the active layer of the OPV cell, such as a donor blend with two acceptors D:A1:A2 or two donors blended with an acceptor D1:D2:A, each with complementary absorption spectra. By combining the beneficial properties of each material, this strategy can improve light absorption, charge generation, charge carrier mobilities, and transport properties, as well as the FF and overall device efficiency under standard 1-sun illumination. In recent years, research on ternary OPVs and improving efficiency has continued to increase, and a record of 18.9% has been achieved under 1-sun conditions[131,132]. This optimization allows for better control over the morphology and composition of the active layer, potentially reducing recombination losses and increasing charge extraction efficiency. However, it is worth noting that ternary blends also face significant

obstacles. A key challenge is the difficulty in engineering the energy levels to establish the correct energy cascade to ensure efficient charge transport between the components. Furthermore, the introduction of a third component may complicate the charge transport pathway, potentially leading to mobility issues or increased recombination, especially if the new component disrupts the phase separation and overall morphology. Despite these challenges, ternary OPVs still have potential advantages, such as higher stability and greater tolerance to environmental changes, making them promising candidates for indoor energy harvesting applications. In 2018, Yin and al. proposed a ternary D1:D2:A strategy to enhance the OPV performance of PCDTBT:PC71CB-based OPVs by incorporating PDTSTPD, a compound with a low HOMO level[77]. The ternary devices exhibited a higher PCE of 6.0% compared to 5.3% for the binary device under 1-sun conditions. Additionally, they demonstrated an impressive PCE of 20.8% under 300 lux FL. The main improvements were observed in the FF and the J_{SC}, attributed to better spectral overlap between the emission spectra of the light sources and the absorption spectra of the ternary BHJ films. In 2022, Lee et al. used a D:A1:A2 configuration by adding the NFA ITIC-TH to a binary blend of PM6:IT-4F[86]. Although ITIC-TH did not significantly enhance the absorption spectra of the ternary blend, it possessed a suitable energy level that facilitated charge transfer, reduced charge recombination, and minimized energy loss (E_{LOSS}). Furthermore, due to the crystalline nature of ITIC-Th, the morphology of the amorphous binary blend was optimized. The resulting ternary device achieved a remarkable PCE of 30.11% under 500 lux LED illumination. To summarize the recent progress of ternary OPV for indoor use, Table 6 lists the performance indicators of ternary systems under different indoor lighting conditions. The table highlights the improvements in key parameters such as V_{OC}, J_{SC}, FF, and PCE achieved by different ternary configurations under indoor light sources such as LEDs and FLs.

Table 6. Summary of previously reported ternary IOPV device properties.

Ternary active layer	Light Sources (lux)	Intensity (lux)	V_{OC} (V)	J_{SC} ($\mu A.cm^{-2}$)	FF (%)	PCE_{MAX} (%)	ref
PCDTBT:PDTSTPD:$PC_{71}BM$	FL	300	0.73	33.3	63.5	20.8	77
PTB7:$PC_{71}BM$:EP-PDI	LED	500	0.65	57	68.5	15.68	32
PBDB-T:ITIC-Th:$PC_{71}BM$	LED	1000	0.72	157.94	65.06	26.4	133
PM6:Y6:Y-TH2	LED	1000	0.701	320.1	74.48	22.72	134
OD:$PC_{71}BM$:PDI2	w-LED	1000	0.643	127.02	70.04	20.54	87
OD:$PC_{71}BM$:PDI4			0.641	119.29	67.79	18.27	
OD:$PC_{71}BM$:IDT			0.634	132.99	71.78	21.13	
OD:$PC_{71}BM$:IDDT			0.642	126.32	64.42	19.05	
PTQ10:TPDI2N-EH:PDI-EDOT-PDI	LED	2000	1.10	101	48	9.2	121
PBQX-TCl:BTA3:BTP-EC9	LED (2700K)	1000	0.71	122.4	78.4	22.5	125
PM6:PDI-TP:IT-4F	LED (3000K)	1000	0.75	125.78	61.84	19.44	135
PBDB-T:$PC_{71}BM$:CN-QA-RH	LED (2700K)	1000	0.76	118.78	71.4	17.90	136
PM6:IT-4F:ITIC-TH	LED (3000K)	500	0.75	74.73	77.10	30.11	86

I.8. Conclusion and objectives of the thesis

In this chapter, we have provided an overview of indoor OSCs, highlighting their growing importance in the context of emerging low-power, off-grid applications connected to the IoT. As IPV systems gain increasing importance in providing continuous power to IoT devices under artificial lighting, OSCs stand out as promising candidates due to their light harvesting efficiency, tunability, flexibility, and low-cost production potential. OSCs offer unique advantages in terms of sustainability and design flexibility compared to other PV technologies, making them well suited to capture a large share of the expanding IPV market.

We review the history of OSC development for indoor applications and discuss the evolution of donor and acceptor materials specifically tailored for indoor conditions, as well as different OSC architectures and basic operating principles under low-intensity artificial lighting. In particular, the inverted BHJ architecture is considered to be very effective for indoor photovoltaic applications. Under indoor low-light conditions, the J_{ph} decreases and the leakage current associated with the R_{SH} becomes more significant. Therefore, achieving a high R_{SH} is critical to maintaining efficient IOPV performance. This analysis highlights the need for new wide-bandgap materials that match the emission spectra of common indoor light sources (especially white LEDs) and mitigate recombination losses to optimize PCE. To address these challenges, our research introduces a strategic approach to enhance the indoor performance of OSCs through material design and device optimization, focusing on developing materials with targeted absorption in the blue region of the spectrum (400-500 nm), and optimizing device architecture and processing methods to minimize V_{OC} losses and recombination.

In our study, we explored two innovative strategies aimed at improving blue light absorption in OSCs. First, we investigated heptazine-based electron acceptor compounds as NFAs, which exhibit tunable electronic properties and high nitrogen/carbon ratios, making them particularly suitable for efficient blue light absorption. This approach aims to improve the overall efficiency of OSCs by capturing the blue photon range that is prevalent in the indoor LED spectrum. Second, we investigated a fluorinated polymer donor, PF2, with strong blue light absorption properties and studied its blending with ITIC to achieve better spectral matching with indoor artificial lighting. The subsequent chapters of this thesis are based on these objectives and present detailed methods and results to advance the field of indoor OSC. In Chapter 2, we take an in-depth look at the fabrication and characterization of OSC devices, focusing on the key parameters that influence the performance under indoor conditions. Chapter 3 introduces heptazine-based NFAs and discusses their potential for absorption in the blue region in IOPV. Chapter 4 studies PF2:ITIC blends with a focus on optimizing their photovoltaic response to the indoor spectrum. Finally, Chapter 5 addresses the challenges of OSC stability under outdoor conditions and explores a new approach to improve stability using LDS to mitigate UV-induced degradation.

Chapter II. Fabrication of OSCs and optoelectronic characterization

II.1. Photovoltaic device fabrication

The purpose of this chapter is to provide a comprehensive explanation of the experimental processes involved in the fabrication of BHJ inverted OPVs at the XLIM laboratory and their optoelectronic characterization. We selected the inverted structure due to its greater stability and compatibility with low-temperature fabrication processes[137,138], which are advantageous for flexible substrates and large-scale manufacturing. Inverted OPVs generally exhibit prolonged stability, and even without encapsulation, they do not degrade within a few days. Furthermore, metal oxides such as ZnO and TiO_2 are preferred as interfacial layers in inverted OPVs due to their superior physical and chemical properties over organic interfacial layers, providing better charge extraction and environmental resistance[139,140]. These properties make inverted OPVs ideal for indoor energy harvesting and long-term applications.

Devices were fabricated using the inverted device structure of ITO/ZnO/active layer/MoO_3/Ag, as shown in Figure 24. Each sample contained two pixels, with an active surface area of 0.18 cm^2 per pixel.

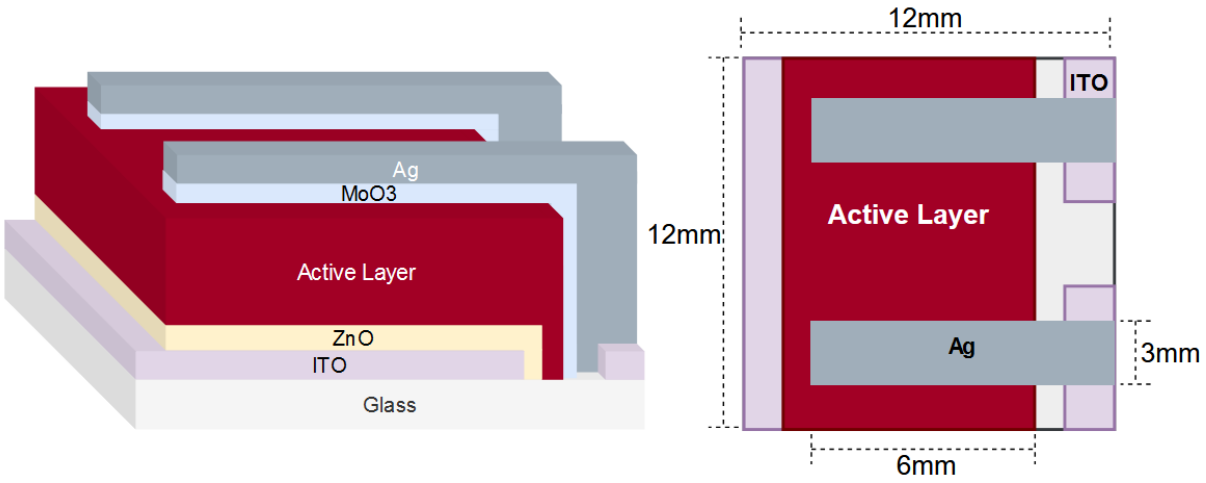

Figure 24. An inverted organic solar cell structure

Materials:

- Photoactive donor materials used:
  - **D18:** *Poly[(2,6-(4,8-bis(5-(2-ethylhexyl-3-fluoro)thiophen-2-yl)-benzo[1,2-b:4,5-b']dithiophene))-alt-5,5'-(5,8-bis(4-(2-butyloctyl)thiophen-2-yl)dithieno[3',2':3,4;2'',3'':5,6]benzo[1,2-c][1,2,5]thiadiazole)]* (M_W 74586, and PDI 2.38).
  - **P3HT:** *Poly(3-hexylthiophene-2,5-diyl)* (Regioregularity 95.2%, M_W 36600, PDI 2).
  - **PBDB-T (PCE12):** *Poly[(2,6-(4,8-bis(5-(2-ethylhexyl)thiophen-2-yl)-benzo[1,2-b:4,5-b']dithiophene))-alt-(5,5-(1',3'-di-2-thienyl-5',7'-bis(2-ethylhexyl)benzo[1',2'-c:4',5'-c']dithiophene-4,8-dione)]* (M_W 75725, and PDI 2.18).

    All of these donor materials were purchased from Ossila Ltd. (UK).

- **PBDB-T-2F (PM6):** *Poly[(2,6-(4,8-bis(5-(2-ethylhexyl-3-fluoro)thiophen-2-yl)-benzo[1,2-b:4,5-b']dithiophene))-alt-(5,5-(1',3'-di-2-thienyl-5',7'-bis(2-ethylhexyl)benzo[1',2'-c:4',5'-c']dithiophene-4,8-dione)]* (M_W 90000-11000, M_n 25000-35000), purchased from Brilliant Matters.
- **PF2 :** *Di-fluorinated copolymer* (M_W 30000, and PDI 3.8), was synthesized by N. Leclerc from the Institut de Chimie et Procédés pour l'Energie, l'Environnement et la Santé (ICPEES) in France. PF2 exhibits strong light-harvesting properties, with an absorption spectrum ranging from 400 to 750 nm[10,141]. Notably, it has good absorption in the blue region, which is unusual for many organic materials and is advantageous for application in IOPVs.

❖ Photoactive acceptor materials used:

- **BTP-4F (Y6):** *2,2'-((2Z,2'Z)-((12,13-bis(2-ethylhexyl)-3,9-diundecyl-12,13-dihydro-[1,2,5]thiadiazolo[3,4-e]thieno[2",3'':4',5']thieno[2',3':4,5]pyrrolo[3,2-g]thieno[2',3':4,5]thieno[3,2-b]indole-2,10-diyl)bis(methanylylidene))bis(5,6-difluoro-3-oxo-2,3-dihydro-1H-indene-2,1-diylidene))dimalononitrile* (purity > 98%, M_W 1451.93).
- **ITIC:** *3,9-bis(2-methylene-(3-(1,1-dicyanomethylene)-indanone))-5,5,11,11-tetrakis(4-hexylphenyl)-dithieno[2,3-d:2',3'-d']-s-indaceno[1,2-b:5,6-b']dithiophene* (purity > 99%, and M_W 1427.94).

  Both of these acceptor materials were purchased from Ossila.
- **Heptazine and its derivatives** were synthesized by P. Audebert from PPSM and XLIM laboratories[9]. TDPH is a derivative of heptazine, known for its ease of synthesis and adaptability for molecular tuning[6]. It was synthesized via a rapid reaction (about 15 min) using aminated heptazine as a precursor. The reaction involves attaching pyrazolyl groups to a heptazine core, and these groups are easily interchangeable, allowing flexibility in tuning the properties of the molecule to optimize performance in specific applications.

❖ Electron transport layer materials: Zinc oxide (ZnO) nanoparticle colloidal solution (5 nm diameter, ZnO 1% wt. semiconductive ink for inkjet printing) was supplied by Genesink under the product name Hélio ETL Jet.

❖ Hole transport layer material: Molybdenum(VI) oxide (MoO_3, purity 99.97%, and M_W 143.94) was purchased from Sigma-Aldrich.

❖ Metallic electrode: Silver (Ag, purity 99.99%) was purchased in the form of a 0.5mm diameter filament from Goodfellow.

❖ Solvents: Chlorobenzene (CB, anhydrous, 99.8%), ortho-dichlorobenzene (o-DCB, anhydrous, 99.8%), chloroform (CF, anhydrous, 99.8%) were all purchased from Sigma-Aldrich.

❖ Solvent additives: 1-Chloronaphthalene (CN, liquid), 1,8-Diiodooctane (DIO, purity 98%, contains copper as stabilizer, liquid), both purchased from Sigma-Aldrich.

The substrate is etched and cleaned as described in the following paragraphs.

Etching ITO substrates

Indium-doped tin oxide (ITO) is commonly used as a transparent conducting electrode in OSCs due to its excellent optical and electrical properties. The ITO substrates used in this study were purchased from VisionTek Systems Ltd (UK). They are coated 12x12 mm glass square substrates, with a glass thickness of approximately 1.1 mm. The ITO has an optical bandgap of around 3.5 eV and exhibits a high transmittance of 81.7% between 350-800 nm. Additionally, the ITO layer features a resistivity of 7 ohms/sq.

To fabricate OSCs at the laboratory scale, the ITO substrate must first be etched. The ITO side of the substrate is identified using an ohmmeter, and a number is inscribed on the glass side using a diamond stylus. Two different tapes are used to mask the desired ITO area. The unmasked ITO area is then etched using zinc powder and hydrochloric acid (HCl) diluted with water (v/v, 1/1) at room temperature. The etched ITO substrate is schematized in Figure 23. After etching, the ITO substrates are thoroughly cleaned by successive washing in acetone, ethanol, and isopropanol using an ultrasonic bath for 15 minutes at each step. This ultrasonic cleaning step effectively removes any contaminants adhering to the ITO surface. The substrates are then rapidly dried using a nitrogen gas gun. Before ETL deposition, the ITO substrates are subjected to UV-Ozone treatment for 20 minutes to finalize the cleaning step, and it also modifies their work function and surface wettability. As the UV-Ozone treatment can heat the substrates, it is recommended that the ITO substrates cool down before proceeding with spin-coating.

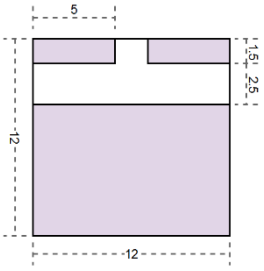

Figure 25. Diagram of ITO substrate after etching.

Deposition of ETL: ZnO

The colloidal solution of zinc oxide (ZnO) nanoparticles is deposited onto the UV-ozone treated ITO substrate by spin-coating, a technique widely used in the laboratory to produce high-quality thin films. In this method, a small drop of the solution is placed on a flat substrate, which is then evenly spread by the centrifugal force generated by the rotation of the substrate. The thickness and quality of the resulting film are strongly influenced by the properties of the solution, including temperature, viscosity, concentration, and homogeneity, as well as the spin-coating parameters, such as rotation speed, acceleration, duration, and whether static or dynamic spin-coating deposition, as shown in Figure 26.

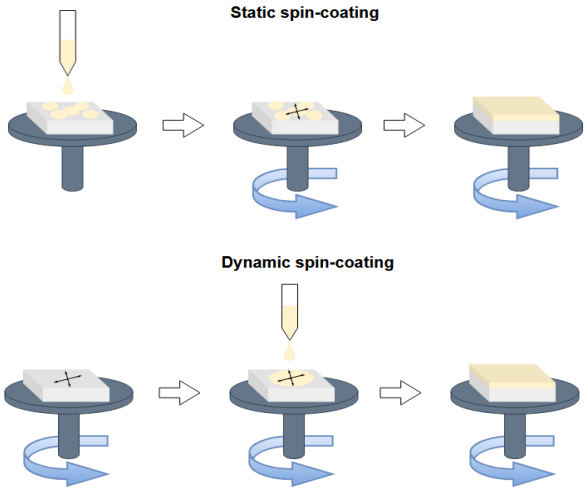

Figure 26. Schematic representation of the static and dynamic spin-coating process.

In static deposition, the solution is applied to the substrate before spinning begins. The substrate is then spun to spread the solution over the surface. In particular, depositing the solution as multiple droplets at different locations on the substrate can help to achieve a more uniform coating. In dynamic deposition, the solution is applied in a single step while the substrate is already spinning, allowing for immediate and uniform spreading.

In this study, a 20 nm thin film of ZnO was statically spin-coated onto cleaned ITO-coated glass substrates under ambient conditions using the WS 650MZ-23NPP spin-coater machine (Figure 25) from Laurell Technologies Corporation. The process was carried out with the following parameters:

Figure 27. A spin-coating machine is used to deposition the transporting layer under ambient conditions.

Solution volume: 60 µL

Speed of rotation: 4000 rpm

Acceleration: 1000 rpm/s

Times: 40s

After spin coating, the substrates were heated in ambient air on a hot plate at 130°C for 10 minutes to dry the films and remove organic components and ligands, as well as any residual solvents. All ZnO-coated ITO substrates were then transferred to a nitrogen-filled glove box.

Active layer solution preparation and deposition

The active layer solution was prepared by dissolving the donor and acceptor materials in an appropriate solvent. For this study, the reference sample consisted of PM6 (donor) and Y6 (acceptor) dissolved in CF to a total concentration of 16 mg·mL^{-1} with a weight ratio of 1:1.2. An additive of 0.5% CN (v/v, CN/CF) was also included. The solution was stirred overnight at room temperature to ensure complete dissolution and homogeneity.

Figure 28. A spin-coating machine is used for the active layer in the glove box.

After preparing the PM6:Y6 solution, it was statically spin-coated onto the prepared ZnO-coated ITO substrates in a nitrogen-filled glove box using the Spin 150 spin-coating machine from SPS-Europe. The following parameters were used to obtain an active layer with a thickness of approximately 100 nm:

- Solution volume: 80 µL
- Rotation speed: 3000 rpm
- Acceleration: 1000 rpm/s
- Times: 30s

Different spin coating speeds were tested to study their effect on the final film thickness. Table 7 summarizes the final thickness of the PM6:Y6 active layer as a function of the deposition parameters. These values show the relationship between spin coating speed and final film thickness, with higher speeds resulting in thinner films. The thickness was measured using a Dektak XT profilometer from Bruker, Germany.

Table 7. The thickness of the PM6:Y6 active layer as a function of deposition.

Speed (rpm)	Acceleration (rpm/s)	Times (s)	Thickness (nm)
2000	1000	30	108±12
3000	1000	30	99±10
4000	1000	30	88±9

The spin-coated films were then thermally annealed at 100°C for 10 minutes in a nitrogen-filled glove box to improve the morphology and crystallinity of the active layer. Finally, the ZnO layer and active layer were etched using a CF-impregnated cotton swab, following the design illustrated in Figure 29, which allows the subsequent deposition of HTL and top electrodes.

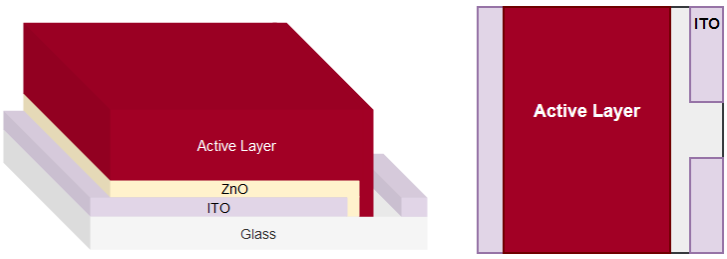

Figure 29. The design scheme of the active layer on top of the ZnO layer

Deposition of HTL and metallic electrode (Ag)

Finally, 10 nm of MoO_3 as the HTL and 100 nm of Ag as the top electrode were deposited by thermal evaporation under vacuum. Thermal evaporation is a common physical vapor deposition technique in which a material is evaporated under a high vacuum, 10^{-6} mbar in our case, using a resistive heating source. The material is then deposited onto the underside of the substrate, forming a smooth film. Thermal evaporation allows us to control the thickness of the evaporated material precisely, using a quartz microbalance in the deposition chamber. The mask used in our case provides for nine potential samples per evaporation to be processed, with two pixels each to create solar cells with an active area of around 0.18 cm², as shown in Figure 24.

II.2. Optical characteristics

II.2.1.1. UV-Visible spectroscopy

UV-visible spectroscopy is a technique used to characterize the absorption spectrum of thin films of organic materials by examining the various optical transitions (π-π*, internal charge transfer, etc.) associated with organic conjugated systems. Most of the transitions of interest for photovoltaic applications usually occur in the visible or near UV region of the electromagnetic spectrum. In UV-visible spectroscopy, molecules absorb photons, causing electrons to transition from their ground state to an excited state. The energy difference between these states corresponds to specific wavelengths of light, which are measured as absorption bands in the UV-Vis spectrum.

In this study, the optical properties of organic thin films deposited on various substrates (bare glass, glass-ITO, quartz) were characterized using UV-Vis spectroscopy with a Cary 300

spectrophotometer from Agilent Technologies (double-beam configuration). To extract the absorption spectrum from the UV-Vis spectrophotometer, we first measured the transmittance (T), which is calculated as the ratio of the intensity of the transmitted light (I) to the intensity of the incident light (I_0): $T = I/I_0$. Absorbance (A) is determined as the negative logarithm of transmittance and is calculated as follows: $A = -\log(T)$. The absorbance versus wavelength is plotted as an absorption spectrum. This calculation assumes that all incident light that does not pass through the sample is absorbed. However, this is a rough approximation and does not take into account reflection or scattering losses from the material surface. In reality, part of the incident light is reflected or scattered by the interfaces between the substrate, the film, and the surrounding air, resulting in a possible overestimation of the absorbance. Reflectivity (R) and scattering losses must be considered to determine the absorption spectrum more accurately. Ideally, the absorption coefficient should be calculated using transmittance and reflectance data to avoid inaccuracies. The correct relationship should be $A=-\log(T+R)$. However, if the reflection is small, we sometimes ignore it to simplify the calculations. This approximation is reasonable when the material or system is known to have low reflectivity or when the goal is to estimate the optical properties of the material roughly.

In addition to determine the absorption spectrum, UV-Vis spectroscopy can also be used to estimate the optical bandgap (Eg) of a material using the Tauc plot method[142]. The optical bandgap represents the energy difference between the HOMO and LUMO, which is a critical electronic property for organic materials used in photovoltaic devices. The Tauc method assumes that the absorption coefficient (α) depends on the photon energy () and the E_g of the material, as shown in Eq. 7:

$$\alpha_{(h\nu)} = \frac{B(h\nu - E_g)^n}{h\nu} \qquad \text{(Equation 7)}$$

where is the absorbance coefficient, is Plank's constant, is the frequency of the light, E_g is the optical band gap energy, B is a constant independent of energy, is a factor that depends on electron transition property. Therefore, the Tauc plot is particularly useful for identifying the optical transitions (direct or indirect) in a material. For indirect band gap transitions: , and for direct band gap transitions: $n = \frac{1}{2}$, and for direct band gap transitions: $n = 2$.[142]

The absorbance coefficient is proportional to the absorbance (Eq. 8):

$$\alpha = \frac{A \ln 10}{l} \qquad \text{(Equation 8)}$$

where is the thickness of the film in cm.

- For a direct band gap material, plot $(\alpha h\nu)^2$ against hv.
- For an indirect band gap material, plot $(\alpha h\nu)^{1/2}$ against hv.

Then, extrapolate in the linear region of the energy axis of the corresponding plot. The intersection with the energy axis is an estimate of the corresponding E_g.

II.2.1.2. Photoluminescence spectroscopy (PL)

PL spectroscopy is a powerful technique used to study the photophysical properties of organic materials, including the dynamic processes of charge carriers between the donor and acceptor within the active layer. In this study, the active layers of OSCs were analyzed using an

Edinburgh FLS980 PL spectrometer, with the setup shown in Figure 30a, to obtain their emission spectra.

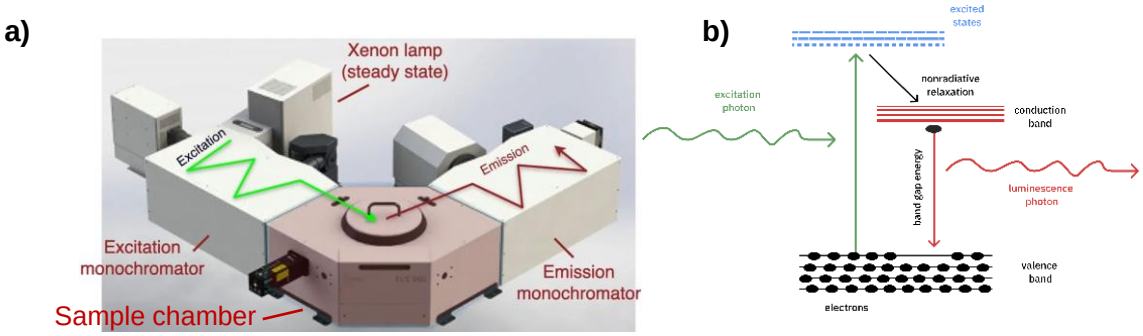

Figure 30. a) Edinburgh FLS980 photoluminescence spectrometer setup. b) Photoluminescence process.

As shown in Figure 30b, the process begins with the absorption of incident light by electrons in the organic materials, causing them to transition to higher energy excited states. These electrons then relax back to their original energy states, emitting photons whose energy corresponds to the energy gap between the excited and ground states of the material. The emitted photons are collected and analyzed using the PL spectrometer, providing emission spectra that represent the wavelengths of light emitted by the OSC materials due to exciton recombination processes. The position and intensity of the peaks in the emission spectra can vary depending on factors such as the molecular structure, purity, and morphology of the OSC materials. Changes in these spectral features can indicate variations in material properties, including the degree of crystallinity, the presence of defects, or the efficiency of exciton generation and recombination.

Additionally, PL decay measurements can capture the lifetime of excitons in the system, which is directly related to the charge transfer process. Faster decay times indicate that the excitons are effectively separated into free charges (rather than recombination), providing insight into the effectiveness of charge transfer between the donor and acceptor materials.

II.3. Near-field characteristics

II.3.1.1. Atomic force microscopy (AFM)

The nanoscale morphology of a mixed system and the crystallinity of the materials can synergistically influence device performance and thermal stability. To investigate this effect, the surface morphology of the binary mixtures was analyzed using AFM. In modern AFMs, the deflection of the cantilever is detected using a laser beam reflected from the back side of the tip and collected by a four-quadrant photodiode (Figure 32a). As the cantilever scans the surface, physical interactions between the tip and the sample cause the cantilever to bend, changing the angle of the reflected laser beam. A photodiode registers this change, and the motion of the reflection changes the output of the photodiode. When scanning with a constant force, an electronic feedback loop is used to maintain a stable signal from the photodiode, ensuring that the tip moves over the surface with a continuous load force. In this way, topographic information on the x, y, and z coordinates of the sample can be obtained and subsequently processed by a computer to generate an image. There are two main configurations, and one design uses a movable stage to scan the sample (in the x and y directions). At the same time, the probe is fixed (i.e., only changes in the z direction are

tracked), and a second design where the sample remains fixed while the probe can be moved in the x, y, and z directions. PeakForce Quantitative Nanomechanical Mapping (PeakForce QNM) is a new AFM mode that allows researchers to simultaneously map nanoscale mechanical properties and image surface topography at high resolution[143-145]. In PeakForce QNM mode, the AFM tip oscillates at a frequency of approximately 2 kHz, which is much lower than the resonance frequency of the cantilever typically used in conventional tapping mode AFM. The lower frequency allows for finer control of the interaction force between the tip and sample[146]. The maximum force exerted during each interaction called the peak force, is precisely controlled and used as a feedback signal in this mode. By controlling the peak force, PeakForce QNM maintains a gentle interaction with the sample, minimizing damage to the tip and surface. For each tap, a force curve is extracted, which contains detailed information about the mechanical properties of the material, as shown in Figure 31b and c[147]. Analysis of these force curves can provide information about the mechanical properties of the material, in particular about deformation, modulus, adhesion, and dissipation, leading to a detailed understanding of the mechanical behavior of materials at the nanoscale.

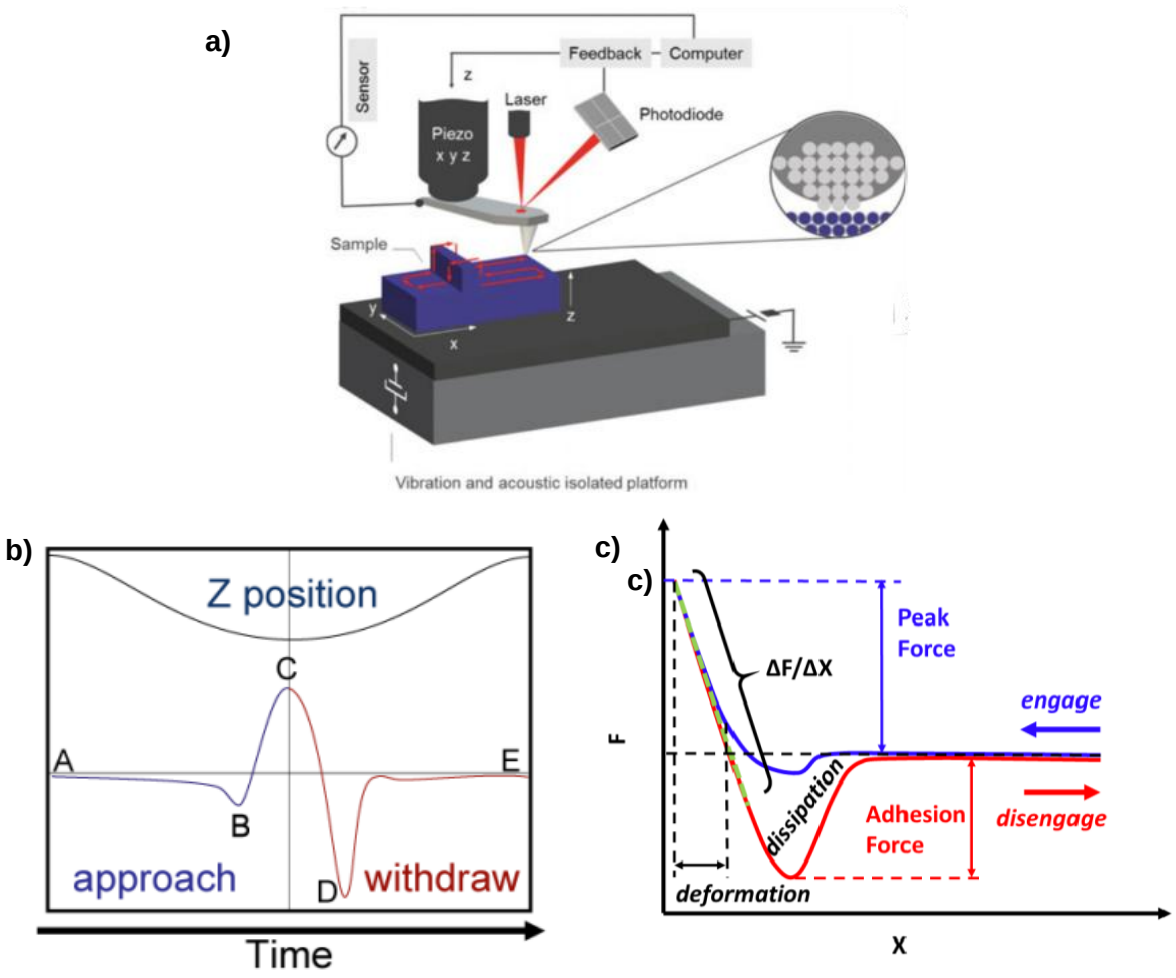

Figure 31. a) Diagram illustrating the AFM measurement principle[143]. b) Force curve measured in PF-QNM mode versus time and c) force curve versus distance between sample and tip using the Derjagin-Muller-Toporov (DMT) model, showing the information that can be extracted from this force curve[147].

In our study, we analyzed the nanoscale surface morphology of thin films of organic active layers using AFM, with measurements performed in our laboratory XLIM and in collaboration

with the Belgian laboratory LPNE. At XLIM, we performed topographic imaging in resonant mode using a Nano-Observer AFM microscope (CSI Nano-Observer) (Figure 32a). In resonant mode AFM, also commonly referred to as tapping mode, the AFM tip oscillates at a frequency close to its resonant frequency while scanning the sample surface. This mode minimizes damage to the AFM tip and sample, making it particularly suitable for use with soft or fragile materials such as organic thin films in OPVs. In addition, at LPNE, we acquired AFM height and adhesion images using a Bruker Dimension Icon I AFM operating in PeakForce quantitative nanomechanics (QNM) (Figure 32b). AFM height images reveal the nanoscale topography of the films, including the root mean square roughness (RMS). Meanwhile, AFM adhesion images revealed that all films exhibited an interpenetrating network structure, which is a characteristic of effective donor-acceptor phase separation. By studying the results from both instruments, we gain valuable insights into the structure-property relationships of binary blends, which is critical for optimizing device performance.

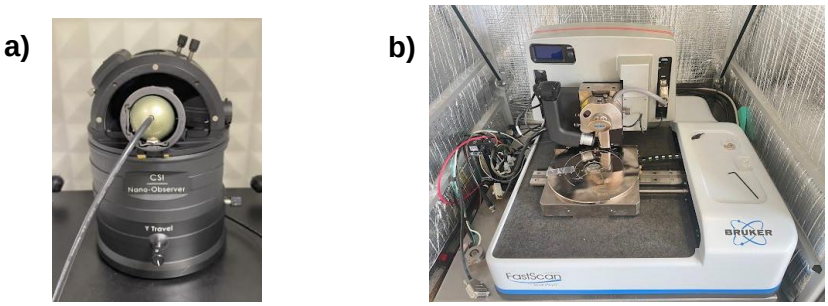

Figure 32. a) Nano-Observer AFM machine at XLIM. b) AFM machine type Bruker Dimension ICON at LPNE.

II.3.1.2. Scanning Microwave Impedance Microscopy (sMIM)

sMIM is a specialized technique in AFM used to map the local electrical properties of materials at the nanoscale. In sMIM, a microwave signal is transmitted through a conductive AFM tip that interacts with the sample surface, and the reflected signal is measured in real-time. This allows the technique to directly probe the conductivity and permittivity of the material beneath the tip. By detecting and processing the reflected signals during scanning, sMIM can image the capacitance (sMIM-C) and resistance (sMIM-R) properties of the material (Figure 33b). These images provide insight into local electrical properties at the nanoscale, enabling the identification of regions with different dielectric and conductive behaviors. This ability to simultaneously map capacitance and resistance is critical for understanding nanoscale electrical behavior in materials such as OPV active layers, where the heterogeneity of the blend plays a key role in device performance.

To complement our studies, we employed this advanced characterization technique in the LPNE laboratory using a Bruker Dimension ICON AFM equipped with sMIM mode (Figure 33a). The resulting sMIM-C and sMIM-R images of the active layer provide valuable information about the electrical properties, helping us analyze the performance of the device.

a) b)

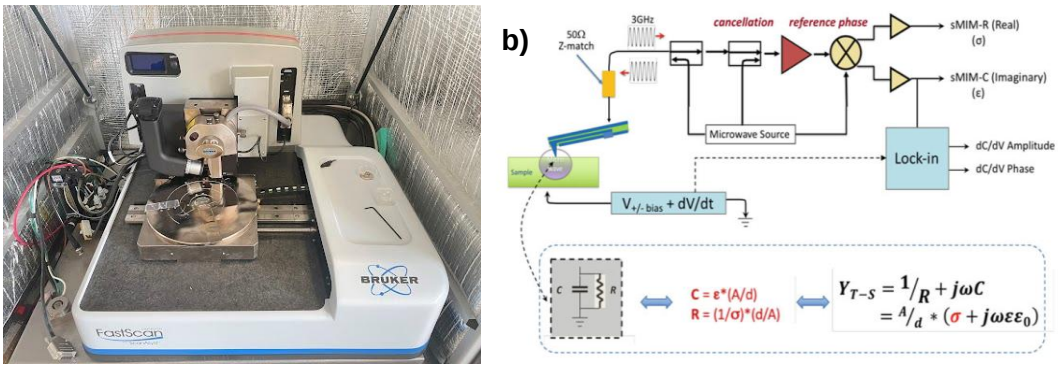

Figure 33. a) Photo of Bruker AFM machine equipped with sMIM mode. b) diagram showing how sMIM works[143].

II.4. Electrical characteristics

II.4.1. Space charge limited current (SCLC)

To further elucidate the charge transport properties in OPV devices, the SCLC method is employed to quantitatively characterize the electron and hole mobilities within the bulk heterojunction[148]. The technique involves applying a voltage across the device and measuring the resulting current to extract carrier mobility. The current in a solid is determined by the intrinsic properties of the material and the concentration gradient of charge carriers, both of which are affected by the density of trapped states. The J-V characteristics derived from SCLC measurements are useful for studying electron and hole transport as well as carrier injection and generation. The analysis uses a current injection to probe defect states in the semiconductor bandgap and evaluate the mobility of the charge carriers, which is critical for optimizing the performance of OPVs. As the injection bias increases, materials exhibiting SCLC can operate in several distinct regimes: ohmic region, trap-filled SCLC, and trap-free SCLC. These states are shown in Figure 34, which describe how charge transport changes with increasing voltage. The behavior of SCLC in OPV devices is defined by the Mott-Gurney equation[75,149,150], as shown in Eq. 9:

$$J_{SCLC} = \frac{9}{8}\varepsilon_0\varepsilon_r\mu\frac{V^2}{L^3} \qquad \text{(Equation 9)}$$

Where ε_0 is the permittivity of free space, ε_r (≈3 for organic semiconductors) is the dielectric constant, and J and μ are the current density and charge carrier mobility. V is the applied voltage. L is the thickness of the active layer.

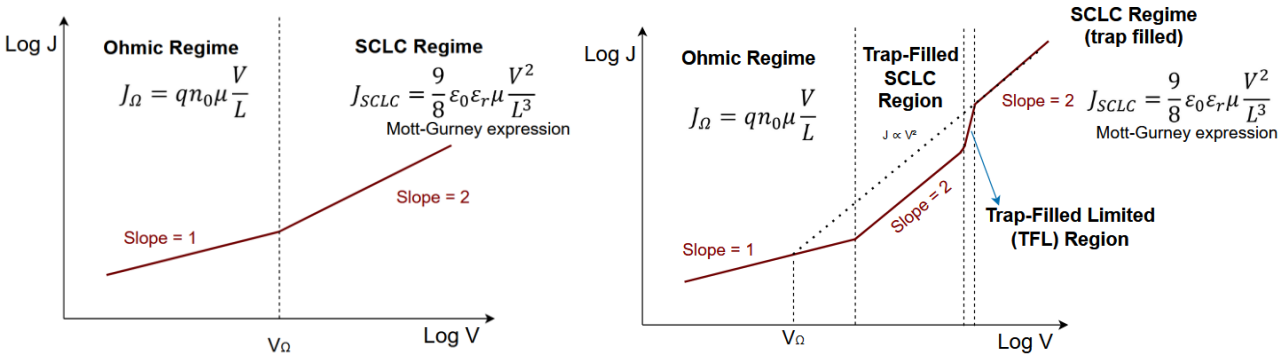

Figure 34. Schematic of J-V characteristics in a: a) pure SCLC regime and b) trap-limited SCLC regime.

The schematic in Figure 34 effectively shows the J-V characteristics in the SCLC region of an organic semiconductor, divided into two key regimes:

a) **Pure SCLC Regime:** This state represents the transition from the Ohmic region (slope = 1) to the SCLC region (slope = 2). In this SCLC regime, charge carrier injection is not significantly affected by traps, and the current is proportional to V^2, indicating the presence of a trap-free SCLC regime.

b) **Trap-Limited SCLC Regime:** At low applied voltages, the ohmic region is observed, where the current increases linearly with voltage, following Ohm's law. This region represents the area where injected charge carriers are not strongly affected by traps, and the intrinsic conductivity of the material limits the current flow. As the voltage is increased, trap states within the material begin to capture the injected charge carriers. This initiates the trap-limited SCLC regime, and the current rate starts to increase with a slope of about 2 on the log-log plot. In this state, the traps gradually fill up as more carriers are injected into the device. When the trap states are saturated, the current increases rapidly. This transition marks the entry into the trap filling limit (TFL) region, with a slope exceeding 2 due to the dominance of filled traps. Once all traps are filled, the current follows a quadratic dependence on voltage, reflecting trap-free transport in the pure SCLC regime. In this region, the Mott-Gurney law applies, and the current is dominated by space charge effects rather than traps, which determines the charge carrier mobility.

In our study, we applied the space charge limited current (SCLC) model to measure the hole mobility in the active layer film using a hole-only device structure: ITO/PEDOT:PSS(40 nm)/active layer/MoO_3 (10 nm)/Ag (100 nm). This structure ensures that only holes participate in the current flow, allowing the hole mobility to be precisely determined without interference from electron transport. To experiment, we applied a voltage across the device with one probe connected to the ITO electrode and the other to the Ag electrode on top of the active layer (Figure 35). The J-V curves in the range of 0-5 V were recorded using a Keithley 2400 source meter while the device was placed on a Linkam© HFS600E stage under vacuum conditions at room temperature. The data were analyzed according to the Mott-Gurney law to extract the hole mobility.

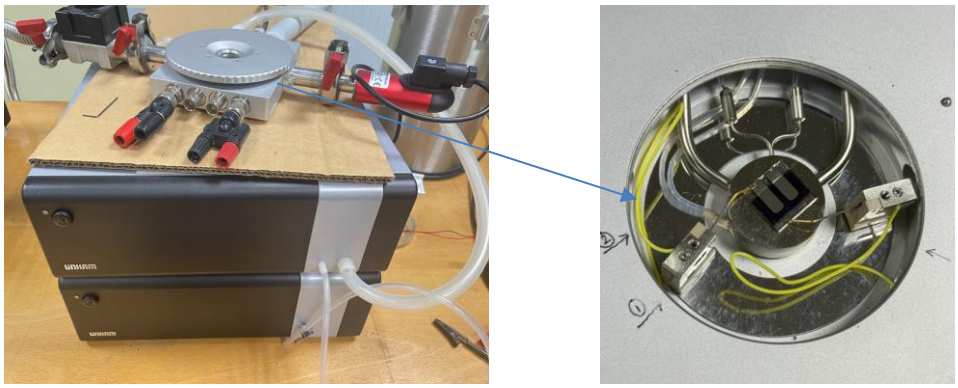

Figure 35. Experimental setup for SCLC measurements under vacuum.

II.5. Optoelectronic characteristics

II.5.1. J-V characterization AM 1.5G solar simulator

As mentioned earlier, J-V measurement is a fundamental technique for evaluating solar cell performance. The method involves using a source meter to apply a controlled voltage bias to the device while measuring the resulting current. Through this process, several key parameters can be extracted, including J_{SC}, V_{OC}, FF, PCE, R_{SH}, and R_S. To ensure comparability of performance data between different studies and laboratories, it is crucial to consider standard test conditions (STC). For outdoor measurements, these conditions have been refined since the 1980s and are widely accepted by the scientific community. The International Electrotechnical Commission (IEC) has published protocols, such as IEC 60904-1, which outlines the “Measurement of Photovoltaic Current-Voltage Characteristics” under standard conditions. In our laboratory, J-V measurements were performed inside a glove box using a computer-controlled Keithley 2400 sourcemeter to maintain an inert environment (Figure 36). The source meter applies a sweeping voltage across the electrodes of the solar cell and records the resulting current density response. For illumination, we used a solar simulator emitting a spectrum conforming to the AM1.5G standard, and measurements were performed without an aperture mask. The solar simulator provides 1000 W/m² of radiant intensity according to the IEC standard spectrum of AM1.5G, simulating sunlight passing through 1.5 times the Earth's atmosphere at a zenith angle of 48.2°. The AM1.5G standard is used to simulate real-world sunlight conditions, ensuring that the measurement results reflect the performance of the solar cell under typical outdoor conditions.

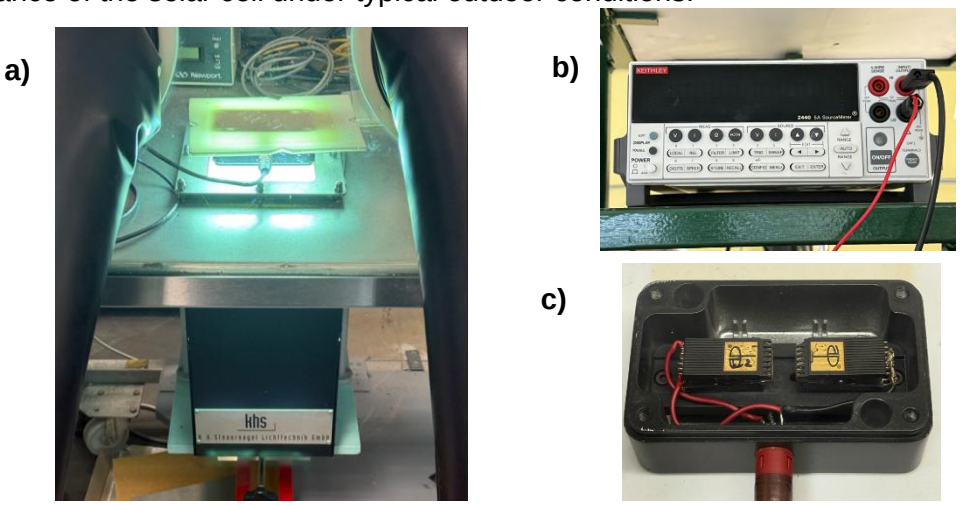

Figure 36. a) J-V measurement setup for solar cell characterization in XLIM laboratory glove box: solar simulator, b) Keithley 2400 source meter, and c) sample holder.

It is important to consider that the spectrum produced by a solar simulator does not exactly match the AM1.5G solar spectrum that represents natural sunlight. Therefore, there may be differences between the actual spectrum used during testing and the AM1.5G reference. To address this issue, a mismatch factor (M) must be applied. This factor helps correct for differences in the spectra, ensuring that the performance of the solar cell is neither overestimated nor underestimated during the J-V measurement. The calculation of M for a given cell requires knowledge of the sensitivity of the cell under test. This sensitivity is linked to the EQE of cell and is measured in compliance with IEC 60904-03.

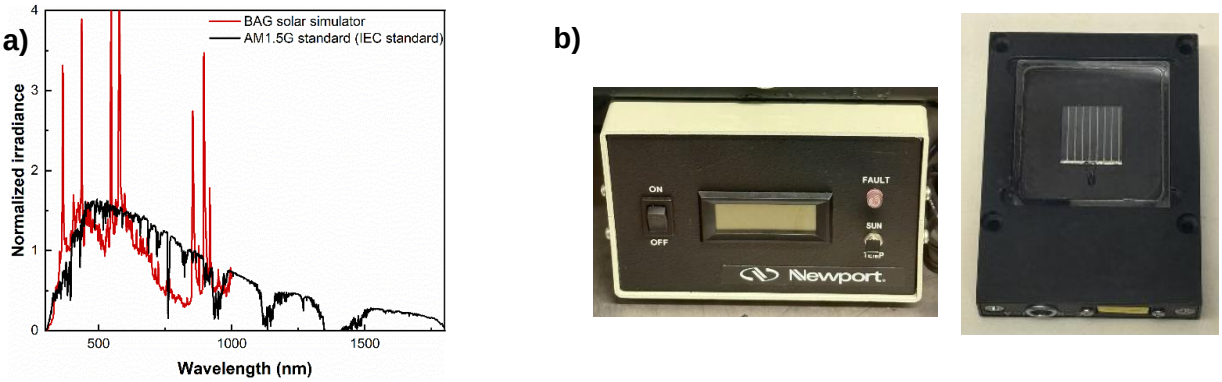

Figure 37. a) Comparison of BAG solar simulator irradiance spectrum with AM1.5G standard solar spectrum (IEC standard), and b) calibration Si reference cell (Newport Company, Oriel instruments, Starford, CT, U.S.A., Model 99150V).

II.5.2. Lighting conditions and Indoor J-V characterization

Unlike outdoor testing, which uses the AM1.5G spectrum to simulate sunlight, indoor characterization is usually performed under artificial lighting conditions that can vary widely. Indoor artificial lights are designed to provide a perception of white. Their spectrum is usually continuous and lies within the range where the human eye's spectral response is significant, i.e., 400-700 nm (see Figure 38). The color temperature of a light source is defined as the absolute temperature (in Kelvin (K)) of a theoretical blackbody radiator that radiates a spectrum similar to that of the light source. The range is typically between 2000 K and 10000 K. Low color temperatures (< 4000 K) produce light that leans toward yellow or red and is often called "warm." These are typical of incandescent and evening light. High color temperatures (> 4000 K) produce light that leans toward blue, called "cool," and is commonly seen in daylight or modern LED and fluorescent lighting. Acceptable white light temperatures for both indoor and outdoor lighting cover this range and are categorized according to their color temperature. Figure 38b specifically illustrates the color temperature correspondence of LEDs used in public lighting applications, which range from warm white to cool bluish-white depending on the color temperature. At the same time, Table 8 compares the characteristics of warm and cool LEDs and their applications.

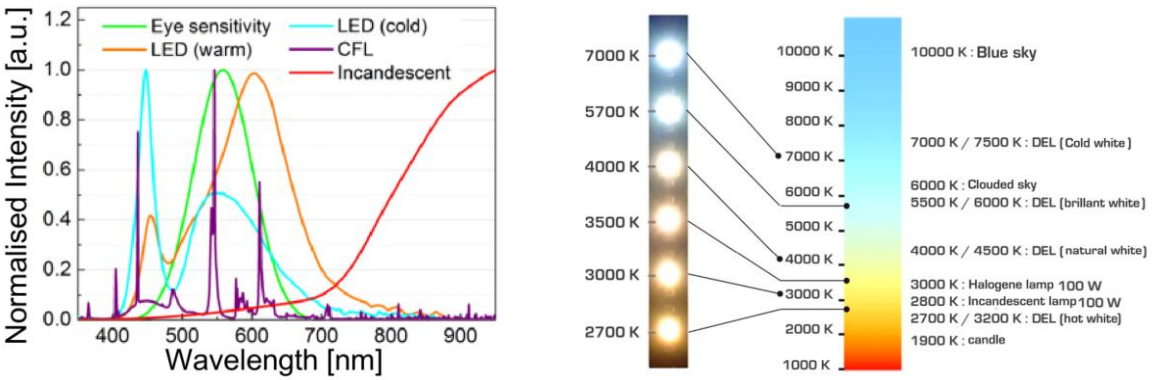

Figure 38. a) Normalized spectra of common light sources measured with the ILT950 spectroradiometer: comparison of the CIE 1931 standard human eye response, warm white LEDs, cool white LEDs, CFLs, and incandescent lamps[151]. b) Color temperatures range from 1,000 K to 10,000 K, showing corresponding light sources and color perception[152].

Historically, indoor testing has lacked standardization, with different labs using different conditions for power and efficiency measurements. This includes using various light sources, such as white LEDs, FLs, and other types of lighting with different color temperatures and a range of light intensities, typically from 200 lux to 2000 lux. This variability creates challenges when trying to compare the reported efficiencies of different PV technologies.

Table 8. Comparison of warm and cold LED characteristics and applications.

Led type	Color temperature	Environment	Applications
Warm Led	2700K to 3000K	Comfortable, relaxing, and warm ambiance	Residential spaces, homes, kitchens, restaurants, hotels
Cold Led	> 5000K	Precision-focused, crisp, and bright lighting	Industrial settings, schools, hospitals, workspaces

The European standard EN 12464-1 defines specific lighting requirements for workplaces to ensure visual comfort and optimal performance of the human eye[153]. This standard provides detailed guidelines for different rooms, areas, and activities, specifying the illuminance required for various environments. As shown in Table 9, the illuminance levels measured in several rooms with different lighting conditions typically range from 100 to 1000 lux, with a few specific environments reaching up to 1500 or even 2000 lux.

Table 9. Examples of the illumination levels for indoor space.

Environment	Illuminance (lux)
Dim corridor, stores	100
Loading bays, switch rooms, plant rooms	150
Foyers, entrance halls, dining rooms	200
Libraries, sports hall, lecture theatres	300
General offices, kitchens, laboratories, retail shops	500
Drawing offices, meat inspection, chain stores	750
General inspection, electronic assembly, paintwork, supermarkets	1000
Fine work and inspection, precision assembly	1500
Assembly of minute items, finish fabric inspection	2000

Until recently, in 2023, the IEC introduced a technical specification for the evaluation of indoor PV equipment: "Nano-enabled Photovoltaics - Device Evaluation Method for Indoor Lighting" (IEC TS 62607-7-2). The standard outlines procedures and guidelines for measuring the power and efficiency of nano-photovoltaic devices under controlled indoor lighting conditions, including classification requirements for light sources that simulate indoor conditions and specifications for measurement conditions, such as temperature requirements, traceability, and spectral mismatch correction. It recommends lighting levels of 50, 200, and 1000 lux to create a consistent indoor test environment. This specification is an important reference for establishing reliable and repeatable indoor PV test protocols. The standard addresses the need for accurate and traceable measurements by specifying requirements for light sources, power measurement instruments, and calibration reference equipment. Adherence to these specifications ensures more consistent comparisons between different laboratories and studies. Table 10 compares STCs for outdoor and IPV luminaires, while Table 11 shows the ISTC specification for testing IPV devices.

Table 10. Standard Testing Conditions (STCs) for both outdoor and indoor photovoltaic.

STCs	Outdoor	Indoor
Source	Sun simulator	Artificial light sources (LEDs, FLs, incandescent bulbs)
Air mass	AM 1.5	Not applicable
Irradiance	1000 $W.m^{-2}$	50, 200, and 1000 lux
Cell temperature (°C)	25	25
Reference	IEC 60904-1	IEC TS 62607-7-2:2023

Table 11. Illuminance levels, irradiance, temperature, and spectrum standards for testing IPV device performance under indoor lighting conditions at ISCT[49].

Illuminance (lux)	Irradiance with LED-B4 spectrum ($mW.m^{-2}$)	Irradiance with FL10 spectrum ($mW.m^{-2}$)
1000	3132	3076
200	626	615
50	157	154
Temperature (°C)	25	
Spectrum	CIE B4-LED reference spectrum (white LED)	CIE FL10 reference spectrum (fluorescent lamp)

Additionally, when discussing indoor test conditions, it is important to distinguish between irradiance and illuminance. Irradiance is the radiant power received per unit area, expressed in W/m^2, while illuminance is the luminous flux per unit area, expressed in lux (lx) or lumens per square meter (lm/m^2). For indoor PV testing, illuminance is more important because it is consistent with human visual perception, especially under common indoor lighting sources.

In our study, we standardized our measurements at 200, 500, and 1000 lux using LED lighting to ensure relevance and comparability between different studies. Although our use of LED spectra in a benchtop setting simplifies the indoor characterization process by avoiding mismatch corrections, variations in indoor light sources must be considered when comparing IPV device performance across studies. The setup in our laboratory for indoor J-V measurements consists of a black box equipped with a stage for sample positioning, as depicted in Figure 39. The artificial light source (either a warm or cold LED from Osram) is located at the top of the measuring station. To minimize the effects of diffuse light, the internal walls of the box are painted black, a practice commonly recommended in the literature[154]. In this setup, the distance between the light source and the sample is fixed. However, we can adjust the illumination level by varying the input power of the lamps. It is achieved using an ISO-TECH IPS 303DD power supply, which provides controlled voltage and current to the LEDs, as mentioned in Table 12 below. It is crucial to ensure complete thermal stabilization of the light source, which usually requires several tens of minutes.

Table 12. Power supply current and voltage corresponding to irradiance levels for indoor J-V measurements under warm and cold LED lighting conditions.

Led type	Nominal illumination (Lux)	Measured illumination (Lux)	Applied current (A)	Applied voltage (V)	Total irradiance ($W.m^{-2}$)
Warm Led	200	206	0.061	17.2	0.66
	500	517	0.183	17.9	1.65
	1000	1035	0.467	19.0	3.29
Cold Led	200	204	0.038	17.2	0.69
	500	509	0.097	17.8	1.73
	1000	1038	0.210	18.6	3.58

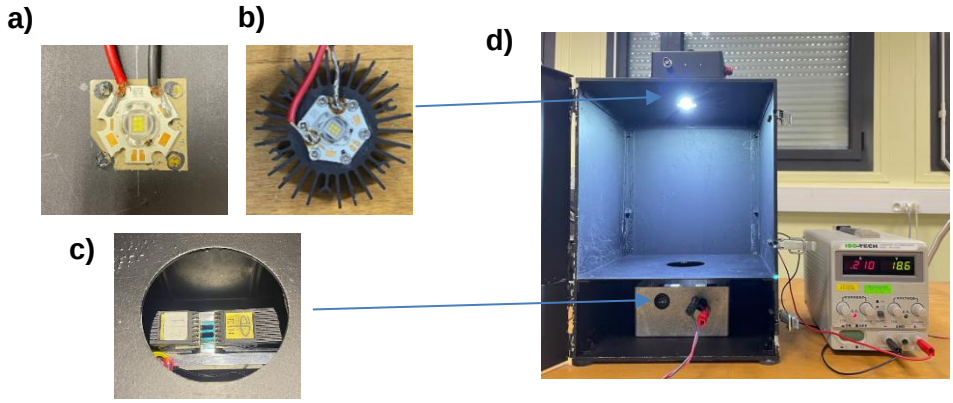

Figure 39. Indoor J-V measurement setup: a) cold LED lighting with radiator, b) warm LED lighting with small radiator, c) sample holder, and d) black box setup with power supply.

To accurately measure the illuminance and optical power densities of the incident light on the device under test (DUT), we used a BLACK-Comet Model Super Range 200-1100 nm spectrometer from StellarNet Inc (USA), paired with a cosine-corrected detector, as shown in Figure 40. The detector, calibrated for accurate irradiance measurements over a broad spectral range, was strategically placed in the center of a black box to minimize stray light and reflections. The distance between the light source and the detector was carefully matched to the distance between the light source and the sample holder. This arrangement ensured consistent and reliable measurements that accurately reflected the conditions experienced by the sample.

Figure 40. Photograph of the spectrometer and detector setup at XLIM.

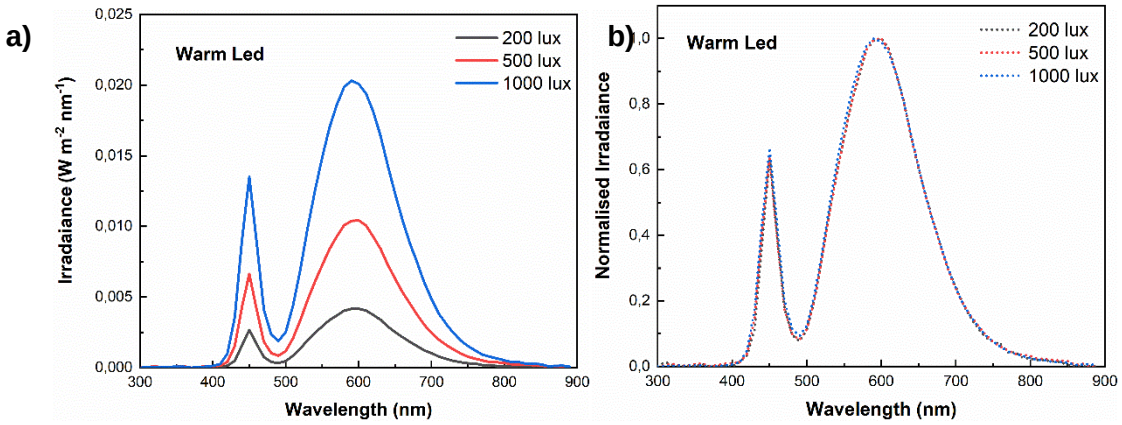

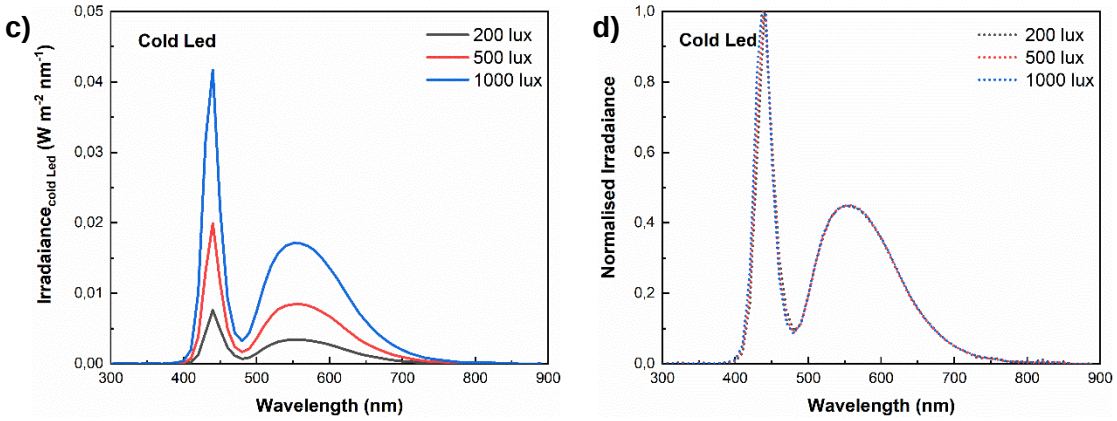

Figure 41. Irradiance and Normalized Spectral Profiles of the Light Output at the Sample Plane Across Three Illuminance Levels (200 lux, 500 lux, and 1000 lux) Using Warm LED (a, b) and Cold LED (c, d) Lighting at XLIM.

Figure 41 shows the irradiance and normalized spectral profiles of light output at the sample plane over three illuminance levels (200 lux, 500 lux, and 1000 lux) using Warm LED (a, b) and Cold LED (c, d) illumination at XLIM. From panels (a) and (c), it can be seen that the irradiance increases proportionally with the input power for both Warm and Cold LEDs, indicating effective control of light intensity. In panels (b) and (d), the normalized spectra show that by adjusting the LED input power, it is possible to achieve varying irradiances with minimal spectral deviation. This consistency across different light levels ensures reliable and comparable measurements under different lighting conditions.

The temporal stability of the LED light source was performed by measuring its illuminance at three different levels, 200, 500, and 1000 lux, every 3 minutes for 30 minutes after a 30-minute pre-heat of the LED to ensure thermal stability, as shown in Figure 42.

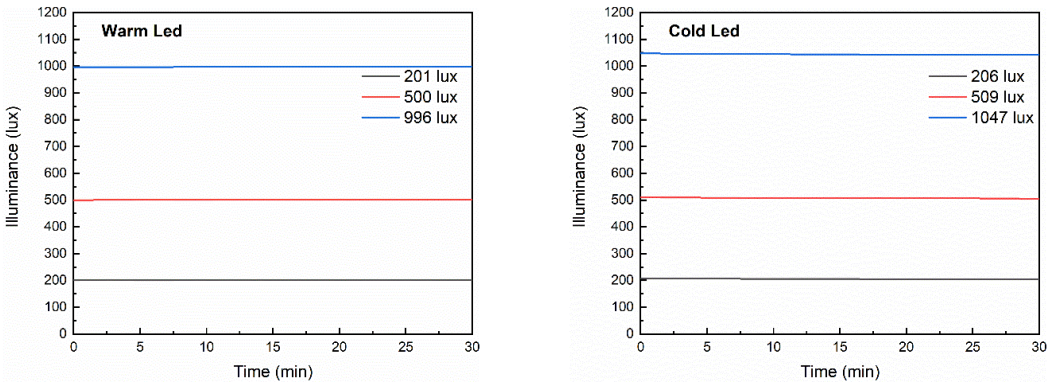

Figure 42. Temporal stability measurements of warm and cold LEDs used in the XLIM lab setup.

The results show very stable performance, with minimal variation in illuminance over the period measured. Specifically, the maximum variation observed was approximately 1%, indicating exceptional consistency in the LED's light output. These measurements were taken sequentially, moving smoothly from 200 lux to 500 lux and then to 1000 lux, with no interruption or fluctuation in performance. These consistent measurements, taken at regular intervals, confirm the reliability of the LED's output at different illuminance levels. The LED was operated continuously and transitioned smoothly between the different lux levels without any significant fluctuations. This stability is substantial for our experimental setup, where the reliability of the light source is crucial to ensure accurate and repeatable results during consecutive measurements taken outside the glove box.

II.5.3. External quantum efficiency (EQE)

EQE, also known as Incident Photon-to-Current Efficiency (IPCE), measures the wavelength-dependent efficiency with which incident photons are converted into electrical current. Analysis of the EQE spectrum provides valuable insight into the light-harvesting efficiency, charge generation, and charge extraction efficiency within the device. EQE is generally calculated using the following formula Eq. 10:

$$EQE = \frac{collected\ charges\ at\ a\ given\ wavelength}{incident\ photons\ of\ the\ same\ wavelength} \qquad \text{(Equation 10)}$$

The theoretical J_{SC} can be calculated by integrating the product of the EQE and the incident light spectrum over all wavelengths for both indoor and outdoor conditions, as shown in Eq. 11:

$$J_{sc} = \frac{q}{hc}\int_{\lambda min}^{\lambda max} EQE\ (\lambda) * P_{in}(\lambda) * d(\lambda) \qquad \text{(Equation 11)}$$

where λ is the wavelength, h is Planck's constant, and c is the speed of light. P_{in} (λ) is the power density of incident light as a function of wavelength. This equation allows J_{SC} to be calculated by taking into account the spectral response of the device and the characteristics of the incident light in both indoor and outdoor conditions.

To obtain accurate EQE measurements, it is critical to calibrate the measurement system against a reference cell. Calibration compensates for system response and ensures precise comparison between the measured solar cell and ideal standard conditions. If the spectral irradiance of the light source used in the EQE setup differs from the light source used for J-V measurements, a mismatch factor may need to be used to avoid overestimation or underestimation of J_{SC}. In our study, EQE measurements were performed using the Enlitech QE-T system (Figure 43), which provides wavelength-resolved EQE data. The obtained spectra were calibrated against a certified reference cell (Si solar cell, see Figure 43a) to ensure accurate determination of the EQE and final J_{SC} of our devices. This process helps eliminate spectral mismatches and ensures that the J_{SC} values derived from the EQE data are consistent with those obtained through J-V characterization, thus improving the reliability of our performance assessments under different lighting conditions.

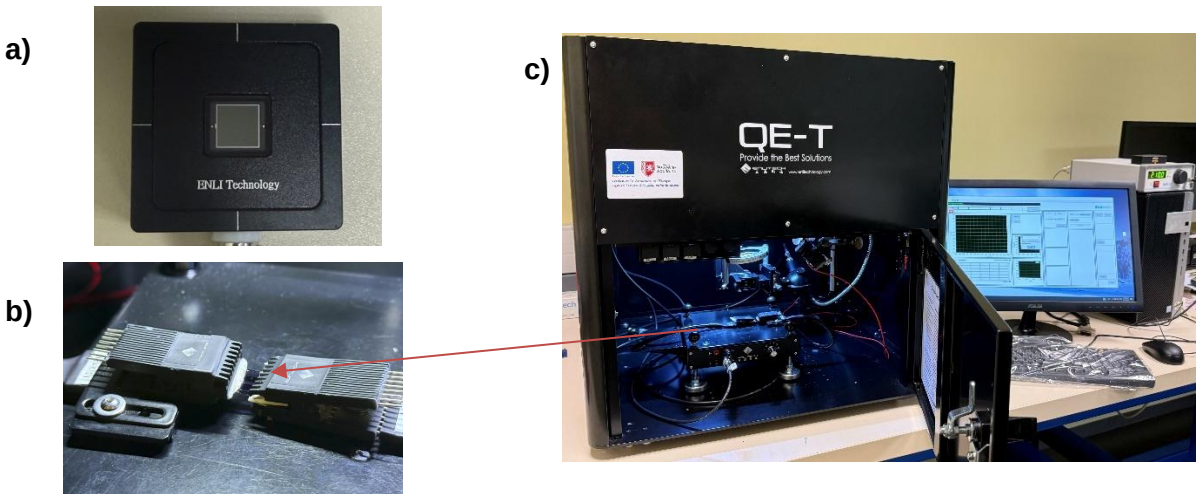

Figure 43. EQE setup at XLIM with reference Si solar cell (a).

Chapter III. Optimization of OCSs for indoor applications using new NFAs Heptazines

In indoor environments dominated by light sources such as white LEDs, the spectral distribution and intensity differ significantly from natural sunlight. To address these unique conditions, the design of OPVs must employ materials that are specifically tuned to efficiently capture and convert the limited, specific spectrum of light. This has led to a growing interest in exploring new molecular materials, particularly NFAs, which offer greater flexibility in tuning electronic properties to match the spectrum of indoor lighting.

In this context, my thesis proposes an innovative strategy to improve the performance of OPV cells under indoor lighting conditions by integrating novel NFAs into the active layers. Specifically, this work focuses on utilizing a molecular platform based on heptazines, a new class of NFAs with high band gaps that absorb in the blue region of the spectrum and support high V_{OC} in OPV devices. The large band gap of heptazine-based NFAs reduces energy losses by minimizing the LUMO shift between donor and acceptor materials, thereby improving the energy conversion efficiency under artificial light sources such as white LEDs.

This work was developed in close collaboration with Prof. Pierre Audebert and his team at the Laboratory of Photo-physique et Photo-chimie Supramoléculaire et Macromoléculaires (PPSM-Université Paris-Saclay, ENS Paris-Saclay, CNRS) and the XLIM ELITE team. They pioneered the synthesis of heptazine derivatives, providing a unique opportunity to explore their integration into OPV devices.

This chapter will cover two main aspects: first, the fabrication and optimization process of organic solar cells will be introduced with the PM6[a]:Y6[b] system as a reference. This section details the key manufacturing processes at XLIM, including material deposition, control of active layer morphology, and influence of the thickness of the active layer; second, an in-depth discussion will be given on the material selection, fabrication techniques, and optimization strategies for developing OPVs suitable for indoor use by integrating novel heptazine NFAs into the active layer.

III.1. OSC manufacturing process using PM6:Y6 as a reference system

PM6:Y6 was chosen as the reference system due to its high efficiency and well-documented performance under standard solar conditions (Figure 44a) [29,155-157]. In 2019, a major advance in OSCs was marked by the development of a new NFA Y6, which features an A-DA'D-A structure and an electron-deficient fused-ring core[29]. When combined with the widely used polymer donor PM6, the Y6-based OSCs achieved an impressive PCE of 15.7% with a high V_{OC} of 0.825 V, a J_{SC} of 25.2 mA.cm^{-2}, and an FF of 74%. We designed the experimental parameters of the PM6:Y6 system based on several important publications that optimized these solar cells for outdoor operation[29,85,158]. As described in Chapter II.1, we followed the established fabrication process for PM6:Y6 OPV devices. ZnO and MoO_3 were used as the electron extraction layer and the hole extraction layer, respectively. Furthermore, we explore

[a] **PM6:** *Poly[(2,6-(4,8-bis(5-(2-ethylhexyl-3-fluoro)thiophen-2-yl)benzo[1,2-b:4,5-b']dithiophene))-alt-(5,5-(1',3'-di-2-thienyl-5',7'bis(2-ethylhexyl)benzo[1',2'-c:4',5'-c']dithiophene-4,8-dione)]*

[b] **Y6:** *2,2'-((2Z,2'Z)-((12,13-bis(2-ethylhexyl)-3,9-diundecyl-12,13-dihydro-[1,2,5]thiadiazolo[3,4 e]thieno[2",3":4',5']thieno[2',3':4,5]pyrrolo[3,2-g]thieno[2',3':4,5]thieno[3,2-b]indole-2,10-diyl)bis(methanylylidene))bis(5,6-difluoro-3-oxo-2,3-dihydro-1H-indene-2,1 diylidene))dimalononitrile*

the effect of active layer thickness by studying three different thicknesses to evaluate their impact on the device performance.

Figure 44 shows the molecular structures of PM6 and Y6 materials, the normalized absorption spectrum of PM6:Y6 blend film, and the stacking configuration of the layers that make up the entire OPV device. In addition, it highlights the energy levels of the materials used (derived from the literature), including HOMO and LUMO levels of donor and acceptor (Figure 44d), which are critical for efficient charge transfer and overall device performance.

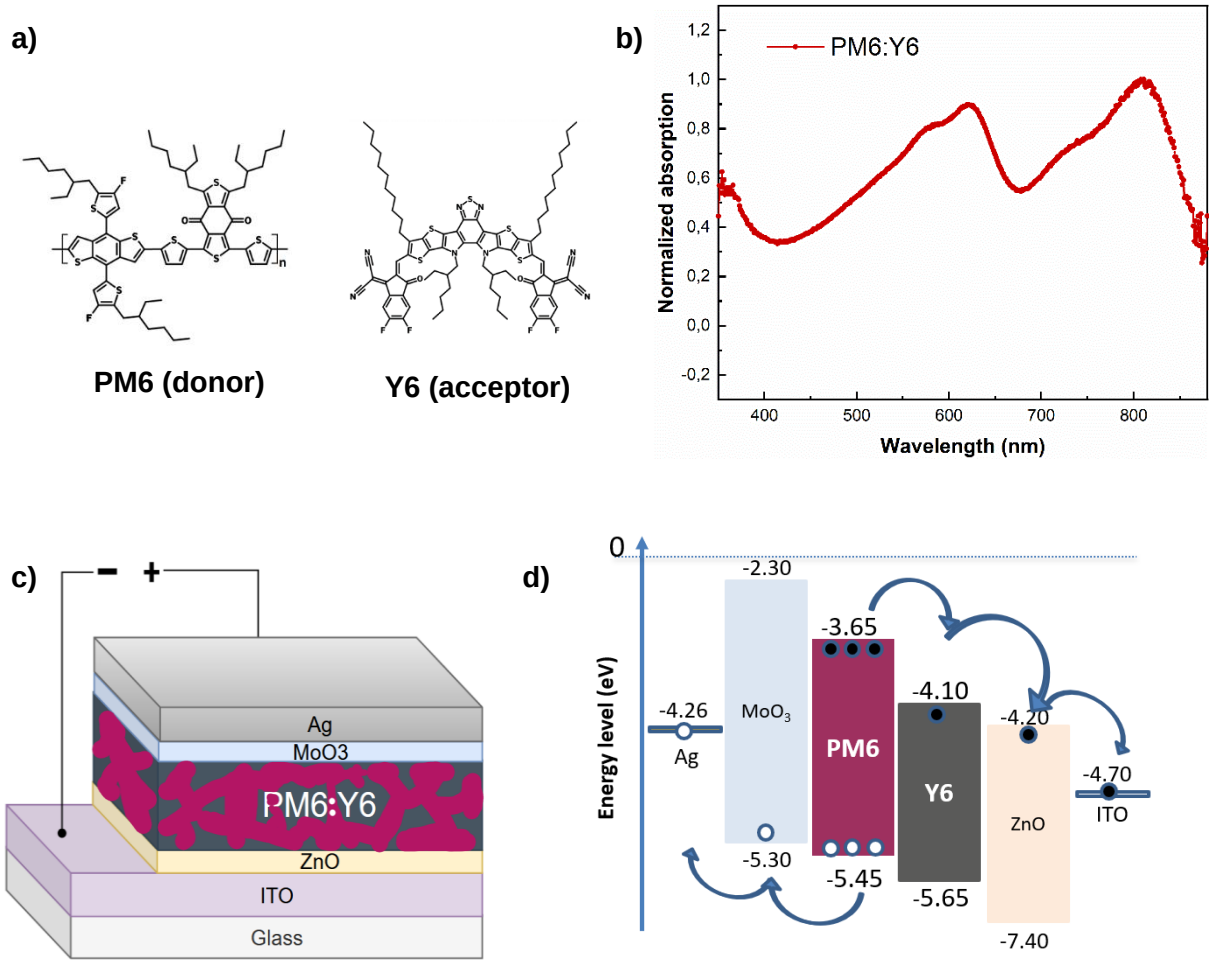

Figure 44. a) Chemical structure of PM6 (donor) and Y6 (acceptor). b) Normalized absorption spectrum of PM6:Y6 blend film. C) Structure of OPV with PM6:Y6. d) Energy levels of the materials used in the OPV device.

The fabrication of the active layer followed the procedure outlined in Chapter II, where a PM6:Y6 mixture was prepared and deposited on a glass/ITO/ZnO substrate. We then used AFM to study the surface morphology and local adhesion of these blends, as shown in Figure 45 below.

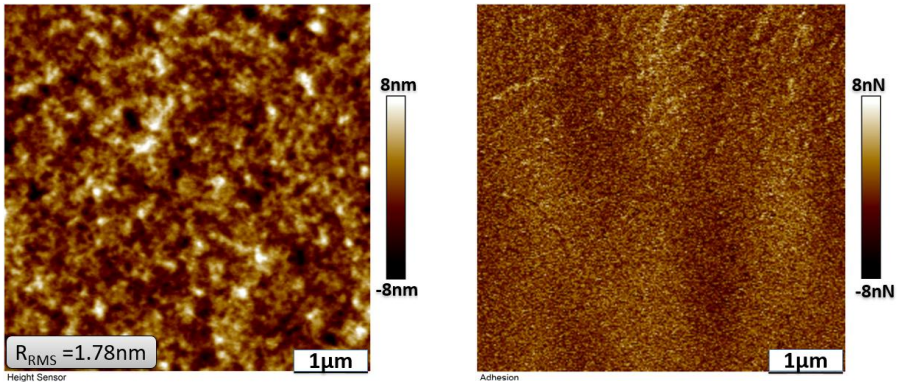

Figure 45. AFM height images (5x5µm, left) and AFM adhesion images (5x5µm, right) of PM6:Y6 blend films.

The height image on the left shows the surface morphology of the PM6:Y6 blend film, revealing the surface features and roughness, with a root mean square roughness (R_{RMS}) value of 1.78 nm, indicating a relatively smooth surface, consistent with Ref. 29. The adhesion image on the right shows an interpenetrating network structure, which is characteristic of effective donor-acceptor phase separation.

The blend films of PM6 and Y6 were integrated into OPV devices using an inverted structural configuration (ITO/ZnO/active layer/MoO_3/Ag). The full description of processing steps are given in Chapter II. Figure 46 and Table 13 show the corresponding JV curves and PV parameters under the solar simulator in AM 1.5G conditions (outdoor).

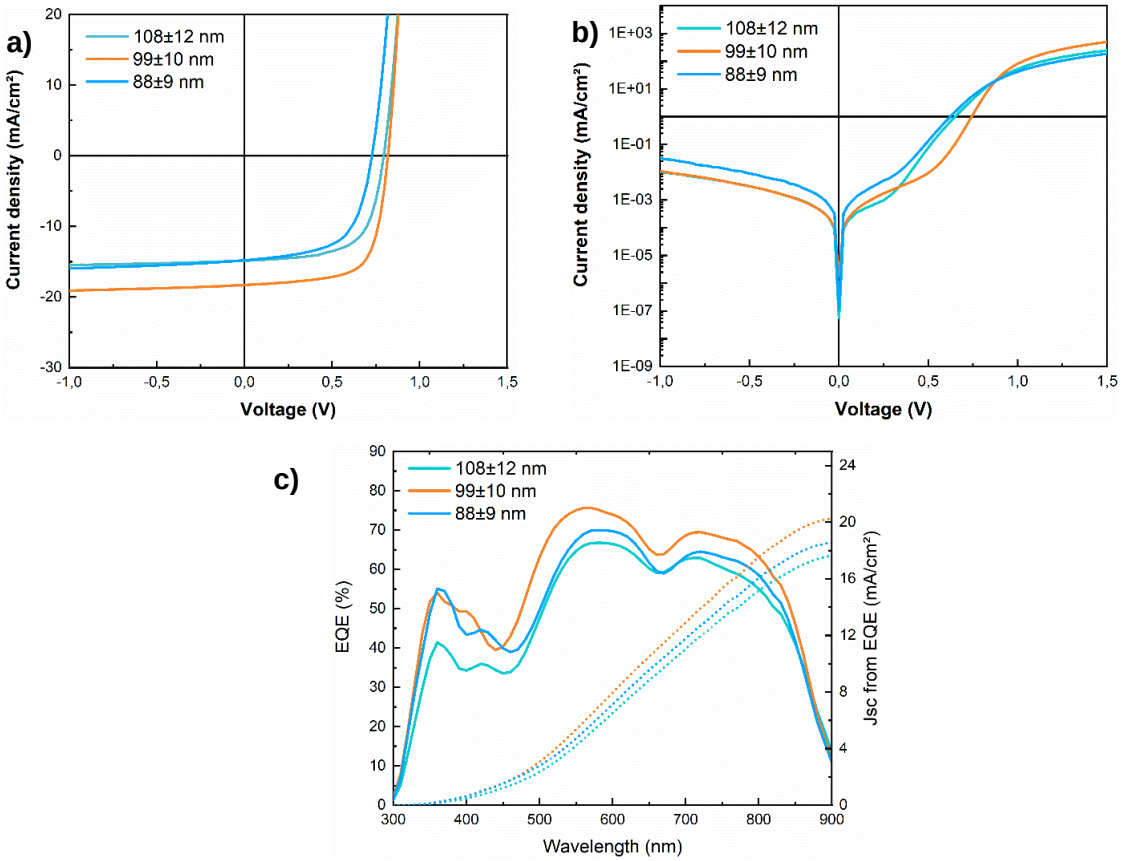

Figure 46. J-V curves of PM6:Y6 reference systems with different thicknesses a) under a solar simulator (AM 1.5 G), b) under dark in semi-logarithm scale. c) EQE spectra showing wavelength-integrated photocurrent through integration over the standard solar spectrum.

Table 13. PV performance of PM6:Y6 OPVs as a function of the active layer thickness under solar simulator (AM 1.5 G). The active surface area is around 0.18 cm². Average J_{SC} and PCE are given in brackets. The average parameters were calculated from 6 cells, and the error estimate was calculated as the standard deviation of these 6 cells. *J_{SC}^{EQE} was calculated using EQE.

Thickness (nm)	V_{OC} (V)	J_{SC} (J_{SCave}) (mA.cm^{-2})	J_{SC}^{EQE} (mA.cm^{-2})	FF (%)	PCE (PCE_{ave}) (%)	R_S (Ω.cm^2)	R_{SH} (Ω.cm^2)
108±12	0.79	15.9 (14.7±0.9)	17.6	64	8.0 (7.7±0.3)	30	6000
99±10	0.80	18.3 (17.7±1.67)	20.3	63	10.3 (9.3±0.9)	20	5200
88±9	0.72	15.8 (15.0±0.6)	18.6	61	6.5 (6.1±0.5)	50	3500

The active layer thickness was varied by adjusting the spin-coating speed, resulting in three different thicknesses: 108±12 nm, 99±10 nm, and 88±9 nm. As shown in Figure 46a and Table 13, the J-V curve obtained under the solar simulator shows that when the thickness is 99 ± 10 nm, the PCE reaches 10.3%, which is the best performance. This optimal thickness achieves a good balance between sufficient light absorption and efficient charge transport, with a V_{OC} of 0.80 V, a J_{SC} of 18.3 mA.cm^{-2}, and an FF of 63%. The dark J-V curve in Figure 46b shows the diode behavior of the device, confirming that charge transport and recombination are directly affected by the thickness of the active layer. Thinner layers exhibit higher R_S and lower R_{SH}, as seen by the increased recombination losses and poor performance of the 88 ± 9 nm layer, which has a lower PCE of 6.5%. As can be seen from Figure 46c, the 99 ± 10 nm device exhibits the highest EQE in the visible and near-infrared (NIR) spectra, especially in the 500-850 nm range, which indicates higher efficiency in light harvesting and charge generation. This is consistent with the higher J_{SC} values and better overall device performance at this optimal thickness. Furthermore, the J_{SC} calculated from the EQE spectra agrees with the J_{SC} values obtained from J-V measurements, further validating the accuracy of the measurements and highlighting the efficiency of the device at this thickness. Furthermore, the PCE of our device is 10.3%, which is lower than the performance of the state-of-the-art PM6:Y6 device with similar configuration, which has a PCE as high as 14.9%, a V_{OC} of 0.82 V, a J_{SC} of 24.6 mA/cm², and a FF of 74%[29,158]. This variation can be due to differences in lab environments as well as differences in active area between devices, both of which can significantly affect performance metrics.

We then measured the performance of the PM6:Y6 OPV devices under indoor lighting conditions. The indoor J-V curves and PV performance of the PM6:Y6 reference system are presented in Figure 47 and Table 14, with measurements taken under 1000 lux warm LED illumination (see Chapter II for the full characteristics of the illumination conditions).

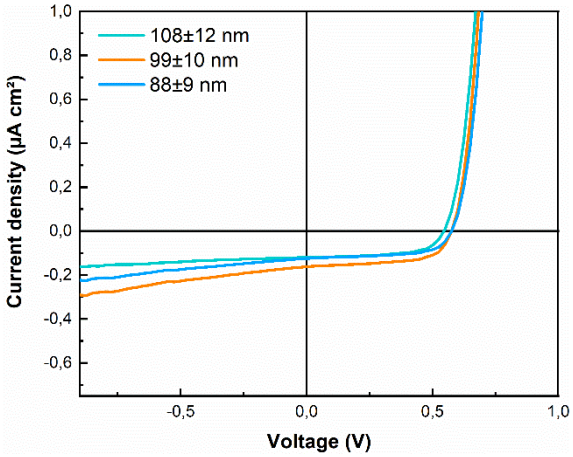

Figure 47. Indoor J-V curves of PM6:Y6 OPVs as a function of the active layer thickness.

Table 14. Indoor PV performance of PM6:Y6 OPVs as a function of the active layer thickness. The active surface area is around 0.18 cm². The average parameters were calculated from 6 cells, and the error estimate was calculated as the standard deviation of these 6 cells, which were given in brackets. *J_{SC} ^{EQE} was calculated using EQE.

Thickness	V_{OC} (V)	J_{SC} (J_{SCave}) (μA.cm^{-2})	J_{SC} ^{EQE} (μA.cm^{-2})	FF (%)	PCE (PCE$_{ave}$) (%)	R_S (Ω.cm^2)	R_{SH} (Ω.cm^2)
108±12	0.55	119 (116±5)	104	61	12.4 (11.6±1.3)	110	1.9x10^5
99±10	0.60	123 (119±10)	117	72	16.4 (15.69±3.12)	91	5.0x10^5
88±9	0.58	114 (120±5)	108	62	13.7 (12.0±2.5)	95	3.3x10^5

The J-V curves obtained under 1000 lux warm LED illumination show that the device with a thickness of 99 ± 10 nm achieves the highest PCE of 16.4%, V_{OC} of 0.60 V, J_{SC} of 123 μA.cm^{-2}, and FF of 72%. This performance correlates well with the results obtained under a solar simulator. It is comparable to the performance reported in a reference study[158], where a PM6:Y6 device exhibits a PCE of 17.6%, a V_{OC} of 0.66 V, a J_{SC} of 157 μA.cm^{-2}, and a FF of 70% under 1300 lux illumination using a similar device architecture. The superior performance at 99 ± 10 nm can be attributed to the optimal balance between light absorption and efficient charge transport, which is particularly important under low-intensity indoor lighting conditions. In comparison, the devices with active layer thicknesses of 108 ± 12 nm and 88 ± 9 nm have slightly lower efficiencies, with PCE_{MAX} values of 12.4% and 13.7%, respectively. Thicker devices have increased R_S, which hinders charge extraction, while thinner devices may suffer from insufficient light absorption, resulting in lower overall efficiency. The device-to-device variation in R_{SH} and R_S further emphasizes the critical impact of active layer thickness on recombination and charge transport properties, with the 99 ± 10 nm device providing the most favorable balance between these factors, leading to superior indoor photovoltaic performance. Although the performance of our PM6:Y6 devices under 1 sun conditions is slightly lower than that reported by other laboratories, achieving competitive results under indoor lighting conditions highlights the reliability of our fabrication process. These reproducible PM6:Y6 reference devices provide a solid foundation for further research and optimization in subsequent chapters of this thesis.

III.2. Materials and devices structure for NFA heptazine system

Heptazines (Figure 48), known for their high nitrogen/carbon atomic ratio, exhibit highly electron-deficient properties, making them ideal candidates for various optoelectronic and photocatalytic applications. Its remarkable optical and electronic behavior is mainly attributed to the conjugated π system, which includes a low-lying π* orbital. The nitrogen atoms embedded in their molecular structure play a key role by lowering the energy of the π* orbitals (due to the high electronegativity of nitrogen), thereby increasing the electron affinity[159,160]. The derivatives have a polycyclic aromatic core with a high nitrogen content (Figure 48a). The core structure maintains a C/N ratio of 0.85, is relatively nitrogen-rich compared to other heterocycles, and allows for strong electronic resonance (aromaticity). This unique combination provides heptazines with a variety of valuable properties, including strong electron affinity.

The optical properties of heptazines are strongly influenced by their highly conjugated π-system and nitrogen-rich structure, which lead to their electronic defect characteristics and unique optical behaviors. Typically, Heptazines absorb light in the UV to near-blue region with a band gap range of 3.5-4 eV[6,161]. These properties are ideal for optoelectronic devices as well as catalytic and photocatalytic applications[162-165].

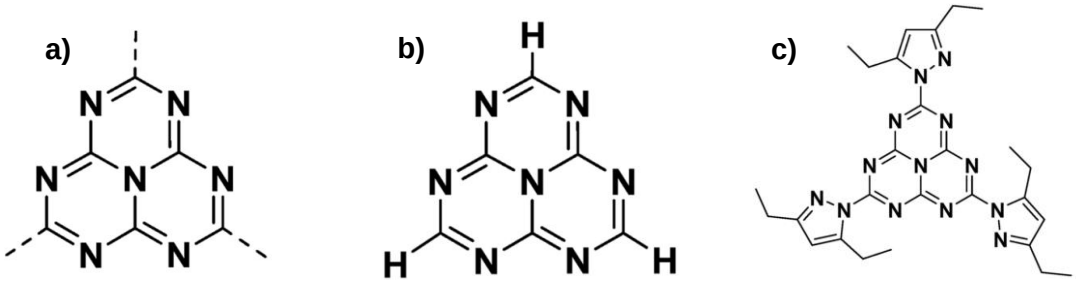

Figure 48. Chemical structure of heptazine, a) heptazine core, b) heptazine (tris-s-triazine), and c) 2,5,8-tris(3,5-diethyl-pyrazolyl)-heptazine (TDPH).

Furthermore, heptazine derivatives are also known for their ability to undergo processes such as delayed fluorescence, where triplet excitons are converted back to singlet excitons, leading to efficient light emission. This makes heptazines attractive candidates for optoelectronic devices, such as organic light-emitting diodes (OLEDs)[5,7]. Moreover, heptazines exhibit excellent thermal and chemical decomposition temperatures exceeding 500 °C, which further enhances their potential for demanding applications[166-168]. Synthesis of materials containing the heptazine core (C6N7) is straightforward and can be achieved by heating common compounds such as urea, cyanamide, ammonium dicyanamide, dicyanamide, or melamine to above 340°C. These properties (excellent stability and easy synthesis) further highlight the potential of heptazines in optoelectronic and photocatalytic applications.

Among the heptazine derivatives, 2,5,8-tris(3,5-diethyl-pyrazolyl)-heptazine (TDPH, see Figure 48c)[6] is particularly noteworthy. As shown in Figure 49, TDPH was synthesized through a rapid mechanic synthesis (approximately 15 minutes) using an aminated heptazine as a precursor[6,9]. The pyrazolyl groups attached to the heptazine core are easily interchangeable, providing flexibility for molecular tuning. TDPH can be produced on a gram scale with a yield of 30-40%, making it useful for lab-scale device fabrication.

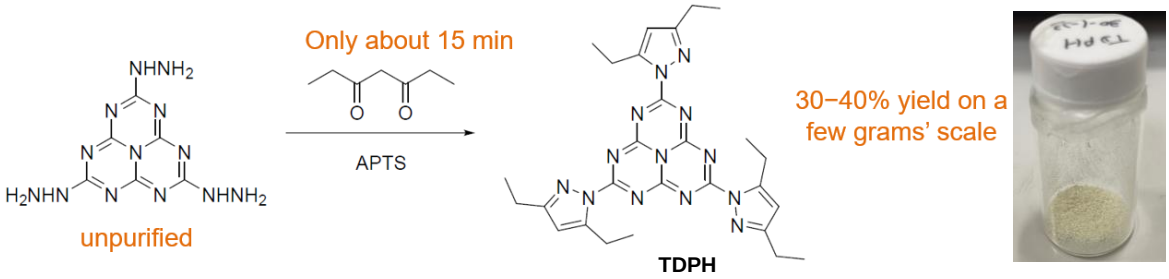

Figure 49. Synthesis of TDPH bearing three pyrazolyl leaving groups[6,9].

In the solid state, TDPH molecules adopt a displaced columnar packing arrangement with strong stacking interactions between the pyrazole substituents (Figure 50b). X-ray diffraction of a single crystal of TDPH obtained from a concentrated dichloromethane (DCM) solution showed that the heptazine core was nearly coplanar with the attached pyrazole groups (Figure 50a). This molecular arrangement facilitates efficient charge transport and improves their stability, both of which are important for high-performance organic devices. These findings suggest that heptazine-based molecules have great potential for application in OPV devices.

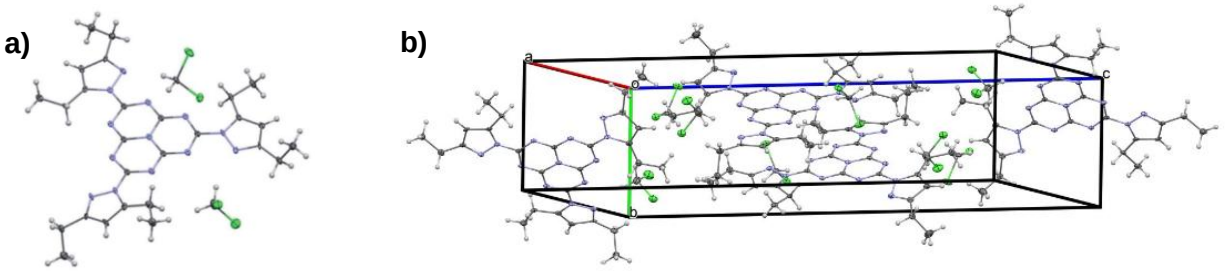

Figure 50. a) ORTEP diagram of TDPH, showing 30% probability ellipsoids. TDPH crystals were obtained from concentrated dissolution in DCM. N atoms are shown in blue, Cl atoms (from DCM molecules co-crystallized with TDPH) are shown in green, b) Crystal packing view of RX in the lattice.

Furthermore, it is possible to fine-tune their absorption region and bandgap by modifying their side chains, particularly in the blue region of the spectrum. This ability to tailor absorption properties matches well with the blue light emitted by modern LED lighting, making heptazines an excellent candidate for IOPVs. For example, TDPH with interchangeable pyrazolyl groups provides flexibility for molecular tuning to optimize performance in low-light environments. By exploiting these unique characteristics, heptazine-based NFAs have the potential to significantly enhance light harvesting in low-light environments, addressing the growing demand for energy-efficient technologies in indoor settings. In 2020, my colleague Ibrahim Zamkoye first proposed the use of TDPH[6] as an interfacial layer in organic devices like solar cells. These thin films were deposited using both thermal evaporation under vacuum and spin-coating techniques[8], illustrating the very good versatility of the material towards integration into devices. In their study, they developed a simple model device where heptazine thin films improved electron transfer from a tris-(8-hydroxyquinoline) aluminum (Alq_3) photo-active layer, as demonstrated by steady-state and transient photoluminescence spectroscopy. Structurally, the heptazine core in TDPH (Figure 49a) is nearly coplanar with its pyrazole substituents, facilitating efficient electron delocalization and further enhancing the potential of heptazine in OPV and other optoelectronic applications.

III.3. Initial integration of TDPH as an NFA: pairing with optimized p-type donor materials for OPV applications

We chose TDPH as the initial NFA for investigation due to its well-understood synthesis and well-characterized electron deficiency. For this reason, TDPH was the natural benchmark heptazine to start our study, although its absorption profile does not match the blue region of the LED emission spectrum (see Figure 51a). Indeed, TDPH absorbs primarily in the UV region, with limited absorption in the blue, where both warm and cool LED lights emit most of their energy. At the beginning of our study, TDPH was however a logical starting point, after which Pierre Audebert's group at the PPSM laboratory began synthesizing other heptazine derivatives presenting red-shifted absorption, better optimized for indoor lighting conditions, especially in the blue region.

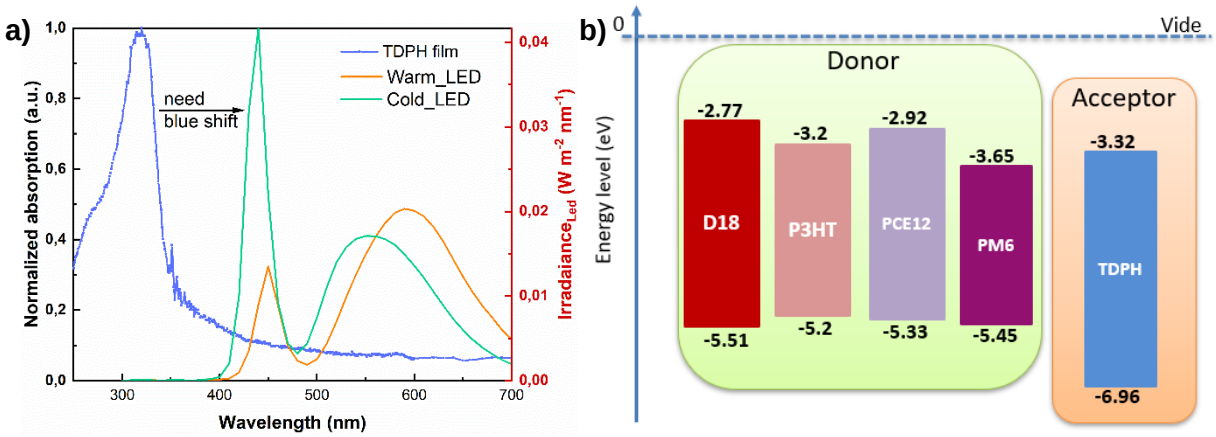

Figure 51. a) The normalized absorption spectrum of TDPH film compared to the irradiance of LED. b) The energy level diagrams.

In this initial phase, we tried to pair TDPH with carefully selected p-type donor materials to maximize charge separation and transport based on reported energy level diagrams (Figure 51b). The LUMO and HOMO energy levels of the heptazines, including TDPH, were determined using electrochemical data and optical absorption spectra. For TDPH, the LUMO was calculated from the first reduction potential, measured at −1.23 V vs. Ag/AgCl in cyclic voltammetry experiments[6,8]. By applying the formula LUMO = - (V_{redox} + 4.55), we obtained a LUMO value of -3.32 eV. The HOMO was derived from the optical E_g, which as determined from a Tauc plot to be 3.62 eV (see Appendix 2.2)[142]. Using the relationship HOMO = LUMO - E_g, the HOMO was calculated to be -6.96 eV.

Compared with PM6, TDPH has a higher LUMO level (−3.32 eV vs. −3.65 eV for PM6). This higher LUMO energy level is beneficial for achieving a larger V_{OC} in OPV devices, which is particularly beneficial for maximizing the energy conversion efficiency of OPV devices. The choice of donor material is crucial to compensate for the suboptimal absorption of TDPH in the visible region. To this end, we focus on donor polymers such as D18, PCE12, and P3HT, which exhibit broad absorption across the visible spectrum. These materials complement the electron-accepting properties of TDPH by efficiently absorbing incident light that TDPH cannot fully capture. OPV systems based on TDPH are therefore relevant to assess the possibility of efficiently dissociating excitons and driving free charges at the electrodes using a heptazine electron acceptor compound, for the first time.

D18:TDPH blend system

These materials, D18 as polymer donor and TDPH as NFA, were used to fabricate inverted structure OPV cells with the following configuration: ITO/ZnO/active layer/MoO_3/Ag.

To prepare the active layer, D18 and TDPH were dissolved in CF as solvent. According to the molar masses of D18 (1360.14 g/mol per repeat unit) and TDPH (539 g/mol), the donor-acceptor ratio in the active layer is usually chosen to balance the charge generation and transport properties of the blend. To target an optimal mixing morphology and efficient charge transfer, we choose two different weight ratios of D18:TDPH, 1:0.5 and 1:0.25. A concentration of 18 mg/mL for D18:TDPH blends were used. The active layer blend was spin-coated onto the ZnO-coated ITO substrates at 3000 rpm for 30 seconds to form a uniform thin film with an optimal thickness of around 100 nm. After the deposition of the active layer, two different film preparation conditions were tested for the D18:TDPH blend system: non-annealing and annealing. In the non-annealing condition, the spin-coated active layer remains in the as-cast state, and no heat treatment is required. Under annealing conditions, the active layer was thermally annealed at 60°C for 10 min. This thermal treatment is expected to improve the molecular order and crystallinity of the D18 polymer[30,169,170] and TDPH acceptor, thereby enhancing charge transport and exciton dissociation.

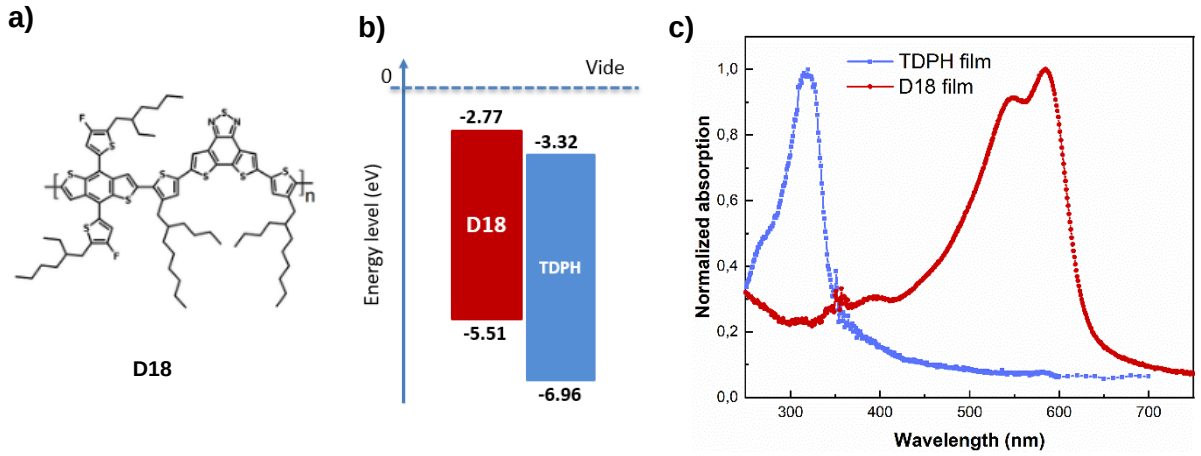

Figure 52. a) Chemical structure of D18. b) Energy levels of D18 and TDPH, and c) their absorption spectrum.

Figure 52a shows the chemical structure of D18, while Figure 52b and 39c summarize the LUMO and HOMO energy levels and optical absorption of these materials. As expected, D18 has a higher HOMO (-5.51 eV) and LUMO (-2.77 eV) compared to the LUMO (-3.32 eV) and HOMO (-6.96 eV) of TDPH. This favorable energy level alignment should ensure the efficient separation of excitons at the donor-acceptor interface, with the LUMO position of TDPH being lower than that of D18, thus facilitating the electron transfer from the donor to the acceptor. Furthermore, the large gap between the LUMO of TDPH and the HOMO of D18 contributes to the improvement of the V_{OC}, which is crucial for maximizing the PCE of OPV devices.

The films were prepared on glass/ITO/ZnO substrates by spin coating and annealed at 60 ° C for 10 min.

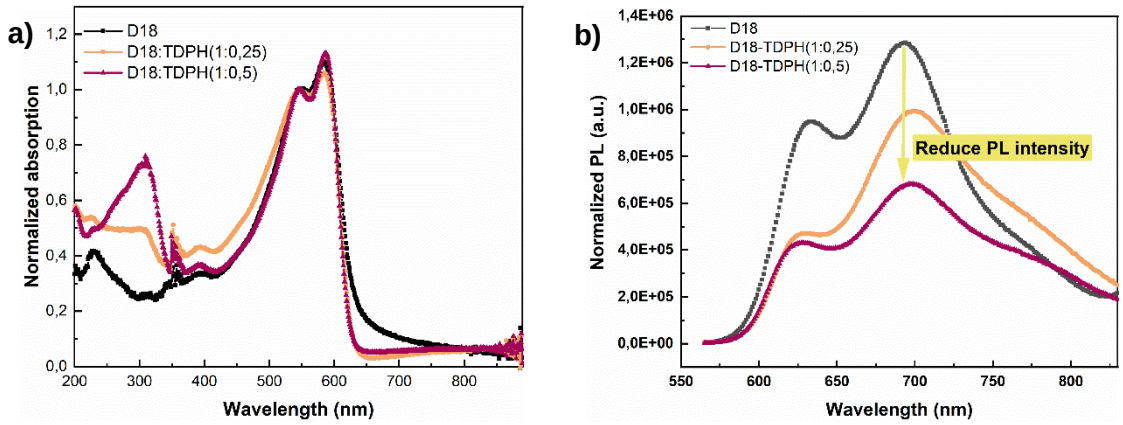

Figure 53. a) Absorption and b) PL spectra for different D18: TDPH blend ratio, compared to pure D18. The excitation was at 545 nm.

The absorption spectra (Figure 53a) of D18 and D18: TDPH blend films showed that pure D18 film absorbs mainly in the visible region, especially between 500 and 700 nm. After mixing with TDPH, additional absorption features appear in the UV regions (200-350 nm), which are assigned to TDPH. As the TDPH content increases from 1:0.25 to 1:0.5 in the blend, the absorption in the UV region becomes more apparent, reflecting the strong absorption of TDPH in this range. However, the overall absorption in the visible region was still mainly dominated by D18, as expected. Figure 53b presents the normalized PL intensity of D18 and D18: TDPH blends upon excitation at 545 nm. The neat D18 film displays the highest emission intensity characteristics of its expected emission, showing three main contributions at 630, 695, and 770 nm[170-172], which correspond to the radiative recombination of excitons in different vibrational states of the polymer. In contrast, the PL intensity of the D18:TDPH was found lower, with greater quenching observed at higher TDPH concentrations (D18 1:0.5). It is noteworthy that, as shown in Figure 52c, TDPH does not show significant absorption at 545 nm, which means that it does not directly contribute to the emission at this excitation wavelength. This is further supported by the fact that the absorption of TDPH occurs mainly in the UV region (below 350 nm). Therefore, the observed PL quenching is primarily due to the exciton dissociation at the D18 interface rather than any emission from TDPH itself. Such evidence supports that TDPH acts as an electron acceptor, facilitating charge transfer from D18, thereby quenching the exciton recombination that would otherwise lead to photoluminescence. The observed PL quenching remains partial however at this stage.

AFM topography images (Figure 54, top row) provide insights into the film surface morphology and roughness. The pure D18 film has a relatively smooth surface with an R_{RMS} of 0.42 nm. When D18 and TDPH are mixed in the ratio of 1:0.25 and 1:0.5, the surface roughness slightly increases to 0.48 and 0.56 nm, respectively, indicating a small effect on phase separation between D18 and TDPH materials. Furthermore, the morphology of the neat D18 film exhibits a typical fibrous structure, which is consistent with the semicrystalline nature of D18 and has been previously reported in the literature[30]. The morphology obtained for the D18:TDPH blends is in agreement with what has been reported in the literature for similar D18:Y6-based systems.

In addition to the topographic images, Figure 54 (bottom row) also shows the phase images of pure D18 and two different ratios of D18:TDPH blends. Phase images further reveal the nanoscale phase separation and distribution of donor and acceptor materials. For the pure D18 film, the phase image exhibits a relatively uniform contrast, indicating that the film is homogeneous without obvious phase separation at large scale. As the TDPH content in the

blend increases, the phase contrast becomes more obvious, indicating an increase in the degree of phase separation between D18 and TDPH. Specifically, the D18:TDPH (1:0.5) blend showed more obvious phase separation compared to the D18:TDPH (1:0.25) blend, as shown by the change in phase contrast. This indicates that with increasing TDPH content, the donor and acceptor domains become more distinct, which affects the charge transport and exciton dissociation processes. Despite the increased phase separation, the blends still maintain a smooth and ordered morphology, as shown in the topography images, which is beneficial for the efficient charge transfer at the donor-acceptor interface. However, an optimal balance between phase separation and domain size is crucial to ensure that charge carriers can be efficiently transported to the corresponding electrodes without significant recombination losses.

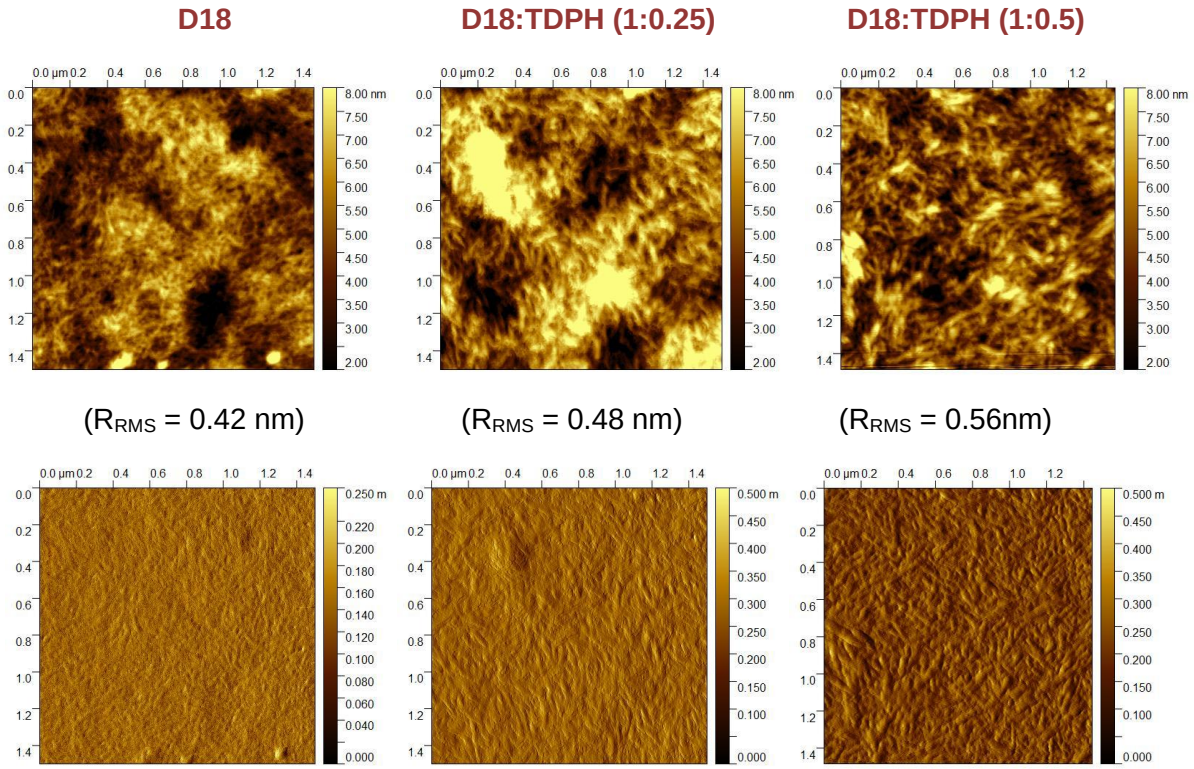

Figure 54. AFM topography images (top row) and phase images (bottom row) for pure D18 and two ratios of D18:TDPH blends in an area of 1.5 × 1.5 µm.

J-V characterization under a solar simulator was performed to evaluate the PV properties of D18:TDPH-based solar cells in an inverted geometry under standard AM 1.5G, as shown in Figure 55 and Table 15. The results present the PV performance parameters of devices using D18 as the donor and TDPH as the NFA under two different conditions: as-cast and annealed at 60°C for 10 minutes.

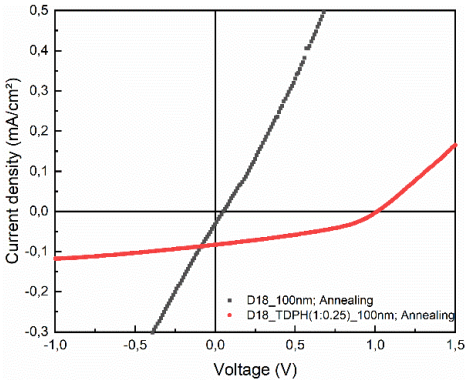

Figure 55. J-V curve of the annealed D18 and D18:TDPH (1:0.25) OPV devices under solar simulator (100 mW.cm^{-2}).

Table 15. PV parameters of D18: TDPH devices under solar simulator (100 mW.cm^{-2}).

Blends	V_{OC} (V)	J_{SC} (mA.cm^{-2})	FF (%)	PCE_{MAX} (%)
D18:TDPH(1:0.25) As-cast	0.55	7.7x10^{-2}	29.0	1.2x10^{-2}
D18:TDPH(1:0.25) With annealing 60°c for 10min	1.01	8.3x10^{-2}	38.1	3.2x10^{-2}
D18:TDPH (1:0.5) As-cast	0.04	3.2x10^{-2}	30.6	0.4x10^{-2}
D18:TDPH (1:0.5) With annealing 60°c for 10min	0.77	3.7x10^{-2}	38.1	1.1x10^{-2}

Although the D18:TDPH systems exhibit a photovoltaic response, the overall performance remains low, primarily due to the very low J_{SC}, less than 0.1 mA/cm². Annealing at 60°C for 10 minutes significantly improves the performance of D18:TDPH OPV devices, particularly in terms of V_{OC} and FF. The observed V_{OC} of 1.01V in the D18:TDPH (1:0.25) devices is especially promising, surpassing the reference PM6:Y6 system of 0.8V. However, despite this encouraging V_{OC}, both J_{SC} and PCE remain low, indicating that several factors still hinder optimal device performance. This suggests several possible hypotheses for the low current extraction.

First, the relatively low J_{SC} indicates poor charge extraction, which may be caused by the inappropriate morphology in the blend. The lack of a bicontinuous network (well-connected donor and acceptor phases) may prevent efficient charge transport to the electrodes. Second, the charge transport within the solid-state TDPH phase may not be optimal, which requires further investigation. It is important to verify the transfer characteristics of TDPH to understand its role in limiting device performance better. Furthermore, PL quenching analysis indicated that a certain degree of electron transfer occurred between D18 and TDPH; however, the observed quenching was relatively weak. This suggests that the charge transfer between D18 and TDPH may not be completely efficient or quantitative. All these factors suggest that further optimization of the device architecture, blend morphology, and possibly the choice of donor materials is necessary. Specifically, the morphology must be tailored to achieve better phase separation and continuous charge extraction pathways. Furthermore, it is crucial to evaluate the charge transport capability of TDPH and ensure efficient electron transport. Despite these

challenges, the remarkable V_{OC} achieved demonstrates the potential of TDPH as an NFA, which is in good agreement with the expected energy level diagram.

P3HT:TDPH blends system

Although D18 is promising for improving V_{OC} using TDPH as the NFA, the relatively low J_{SC} and limited charge transport observed in the D18:TDPH system require further optimization. To explore whether different donor materials could better address these challenges, P3HT was selected as an alternative donor. While the choice of P3HT does not directly resolve the transport limitations within TDPH, it enables the evaluation of whether another donor is better suited for electron transport, morphology optimization, or charge transport improvements. P3HT is a well-established donor in the OPV system and is known for its strong absorption in the visible region from 450 to 650 nm[91,95,96], as shown in Figure 56b. Its absorption curve makes it particularly suitable for indoor applications where artificial light sources such as LEDs emit strongly in this range. Referring to the Shockley-Queisser limit for indoor photovoltaics, the optimal band gap of the material is about 1.9 eV, which is very close to the 2 eV band gap of P3HT, making it a very promising candidate for indoor OPVs.

Moreover, P3HT exhibits high crystallinity in the solid state, especially after soft annealing treatment[96,173,174]. This high crystallinity helps form an ordered structure that facilitates charge transport, thereby improving the overall efficiency of OPV devices. The energy levels between P3HT and TDPH are also well aligned, with the LUMO of P3HT being -3.2eV and the LUMO of TDPH being -3.32eV (Figure 56c). His slight difference in LUMO energy levels provides sufficient driving force for exciton dissociation, ensuring efficient charge separation at the donor-acceptor interface. When comparing this system to the D18 system, which has a LUMO of -2.77 eV, the driving force for charge separation is lower for the P3HT system. However, this lower driving force reduces energy losses, potentially improving efficiency. On the other hand, the HOMO of P3HT is -5.2 eV, which is higher than the HOMO of D18 (-5.51 eV), indicating that the V_{OC} of the P3HT system may be lower than that of the D18 system.

To evaluate the potential of the P3HT system, we treated the mixture using CF as a solvent with a total material concentration of 18 mg/mL and a weight ratio of P3HT to TDPH of 1:1. These were chosen to optimize morphology, phase separation, and to achieve an active layer thickness of 100 nm. The devices were fabricated using the same inverted structure configuration: ITO/ZnO/active layer/MoO_3/Ag.

The PL spectra in Figure 56d show the normalized PL intensity of P3HT and P3HT: TDPH blends at different annealing temperatures under 550 nm excitation. Pure P3HT film exhibits the highest emission intensity, which is characteristic of its exciton radiative recombination, with a peak around 735 nm. In contrast, the PL intensity of the P3HT:TDPH (1:1) blend decreases significantly, indicating that the PL is strongly quenched when TDPH is added to the system. Similar to the behavior observed in D18:TDPH blends, the quenching in P3HT: TDPH could indicate the effective dissociation of excitons at the donor-acceptor interface. Moreover, TDPH has no significant absorption at 550 nm, which means that it does not contribute to the emission at this excitation wavelength, which means that the PL quenching observed in the P3HT:TDPH blends is mainly due to the exciton dissociation at the P3HT interface rather than any emission from TDPH itself. As the annealing temperature increases to 120 °C, the PL intensity further decreases, confirming that TDPH acts as an electron acceptor and promotes more efficient charge transfer of P3HT at 120 °C annealing

temperature. The stronger quenching at 120 °C suggests that higher temperature promotes better molecular ordering or phase separation, enhancing exciton dissociation and charge transfer. Furthermore, the quenching effect in the P3HT: TDPH system is relatively stronger compared to that in the D18:TDPH system, indicating that TDPH interacts more efficiently with P3HT, leading to more significant exciton dissociation and charge transfer at the donor-acceptor interface.

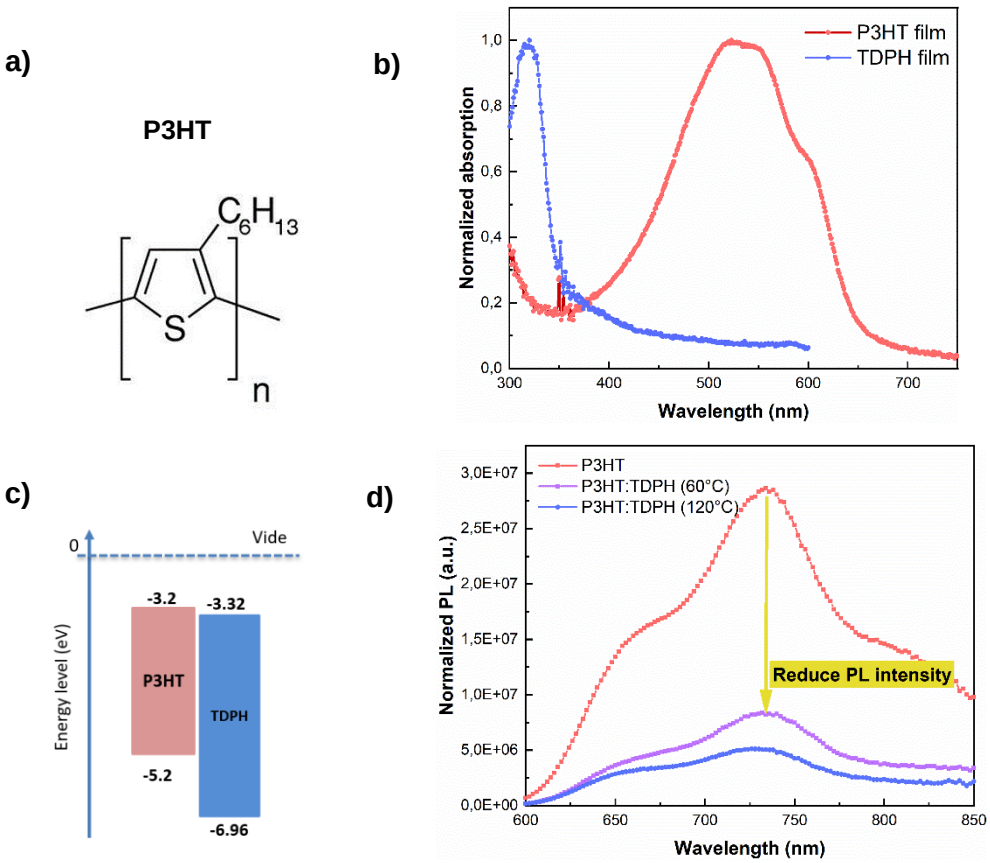

Figure 56. a) Chemical structure of P3HT. b) Absorption spectrum of P3HT film and TDPH film, c) their energy levels, and d) PL spectra of P3HT: TDPH blends at different annealing temperatures, compared with pure P3HT. The excitation was at 550 nm.

Again, J-V characterization was used to evaluate the PV properties of P3HT: TDPH-based solar cells in an inverted geometry under standard AM 1.5G solar spectrum, as shown in Figure 57 and Table 16. Two annealing conditions are compared (60°C or 120°C, both for 10 min under an inert atmosphere) [95,96]. In general, and as largely reported for the P3HT-based blends in the OPV field, the device annealed at 120°C exhibited improved performance due to better phase separation between P3HT and the molecular acceptor.

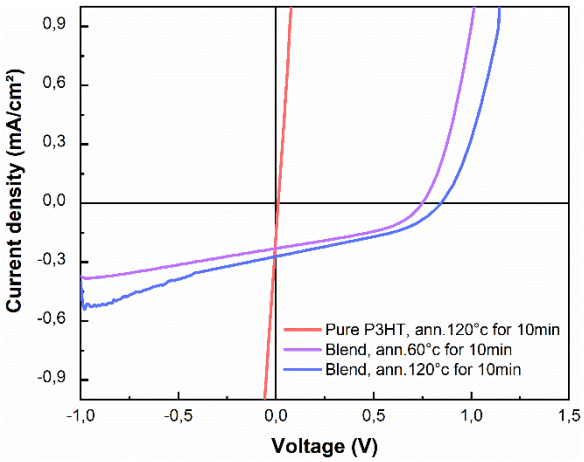

Figure 57. J-V curve of the P3HT: TDPH annealed OPV devices under solar simulator (100 mW.cm^{-2}, AM 1.5G).

Table 16. PV parameters of P3HT: TDPH devices under solar simulator (100 mW.cm^{-2}).

Blends	**V_{OC} (V)**	**J_{SC} (mA.cm^{-2})**	**FF (%)**	**PCE_{MAX} (%)**
P3HT:TDPH ann.60°c for 10min	0.75	0.23	41.9	7.2x10^{-2}
P3HT:TDPH ann.120°c for 10min	0.84	0.27	38.9	8.9x10^{-2}

In general, we observe that the device annealed at 120°C for 10 min performs slightly better than the device annealed at 60°C.

As mentioned earlier, although we do not provide direct evidence by morphological analysis, the PL spectrum shown in Figure 56d suggests that the stronger quenching at 120 °C may be due to improved molecular ordering or phase separation at higher temperatures, thereby enhancing exciton dissociation and charge transfer. This effect may trigger more future studies, such as in-depth AFM analysis, to further investigate the effect of annealing on the morphology.

P3HT: TDPH devices showed a better overall performance in terms of J_{SC} and PCE compared to D18: TDPH devices. The J_{SC} of P3HT-based devices, with a value of 0.27 mA.cm^{-2}, was much higher than the 0.083 mA.cm^{-2} observed in D18-based devices. However, P3HT-based devices had a lower V_{OC} of 0.84 V, compared to the higher 1.01 V achieved in D18-based devices. This lower V_{OC} is due to the difference in the HOMOs of the donors: P3HT (-5.2 eV) is higher than D18 (-5.51 eV), as expected when comparing the energy levels of P3HT and D18 earlier in this section.

III.4. Exploration of other heptazine derivatives with a red-shifted absorption

Clearly, and despite the fact that the reference TDPH compound shows interesting potentialities for the OPV field, its optical absorption, which is far limited in the UV region, is not suitable for harvesting most of the blue wavelength emitted by indoor light sources. As a consequence, the system should evolve towards heptazine derivatives with narrower bandgaps.

In this context, two other heptazine derivatives were therefore synthesized and investigated to address the demand for improved absorption in the blue region: 2,4-difluoro-Heptazine (2,4-diF-Hep) and 2,4-dimethyl-Heptazine (2,4-DM-Hep). The structural modifications at the 2,4 positions of the heptazine core are highlighted by red circles, as shown in Figure 58. These modifications were introduced to fine-tune the electronic and absorption properties of the heptazine derivatives, aiming to better align their absorption with the emission spectra of indoor light sources, especially LEDs. The main chemical challenge in shifting the absorption of heptazines from the UV to the blue region is to achieve this without compromising their stability and electron-deficient properties. Heptazines naturally absorb UV light due to their nitrogen-rich conjugated structure, but shifting this absorption toward the blue spectrum requires precise modifications. For example, the introduction of electron-withdrawing groups such as fluorine can tune the absorption, although such changes may also affect the electronic structure and charge transport.

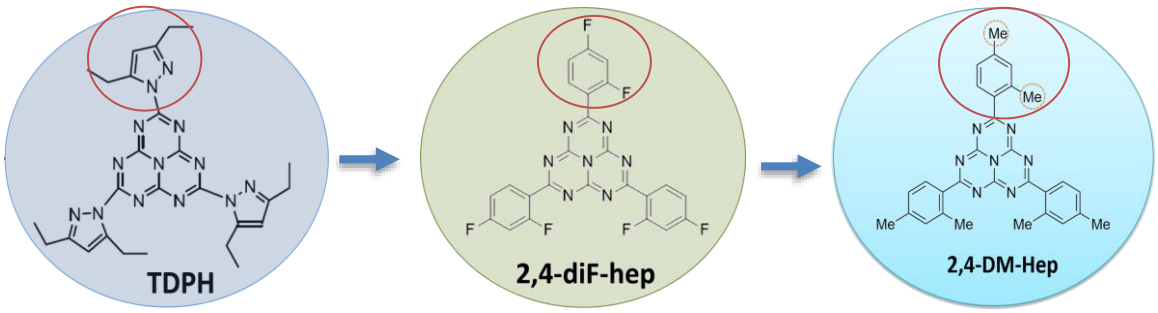

Figure 58. Chemical structure of three heptazine derivatives: TDPH, 2,4-diF-hep, 2,4-DM-hep.

2,4-diF-hep: The Fluorine substitutions were introduced at the 2,4-positions of the heptazine core, which introduce electron-withdrawing effects. The presence of highly electronegative fluorine atoms slightly changes the electronic properties, thus enhancing the performance of OPV devices.

2,4-DM-hep: Methyl groups were added to the 2,4-positions to tune the absorption and improve solubility. The methyl group donates electrons via the inductive effect, slightly increasing the energy of HOMO, resulting in a slight red shift in the absorption spectrum, such as 2,4-DM-Hep compared with TDPH and 2,4-diF-Hep. Furthermore, the hydrophobicity of the methyl groups enhances the overall solubility of the molecules in the solvent, helping to fabricate films with a more uniform morphology.

Figure 59 compares the normalized optical absorption spectra of these heptazine films on quartz. Although 2,4-diF-Hep and 2,4-DM-Hep films exhibited a red shift compared with TDPH film, as expected through the molecular tuning performed, this shift is not sufficient to fully overlap with the blue region of the emission spectrum of LEDs (400-500 nm) required for indoor applications. The absorption peak of 2,4-diF-Hep is around 324 nm, while the absorption peak of 2,4-DM-Hep is around 356 nm.

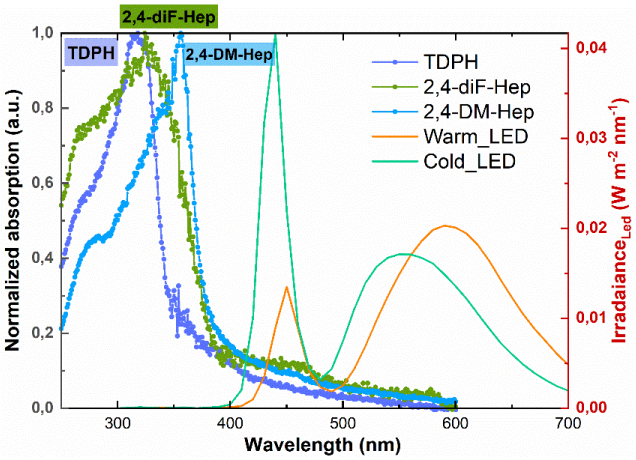

Figure 59. Normalized absorption spectra of TDPH, 2,4-diF-Hep, and 2,4-DM-Hep films alongside the irradiance spectra of warm and cold LEDs.

Although the red-shift in absorption might not be large enough for these two compounds, the strategy shows a reasonably suitable trend, and further optimizations are now open to really demonstrate a blue absorption. For preliminary performance evaluation, both 2,4-diF-Hep and 2,4-DM-Hep were blended with P3HT in OPV devices with a standard inverted configuration ITO/ZnO/active layer/MoO_3/Ag. P3HT:2,4-diF-Hep and P3HT: 2,4-DM-Hep blends were prepared in CF solvent with a total material concentration of 18 mg/mL, and an optimal active layer thickness of approximately 100 nm. A 1:1 donor to acceptor weight ratio was used because this ratio is often used in preliminary screening to simplify comparisons between different systems. Furthermore, since the molar masses of the acceptors are similar: TDPH (539 g/mol), 2,4-diF-Hep (509 g/mol), and 2,4-DM-Hep (485 g/mol), a 1:1 weight ratio becomes a reasonable approximation for initial comparison.

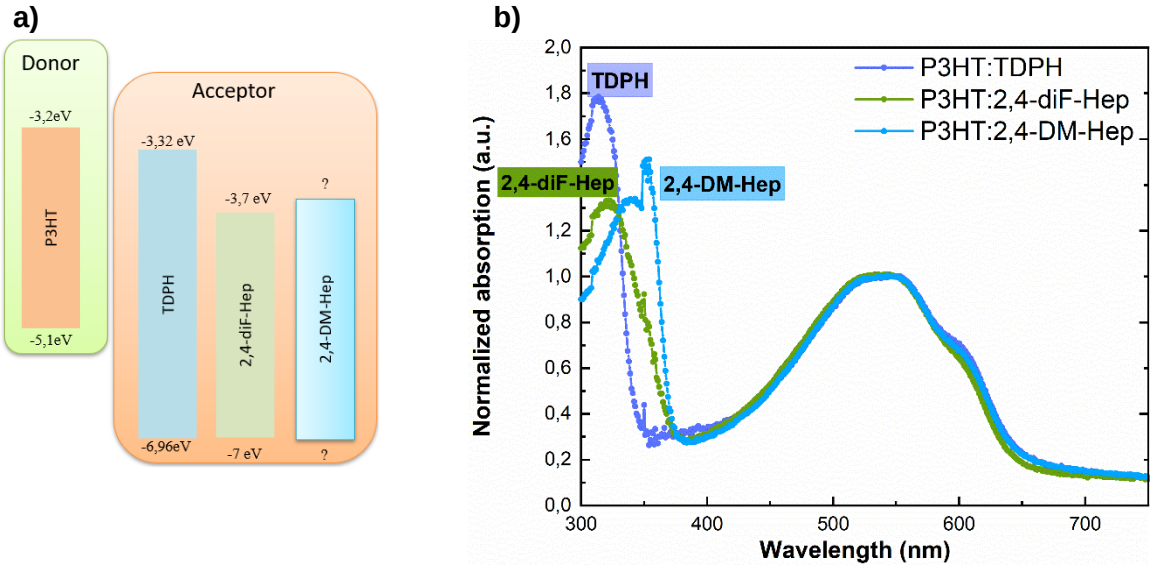

Figure 60. a) The energy levels of P3HT and three heptazines. b) The normalized absorption spectra of the three P3HT: heptazine blends.

Like TDPH, the LUMO and HOMO energy levels of 2,4-diF-Hep is derived from its electrochemical data and optical absorption spectra using the Tauc plot method. The corresponding energy levels are displayed in Figure 60a, and the absorption properties of the deposited thin film blends (around 100 nm in thickness) are summarized in Figure 50b. 2,4-

diF-Hep showed a lower LUMO of -3.7eV compared to TDPH, potentially leading to slightly lower V_{OC} when associated with P3HT. The LUMO of 2,4-DM-Hep has not been precisely determined, but based on its structural modifications, its LUMO range is expected to be similar to other heptazine derivatives.

The energy levels of heptazines were indicated: 2,4-diF-Hep showed a lower LUMO of -3.7eV compared to TDPH, potentially leading to slightly lower V_{OC} in P3HT: 2,4-diF-Hep blends but better electron-accepting capability. The LUMO of 2,4-DM-Hep has not been precisely determined, but based on its structural modifications, its LUMO range is expected to be similar to other heptazine derivatives.

Figure 60b shows the normalized absorption spectra for the three P3HT blends (P3HT: TDPH, P3HT:2,4-diF-Hep, and P3HT:2,4-DM-Hep). The blends of P3HT with 2,4-diF-Hep and 2,4-DM-Hep show slightly improved absorbance in the near-UV range compared with TDPH but still do not achieve sufficient blue light absorbance to harvest the emission of indoor LED light sources fully. In the visible region, the absorption curves of the three blends are dominated by P3HT, which can effectively absorb light between 450 and 650 nm. The overall absorbances of these blends remain similar in this region, highlighting the dominance of P3HT in visible light absorption. Figure 61 below presents the PL emission spectra of the films upon excitation at 550 nm (probing the polymer emission properties).

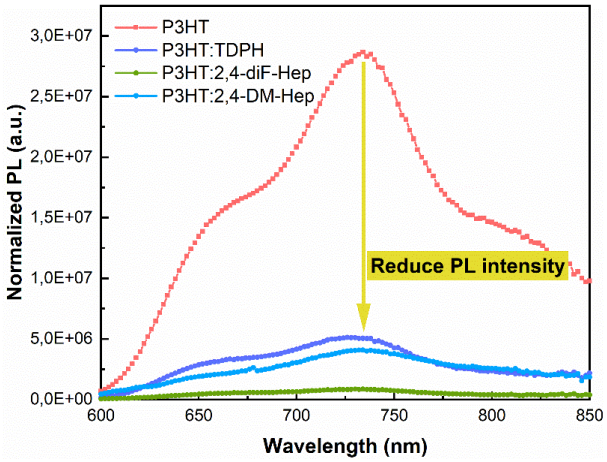

Figure 61. PL spectra for pure P3HT and its blend with three different heptazines, with excitation at 550 nm.

The pristine P3HT film exhibits a strong PL peak around 750 nm (Figure 61), which is typical for P3HT and indicates efficient exciton generation and recombination. Since no acceptor material was present, there was minimal exciton dissociation, resulting in high PL intensity. In contrast, the PL intensities of all blends decreased drastically compared with pure P3HT, confirming that efficient photo-induced charge transfer is achieved in the presence of the heptazine acceptor. The strongest quenching is observed in the P3HT: 2,4-diF-Hep blend, with a quenching percentage of 96.9%, indicating that it may have the most favorable charge transfer kinetics among the tested heptazine derivatives. Quantitatively, the quenching for the P3HT: TDPH blend is 81.5% and for P3HT: 2,4-DM-Hep, it is 84.2%. In this case, the PL spectra were normalized by the light absorbance at an excitation wavelength of 550 nm. These quenching percentages were calculated using the formula (Eq. 12):

$$Quenching\ percentage = \left(1 - \frac{\text{area of the emission spectrum of the blend}}{\text{area of the emission spectrum of pure P3HT}}\right) \times 100$$

(Equation 12)

Solar cells were finally processed from the different blend compositions, and the corresponding J-V curves, EQE spectra, and photovoltaic parameters are summarized in Figure 62 and Table 17.

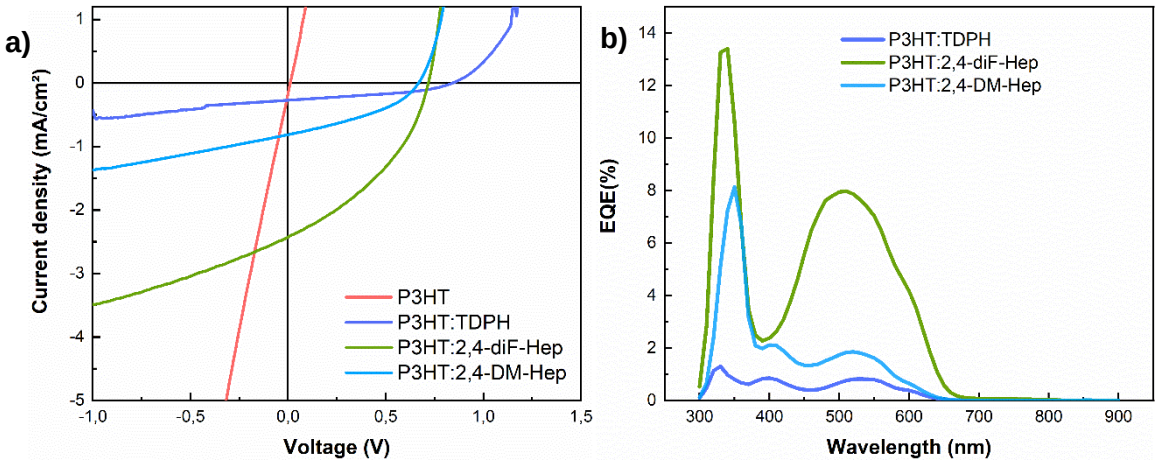

Figure 62. a) J-V curve of the P3HT: heptazines OPV devices under solar simulator (100 mW.cm^{-2}, AM 1.5G). b) EQE spectra of P3HT-based blends (measured one year after manufacture) comparing P3HT:TDPH, P3HT:2,4-diF-Hep and P3HT:2,4-DM-Hep.

Table 17. PV parameters of P3HT:heptazines OPV devices under solar simulator (100 mW.cm^{-2}, AM 1.5G).

Blends	V_{OC} (V)	J_{SC} (mA.cm^{-2})	FF (%)	PCE_{MAX} (%)	R_S (Ω.cm^2)	R_{SH} (Ω.cm^2)
P3HT:TDPH ann.120°c for 10min	0.84	0.27	38.9	8.9x10^{-2}	1680	3.3x10^4
P3HT:2,4-diF-Hep ann.120°c for 10min	0.72	2.43	38.2	6.7x10^{-1}	50	5.3x10^3
P3HT:2,4-DM-Hep ann.120°c for 10min	0.67	0.81	37.5	2.0x10^{-1}	130	1.2x10^4

P3HT:2,4-diF-Hep exhibits the best overall performance, with significantly higher J_{SC} (2.43 mA.cm^{-2}) and PCE (0.67%) compared to the other P3HT: heptazines blends. One of the reasons is that the electron-withdrawing property of fluorine lowers the LUMO energy level of the acceptor, improves exciton dissociation, and increases J_{SC}. However, it also reduces the V_{OC}, which is directly related to the energy difference between the HOMO of the donor and the LUMO of the acceptor. In OPV devices, a balance is usually struck between optimizing the LUMO offset between donor and acceptor and maintaining the V_{OC}. While strong PL quenching is observed in all blends, the low J_{SC} in P3HT: TDPH (0.27 mA.cm^{-2}) and P3HT:2,4-DM-Hep (0.81 mA.cm^{-2}) is attributed to the poor charge transport, as indicated by their higher R_S (1680 and 130 Ω.cm², respectively). This suggests that, although exciton dissociation is efficient, charge extraction is hampered by suboptimal morphology or low mobility, leading to recombination losses. In contrast, the significantly lower R_S in P3HT:2,4-diF-Hep (50 Ω.cm²) allows for more efficient charge extraction, thus improving its J_{SC}. To gain further insights, future AFM measurements are essential to understand the morphology and phase separation of the mixtures. Furthermore, studying the charge mobility in the donor and acceptor materials can help determine whether poor charge transport leads to low J_{SC}.

To supplement the performance data, we measured the EQE of the P3HT-based blends one year after they were first made (Figure 62b). Although ideally, EQE data should be captured soon after device fabrication to more directly align with initial J-V measurements, these measurements still provide valuable insights. OPV devices may degrade over time due to factors such as oxidation, moisture exposure, and morphological changes within the active layer, which may reduce the absolute EQE values compared to freshly prepared samples. Despite the overall decrease in EQE, the relative performance trends between the blends remained consistent. Notably, P3HT:2,4-diF-Hep continues to exhibit the highest EQE among the blends, outperforming P3HT:TDPH and P3HT:2,4-DM-Hep, which is consistent with the trend observed in the J-V measurements.

As OPVs are considered future indoor energy resources, the photovoltaic operation of the P3HT: Heptazine OPVs was measured under low-intensity artificial indoor lighting (1000 lux cold LED).

Table 18. PV parameters of P3HT blended with heptazines OPV devices under 1000 lux cold LED.

Blends	V_{OC} (V)	J_{SC} ($\mu A.cm^{-2}$)	FF (%)	PCE_{MAX} (%)	R_S ($\Omega.cm^2$)	R_{SH} ($\Omega.cm^2$)
P3HT:TDPH ann.120°c for 10min	0.43	1.19	55.5	$6.1x10^{-2}$	$1.0x10^4$	$1.1x10^7$
P3HT:2,4-diF-Hep ann.120°c for 10min	0.28	13.02	32.1	$2.5x10^{-1}$	$4.7x10^3$	$2.4x10^5$
P3HT:2,4-DM-Hep ann.120°c for 10min	0.15	3.47	37.5	$5.4x10^{-2}$	$2.9x10^4$	$7.4x10^5$

As observed under 1-sun conditions, P3HT:2,4-diF-Hep shows the best overall performance under indoor lighting conditions, primarily due to its significantly higher J_{SC} ($13.02\mu A.cm^{-2}$). The incorporation of fluorine atoms in 2,4-diF-Hep enhances exciton dissociation and improves current generation and efficiency. However, despite these advantages, the V_{OC} and absolute photocurrent are low, which limits the overall PCE. The R_S and R_{SH} provide further insight into device performance. The lower R_S of P3HT:2,4-diF-Hep ($4.7x10^3$ $\Omega.cm^2$) compared to P3HT:2,4-diF-Hep ($1.0x10^4$ $\Omega.cm^2$) and P3HT:2,4-DM-Hep ($2.9x10^4$ $\Omega \cdot cm^2$) indicates more efficient charge extraction and transport, which contributes to the improvement of J_{SC} and overall efficiency. Additionally, the R_{SH} of P3HT:2,4-diF-Hep ($2.4x10^5$ $\Omega.cm^2$) is moderate, indicating fewer leakage paths and reduced recombination. At the same time, the R_{SH} of P3HT: TDPH ($1.1x10^7$ $\Omega.cm^2$) is much higher, indicating some insulation but poor current generation due to high R_S.

As mentioned earlier, the HOMO of P3HT is -5.2 eV, which is higher than that of D18 (-5.51 eV), which indicates that the V_{OC} of the P3HT system may be lower than that of the D18 system. To address this issue and potentially improve V_{OC}, we propose to blend 2,4-diF-Hep with a different donor material, PCE12, which may provide better energy level alignment and thus improve V_{OC}.

PCE12: 2,4-diF-Hep blend system

PCE12, also known as PBDB-T, is a promising donor polymer with a lower HOMO (-5.33 eV)[24,175] compared to P3HT (-5.2 eV), which can lead to a larger energy gap between the HOMO of the donor and the LUMO of 2,4-diF-Hep, potentially increasing the V_{OC}, as shown in Figure 63a.

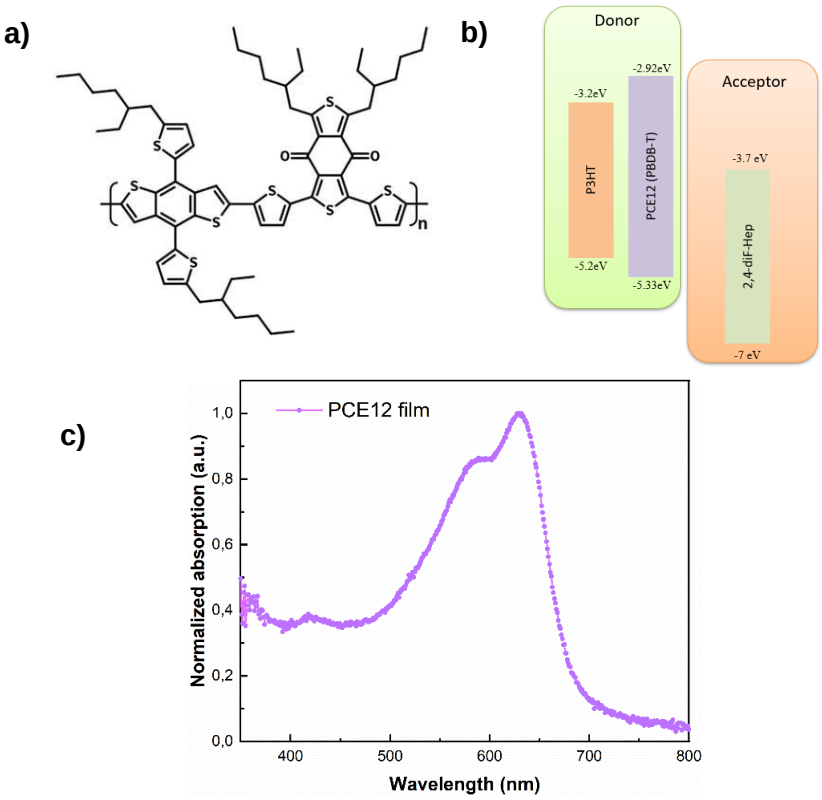

Figure 63. a) Chemical structure of PCE12. b) Energy levels of the donor materials (P3HT and PCE12) and the acceptor material (2,4-diF-Hep). c) Normalized absorption spectra of PCE12 film.

The PCE12 film has a strong absorption in the visible region from 500 nm to 700 nm, which is a good match for many acceptor materials, especially those that absorb in the blue region under low-light conditions. The PCE12:2,4-diF-Hep blend was prepared at a donor-to-acceptor weight ratio of 1:0.4 in CF, based on the molar masses of PCE12 (1183.86 g/mol per repeat unit) and 2,4-diF-Hep (509 g/mol). The devices were fabricated using the same inverted architecture: ITO/ZnO/active layer/MoO_3/Ag.

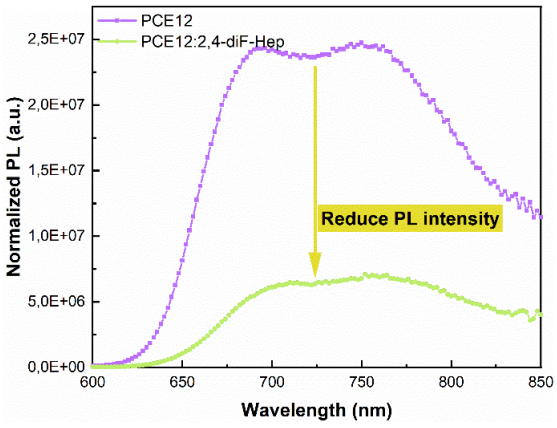

Figure 64. Normalized PL spectra of the pure PCE12 film and PCE12: 2,4-diF-Hep blend film, with excitation at 580 nm.

To understand the excitation and charge transfer states in the active layer, the normalized PL spectra are measured, as shown in Figure 64, with excitation at 580 nm, which is mainly absorbed by PCE12. The normalized PL spectra are obtained relative to the fraction of light absorbed at the excitation wavelength. The pure PCE12 film has strong PL emission peaks at

660 nm and 760 nm. These emission peaks are associated with the radiative recombination of singlet excitons, resulting from π-π transitions within the conjugated polymer backbone of PCE12, as commonly reported in the literature[176]. The higher PL intensity indicates that in the absence of acceptor material, excitons mainly recombine by radiation rather than dissociating into free charges. When PCE12 is mixed with 2,4-diF-Hep acceptor, the PL quenching percentage is 73.6%, calculated from Eq. 12. Although this quenching is significant, it does not reach the levels (90% or higher) that would typically indicate efficient charge transfer. This suggests that the morphology may not be ideal, that some excitons experience an environment similar to that in neat PCE12 due to the large domain size relative to the exciton diffusion length, or that the electron transfer between PCE12 and 2,4-diF-Hep is not completely efficient.

Since OPVs are considered a future indoor energy source, the PV operations of PCE12:2,4-diF-Hep OPVs with/without annealing were measured under 1-sun AM 1.5G and low-intensity artificial indoor lighting (1000 lux cool LED). The corresponding PV parameters are summarized in Figure 65 and Table 19.

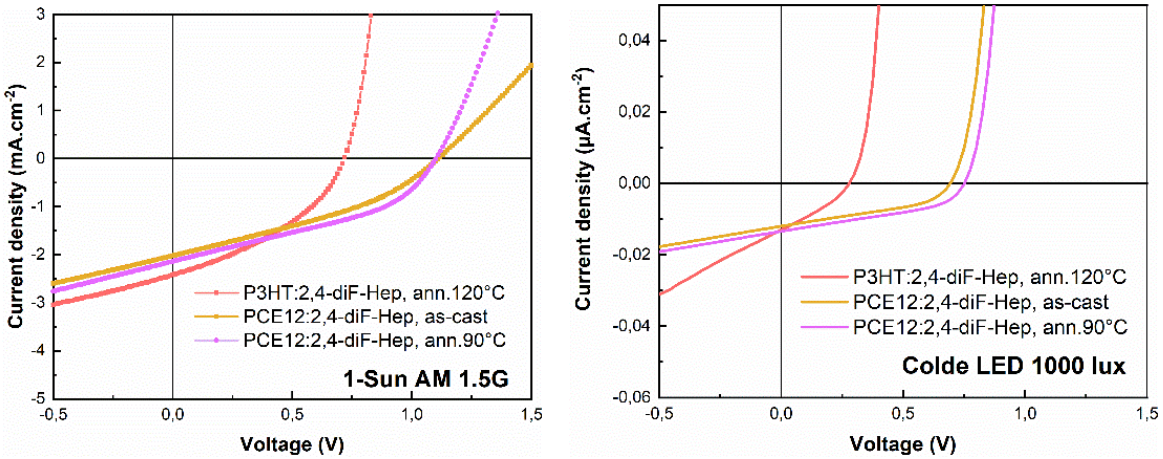

Figure 65. Comparison of J-V curves of PCE12:2,4-diF-Hep OPV devices with/without annealing and annealed P3HT:2,4-diF-Hep OPV device under solar simulator (100 mW.cm^{-2}) and 1000 lux cold LED.

Table 19. PV parameters of PCE12: 2,4-diF-Hep OPV devices with/without annealing under solar simulator (100 mW.cm^{-2}) and 1000 lux cold LED.

Blends		**V_{OC} (V)**	**J_{SC}**	**FF (%)**	**PCE_{MAX} (%)**	**R_S (Ω.cm^2)**	**R_{SH} (Ω.cm^2)**
PCE12:2,4-diF-Hep As-cast	Sun	1.10	2.02 mA.cm^{-2}	35.2	7.9x10^{-1}	1500	5820
PCE12:2,4-diF-Hep ann.90°c for 10min	Sun	1.10	2.14 mA.cm^{-2}	39.5	9.3x10^{-1}	360	5890
PCE12:2,4-diF-Hep As-cast	LED 1000 lux	0.70	11.98 µA.cm^{-2}	40.6	9.3 x10^{-1}	4450	7.4 x10^5
PCE12:2,4-diF-Hep ann.90°c for 10min	LED 1000 lux	0.75	13.42 µA.cm^{-2}	41.4	1.2	3700	7.4 x10^5

As expected, the transition from P3HT to PCE12 as the donor material resulted in a significant increase in V_{OC} and PCE. The V_{OC} of the PCE12:2,4-diF-Hep blend increased significantly, reaching 1.10 V under 1-sun condition and 0.75 V under indoor lighting (1000 lux cool LED). This is notably higher than the V_{OC} observed in the P3HT:2,4-diF-Hep blend (0.72 V under 1-

sun condition and 0.28 V under indoor lighting). In addition, the J_{SC} of the PCE12:2,4-diF-Hep blend reaches 2.14 mA.cm^{-2} under 1-sun condition, which is comparable to the performance observed in the P3HT:2,4-diF-Hep blend. However, despite the improvements in V_{OC} and J_{SC}, the series R_S and R_{SH} values indicate that significant transfer issues still exist. For the PCE12:2,4-diF-Hep blend, the R_S at 1-sun decreases significantly with annealing (1500 Ω.cm² to 360 Ω.cm²), which contributes to the improved charge transport and efficiency. However, under indoor lighting conditions, R_S remains relatively high (4450 Ω.cm² for as-cast film and 3700 Ω.cm² after annealing), indicating that the charge transport bottleneck persists.

In addition to these transmission limitations, although the absorption of these heptazine derivatives exhibits a modest red shift, this is not optimal for fully capturing light in the visible blue region (400-500 nm), which is critical for indoor applications. The lack of strong absorption in this region may reduce the effective photon absorption and further lead to poor device performance. These observations, together with the relatively high R_S and moderate R_{SH}, suggest that the morphology of these blends is far from being optimized. Poor phase separation or larger domains may hinder charge transport and increase recombination, indicating the need for further tuning of the blend morphology and processing conditions. To better understand and optimize the morphology, detailed morphological analysis such as AFM is essential. This will help elucidate domain size and phase separation within the active layer, providing insights into how to improve charge transport and reduce recombination. Further molecular modifications or the development of alternative acceptor materials are needed to enhance absorption in the blue region. These adjustments will lead to more efficient light collection and higher PCE, especially in low-light environments such as indoors.

III.5. Exploration of Di-PDI as an alternative NFA with strong blue-region absorption

As a complementary part of my study, another commercial NFA, Bay-linked perylene diimide (di-PDI)[177-179], was introduced to explore OPV systems with enhanced absorption in the blue visible region (Figure 66a). Unlike previously studied heptazine derivatives that exhibit limited absorption in the blue spectrum, di-PDI has a stronger and broader absorption region between 400 and 600 nm, as shown in Figure 66c, making it particularly suitable for indoor light harvesting applications under LED lighting.

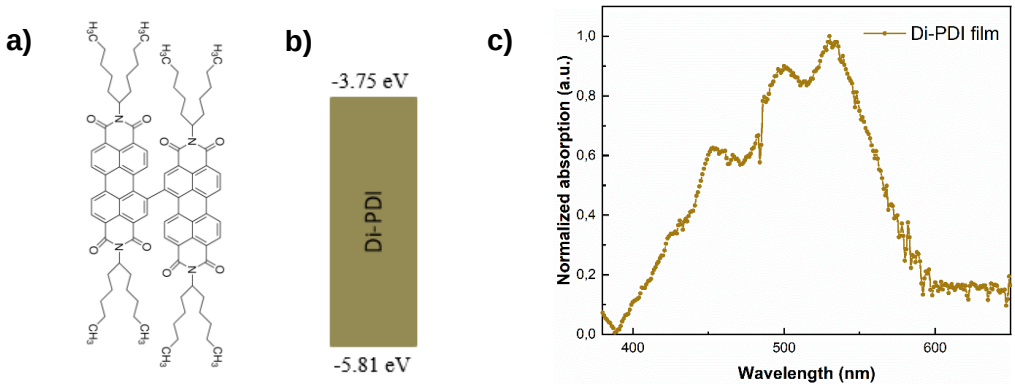

Figure 66. a) Chemical structure of Di-PDI, b) its energy levels[178,180], and c) its absorption.

PTB7-Th: Di-PDI blend system

The LUMO level of the Di-PDI film is -3.75 eV, and the HOMO level is -5.81 eV (Figure 66b), resulting in a band gap of 2.06 eV. Referring to the Shockley-Queisser limit for indoor

photovoltaics, the optimal band gap of this material is about 1.9 eV, which is very close to the 2.06 eV band gap of Di-PDI. Given these properties, rational donor material selection should include choosing materials with HOMO levels around -5.0 eV to -5.3 eV to ensure a good balance between maximizing V_{OC} and efficient charge transfer. For example, PTB7-Th[23,181]with a HOMO of approximately -5.24 eV could be a strong candidate for pairing with Di-PDI because of its complementary energy levels and strong absorption between 600 nm and 750 nm, which complements the absorption of Di-PDI in the blue region. In addition, PTB7-Th has demonstrated high PCEs in OPV devices when paired with other NFAs, making it a strong candidate for further improvement when combined with di-PDI. Furthermore, a relevant study on PTB7-Th: di-PDI[177] blends was found, supporting the potential of this combination in high-performance OPV devices. However, this blend system was not considered for indoor energy harvesting.

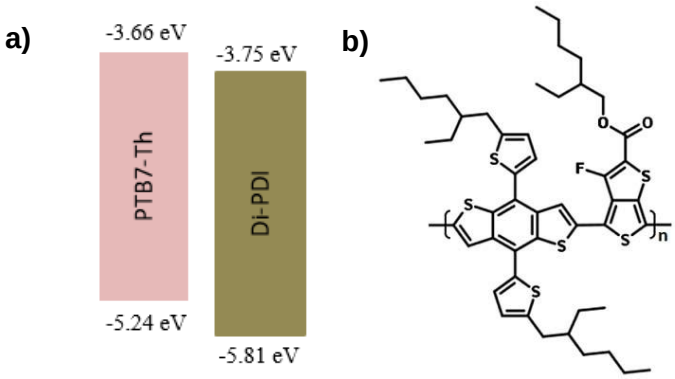

Figure 67. a) Energy levels of the PTB7-Th and di-PDI. b) Chemical structure of PTB7-Th.

We designed the experimental parameters for this system based on several publications on PDI-based solar cells optimized for outdoor operation[175,177,178]. As discussed and demonstrated in Ref. 177, the use of 1,8-diiodooctane (DIO) and 1-chloronaphthalene (CN) helps optimize phase separation and enhance overall device performance. A thickness of 105 nm was selected as it strikes a balance between maximizing light absorption, ensuring efficient charge transport, and minimizing recombination, which is critical for achieving a high PCE of 5.73%. Additionally, annealing at 100°C for 10 minutes helps further optimize the active layer morphology. Therefore, our solution was prepared by dissolving PTB7-Th and Di-PBI at a 1:1 weight ratio with a concentration of 18 mg/mL in o-dichlorobenzene (o-DCB). The mixture was stirred overnight to ensure complete dissolution and then filtered through a 0.22 µm polytetrafluoroethylene (PTFE) filter. Following the approach in the literature, 1% DIO and 2% CN were introduced into the solution. To achieve the optimal active layer thickness of 105 nm, the spin coating parameters were set as follows: rotation speed of 800 rpm, heating rate of 600 rpm/s, and a spin coating duration of 120 seconds. After spin coating, the films were annealed at 100°C for 10 minutes to refine the morphology further.

To check the global homogeneity of the deposited blend films, we recorded optical microscope images, as shown in Figure 68.

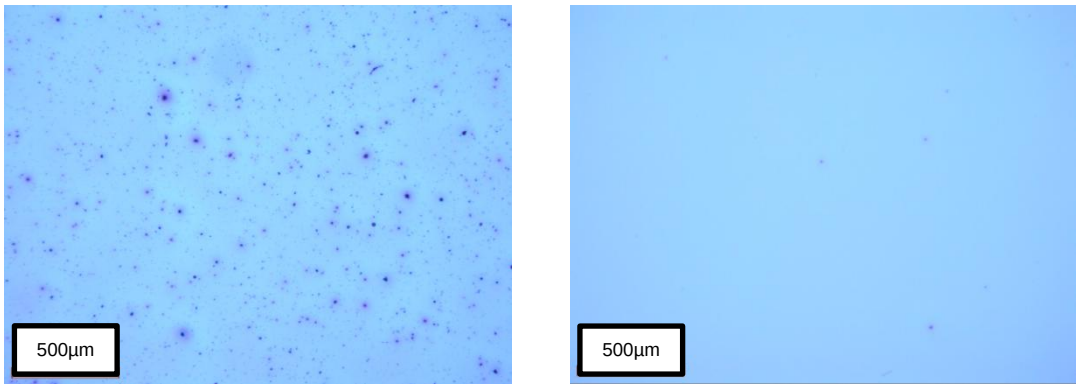

Figure 68. Microscope images of the active layer solution before (left) and after (right) filtering through a 0.22 µm PTFE filter.

In the left image of Figure 68, taken before filtration, a high density of aggregates and impurities can be observed, indicating the presence of insoluble particles in the solution. These particles can adversely affect the homogeneity of the film and the performance of the OPV device. After filtering, the number of visible impurities is significantly reduced, as shown in the right image, resulting in a much cleaner and more uniform solution.

The absorption spectra of PTB7-Th and di-PDI are shown in Figure 69. Di-PBI, with an intense absorption band between 400 and 600 nm, complements well the absorption of PTB7-Th, which has an intense band between 600–750 nm. This complementary absorption profile allows the active layer to capture a wider portion of the indoor light spectrum, particularly from LED sources.

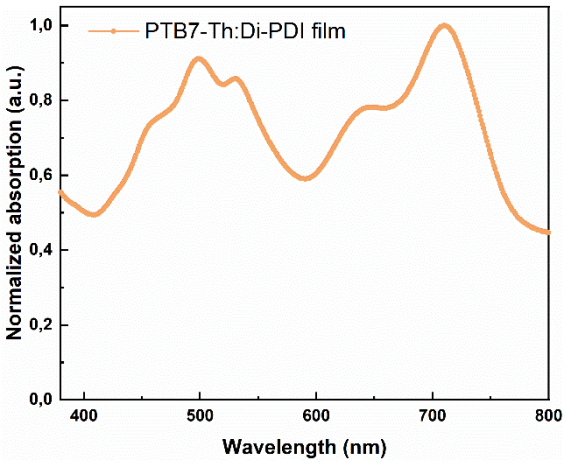

Figure 69. Normalized absorption in PTB7-Th: Di-PDI solid film state.

Blend films of PTB7-Th and di-PDI were integrated into OPV devices using the inverted architecture configuration (ITO/ZnO/Active Layer/MoO_3/Ag), and the corresponding JV curves and photovoltaic parameters are given in Figure 70 and Table 20.

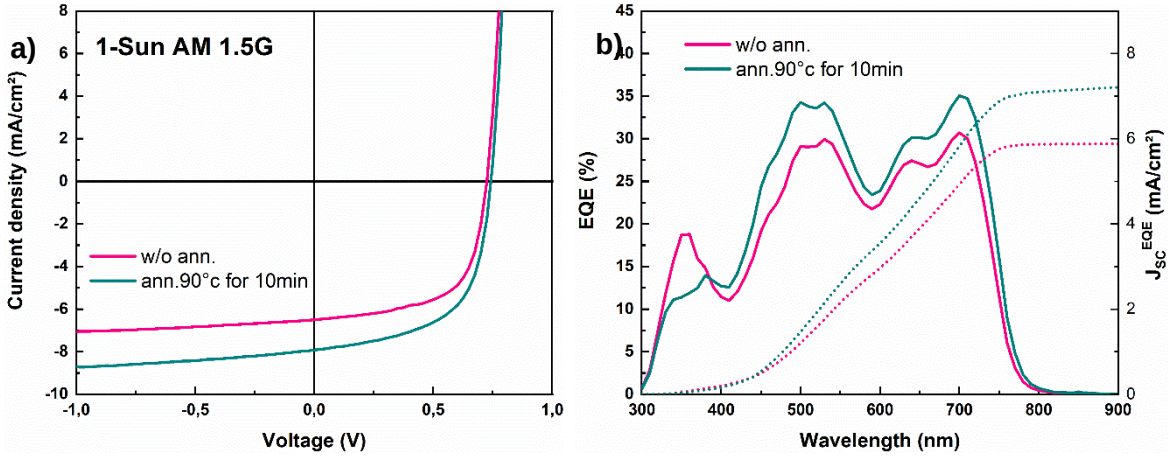

Figure 70. a) J-V curve of PTB7-Th: di-PDI OPV devices under solar simulator, and b) their EQE spectra showing wavelength-integrated photocurrent through integration over the standard solar spectrum.

Table 20. PV parameters of PTB7-Th: di-PDI OPV devices under solar simulator (100 mW.cm-2). * J_{SC}^{EQE} is calculated using EQE.

Blends	V_{OC} (V)	J_{SC} (mA.cm^{-2})	J_{SC}^{EQE} (mA.cm^{-2})	FF (%)	PCE_{MAX} (%)
PTB7-Th: di-PDI w/o ann.	0.73	6.5	5.9	62.5	2.9
PTB7-Th: di-PDI ann.100°c for 10min	0.75	7.9	7.3	58.9	3.5

Without annealing (Table 20), the device achieved a V_{OC} of 0.73 V, a J_{SC} of 6.5 mA.cm^{-2}, an FF of 62.5%, and a PCE_{MAX} of 2.9%. After annealing at 100°C for 10 minutes, the device performance improved with a higher V_{OC} of 0.75V, J_{SC} of 7.9 mA.cm^{-2}, and a PCE_{MAX} of 3.5%, although the FF slightly decreased to 58.9%. The J-V curve (Figure 70a) illustrated the enhanced performance of the device after annealing, as evidenced by higher current density and improved overall photovoltaic response.

The EQE spectra (Figure 70b) were well correlated with the J-V results, as the device with thermal annealing showed higher EQE values across the visible spectrum, particularly in the 400–600 nm and 700 nm ranges, which directly corresponded to the improvement in J_{SC} and overall device performance observed in the J-V measurements.

The PTB7-Th:di-PDI OPV devices were also tested with and without annealing under indoor lighting conditions ranging from 200 to 1000 lux under warm LED light to evaluate their performance under low light conditions, and the corresponding JV curves and photovoltaic parameters are shown in Figure 71 and Table 21.

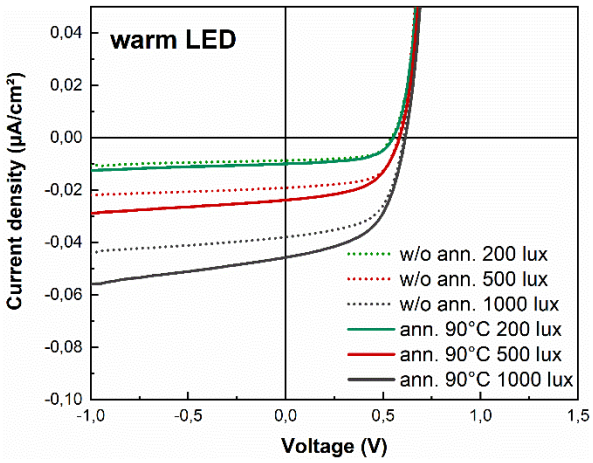

Figure 71. The corresponding J-V curves of PTB7-Th: di-PDI OPV devices with/without annealing under indoor illumination from 200 to 1000lux at warm LED.

Table 21. PV parameters of PTB7-Th: di-PDI OPV devices under LED (200, 500, 1000 lux).
* J_{SC} ^{EQE} is calculated using EQE.

Blends	LED 1000 lux	V_{OC} (V)	J_{SC} (μA.cm^{-2})	J_{SC} ^{EQE} (μA.cm^{-2})	FF (%)	PCE_{MAX} (%)
PTB7-Th: di-PDI w/o ann.	200	0.55	8.7	7.9	60.9	4.0
	500	0.58	19.1	19.7	62.0	4.1
	1000	0.60	37.9	39.4	59.2	4.1
PTB7-Th: di-PDI ann.100°c for 10min	200	0.55	10.0	8.9	57.7	4.4
	500	0.58	23.8	22.2	55.2	4.5
	1000	0.63	45.7	44.4	53.2	4.7

The trends of these J-V curves provide further insight into how thermal annealing and light intensity affect device performance. The J-V curves strongly suggest that morphology plays a key role in device performance and that annealing improves the structure of the active layer by enhancing charge transport and reducing recombination. The performance data in Table 21, measured under LED lighting for different light intensities (200, 500, and 1000 lux), showed trends that closely align with those observed under solar simulator (1-sun) conditions. Specifically, the annealing treatment at 100°C for 10 minutes consistently improved both J_{SC} and PCE under both indoor and outdoor conditions, confirming the beneficial effect of thermal annealing on device morphology and charge transport. At 1000 lux, with 100°C annealing for 10 minutes, the device exhibits the best performance with a V_{OC} of 0.63 V, a J_{SC} of 45.7 μA.cm^{-2}, and a PCE_{MAX} of 4.7%. While the system is not yet fully optimized, it is expected to reach this level of performance. However, as indicated by the relatively modest overall PCE, there is

still a need for more in-depth morphological studies, particularly using techniques like AFM, to understand better the nanoscale structure of the active layer, which could further enhance the applications of indoor and outdoor OPVs.

III.6. Conclusion

In this chapter, we have explored the development of OPV devices, which have a clear target of improving the absorption of the active layer in the blue region by transitioning from heptazine-based NFAs to di-PDI. Our study started with the PM6:Y6 reference system, a well-established and efficient reference in OPV technology. The PM6:Y6 blend exhibits strong photovoltaic performance under simulated sunlight (outdoor conditions), achieving a PCE of 10.3% at 1-sun with an optimum active layer thickness of 99 ± 10 nm. The system shows a good balance between light absorption, charge generation, and transport, making it an ideal benchmark for OPV performance. Furthermore, under 1000 lux warm LED indoor lighting, the PM6:Y6 system achieves an impressive PCE of 16.4%, a V_{OC} of 0.60 V, a J_{SC} of 123 µA.cm^{-2}, and a FF of 72%. These results highlight its efficiency under indoor conditions, making PM6:Y6 a strong candidate for both indoor and outdoor OPV applications. Our results are comparable to those reported in the literature, and the system achieves a PCE of 17.6% at 1300 lux, further validating the high performance of the system in indoor environments.

Following the promising results obtained with PM6:Y6, we explored the potential of heptazine-based NFAs as a novel material platform for OPVs. The goal is to increase the absorptivity of the active layer, especially in the blue region of the spectrum, to enhance light harvesting. Despite the good tunability of the electronic properties of heptazine derivatives, their absorbance in the ultraviolet region remained suboptimal (as far from the blue region of the LED emission), limiting their effectiveness in improving OPV performance. We have tried various methods to modify the side chains of heptazine derivatives to optimize their absorption profiles but failed to improve the photovoltaic performance significantly. This restriction to absorption in the blue region ultimately limits their ability to improve OPV efficiency, making them less suitable for high-performance applications, especially in indoor lighting conditions where blue light plays a key role.

In contrast, we turned to the use of di-PDI as alternative NFAs with more promising results. The di-PDI-based system, especially when combined with PTB7-Th as a donor, showed improved absorbance in the blue region and better overall photovoltaic performance. Under 1-sun conditions, the PTB7-Th blend achieved a PCE of 3.5% after annealing at 100°C, which is a significant improvement over the heptazine-based system. Furthermore, under 1000 lux LED indoor lighting, the di-PDI-based device showed potential with a PCE of 4.7% after annealing. However, while the di-PDI-based system shows promise, further research is needed to improve its performance, especially under low-light conditions. Future efforts should focus on exploring other side-chain modifications and identifying other NFAs to optimize absorption in the blue region further and enhance charge transport. Furthermore, additional morphological optimization of the active layers is critical to push the efficiency of these devices to higher levels, especially in indoor environments.

Chapter IV. Di-fluorinated copolymer PF2 Donor for IOPVs

In the previous chapter, we investigated the potential of heptazine-based NFAs in OPV devices for indoor applications. Despite their tunable electronic properties, a significant challenge is their limited absorption in the blue region of the spectrum, which restricts their ability to improve the overall PCE. This poses a particular problem for indoor OPVs, as indoor light sources such as LEDs emit a large portion of their light in the blue region. Efficiently capturing and converting this portion of the spectrum is critical to improving OPV performance under indoor lighting conditions. Although many efforts have been made to modify the side chains of heptazine derivatives to broaden their absorption, these modifications have not achieved the desired red shift. Therefore, we found it necessary to reconsider our approach and explore alternative strategies to address this limitation.

Our new approach focuses on finding another material that exhibits a broad and extended absorption spectrum in the blue region, which is a key requirement for improving light harvesting under indoor lighting. While most state-of-the-art high-efficiency OPV materials are well suited for outdoor applications, they often fall short in indoor conditions because their low V_{OC} levels are insufficient to effectively harvest energy from the low-intensity light sources typically found indoors. Based on a comprehensive review of the literature and the state-of-the-art OPV materials, we believe that the fluorinated polymer donor PF2 is a promising candidate[10,11,141]. PF2 meets the necessary criteria, with a medium bandgap and strong absorption in the blue region of the spectrum, making it ideal for capturing light from indoor LED sources. Furthermore, PF2 has been shown to possess good charge transport properties and compatibility with FA $PC_{71}BM$[141] and NFA Y6[11], making it a versatile material for OPV device optimization. The selection of PF2 as donor material represents a strategic shift from our previous focus on heptazines, which is in line with the requirements for high-efficiency IOPV applications. To complement PF2, we chose (3,9-bis(2-methylene-(3-(1,1-dicyanomethylene)-indanone))-5,5,11,11-tetrakis(4-hexylphenyl)-dithieno[2,3-d:2',3'-d']-s-indaceno[1,2-b:5,6-b']dithiophene) (ITIC)[24,182-184], a widely studied NFA known for its excellent charge separation and transport properties. The energy levels of ITIC are well matched to those of PF2, allowing efficient charge transfer and the potential to achieve high V_{OC} in this system, which will be further discussed in the next paragraph with reference to Figure 72e. This PF2:ITIC system not only addresses the limitations of heptazine but also improves the performance of the device in both outdoor and indoor conditions.

The approach in this chapter builds on the insights gained from the challenges faced in Chapter III. Here, we focus on optimizing the performance of PF2:ITIC blends while taking into account the active layer morphology, the donor-to-acceptor (D:A) ratio, and the thickness of the active layer. These parameters are crucial to achieve a proper balance between light absorption and charge transport. The research involved systematically tuning processing conditions, such as the choice of solvents for processing the active layer and annealing treatments, which have been shown to affect crystallinity and phase separation within the active layer. Furthermore, by fine-tuning the thickness of the active layer, we aim to maximize light absorption while maintaining efficient charge extraction, minimizing recombination losses, and ensuring optimal performance under 1-sun and indoor LED lighting conditions.

IV.1. Materials and devices structure for PF2:ITIC system

PF2, a di-fluorinated copolymer donor based on thienothiophene and a difluorinated benzothiadiazole moiety with two thiophene units substituted by two octyl-dodecyl alkyl side

chains at the β-position (Figure 72a), has been synthesized by the ICPEES laboratory in France (group of Dr. Nicolas Leclerc). PF2 exhibits strong light-harvesting properties with an absorption spectrum ranging from 400 to 750 nm (Figure 72b). Notably, PF2 shows a good significant absorption in the blue region of the spectrum, which is quite unusual for many organic materials. This property makes PF2 particularly suitable for indoor applications, which directly supports the aims of this thesis. PF2 is also characterized by suitable molecular energy levels and the ability to self-assemble into crystalline lamellae with a mixed face-on/edge-on orientation, which enhances charge transport properties[10,141]. ITIC[24,185,186] (Figure 72a) is a well-known electron-accepting small molecule characterized by strong absorption in the visible region and high electron affinity. Furthermore, ITIC has the potential in the PM6:ITIC system to achieve a high V_{OC} of 1.04 V[184]. This makes ITIC an ideal choice for the NFA in our study, and it was commercially sourced from Ossila.

These materials (PF2 as polymer donor and ITIC as NFA) were used to fabricate an inverted structure OPV cell with the structure shown in Figure 72c: ITO/ZnO/active layer/MoO_3/Ag. Figure 72a shows the chemical structures of PF2 and ITIC, while Figure 72d summarizes the energy levels, showing the LUMO and HOMO values for each material in a simplified representation. Specifically, the HOMO of PF2 is −5.42 eV, and the LUMO is −3.76 eV, while the HOMO of ITIC is −5.48 eV, and the LUMO is −3.83 eV. In Figure 72e shows the energy levels of different acceptors (ITIC, PC71BM, and Y6) compared with the energy levels of the donor material PF2. The corresponding data are derived from the literature at this stage[24,141,187].

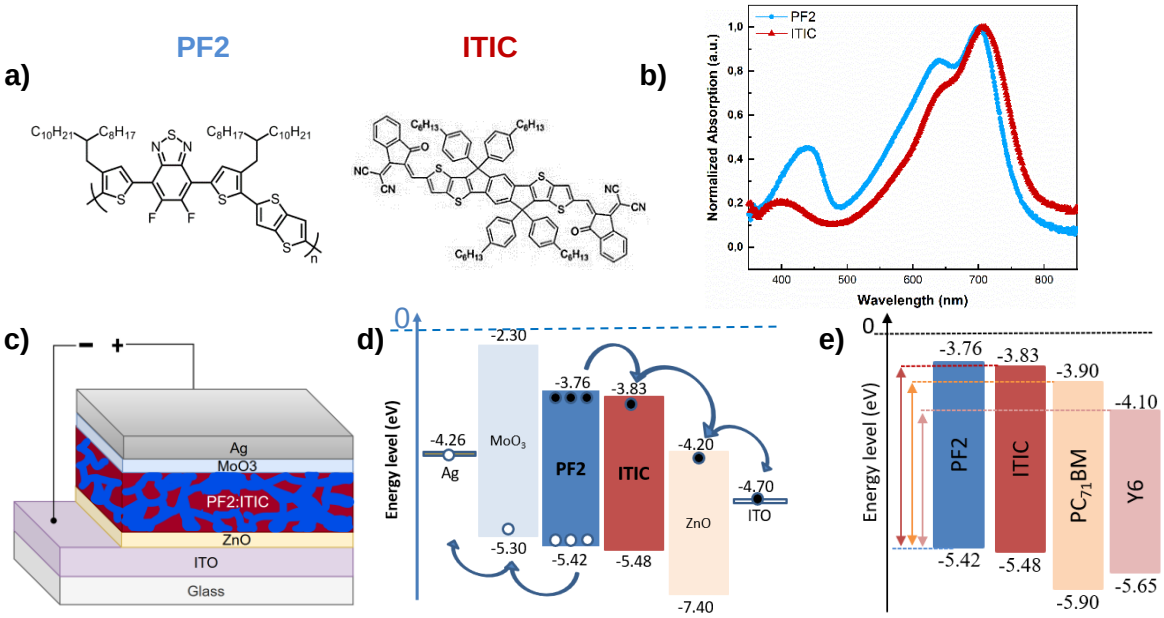

Figure 72. a) Chemical structures of PF2 and ITIC. b) Normalized absorption spectrum of PF2 and ITIC in film. c) Structure of OPV with PF2:ITIC. d) Energy levels of the materials used in the OPV device. e) Energy levels of various acceptors are compared with the energy levels of PF2.

As mentioned earlier, achieving high V_{OC} is particularly important for indoor applications, where the V_{OC} is determined by the energy difference between the LUMO of the acceptor and the HOMO of the donor. In Figure 72e, we observe that ITIC has a higher LUMO level compared to other acceptors, such as $PC_{71}BM$ and Y6, which have a LUMO level of -3.90 eV and -4.10 eV, respectively. This increased LUMO level of ITIC is −3.83 eV, therefore, could contribute significantly to a higher V_{OC}[78], making it a more suitable choice for enhancing the efficiency of

OPV devices under indoor conditions. PF2 has been previously studied with various receptors, particularly for outdoor applications. In 2019, Nicolas Leclerc's team achieved a PCE of 10.5%, a V_{OC} of 0.75 V, a J_{SC} of 19.5 mA/cm², and a FF of 72% using the PF2:$PC_{71}BM$ system[141]. In 2020, Xiaoling Ma worked with them further enhanced the PF2-based system by using two polymer donors to create a ternary organic photovoltaic cell that minimized energy losses and achieved a PCE of 12.12%, a J_{SC} of 24.97 mA/cm², a FF of 64.70%, and a V_{OC} of 0.75 V[11]. However, these studies have mainly focused on outdoor conditions, and the potential of PF2-based systems under indoor lighting has not yet been explored. Therefore, this study aims to explore the PF2 system as a new approach for indoor OPVs.

IV.2. Adjusting active layer morphology with solvents

Optimizing the active layer of OPV devices through careful solvent selection and processing is a critical step in improving device performance. The choice of solvent significantly affects the morphology of the active layer, which in turn influences vital parameters such as charge generation, transport, and recombination. In this study, we focused on three chlorinated solvents: CB, CF, and o-DCB, all of which are capable of dissolving both the polymer and the small molecule of the active layer.

To predict and evaluate the solubility of PF2 in these solvents, we used Hansen Solubility Parameters (HSP)[188], a widely recognized method for characterizing the solubility of materials. Introduced by Charles M. Hansen in the 1960s, HSP is based on the premise that substances with similar HSP values are likely to be compatible. These parameters are expressed in units of MPa0.5 and consist of three components:

- ✓ Dispersion forces interaction parameter (δD)
- ✓ Polar force interaction parameter (δP)
- ✓ Hydrogen bonding force interaction parameter (δH)

These three parameters can be visualized as coordinates in three-dimensional Hansen space, which defines a Hansen solubility sphere for organic materials with a specific interaction radius R0. The distance Ra between the HSPs of a material and a solvent in Hansen space is calculated using the following formula:

$$(\mathrm{R_a})^2 = 4(\delta_{\mathrm{D1}} - \delta_{\mathrm{D2}})^2 + (\delta_{\mathrm{P1}} - \delta_{\mathrm{P2}})^2 + (\delta_{\mathrm{H1}} - \delta_{\mathrm{H2}})^2$$

(Equation 13)

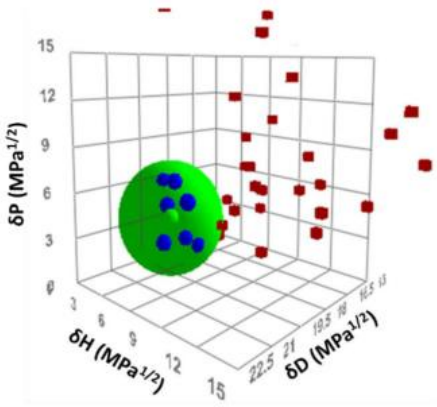

Figure 73. shows the Hansen solubility sphere of PF2, measured from 36 different solvent solutions, where blue spheres present suitable solvents and red cubes present poor solvents[141].

The relative energy difference (RED) between a material and a solvent, combined with R_0, can be used to estimate whether a material will dissolve in a solvent, as defined in Eq. 14:

$$RED = \frac{R_a}{R_0} \quad \text{(Equation 14)}$$

If RED < 1 indicates that the material is likely to dissolve in the solvent, RED = 1 indicates that the material will partially dissolve in the solvent. In contrast, RED > 1 indicates that the material is unlikely to dissolve in the solvent. The HSP values of PF2 and those of CF and o-DCB were obtained from the literature (Refs. 137 and 186). In addition, the HSP values of CB were calculated using Eq. 13 and Eq. 14 to complete the dataset, as shown in Table 22.

Table 22. HSP parameters of PF2[141] and different solvents[189].

Materials	δD	δP	δH	R_0	R_a	RED	Solubility
PF2	19.15	3.87	2.83	4			
chlorobenzene	19.0	4.3	2.0		0.98	0.25	Good
chloroform	17.8	3.1	5.7		4.01	1.00	Partial
o-dichlorobenzene	19.2	6.3	3.3		2.48	0.62	Good

For CB and o-DCB, the RED values are less than 1, with RED values of 0.25 for CB and 0.62 for o-DCB, indicating that PF2 is highly soluble in these solvents. In particular, the lower RED value for CB suggests that it provides a more favorable environment for the dissolution of PF2, as the solubility of a material increases as the RED value decreases. It is because a lower RED value indicates that the solvent's solubility parameters of the solvent (δD, δP, and δH) are closer to those of PF2, resulting in better compatibility and interaction at the molecular level. In contrast, CF has a RED value of exactly 1, which places PF2 at the critical threshold between solubility and insolubility. At this threshold, the interaction between PF2 and CF is just sufficient to dissolve the polymer, but the solution may not be as stable or homogeneous as when using CB or o-DCB.

Based on the initial solvent selection and solubility assessments, we proceeded with the preparation and deposition of the PF2:ITIC blend using three chlorinated solvents: CB, CF, and o-DCB. The boiling point of each solvent has a significant influence on the processing conditions, which were carefully optimized to obtain a uniform layer. In fact, PF2 solutions show a strong temperature dependence, especially in terms of viscosity, which directly affects the thickness of the deposited films. Temperature fluctuations can cause significant changes in solution viscosity, resulting in inconsistent PF2:ITIC film thickness. In order to ensure consistency and reproducibility of the PF2:ITIC film thickness, it is essential to maintain a stable temperature throughout the process. To this end, the substrates were pre-heated to the same temperature as the PF2:ITIC blend solution, and this latter was maintained on a hot plate during active layer deposition to minimize the temperature difference between the moment the solution was taken from the vial and the moment it was deposited onto the pre-heated substrates. We tried to adopt a procedure at the lab-scale to achieve reproducible results in a complex process, as even a small change in parameters can cause significant variations in thickness. This requires meticulous attention to detail and strict control of all processing conditions. All solvents and materials were stored in a separated glove box that was used for film deposition to reduce atmosphere pollution and maintain reproducible conditions. Materials were weighed in the globe box, as well as solution preparation. The detailed procedures for each solvent are described below:

PF2:ITIC blend in CB

The D:A mass ratio and solution concentration used in this study were selected based on previously published results for similar systems (PF2:$PC_{71}BM$ and PF2:Y6)[11,187], which provide a theoretically solid starting point for optimizing the PF2:ITIC blend. Specifically, a D:A mass ratio of 1:1.5 and a total concentration of 17.5 mg/mL (7 mg PF2 and 10.5 mg ITIC dissolved in 1 mL CB) were used. Given that the boiling temperature of CB is 132°C, the solution was stirred at 80°C for 24 hours to ensure complete dissolution and homogeneity. The blend was then statically spin-coated at 2000 rpm with an acceleration of 1000 rpm/s for 40 seconds to form an active layer approximately 100 nm thick. Prior to deposition, the ZnO-coated substrates were preheated at 80°C for 15 minutes to improve film uniformity.

PF2:ITIC blend in CF

The same D:A ratio of 1:1.5 was used, but the concentration was adjusted to 13 mg/ml (7 mg PF2 and 10.5 mg ITIC dissolved in 1.35 ml CF). The solution was stirred at room temperature for 24 hours. Due to the lower boiling point (61°C) and rapid evaporation rate of chloroform, the blend was spin-coated at 4000 rpm with an acceleration of 1000 rpm/s for 30 seconds without additional substrate preheating. This process produced a uniform active layer of approximately 100 nm thickness.

PF2:ITIC blend in o-DCB

The same D:A ratio of 1:1.5 and concentration of 17.5mg/ml was used. The solution was stirred at 100°C for 24 hours to ensure complete dissolution, as the boiling temperature of o-DCB is 179°C. Spin-coating parameters were set at 2000 rpm and 1000 rpm/s for 40 seconds. The ZnO-coated substrates were preheated at 100°C for 15 minutes to obtain a uniform active layer of approximately 100 nm thickness.

We then studied the surface morphology using SEM and AFM of the PF2:ITIC blends in three solvents obtained from the deposition of the active layer on top of glass/ITO/ZnO substrates, as depicted in Figure 74 below:

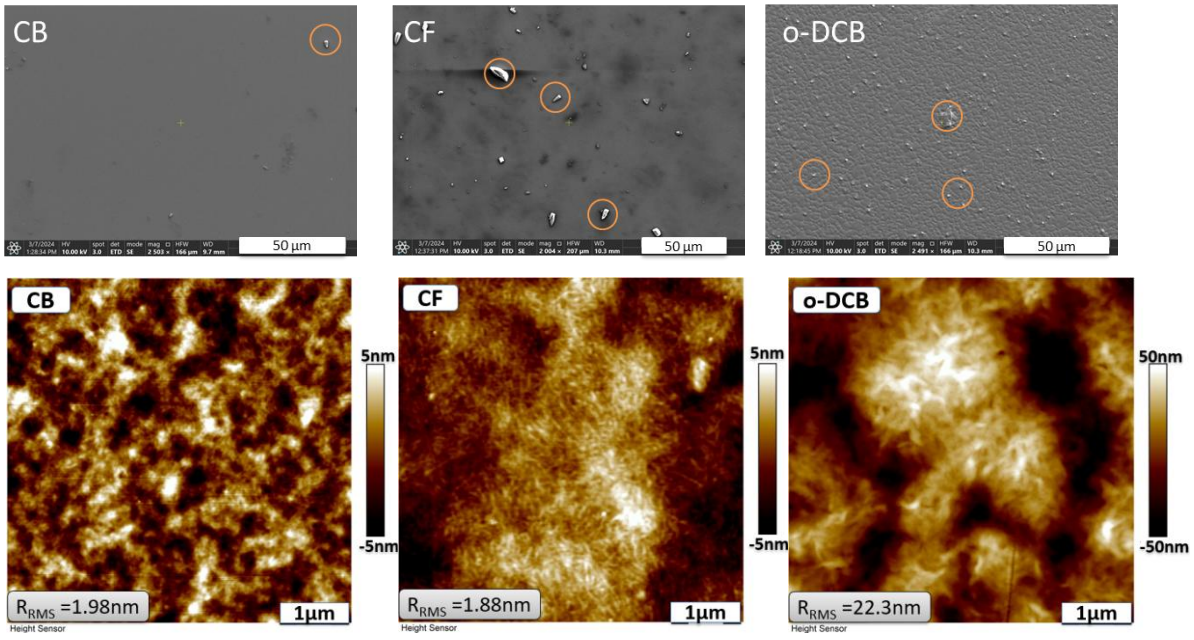

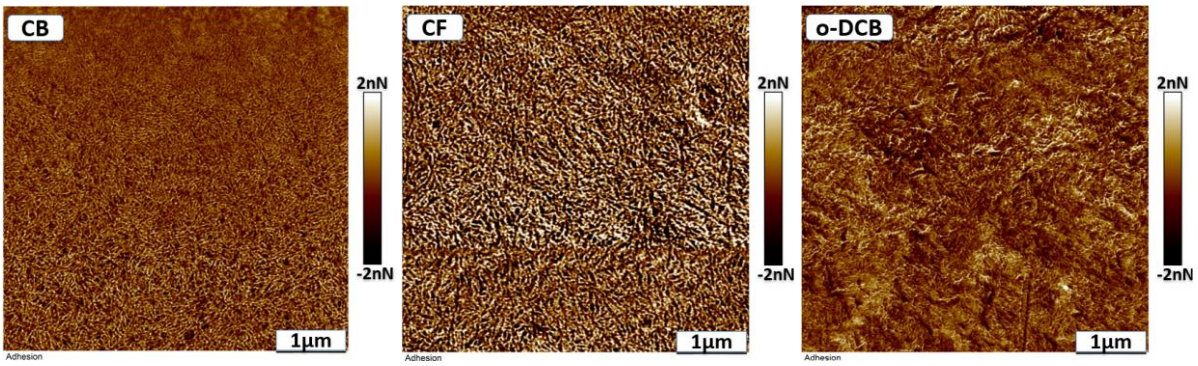

Figure 74. SEM images (top row), AFM height images (5x5µm, middle row), and AFM adhesion images (5x5µm, bottom row) of PF2:ITIC blend films of CB, CF, and o-DCB.

Large-scale SEM analysis:

The SEM images showed significant differences in the surface morphology of the films depending on the solvent used. The blend film processed with CB showed a smooth and homogeneous surface, indicating good solubility and uniform film formation. In contrast, the films prepared with CF and o-DCB showed visible aggregates on their surfaces. These aggregates were more pronounced in the film processed with CF, which can be attributed to the lower solubility of PF2 in CF, as indicated by the previously discussed RED value. The presence of larger aggregates in the CF-processed film is of particular concern, as these can lead to discontinuities or "short circuits" in the active layer, which can negatively affect device performance. On the other hand, although aggregates were also observed in the o-DCB-processed film, their size and quantity were less pronounced compared to the CF-processed film. This difference may be attributed to the better solubility and slower evaporation rate of o-DCB compared to CF, which allows a more gradual film formation process and, consequently, reduces the extent of aggregate formation.

Nanoscale AFM height images analysis:

AFM provided further insight into the nanoscale surface structure of PF2:ITIC blend films processed with three different solvents. AFM height images reveal the nanoscale topography of the films, showing that the nanoscale morphology varied with the solvent used. RMS surface roughness measurements revealed significant differences: the CB-processed film had an RMS roughness of 1.98 nm, indicating a smooth surface; the CF-processed film had a slightly lower RMS roughness of 1.88 nm, despite the presence of larger aggregates seen in SEM; and the o-DCB-processed film had a much higher RMS roughness of 22.3 nm, reflecting the uneven surface. These differences in surface roughness and morphology at the nanoscale are closely related to the solubility of PF2 in the solvents; CB, with its favorable solubility, produced the most uniform and smooth film, which is expected to translate into higher PCE for OSCs. Conversely, the larger aggregates and higher surface roughness observed in films processed with CF and o-DCB are likely to induce limitations in device operation, as they often cause increased recombination losses and/or poor charge transport properties.

The observed morphological variations can be further explained by the interplay between the thermodynamics of phase separation and the kinetics of solvent evaporation. The evaporation rate of the solvent significantly affects the arrangement of polymer chains and molecular domains, leading to different degrees of crystallization and phase separation, as evidenced by AFM observations. From a thermodynamic point of view, the miscibility of PF2 and ITIC in the solvent determines the initial state of the blend solution. Solvents such as CB and o-DCB have

better solubility compared to CF, as indicated by their higher boiling points and RED values. This enhanced solubility ensures solution homogeneity during preparation. The kinetics of solvent evaporation further determine the phase separation rate. The rapid evaporation of the low-boiling-point solvent CF (61 °C) leads to rapid solidification, restricting the mobility of the polymer chains and preventing the system from reaching thermodynamic equilibrium. This leads to the formation of larger aggregates and less ordered domains, as shown in the SEM and AFM images of the CF-treated films. Despite the presence of aggregates, the relatively smooth AFM height profile (RMS roughness of 1.88 nm) suggests that rapid solidification kinetically captured the structure. In contrast, the slower evaporation rates of CB (boiling point 132°C) and o-DCB (boiling point 179°C) bring the system close to equilibrium, promoting molecular rearrangement and thermodynamically driven phase separation. The CB-treated films exhibited a fine interpenetrating network of small, evenly distributed domains, indicating that the morphology was thermodynamically controlled. However, the slower evaporation rate of o-DCB promotes excessive molecular rearrangement, resulting in the formation of larger and more distinct domains, as reflected in the significantly higher RMS roughness of 22.3 nm and irregular domain structure observed in the adhesion images.

Nanoscale AFM adhesion image analysis:

In addition, the adhesion images reveal an interpenetrating network structure across all films, with variations in domain size and contrast that depend on the solvent. The color contrast in the adhesion images represents different material properties and may correspond to donor-rich and acceptor-rich phases. Darker areas may be associated with the donor-rich phase, and lighter areas may be associated with the acceptor-rich phase, but additional material-specific studies are required to assign each color to a specific material definitively. Nevertheless, the presence of the interpenetrating network is a positive sign as it enables efficient charge separation and minimizes recombination within the BHJ. The adhesion image of CB-processed film shows a fine interpenetrating network with relatively small, evenly distributed dark and light areas. It indicates that the morphologies are well mixed, with effective phase separation between the donor-rich phase and the acceptor-rich phase. This network is essential for efficient charge separation and transport. In contrast, the CF-treated film also shows an interpenetrating network, but the domains are slightly larger, and the contrast between dark and light areas is more pronounced. Although phase separation is essential for charge transport, excessively large domains hinder efficient charge extraction and may lead to increased recombination. The o-DCB-processed films showed irregular and larger-scale network structures in the adhesion images, with large variations in domain size. The presence of larger isolated domains may indicate inefficient mixing and poor phase separation, which may be due to the slow evaporation of o-DCB, leading to the formation of larger domains. This morphology is less than ideal for charge separation and transport because it may lead to isolated regions without sufficient pathways for efficient charge extraction.

In order to better understand the relation between active layer morphology and electrical/dielectric properties, we carried out further characterization using sMIM to probe the local electrical properties of the PF2:ITIC blend films processed with different solvents. This is the first time that a conjugated polymer-based system has been characterized using the sMIM technique. The data corresponding to conductivity and capacitance images are summarized in Figure 75.

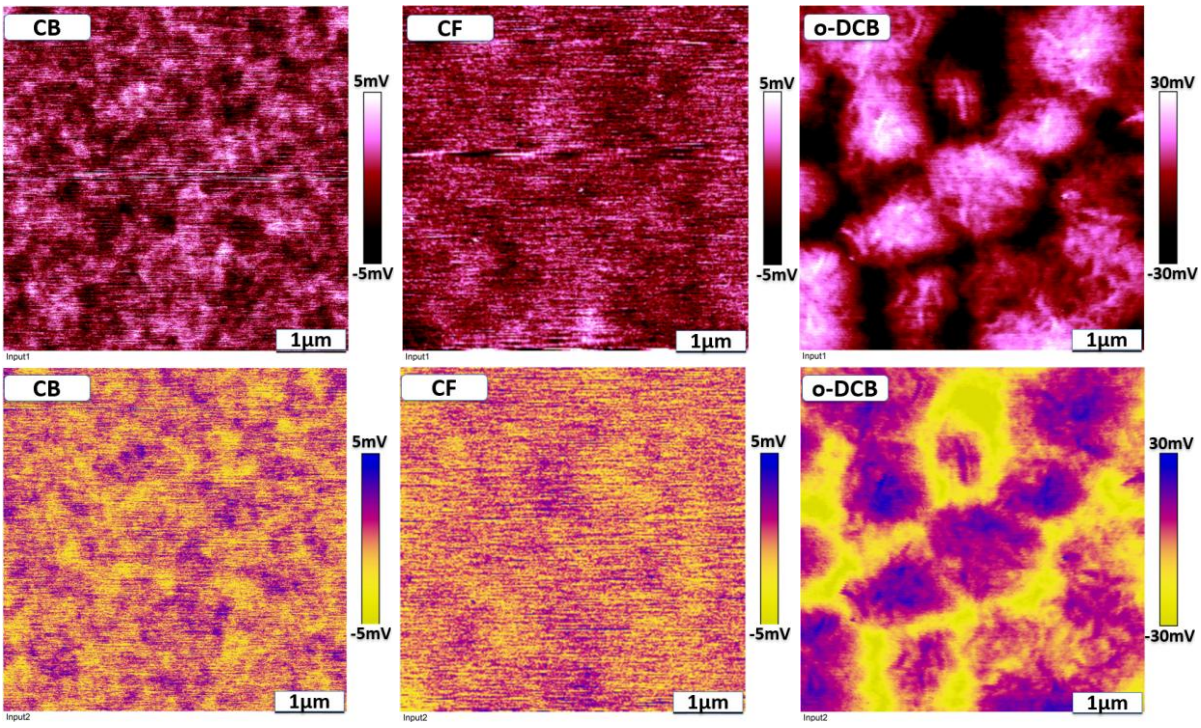

Figure 75. sMIM-conductivity images (5x5µm, top row), and sMIM-capacitance images (5x5µm, bottom row) of PF2:ITIC films processed with CB, CF, and o-DCB.

Our observations indicate that the blends processed with CB and CF have relatively uniform dielectric properties, as shown by the sMIM images, which reveal a nanoscale contrast homogeneously distributed over the entier probed area of the device. This uniformity closely matches the corresponding topographical images, suggesting that CB and CF facilitate the formation of well-mixed, homogeneous films of low surface roughness. In contrast, the blend processed with o-DCB shows clear phase separation, which is consistent with the larger domain sizes observed in AFM and SEM analyses. The conductivity image in Figure 76 below further highlights these features, showing the well-defined polymer-rich high conductivity regions and the length of the PF2 polymer chains in the mixture.

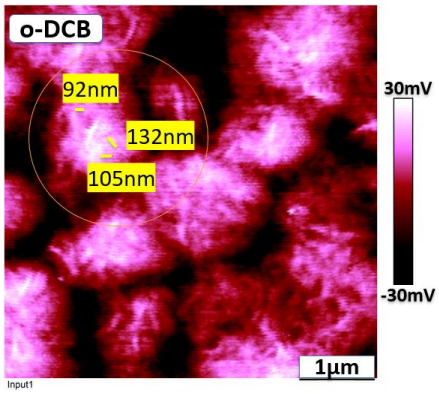

Figure 76. Conductivity image of o-DCB processed PF2:ITIC blend film highlights polymer-rich high conductivity domains and length of the PF2 polymer chain

For the o-DCB treated films, although the overall morphology seems less ideal compared to the other solvents, the presence of contrasting domains provides valuable insights. These well-defined regions allow us to identify features that likely correspond to polymers, as indicated by the orange oval in the images. The distinct regions of high conductivity can be attributed to the

polymer-rich regions within the film, suggesting that these regions are primarily associated with the PF2 polymer phase. The estimated length of the PF2 polymer chain is approximately 103 nm (see Appendix 2.3), and the observed domain sizes in the conductivity image (92, 105, and 132 nm) are in close agreement with this theoretical length, corresponding to a polymer with 29 repeat units.

To further explore the effect of solvent choice on the optoelectronic properties, we now examine the optical absorption and PL spectra of the PF2: ITIC films processed with the three different solvents (Figure 77).

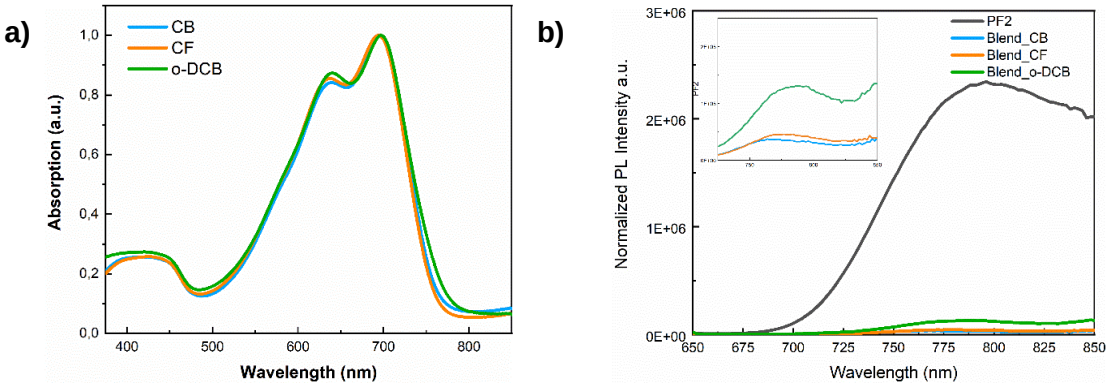

Figure 77. a) Normalized absorption spectra of PF2:ITIC films processed with CB, CF, and o-DCB. b) PL spectra of neat PF2 and PF2:ITIC blend films processed with CB, CF, and o-DCB under 640 nm light excitation.

All three films exhibit a broad absorption range from 400 nm to 780 nm, which matches the emission spectra of indoor light sources well. The absorption profiles of the films are pretty similar, with three peaks observed at 440 nm, 640 nm, and 700 nm, indicating that the choice of solvent does not significantly alter their main light-harvesting capabilities. The peak at 440 nm with high energy can be attributed to a π-π* transition, typical of conjugated polymer systems, indicating electronic transitions within the aromatic rings of PF2. This transition is significant as it supports efficient light absorption in the blue region, which is critical for indoor OPV applications. The peaks at 640 nm and 700 nm may be due to intramolecular charge transfer (ICT) transitions that occur between electron-rich and electron-deficient units[182,190]. These transitions can be attributed to PF2 and ITIC, as both materials exhibit similar ICT properties. In PF2, these peaks arise from the charge transfer on the conjugated main chain and are enhanced by the fluorinated side groups, while in ITIC, these peaks originate from its strong electron-accepting properties, which also support the charge transfer. The slight variations in peak intensities and shapes between the different solvent-treated films indicate that while all three solvents allow good absorption over the desired spectral range, the choice of solvent slightly affects the optical density and perhaps the packing or orientation of the molecules within the film.

The PL intensity of the pure PF2 film is significantly higher than that of the blend films, which is expected due to efficient exciton quenching in the donor-acceptor blends. Among the blends, the film processed with CB shows the lowest PL intensity, indicating the most efficient exciton dissociation and charge transfer, which is beneficial for achieving high PCE. The films processed with CF and o-DCB show higher PL intensities, indicating that the exciton quenching is less efficient in these films. This could be related to the presence of aggregates and higher surface roughness observed in the morphology studies, which may hinder charge separation through a reduced D-A interface and lead to increased recombination losses.

J-V characterization and EQE analysis were used to evaluate the photovoltaic properties of PF2:ITIC-based solar cells in an inverted geometry under standard AM 1.5G, as depicted in Figure 78 and Table 23.

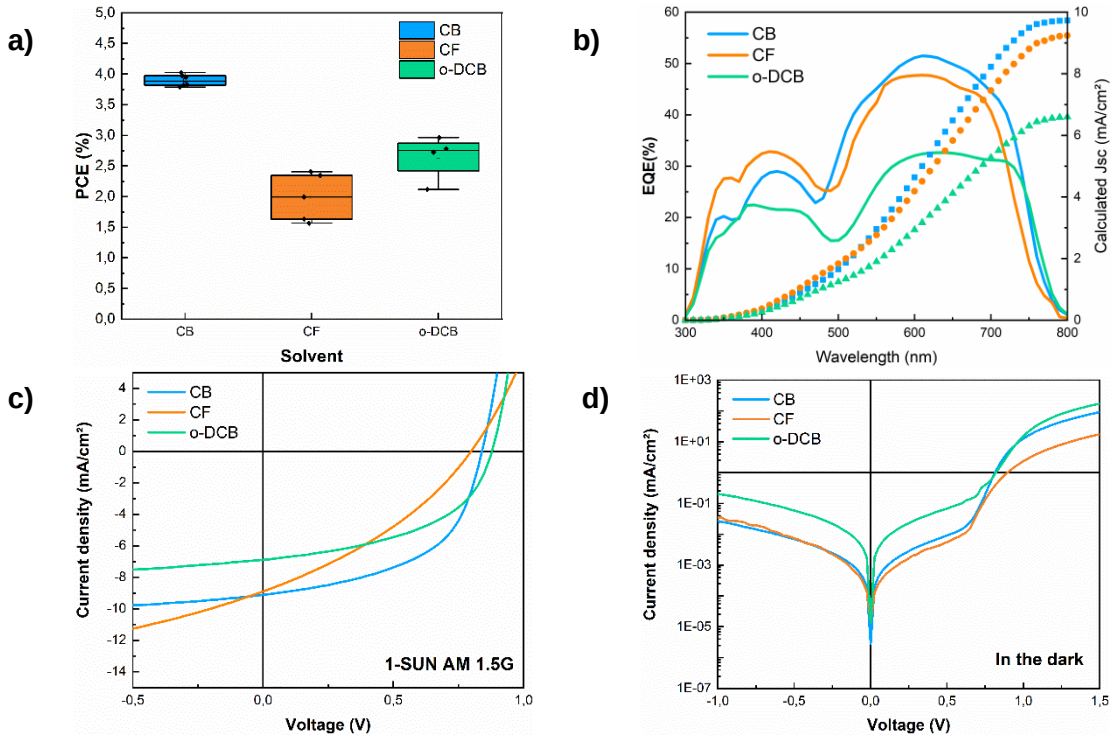

Figure 78. a) Dispersion of PCE of six PF2:ITIC OPVs processed with CB, CF, and o-DCB under standard AM 1.5G illumination. b) EQE spectra showing wavelength-integrated photocurrent through integration over the standard solar spectrum. c) J-V curves of representative PF2:ITIC OPVs showing typical device performance under solar simulator (100mW.cm^{-2}); d) In the dark in semi-logarithm scale.

Table 23. Photovoltaic parameters of the corresponding devices under solar simulator (100mW.cm^{-2}). The active layer is around 0.18cm². Average J_{SC} and PCE are given in brackets. The average parameters were calculated from 6 cells, and the error estimate was calculated as the standard deviation of these 6 cells. * J_{SC} EQE is calculated using EQE;

Solvent	V_{OC} (V)	J_{SC} ($J_{SC\ ave}$) (mA.cm^{-2})	J_{SC}^{EQE} (mA.cm^{-2})	FF (%)	PCE (PCE$_{ave}$) (%)	R_S (Ω.cm²)	R_{SH} (Ω.cm²)
CB	**0.83**	**9.0 (9.1±0.3)**	**9.7**	**55.4**	**4.1 (4.0±0.1)**	**30**	**4700**
CF	0.80	8.9 (7.8±1.1)	9.3	33.8	2.4 (2.0±0.4)	140	1200
O-DCB	0.88	6.9 (6.7±0.2)	6.6	49.1	3.0 (2.7±0.4)	20	4500

Under standard AM 1.5G conditions, the highest PCE achieved with the CB-processed PF2:ITIC is 4.1%, with minimal dispersion across the six devices tested. In contrast, the highest PCEs achieved with CF and o-DCB are significantly lower, at 2.4% and 3.0%, respectively. They also show greater variability, as seen from the box plots of Figure 78a. This performance disparity is closely related to the differences in the morphology and nanoscale structure of the active layers processed with these solvents, as well as their corresponding PV parameters, summarized in Table 23. The improved performance for CB-processed devices can be attributed to the smooth and homogeneous morphology of the active layer, as indicated by the SEM and AFM analyses discussed earlier. This uniform morphology likely enhances charge

transport and minimizes recombination losses, resulting in a stronger J_{SC} (9.0 mA.cm^{-2}) and FF of 55.4% for the CB-treated devices compared to those processed with other solvents. The lower R_S of 30 Ω.cm² observed in the CB-treated device supports the hypothesis of improved charge transport, as lower R_S facilitates more efficient charge extraction from the electrode. Furthermore, the higher R_{SH} of 4700 Ω.cm² in the CB-treated device indicates reduced recombination losses, which are critical for efficient charge collection and contribute to the overall efficiency of the device. The J_{SC} values for the CB- and CF-processed devices are similar and significantly higher than those for o-DCB, which are consistent with the J_{SC} values calculated from the EQE data (Figure 78b). The close agreement between the measured J_{SC} and the EQE-derived J_{SC} values confirms the reliability of the J-V measurements. In addition, the CB-processed PF2: ITIC devices show a slightly higher V_{OC} of 0.83V compared to our reference system PM6:Y6, which has a V_{OC} of 0.80V.

In the dark (Figure 78d), the current density behavior primarily reflects the diode characteristics of the solar cell, as there is no photogenerated current[191]. The current density at low forward bias (near 0V) is indicative of leakage, and we note that the CB- and CF- processed devices exhibit much less leakage than the o-DCB device. The slope of the current density – voltage curve in the reverse bias region reflects $R_{SH,}$ and in the high forward bias region, it reflects R_s. PF2:ITIC devices processed with CB offer the most favorable electrical properties, with high R_{SH} and low R_s, resulting in minimal leakage currents and efficient charge transport. In contrast, CF and o-DCB processed devices exhibit higher leakage currents and increased R_s, probably due to suboptimal film morphologies.

As OPVs are considered future indoor energy resources, the photovoltaic operation of the PF2:ITIC OPVs using three different solvents was measured under low-intensity artificial indoor lighting from a warm LED at 1000 lux. The rationale for using warm LEDs instead of cool LEDs is their spectral compatibility with PF2. Although PF2 exhibits strong absorption in the visible region, its absorption in the blue region is still not ideal. The emission spectrum of warm LEDs is more consistent with the absorption characteristics of PF2, thus optimizing the performance of the device under indoor conditions.

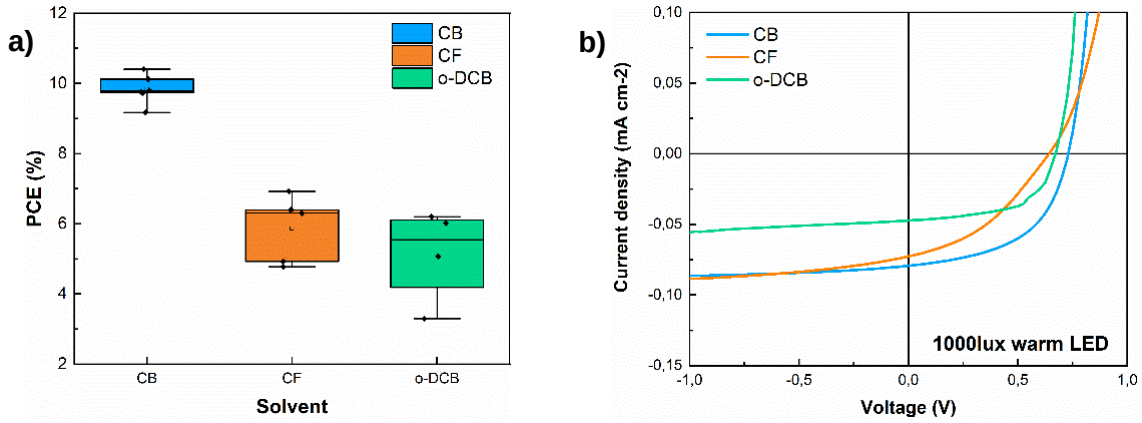

Figure 79. a) Dispersion of PCE of six PF2:ITIC OPVs processed with CB, CF, and o-DCB under 1000 lux warm LED illumination. b) J-V curves of representative PF2:ITIC OPVs showing device performance under 1000 lux warm LED illumination.

Table 24. PV Parameters of the Corresponding Devices under 1000 lux warm LED Illumination.

Solvent	V_{OC} (V)	J_{SC} ($\mu A.cm^{-2}$)	J_{SC}^{EQE} ($\mu A.cm^{-2}$)	FF (%)	PCE (PCE_{ave}) (%)	R_S ($\Omega.cm^2$)	R_{SH} ($\Omega.cm^2$)
CB	0.73	76.3	71.2	56.6	**10.7 (10.0±0.5)**	$8x10^2$	**$6x10^5$**
CF	0.64	72.7	65.7	38.5	6.4 (5.9±1.0)	$2x10^4$	$2x10^5$
O-DCB	0.68	47.3	46.8	58.8	6.0 (5.2±1.3)	$4x10^2$	$3x10^5$

Figure 79 and Table 24 show the J-V characteristics of the three devices made with different solvents under 1000 lux warm LED. Similar to the results under standard AM 1.5G conditions, the highest PCE of 10.7% is achieved with CB, outperforming the CF and o-DCB-based devices, which have PCEs of 6.4% and 6.0%, respectively. The V_{OC} and J_{SC} for CB were higher than those for CF and o-DCB, mirroring the trend observed under AM 1.5G illumination. To ensure the reliability of the indoor photovoltaic characteristics, we calculated the theoretical J_{SC} by integrating the EQE spectra of each device (Figure 78) and the irradiance spectrum of a warm LED at 1000 lux. The calculated J_{SC} values were 71.2 , 65.7, and 46.8 $\mu A.cm^{-2}$ for CB, CF, and o-DCB, respectively, which were in agreement with the measured J_{SC} values within the measurement error ranges. In terms of R_S and R_{SH}, under indoor conditions, the photocurrent is inherently low, and the impact of R_S on performance is reduced. However, R_{SH} becomes more critical because leakage current has a proportionally larger impact on efficiency in low-light environments. For the CB-processed device, R_S is relatively low (800 $\Omega.cm^2$), supporting efficient charge extraction, while R_{SH} is significantly higher than that of CF and o-DCB ($6x10^5$ $\Omega.cm^2$). This high R_{SH} value indicates reduced recombination and leakage currents, which is critical to maintaining high performance under indoor lighting.

IV.3. Optimization of the ratio of PF2:ITIC

In addition to optimizing solvent selection and active layer thickness, fine-tuning the D:A ratio in the active layer is another critical factor in improving the performance of OPV devices. The D:A ratio directly influences the morphology, including the size and the donor and acceptor domains, the phase separation, and the charge transport dynamics within the BHJ, which are the critical determinants of the PCE. In this study, we systematically varied the D:A ratio of PF2:ITIC blends to identify the optimal composition that maximizes device performance. The following D:A ratios were explored: 1:1 and 1:1.5. Each blend was prepared under identical processing conditions to ensure that any observed differences in device performance were solely due to changes in the D:A ratio.

To prepare the blends, PF2 and ITIC were weighed in appropriate proportions and dissolved in CB, following the same procedures as in the solvent and thickness optimization experiments. The solutions were then stirred at 80°C for 24 h to ensure complete dissolution and homogeneity, providing uniform films in each case with a target thickness of around 100 nm.

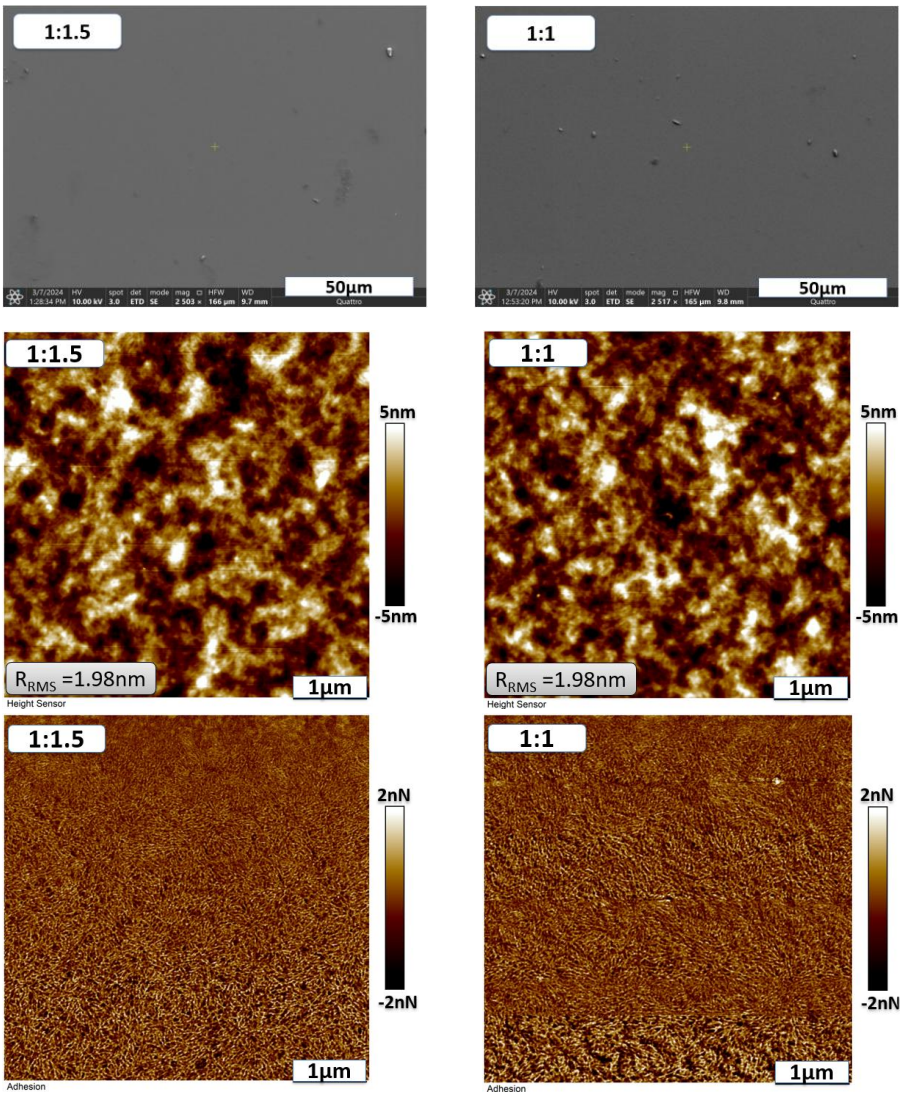

Figure 80. SEM images (top row), AFM height images (middle row), and AFM adhesion images (bottom row) of PF2:ITIC blend films with two different D:A ratios.

Figure 80 presents a comparative analysis of the surface morphology of PF2:ITIC blend films at two different D:A ratios, 1:1.5 and 1:1, using both SEM and AFM imaging techniques. Both of these show that the 1:1.5 and 1:1 blend films have similar smoothness, uniformity, and nanoscale domain structures.

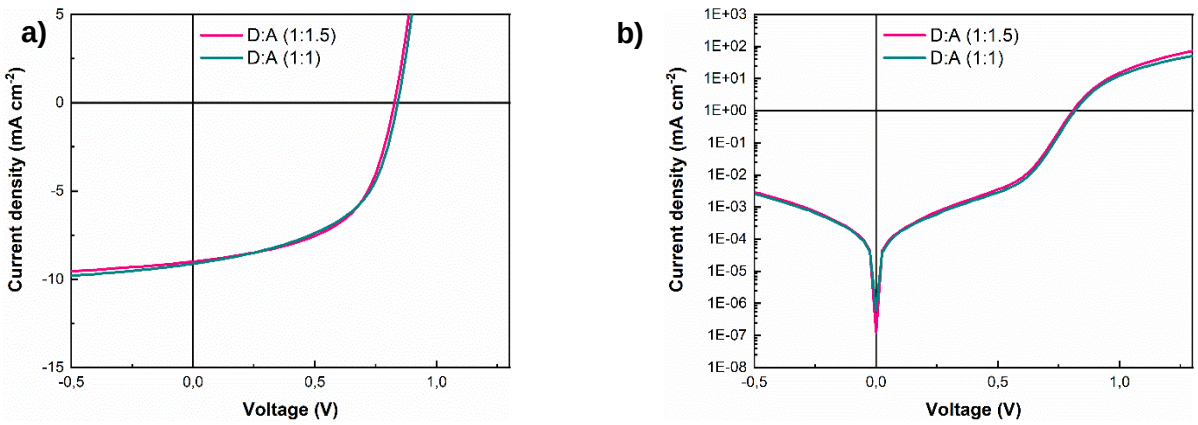

Figure 81. J-V curves of solar cells based on PF2:ITIC with different D:A ratios a) under AM 1.5G and b) in the dark.

Table 25. PV performance of PF2:ITIC OPVs fabricated with two different D:A ratios under both AM 1.5G and indoor warm LED (1000 lux) illumination conditions.

D:A	Light source	V_{OC} (V)	J_{SC}	FF (%)	PCE (%)	R_S ($\Omega.cm^2$)	R_{SH} ($\Omega.cm^2$)
1:1.5	1 sun AM 1.5G	0.83	9.0 ($mA.cm^{-2}$)	55.4	4.1 (4.0±0.2)	30	$5x10^3$
	Warm LED 1000 lux	0.73	76 ($\mu A.cm^{-2}$)	56.6	**10.7 (10.0±0.5)**	800	$6x10^5$
1:1	1 sun AM 1.5G	0.83	9.1 ($mA.cm^{-2}$)	51.9	4.0 (3.9±0.1)	30	$3x10^3$
	Warm LED 1000 lux	0.73	79 ($\mu A.cm^{-2}$)	52.5	10.4 (9.7±0.4)	600	$4x10^5$

CB was used as a solvent to prepare the solutions at both ratios, and the films were processed to achieve a uniform thickness of 100 nm to ensure sample consistency. From Table 25 and Figure 81, the comparison of these two D:A ratio shows that while the overall performance under AM 1.5G illumination is similar for both ratios, the 1:1.5 ratio exhibits slightly better performance under indoor conditions, as evidenced by the higher FF and PCE. The slight variations in R_S and R_{SH} between the two ratios suggest differences in film morphology and charge transport dynamics that are more pronounced under low light conditions. The consistent V_{OC} across both ratios and light conditions indicates that the energy alignment between donor and acceptor remains optimal regardless of the mixing ratio. This suggests that while the D:A ratio can influence the detailed balance of charge transport and recombination, both ratios are well suited for use in PF2:ITIC OPVs under varying illumination conditions.

IV.4. Optimization of active layer thickness

The thickness of the active layer directly affects the critical balance between light absorption and charge transport, both of which are essential for achieving high efficiency, especially at low light levels. In organic semiconductors, the exciton diffusion length (the distance an exciton can travel before recombination) mainly affects the size of the donor-acceptor (D/A) domains. Smaller domain sizes favor efficient dissociation of excitons into free charges at the donor-acceptor interface. However, the overall thickness of the active layer is usually limited by the diffusion length of free carriers. The mobility of free carriers, carrier concentration, and the properties of the bicontinuous network structure are key factors that determine how effectively the charge is transported to the electrodes. In conventional OSCs, the active layer is usually limited to around 100 nm due to the moderate mobility of free carriers, which limits the charge extraction efficiency at larger thicknesses. More continuous nanostructured pathways in the D/A network enable efficient charge transport even at larger thicknesses. In theory, if the carrier mobility is significantly higher, then thicker active layers with nanoscale D/A domains could maintain efficient exciton dissociation and charge transport, thereby achieving higher absorption without compromising efficiency[29,30,120].

To gain further insight into the bland properties, we performed electrical characterization of hole-only devices based on the PF2:ITIC blend, using SCLC measurements for a 100 nm active layer using a hole-selective device structure: ITO/PEDOT:PSS (40 nm)/active layer/MoO_3/Ag, as depicted in Figure 82 and Table 26.

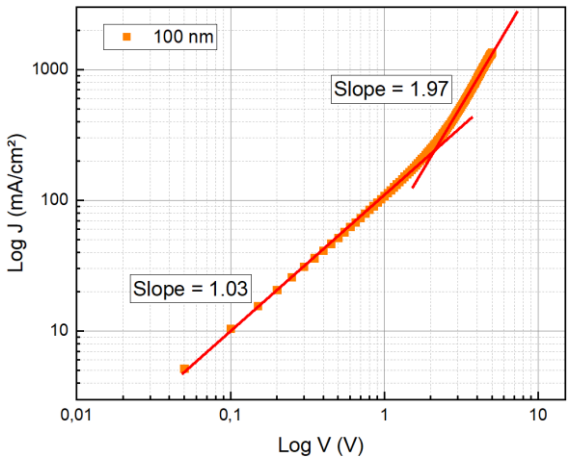

Figure 82. SCLC J-V characteristic of PF2:ITIC (1:1.5) blend film (100 nm thick) processed in CB to determine the hole mobility (μ_h^{SCLC}).

Table 26. μ_h^{SCLC} in various PF2-based blends with different acceptors and active layer thickness, derived from SCLC measurements.

Active layer	Thickness (nm)	μ_h^{SCLC}(cm2/V.s)	Ref
PF2:ITIC (1:1.5)	100	(1.5±0.2)x10^{-4}	this study
PF2:Y6(1:1.5)	100	6.2×10^{-4}	[11]
PF2:PC$_{71}$BM (1:1.5)	265±5	(3.2 ± 0.4)x10^{-3}	[10]

In the Figure 82, the clear SCLC regime has a slope of 1.96 close to 2, indicating a trap-free transport process. This pure SCLC behavior, where $J \propto V^2$, means that the PF2:ITIC system has minimal trap states within the active layer, enabling efficient hole transport without significant recombination losses due to traps. The absence of a trap-filled limited regions confirms that the charge transport is dominated by the space-charge effect rather than trap-assisted processes. This high hole mobility of (1.49±0.18)x10^{-4} cm2/V.s supports the potential for thicker active layers as the charge carriers can move efficiently without being hindered by traps. Furthermore, PF2 blended with PC$_{71}$BM exhibits good mobility at a thickness of 265±5 nm, a property that allows the active layer thickness to be extended beyond the traditional 100 nm limit[10,192]. In the PF2:ITIC system, increasing the active layer thickness enhances photon absorption without compromising charge transport efficiency, thereby generating more charge carriers. This property is particularly advantageous for IPV applications, as indoor light intensity is significantly lower than outdoor conditions, and a thicker active layer can improve device efficiency by absorbing more light[119,124].

To explore the benefits of increased active layer thickness, we attempted to produce PF2:ITIC films with a thickness of several hundreds of nanometers. Considering the range of our experimental parameters (associated with solution concentration, range of viscosity, and range of rotation of the spin-coater), we were able to achieve thicknesses around 270 nm. In this case, the same PF2:ITIC blend solution based on the CB solvent was used as in the previous experiments. The blend solution was prepared with a D:A ratio of 1:1.5 with a total concentration of 17.5 mg/mL (7 mg PF2 and 10.5 mg ITIC dissolved in 1 mL CB). The solution was stirred at 80°C for 24 hours to ensure complete dissolution and homogeneity. We modified

the spin-coating parameters to obtain a uniform and thick active layer. However, when spin-coating with viscous, high-boiling point solvents at very low spin speeds, the process can become challenging as the center of the substrate often dries faster than the edges of the substrate. To overcome this problem, we used a three-step spin-coating program combined with a dynamic dispense, as used in Ref. 10. The deposition parameters are given in Table 27 below:

Table 27. Spin-coating parameters for deposition of a thick PF2:ITIC active layer.

Step	Speed (RPM)	Acceleration (RPM/S)	Time (S)
Step 1	600	600	20
Step 2	900	600	40
Step 3	2000	600	120

In the first and second steps, the spin speed was kept low to allow the film to thicken and dry evenly. This slow spin allows the viscous solution to spread evenly over the substrate. In the final step, a higher spin speed was used to remove excess solution from the edges and ensure a smooth, uniform film over the entire substrate.

We then examined the morphology of the PF2:ITIC blend films at two different thicknesses (100 nm and 270 nm) using SEM and AFM to understand how the increased thickness affects the micro- and nano-morphology of the films, as shown in Figure 83 below:

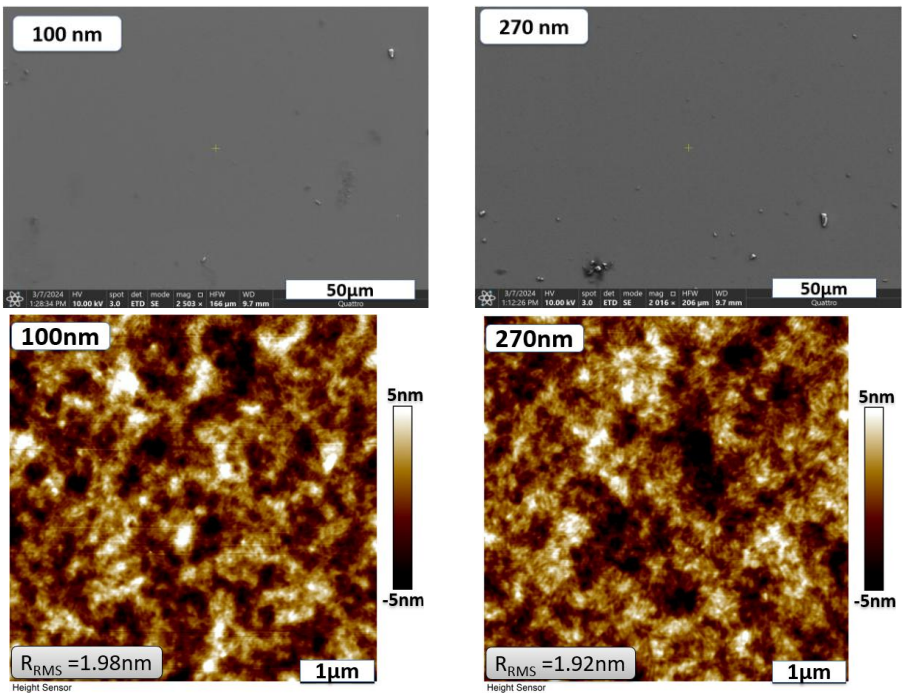

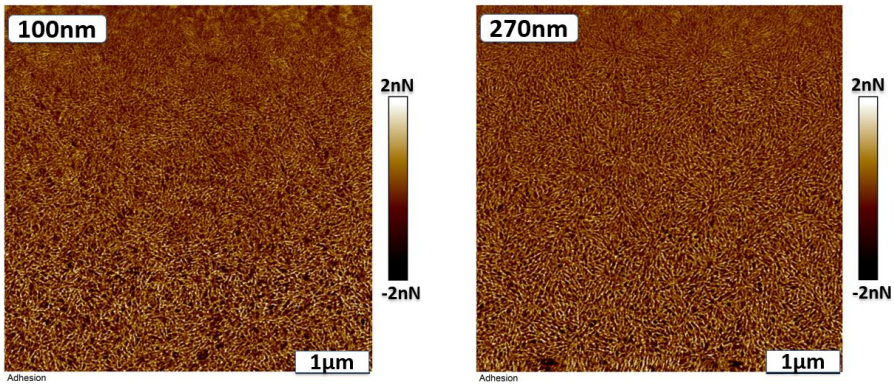

Figure 83. SEM images (top row), AFM height images (middle row), and AFM adhesion images (bottom row) of PF2:ITIC blend films with thicknesses of 100 nm and 270 nm.

SEM analysis shows that the CB-processed films have smooth, homogeneous, and uniform surfaces regardless of thickness. Both the 100 nm and 270 nm films are free of significant defects or irregularities, with only minimal aggregates observed on the surface, indicating that the thicker film retains the high-quality morphology seen in the thinner film.

AFM height images provide further insight into the surface topography, with the RMS roughness values being very similar for both thicknesses. The 100 nm film has an RMS roughness of 1.98 nm, while the 270 nm film has a slightly lower RMS roughness of 1.92 nm. This similarity in roughness indicates that increasing thickness does not adversely affect the surface smoothness of the film, suggesting that the film deposition process remains well controlled even at greater thicknesses. In addition, AFM adhesion images show that both films have an interpenetrating network structure. This consistent network structure over different thicknesses suggests that the PF2:ITIC blend forms a stable morphology that supports the effective operation of OSCs even as the active layer thickness is increased.

In order to fully assess the influence of the active layer thickness on the performance of PF2:ITIC OSCs, we carried out a detailed analysis of the EQE and J-V measurements (Figure 84).

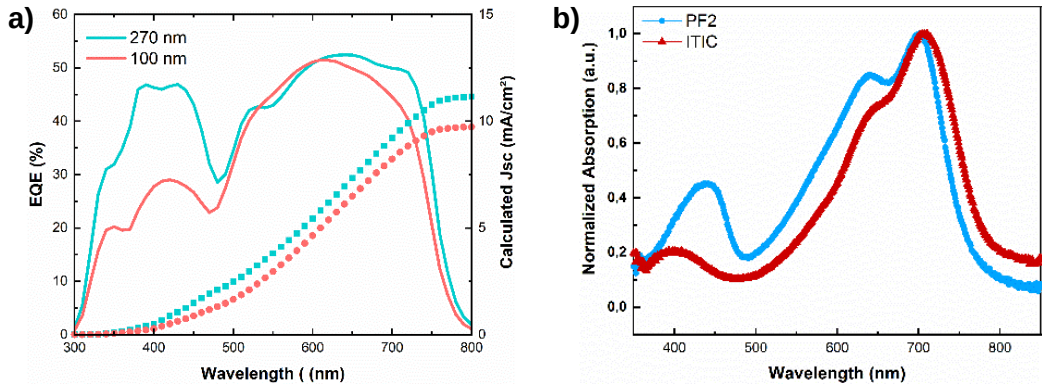

Figure 84. a) EQE spectra of PF2:ITIC with thickness of 100 nm and 270 nm. b). Normalized absorption spectra of PF2 and ITIC neat film.

As previously discussed, both PF2 and ITIC materials exhibit efficient light harvesting in the 500-700 nm region, where a 100 nm thick active layer is sufficient for optimal absorption and charge generation. However, in the blue region (400-500 nm), light harvesting is comparatively lower, and a 100 nm layer is insufficient. Notably, PF2 demonstrates superior light-harvesting properties in the blue region compared to ITIC. To address this, we increased the active layer

thickness to 270 nm with the goal of enhancing light absorption in the blue region and consequently boosting carrier generation. This trend is confirmed by the EQE measurements (Figure 84a). For the 100 nm thick active layer, the EQE is relatively high in the 500 to 700 nm region, consistent with the absorption characteristics of PF2 and ITIC. However, the EQE is lower in the 400 to 500 nm region, indicating that the thinner layer does not fully capture and utilize the available photons in the blue region.

In contrast, the 270 nm thick active layer shows a significant increase in EQE in the 400 to 500 nm region. This improvement is directly related to the increased light absorption resulting from the increased thickness, which allows more photons to be absorbed and converted into charge carriers. Consequently, the thicker active layer results in improved performance in the blue region, making it more effective in indoor lighting conditions where the spectrum often contains a significant blue component.

The PV performance of PF2:ITIC OPV devices has been systematically investigated by varying the active layer thickness and evaluating their efficiency under standard AM 1.5G illumination and in the dark, as shown in Figure 85 and Table 28 below:

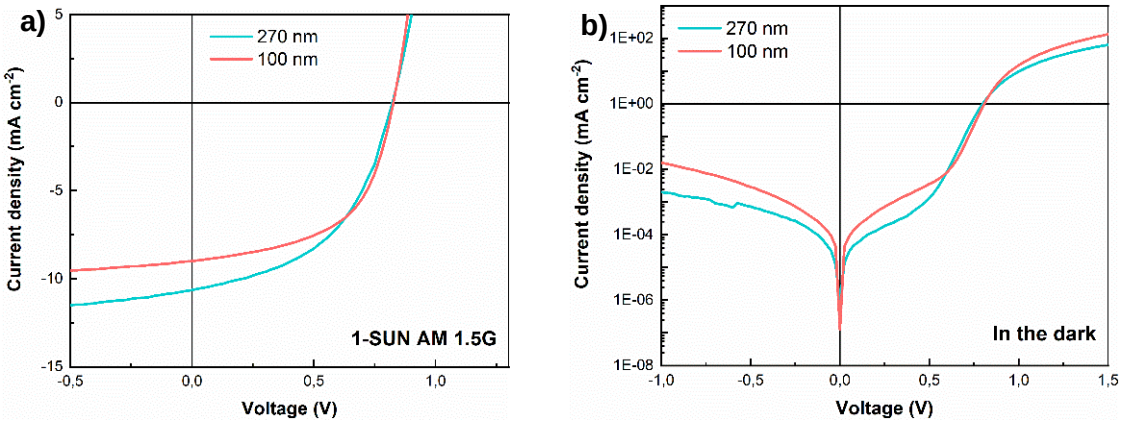

Figure 85. The corresponding J-V curves of solar cells based on PF2:ITIC with different thicknesses a) under solar simulator (100mW.cm^{-2}); b) In the dark.

Table 28. PV performance parameters of PF2:ITIC OPVs with different thicknesses under solar simulator (100mW.cm^{-2}).

Thickness	V_{OC} (V)	J_{SC} (mA.cm^{-2})	J_{SC}^{EQE} (mA.cm^{-2})	FF (%)	PCE_{MAX} (%)	R_S (Ω.cm^2)	R_{SH} (Ω.cm^2)
100 nm	0.82	9.4 (9.1±0.3)	9.7	54±2	4.1 (4.0±0.1)	30±2	3400±1460
270 nm	0.82	10.7 (10.6±0.1)	11.1	48±2	4.3 (4.1±0.2)	50±5	2620±270

Table 28 presents the PV performance parameters of PF2:ITIC with 100 nm and 270 nm, measured under a solar simulator (100 mW.cm^{-2} AM 1.5G). It can be seen that both devices have an identical V_{OC} of 0.82V; the variation of the PF2:ITIC layer does not affect the V_{OC} of the devices. This consistency suggests that the energy level alignment between the PF2 and ITIC remains stable, regardless of the thickness of the active layer. It also indicates that thicker layers (up to 270 nm) do not drastically increase charge recombination. The J_{SC} for the 270 nm thick device is higher at 10.7 mA.cm^{-2} compared to 9.4 mA.cm^{-2} for the 100 nm thick device. This increase is consistent with the EQE data, which shows enhanced light absorption and charge generation in the thicker device, particularly in the blue region (400-500 nm). We

calculated J_{SC} values based on the EQE spectra (Figure 84a) to support these measurements, indicating reliable data.

Conversely the FF decreased from 54% for the 100 nm devices to 48% for the 270 nm devices. This reduction in FF can be attributed to the increased Rs and decreased R_{SH} in the ticker device, which may be due to the increased recombination current of the photogenerated charges. The lower R_{SH} is unexpected as it does not typically decrease with thickness alone, suggesting that thicker active layers may promote more recombination pathways. Despite the decrease in FF, the overall PCE of the 270 nm device (4.3%) is slightly higher than that of the 100 nm device (4.1%), primarily due to an approximate 14% increase in J_{SC} under AM 1.5G illumination. This increase in PCE is consistent with the increased light absorption and carrier generation in the thicker device, as reflected in the EQE measurements. Figure 85b shows the dark J-V curve. The 100 nm devices have lower leakage currents, which is consistent with the observed higher FF.

We then analyzed the PV performance of PF2:ITIC with different thicknesses under 1000 lux warm LED illumination. The corresponding J-V characteristics under these indoor conditions are presented in Figure 86 and Table 29.

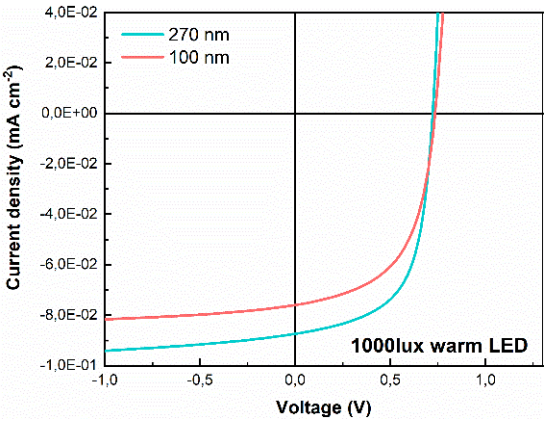

Figure 86. J-V curves of solar cells based on PF2:ITIC with different thicknesses under 1000 lux warn LED.

Table 29. PV performance of PF2:ITIC OPVS with different thicknesses under 1000 lux warm LED.

Thickness	V_{OC} (V)	J_{SC} (μA.cm^{-2})	FF (%)	PCE_{MAX} (%)	R_S (Ω.cm^2)	R_{SH} (Ω.cm^2)
100 nm	0.70	73.3±3.0	61±3	10.7 (10.0±0.5)	650±250	(6.2 ±1.3)x10^5
270 nm	0.72	86.6±2.1	59±2	**12.0 (11.6±0.2)**	810±140	(6.0 ±1.3) x10^5

We observed a significant improvement in the J_{SC} of the 270 nm thick device, which recorded a J_{SC} of 86.6 μA cm^{-2}, compared to 73.3 μA cm^{-2} for the 100 nm device. This increase is consistent with the previously discussed EQE measurements, where the thicker active layer showed increased light absorption, particularly in the blue region (400-500 nm), leading to more efficient charge carrier generation under indoor lighting conditions. The FF of both devices is relatively stable, and as we discussed earlier, under indoor lighting, lower photocurrent reduces the impact of R_S on performance. However, R_{SH} becomes more critical at low light levels, as minimizing leakage current is essential to achieve high efficiency. The thicker 270 nm device achieves the highest PCE of 12.0%, outperforming the 100 nm device,

which has a PCE of 10.7%, primarily due to an approximate 18% increase in J_{SC} under warm LED illumination. These results demonstrate that increasing the active layer thickness to 270 nm significantly enhances the performance of PF2:ITIC OPVs under indoor lighting conditions, especially in the blue region. The improved J_{SC} and PCE, combined with the stable FF, highlight the potential of optimizing active layer thickness to achieve higher efficiencies in low-light environments, making these OPVs more effective for indoor applications.

In addition, the PF2:ITIC device achieves a higher V_{OC} (0.83 V), making it ideal for indoor applications. This is an improvement over reference systems such as PM6:Y6 (as described in Chapter III.1.), which has a V_{OC} of 0.8 V in outdoor conditions and also offers an advantage under 1000 lux warm LED lighting, where PF2:ITIC produces a V_{OC} of 0.72 V compared to 0.60 V for PM6:Y6. The combination of high V_{OC}, strong absorption in the blue region, and improved J_{SC} and PCE in the PF2:ITIC device highlights the potential of PF2 as a donor material for indoor OPVs.

Next, we analyzed the performance of PF2:ITIC OPV devices with different active layer thicknesses under warm indoor LED illumination, ranging from 200 lux to 1000 lux.

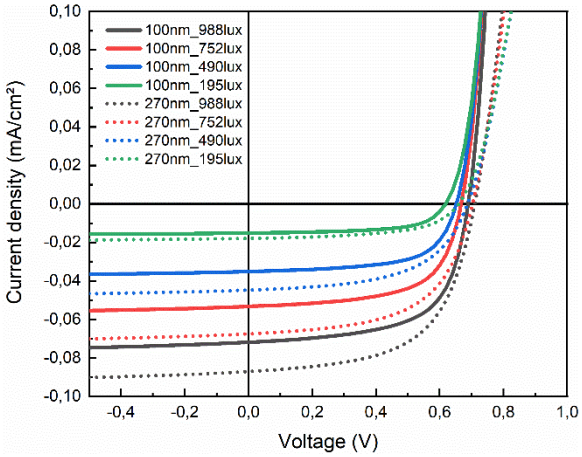

Figure 87. The corresponding J-V curves of PF2:ITIC with different thicknesses under indoor illumination from 200 to 1000 lux at warn LED.

Table 30. PV performance of PF2:ITIC with different thicknesses under indoor illumination from 200 to 1000 lux at warm LED.

Thickness	Warm led (lux)	V_{OC} (V)	J_{SC} ($\mu A.cm^{-2}$)	FF (%)	PCE_{MAX} (%)
100 nm	200	0.62	15.1	62.5	9.7
	500	0.66	35.1	62.3	9.5
	750	0.66	53.2	63.0	9.5
	1000	0.68	71.9	63.6	10.0
270 nm	200	0.66	17.9	57.4	11.2
	500	0.68	44.8	56.3	11.3
	750	0.70	67.4	57.8	11.7
	1000	0.72	87.0	59.5	11.7

The results demonstrate that a thicker active layer of 270 nm in PF2:ITIC OPVs significantly improves performance under warm LED lighting over a range of illuminances from 200 lux to 1000 lux. The improvement in J_{SC} and PCE is particularly notable, affirming the potential of thicker active layers in optimizing OPV devices for low-light indoor environments.

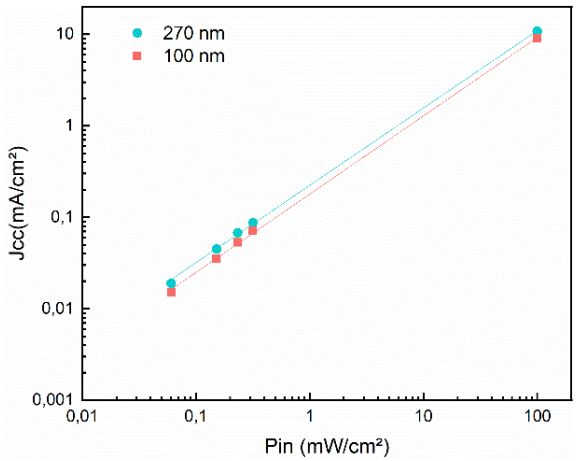

Figure 88. Relationship between the J_{SC} and the Pin for different thicknesses of the active layer (100 nm and 270 nm).

Figure 88 shows the relationship between the J_{SC} and the incident light power density (Pin) for organic solar cells with different active layer thicknesses (100 nm and 270 nm). The data points for each thickness are plotted on a log-log scale to observe the behavior of the devices over a wide range of light intensities. It shows an almost linear relationship between J_{SC} and P_{in} over the whole range of light intensities for both thicknesses. This linearity suggests that the charge generation and extraction processes in the PF2:ITIC blend are efficient and that there are minimal losses due to recombination, even at low light intensities. Given the modest slope, the dominant recombination mechanism appears to be trap-assisted recombination, which may result in some charge loss but is relatively controllable in this system. This characteristic makes the PF2:ITIC blend particularly suitable for indoor photovoltaic applications. Additionally, the 270 nm film shows slightly higher J_{SC} values across all light intensities, which is consistent with the idea that a thicker active layer can absorb more light and thus generate more charge carriers.

IV.5. Conclusion

In this study, we have carried out a detailed investigation of the performance of a new OPV active layer system based on PF2:ITIC for indoor applications, considering the particular ability of the PF3 polymer to harvest blue photons. We focused our study on the influence of solvent selection, active layer thickness, and D:A ratio on the device efficiency. Our results have provided valuable insights into the optimization strategies required to improve the performance of OPVs, particularly for indoor applications.

Our experiments identified CB as the most effective solvent for processing the PF2:ITIC blend, resulting in a smooth and homogeneous active layer morphology. Through systematic optimization, we found that increasing the active layer thickness from 100 nm to 270 nm significantly improved light absorption in the blue region (400-500 nm), which is critical for indoor environments dominated by artificial light sources. This improvement in light absorption translated directly into a higher photocurrent, enabling us to achieve an impressive PCE of 12.0% under warm LED illumination at 1000 lux. Moreover, this optimal thickness not only improves light absorption and charge generation but also demonstrates the robustness of the PF2:ITIC system to layer thickness variations, which is an advantage for scalable manufacturing techniques such as roll-to-roll printing.

Furthermore, the PF2:ITIC system exhibits a high V_{OC} of 0.72 V under 1000 lux warm LED, outperforming commonly used systems such as PM6:Y6, which typically have a V_{OC} of around 0.60 V under the same conditions. This high V_{OC}, coupled with strong absorption in the blue region, highlights the potential of PF2 as a donor material for next-generation indoor photovoltaic devices.

Overall, this study highlights the importance of optimizing material properties and processing conditions to develop high-performance OPVs tailored for indoor environments. The identification of PF2 as a highly effective donor material, capable of efficient light absorption in the blue region and achieving a high V_{OC}, represents a significant advancement towards the development of OPVs that can effectively harness indoor light for energy generation.

Chapter V. Luminescence down-shifting molecules for UV protection of OSCs

Recent advancements in OSCs have led to remarkable improvements in outdoor PCE, with current records surpassing 19% under standard 1-sun conditions. This makes OSCs a promising candidate for low-cost, flexible, and lightweight solar power generation. However, device stability remains a significant challenge, limiting the commercialization and widespread adoption of OSC technology, especially when OSCs are exposed to harsh outdoor environments. These stability issues have attracted extensive research attention, leading to a substantial increase in publications on OSC stability in recent years[193-195]. In 2019, Brabec et al. demonstrated a NFA-based OSC with an estimated lifetime of nearly 10 years[196]. Another study showed that polymer solar cells made of PCDTBT and $PC_{71}BM$ have an extrapolated lifetime of nearly 15 years when operated in an environment with oxygen and water content below 0.1 ppm, highlighting the long-life potential of OSCs[41]. Despite these advances, environmental stressors such as temperature fluctuations[197], humidity[198], and UV radiation[199,200] still pose significant challenges to OSC stability. In particular, UV radiation is extremely harmful due to its high energy, which can trigger photo-oxidation reactions of the organic materials in the active and interfacial layers, leading to molecular degradation and shortening the lifetime of OPV devices. UV irradiation induces multiple degradation pathways in OSCs, including photooxidation of donor and acceptor materials (e.g., fullerene derivatives or NFAs) and scission of polymer chains in conjugated polymers, which together degrade the optical and electrical properties of the devices, thereby reducing the efficiency and stability of the device[200,201]. For example, in PM6:Y6 OSCs, studies using long-pass filters during the aging process have shown that UV and near-UV photons are primarily responsible for the photochemical decomposition of the Y-series acceptors, which is considered to be a key factor in early performance loss[202,203]. When aged without a UV filter, the PM6:Y6 OPV showed a substantial 44% drop in PCE over 200 h of testing, with an 8% drop in V_{OC}, a 28% drop in FF, and a 19% drop in J_{SC}. In contrast, devices aged using 420 nm and 500 nm long-pass filters lost less than 7% of their PCE over the same period, highlighting the effectiveness of UV protection in minimizing photodegradation and maintaining OSC performance[202].

To enable OSCs to be used in long-term outdoor applications, it is possible to integrate UV protection strategies that can prevent or mitigate the damaging effects of UV radiation. An effective way to improve OSC stability is to use UV-cut filters (UCFs) that block harmful UV rays. Jeong et al. showed that adding a UCF that blocks wavelengths below 403 nm significantly slowed the degradation of OSCs, after 14 hours of continuous illumination (AM 1.5G, 80 mW/cm²), the PTB7-Th:$PC_{71}BM$ OPV devices with the filter retained about 90% of its initial efficiency, compared with only 20% for the device without the filter[204]. Although UCFs can protect OSCs from UV damage, they are costly and reduce the sunlight available for conversion, limiting overall efficiency. Another promising strategy to address this problem is to use materials promoting luminescence down-shifting (LDS), which absorb high-energy UV photons and re-emit them as lower-energy photons in the visible range, thus reducing the risk of UV-induced degradation in the active layer and allowing the harvesting of the converted photons by the active layer of the device. In order for an LDS to be effective, certain performance criteria must be met. LDS materials should have a high photoluminescence efficiency (PLQY) to ensure that a significant fraction of absorbed UV photons is re-emitted as usable light. Furthermore, a large Stokes shift is desirable to minimize self-absorption energy losses by separating the absorption and emission spectra, thereby allowing more emitted photons to reach the active layer without being reabsorbed by the LDS layer itself. In terms of

spectral properties, LDS materials should have strong absorption in the UV range (300-400 nm) and emit in the visible spectrum (400-700 nm) to ensure overlap with the absorption curve of the OSC active layer[205]. Ideally, the emission peak of the LDS material should coincide with the maximum absorption wavelength of the active material (e.g., PM6:Y6, which has a peak absorption in the visible range between 550-650 nm) to maximize the conversion of re-emitted photons into photocurrent. In addition, LDS materials should possess strong photochemical and environmental stability to ensure long-term performance under practical conditions.

In recent years, LDS materials have been widely studied and applied in photovoltaics to improve PCE and enhance stability under UV exposure. There are a variety of LDS materials to choose from, including quantum dots (QDs)[206], oxides, organic dyes[207], and luminescent glasses. Among them, organic dyes are a particularly promising class of materials due to their high absorption efficiency and PLQY, as well as their wide availability and low cost compared to alternatives such as europium complexes(Eu)[208], QDs, and nanophosphors[209]. Fernandes et al. introduced three organic dyes, coumarin 7 (C7), coumarin 153 (C153), and Kramer's blue (KB), and demonstrated their potential as LDS materials with absorption spectra below 450 nm and photoluminescence emissions within the absorption range of the P3HT:PCBM active layer[207]. Mixed in a polymethyl methacrylate (PMMA) matrix, their respective PLQYs were 37.4%, 20.2%, and 9.2%, respectively. The PLQYs of these dyes were significantly improved when the two dyes were mixed in different ratios, especially the PLQY of the KB:C153 mixture reached 88.0%, which is much higher than that of either dye alone. After experimental optimization, the KB:C153 LDS layer improved the photocurrent density of P3HT:PCBM solar cells by 20%, highlighting the advantages of optimized LDS materials in enhancing OSC performance.

My research builds on previous studies by my group on the yellow-emitting tetrazine molecule, NITZ molecules, as a DSL material for UV protection in organic and perovskite solar cells. In 2017, Ourahmoun et al. from our group introduced NITZ as a DSL for P3HT:PCBM OSCs, using polystyrene (PS) as the matrix[13]. In this setup, a NITZ-coated glass substrate is placed on the OSC to absorb UV light and re-emit it as visible light. At the optimized 2% concentration, NITZ exhibited strong UV absorption and visible emission with a PLQY of 30%. The OSC with the NITZ layer reached a PCE of 3.28%, compared to 3.08% in the control device. Furthermore, the NITZ layer extended the lifetime of the device, probably by reducing UV degradation. In 2018, Gheno et al. applied NITZ to perovskite solar cells that are particularly sensitive to ultraviolet light[205]. This study showed that the down-conversion properties of NITZ effectively reduce the effects of UV light by converting UV photons into visible light that can be utilized by the active layer. The PLQY of the NITZ:PS layer is 30%, which can reduce the J_{SC} losses caused by using conventional UV filters, even though no net gain in photocurrent is achieved in this case. The study also explored the theoretical effectiveness of LDS materials for different active materials and considered the potential to further improve stability using alternative electron transport layers such as WO_3, which could interact with UV light and degrade performance.

During my thesis, in addition to optimizing OSCs for indoor applications, we also worked with Prof. Pierre Audebert's organic molecules on a project involving LDS materials, extending previous research. The project focused on the use of tetrazine-based NITZ molecules as LDS materials dissolved in hemicellulose xylan films to provide UV protection for OSCs (Figure 89).

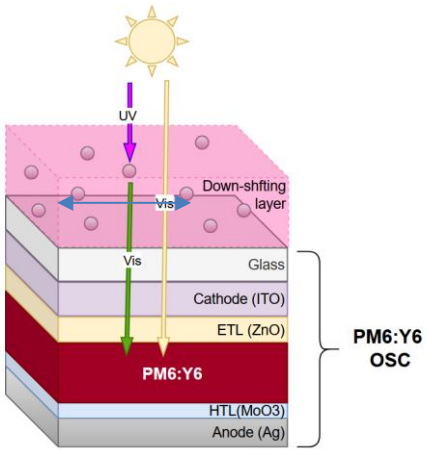

Figure 89. Schematic diagram of PM6:Y6 OSC structure with NITZ-based DSL.

Hemicellulose xylan is a natural polymer matrix derived from biomass that can serve as a sustainable alternative to synthetic polymers such as PMMA or PS, which is commonly used in LDS applications. As a biomimetic material, xylan can not only form a stable film for integrating LDS molecules but also meet sustainable development goals due to its biodegradability and renewable nature. The use of xylan as a matrix material highlights the potential for incorporating environmentally friendly bio-based materials in solar technology, with the advantages of recyclability and reduced environmental impact. This study is a collaboration between three teams: XLIM, PPSM, and the LABCiS laboratory in Limoges. The xylan films used in this study were synthesized by Marine Petitjean, a PhD student at LABCiS, under the supervision of Vincent Chaleix. The NITZ fluorophore embedded in the xylan matrix was synthesized by the PPSM laboratory led by Pierre Audebert. This project was funded by the Labex SigmaLim.

V.1. Materials

The LDS layer consists of the fluorophore molecule N-(2-(6-chlorotetrazin-3-yloxy)ethyl)-naphthalimide (NITZ)[13,205] incorporated into a xylan matrix. The NITZ fluorophore operates via a three-step process (Figure 90): First, the naphthalimide moiety absorbs UV light at about 334 nm, followed by intramolecular energy transfer proceeds via the Förster resonance energy transfer (FRET) mechanism between the naphthalimide and tetrazine moieties. Finally, the tetrazine moiety re-emits the energy as visible light at about 566 nm, thus providing UV protection, eventually allowing improving the light-harvesting efficiency of OSCs. The calculated brightness of NITZ in DCM is 2766, indicating its strong potential for efficient photoconversion (see Appendix 3.1.)

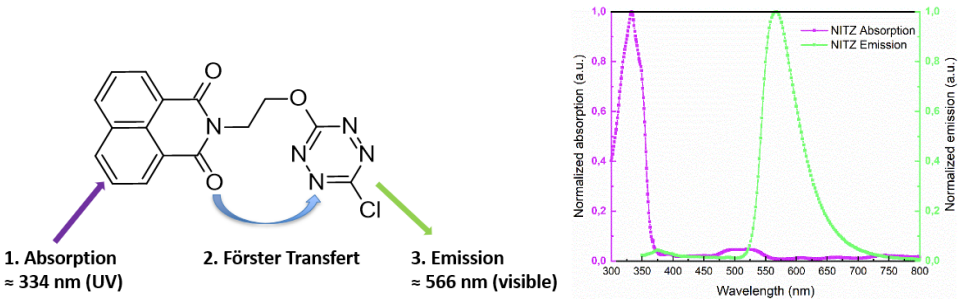

Figure 90. a) Fluorophore molecule:NITZ[205]. b) Absorption and emission spectra of the NITZ molecule in films.

The NITZ molecule exhibits a very significant Stokes shift (Figure 90b), with a large difference between its absorption peak and its emission peak. The main absorption range of the NITZ molecule is between 300 and 375 nm, with an absorption peak at 334 nm, which is in the near-UV region, well below the visible spectrum. When excited at 334 nm, the emission spectrum ranges from 525 nm to 700 nm, with a peak at around 570 nm. This high stokes shift minimizes re-absorption losses, allowing more efficient LDS of UV light into visible light. Moreover, this emission is particularly advantageous because it overlaps with the absorption region of the organic active layer, thereby maximizing the light generation rate.

However, there is another weak absorption in the 520-550 nm range, which means that the overlap between the emission and absorption spectra of NITZ is small, which prevents the efficient recycling of the re-emitted photons. As described in Ref. 205, for an LDS material to significantly improve solar cell efficiency, it must achieve an ideal balance between high absorption in the UV region and strong, non-overlapping re-emission in the visible. This prevents self-absorption losses and allows the maximum number of re-emitted photons to reach the active layer of the solar cell. In the case of NITZ, the observed photoluminescence originates mainly from the π-π* transitions, with a weaker excitation band around 550 nm attributed to the n-π* transitions[210,211]. Although NITZ provides effective UV protection, these spectral properties suggest that it may not fully optimize photon recycling to enhance device performance.

Xylan (C4-C12): This is a hemicellulose-based polymer (xylan) extracted from beech wood and chemically modified by esterification to enhance its functionality as a matrix for LDS layers. This modification introduces ester groups of different chain lengths, as shown in Figure 91: butyryl (C4), valeryl (C5), octanoyl (C8), and lauroyl (C12) chains.

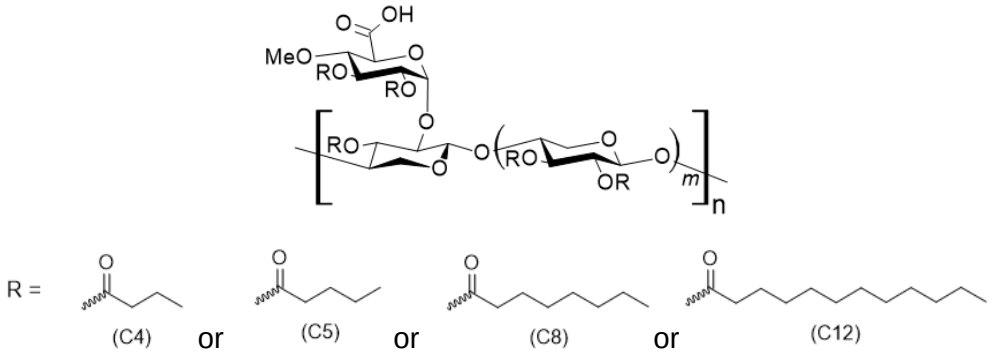

Figure 91. Chemical structure of xylan with varying chain lengths.

These different chain lengths affect the physical properties of xylan: shorter ester chains (C4, C5) allow for more uniform incorporation of high concentrations of fluorophores, ensuring a homogeneous distribution within the LDS layer. At the same time, longer chains (C8, C12) increase the flexibility of the film and reduce its brittleness, thus improving the mechanical stability of the downshifted layer. The self-film-forming property of xylan allows it to form stable films without the need for additional binders, making it an ideal matrix for embedding fluorophores while maintaining structural integrity and ease of processing.

V.2. Optical properties

Pure xylan films

Xylan films were prepared by Marine Petitjean. Xylan powder (C4, C5, C8, or C12) was dissolved in CF to form a homogeneous solution. Each solution was then poured into petri dishes of the same size and left overnight to allow the chloroform to evaporate. Once the solvent had completely evaporated, the films were formed and ready for analysis. After formation, each film was cut into 14 mm diameter disks using a circular cutter to ensure consistent sample size for PL measurements in an integrating sphere. The thickness of the film is approximately 20±10 µm, as measured using a Bruker Dektak XT profilometer. This thickness variation was attributed to the drop casting method, which can result in non-uniform thickness across the film surface. Figure 92 presents the aspect of the resulting self-supporting films as a function of the chain length of the ester groups of xylan prior to cutting, as well as their optical transmittance spectra. No chromophores were incorporated in this case.

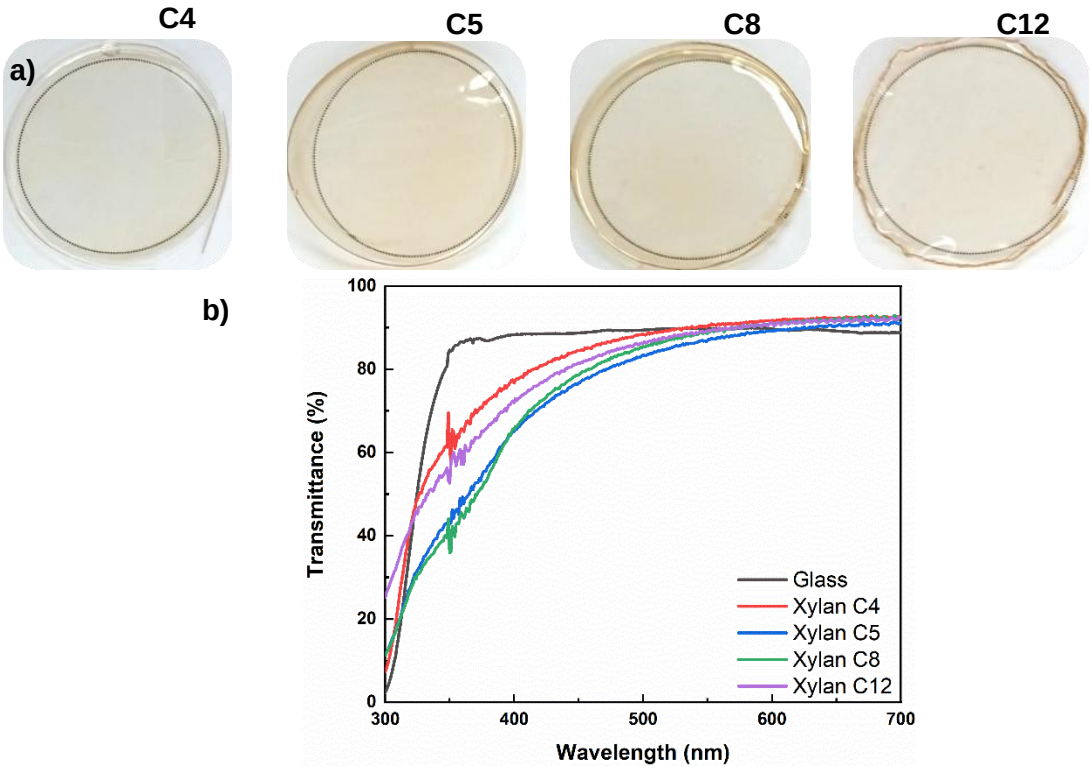

Figure 92. a) Photo of self-filming xylan films. b) Optical transmittance properties of the xylan films (C4, C5, C8, and C12).

The transmittance properties of the xylan films (C4, C5, C8, and C12) show that all films exhibit increasing light transmittance as the wavelength moves into the visible region, reaching over 90% transmittance at higher wavelengths. However, a notable drop in transmission is observed around 500 nm for all samples. This behavior indicates that although the films are highly transparent in the visible spectrum, they may absorb or scatter light in this region. The glass reference has a higher overall transmittance, serving as a baseline comparison. The variation in the transparency of the xylan films, especially for different ester chain lengths, highlights their influence on the optical properties of the material.

LDS layers

The LDS layer consists of the NITZ fluorophore incorporated into an esterified xylan matrix at concentrations ranging from 2.5% to 15% by mass, dissolved in CF to form a homogeneous solution. After evaporation of the CF, the fluorophore molecules are uniformly distributed

throughout the xylan matrix, resulting in a fluorescent film that emits light under UV excitation, as shown below:

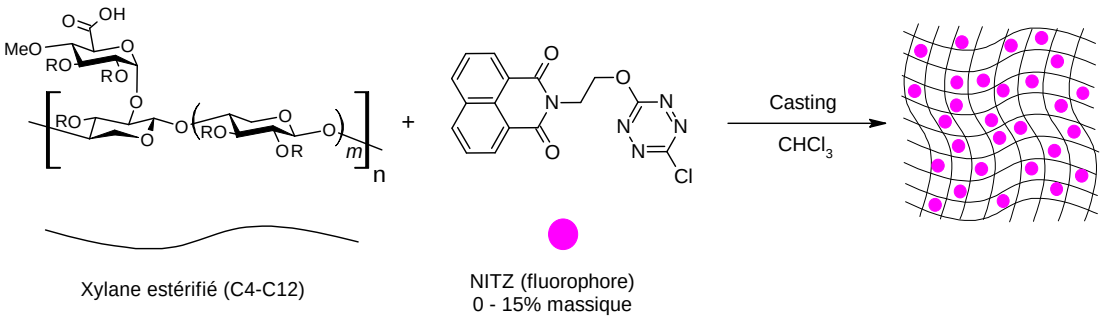

Figure 93. Process of incorporating the NITZ fluorophore into the xylans matrix to create LDS films.

C4, C5, C8, and C12 xylan films all exhibited similar optical properties when conjugated to the NITZ fluorophore; however, we chose the C5 xylan film for detailed analysis due to its superior homogeneity, allowing for more consistent conjugation of the fluorophore, while the results for the other xylan types are presented in the appendix. Photographs and microscope images of C5 xylan films with varying concentrations of the NITZ fluorophore (0%, 2.5%, 5%, 10%, and 15%) are shown in Figure 94a and 94b. The films were cut to a consistent diameter of approximately 14 mm for standardized measurements. The thickness of each film was measured using a Bruker Dektak XT profilometer, showing variability both within each film and between different concentrations: 0% NITZ: 28 ± 6 µm; 2.5% NITZ: 14 ± 3 µm; 5% NITZ: 25 ± 3 µm; 10% NITZ: 24 ± 3 µm; and 15% NITZ: 37 ± 5 µm.

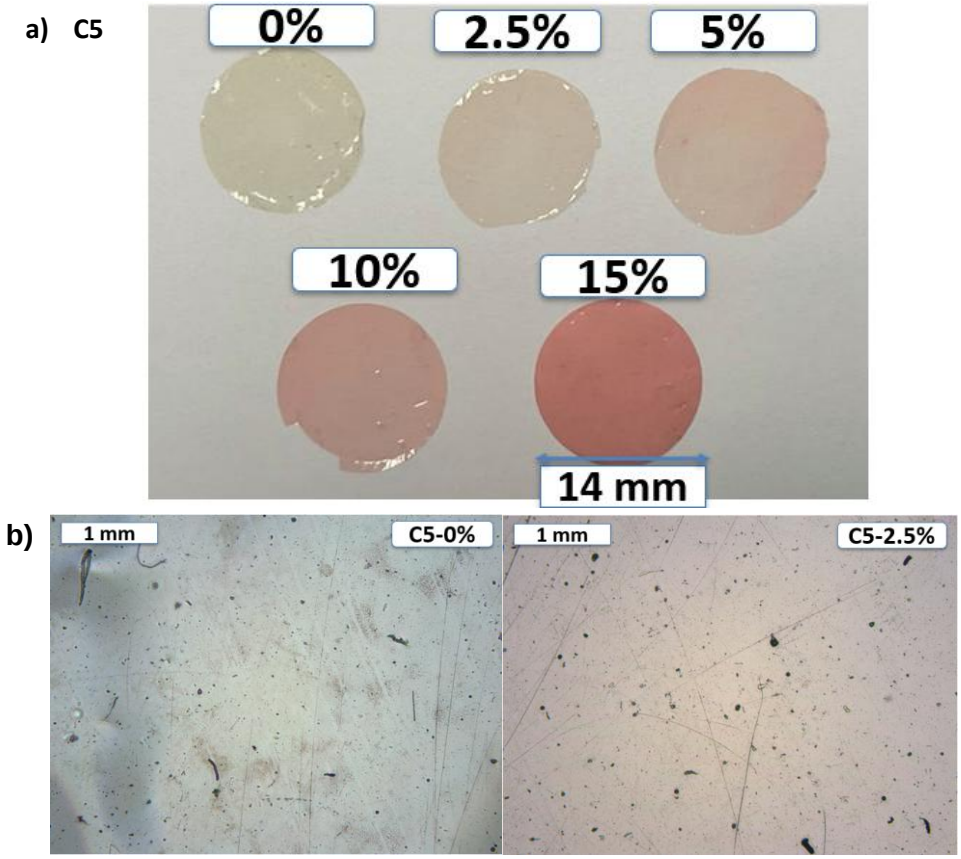

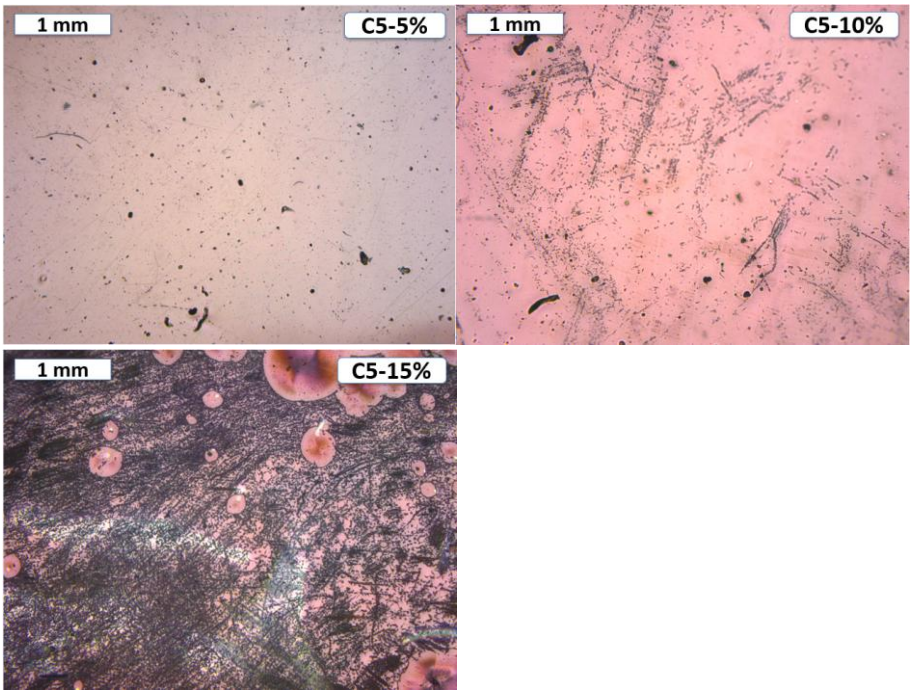

Figure 94. a) Photographs of C5 xylan films with different concentrations of NITZ (0%, 2.5%, 5%, 10%, and 15%). b) Optical microscope images of C5 xylan films at different NITZ concentrations (0%, 2.5%, 5%, 10%, and 15%).

Figure 94a shows that as the NITZ concentration increases, the films exhibit a gradually deepening pink hue, with the 15% NITZ film showing the strongest coloration compared to the nearly transparent 0% film. Microscope images further illustrate the structural changes that occur with increasing NITZ concentration: the 0% film appears relatively clear and uniform, with minimal visible defects. However, with increasing NITZ concentration, the films showed increased surface texture and roughness. When the NITZ concentration reaches 10%, a more obvious pink hue can be seen, while when the NITZ concentration reaches 15%, obvious aggregation occurs, with larger particles or clusters forming within the structure. This aggregation may affect the uniformity and optical properties of the LDS layer. Following this, we analyzed the absorption and fluorescence spectra of C5 xylan films to further explore how NITZ concentration affects its optical properties.

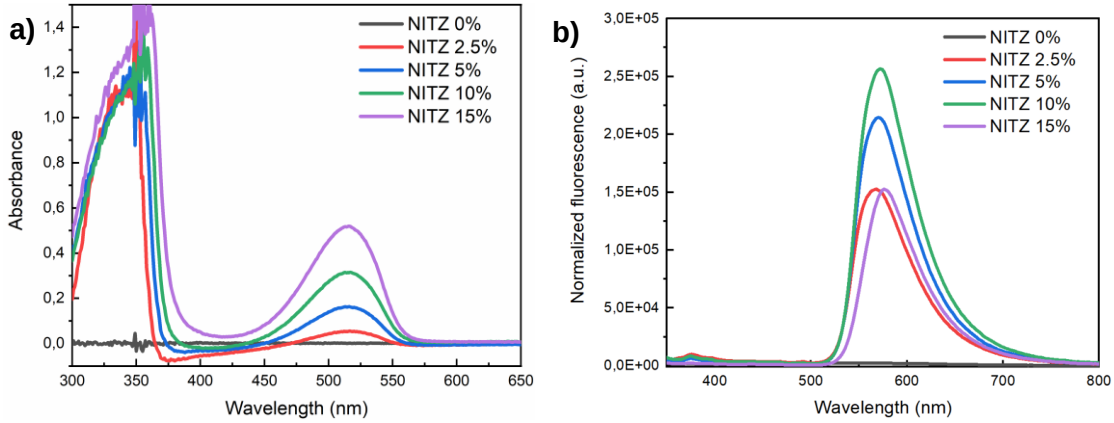

Figure 95. a) Absorption spectra of C5 xylan films, and b) normalized fluorescence emission spectra of C5 xylan films with varying concentrations of NITZ with λ_{ex} = 334 nm.

The absorption spectra (Figure 95a) display stronger absorption in the UV region around 334 nm as the NITZ concentration increases, correlating with the higher fluorophore content. In addition, there is a secondary absorption band between 450 and 560 nm, which is attributed to the n-π* transition. This overlap between the absorption and fluorescence emission spectra in the 520–550 nm range (Figure 95b) suggests potential limitation due to reabsorption, as the emitted photons are partially reabsorbed by the NITZ molecules themselves instead of reaching the active layer of the OSCs. It is worth noting that the negative absorption observed is due to the use of 0% NITZ film as the baseline and the different thicknesses of the layers. The thickness of the 0% NITZ film (28 ± 6 µm) is much higher than that of the 2.5% NITZ film (14 ± 3 µm).

The fluorescence spectra were normalized by the light absorbance at an excitation wavelength of 334 nm. The fluorescence emission spectra (Figure 95b) show that the emission intensity increases with the increase of NITZ concentration, with a peak at around 570 nm. However, saturation is observed at 10% NITZ concentration. Although 15% NITZ film still exhibits strong emission, its intensity does not significantly exceed that of 10% film. This suggests that the emission saturates at 10%, with minimal additional fluorescence gain at 15%. This plateau may result from self-quenching or other limiting effects at higher fluorophore concentrations, as well as reabsorption losses due to spectral overlap. These findings emphasize that the overlap between the n-π* absorption band and the PL emission spectrum limits the effectiveness of NITZ as a downshift material at higher concentrations. This limitation may explain why lower NITZ concentrations (below 5%) were more effective in previous studies, such as the study by Alexandre Gheno[205] and Ourida Ourahmoun[13], where reabsorption losses were minimized.

PLQY is a measure of how efficiently a material converts absorbed photons (UV) into emitted photons (visible). PLQY is measured using photoluminescence spectroscopy with an integrating sphere. It is expressed as the ratio of the number of photons emitted to the number of photons absorbed and is calculated as in Eq. 15:

$$PLQY = \frac{Number\ of\ photons\ \ emitted}{Number\ of\ photons\ absorbed} \qquad \text{(Equation 15)}$$

Table 31. PLQY values for different concentrations of NITZ in a C5 xylan matrix.

	PLQY (%)
2.5%NITZ:C5 xylan	42.6±3
5%NITZ:C5 xylan	41.5±3
10%NITZ:C5 xylan	42.5±2
15%NITZ:C5 xylan	40.4±2

The optical properties of the xylan system showed clear advantages compared to previous LDS systems using NITZ embedded in synthetic polymer matrices such as PS. In the xylan matrix, the achieved PLQY was relatively high, as shown in Table 31. The PLQY of the xylan film remained stable at various NITZ concentrations, exceeding 40%. This is significantly higher than the typical PLQY values observed in NITZ:PS systems (2% NITZ:PS, PLQY is around 30%), where doping levels exceeding approximately 5% generally result in decreased

optical properties[205]. Even at elevated NITZ concentrations (up to 15%), xylan maintained high PLQY, suggesting that it provides a more favorable environment for NITZ molecules, likely due to its natural polymer structure and uniform fluorophore binding.

In comparison, the PLQY of NITZ in solution (dissolved in DCM) is only 32%[211], indicating that embedding NITZ into the xylan matrix could enhance its photoluminescence efficiency, which can reach around 42% in a C5 xylan matrix. This improvement may be attributed to the stabilizing environment provided by xylan, in which the hydrophilic -OH groups create a more structured environment, segregating the NITZ molecules, reducing intermolecular interactions and restricting molecular rotation. This isolation minimizes non-radiative attenuation pathways, thereby increasing luminescence efficiency. In addition, this high doping tolerance of xylan films may contribute to the improved UV absorbance and enhanced visible light emittance, thus enhancing the potential for downshifting applications. Furthermore, as a bio-based matrix, xylan is in line with sustainable development goals and provides a renewable alternative with favorable structural and optical properties for LDS applications.

V.3. Improving PCE by using a LDS layer

We have integrated the NITZ:C5 xylan layer onto our OPV device, which is based on a PM6:Y6 active layer. The OPV has an inverted structure consisting of Glass/ITO/ZnO/ PM6:Y6/MoO_3/Ag, as shown in Figure 96. C5 xylan was chosen over other chain lengths (C4, C8, C12) because it has the best balance of properties for this application. Similar to C4 xylan, C5 xylan can more evenly incorporate a large amount of NITZ fluorophore, thus ensuring a uniform distribution within the LDS layer. Furthermore, C5 provides a more flexible and less brittle film compared to C4, therefore enhancing the mechanical stability of the LDS layer on OPV devices. The LDS layer, consisting of NITZ:C5 xylan, is deposited directly onto the OPV device. It is expected to boost its performance by converting UV light into visible light that the active layer can absorb (Figure 96).

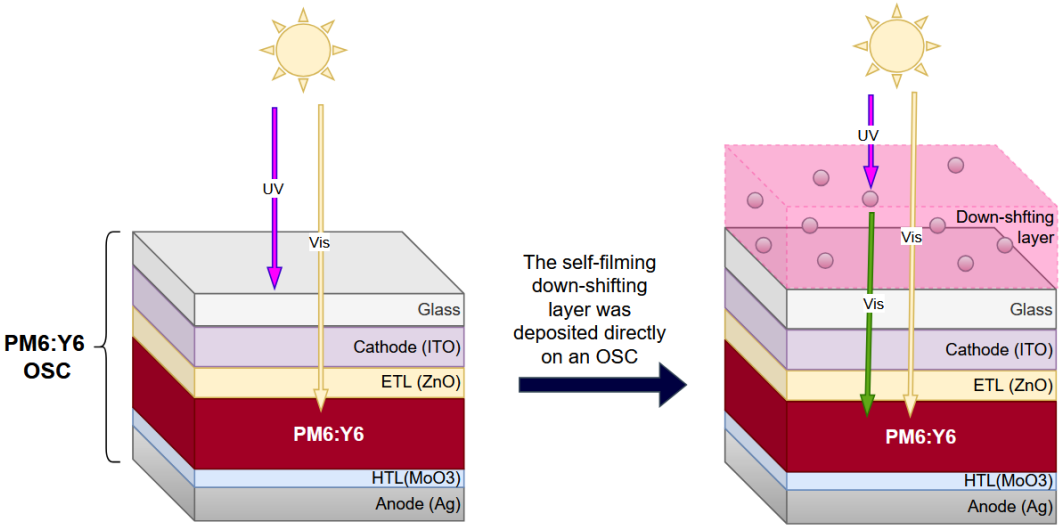

Figure 96. Integration of the self-filming LDS layer onto an inverted OSC based on PM6:Y6.

Following the integration of the NITZ:C5 xylan LDS layers with different concentrations of NITZ (0%, 2.5%, 5%, 10%, and 15%) onto the OPV device, we proceeded with EQE measurements to evaluate its impact on the device's performance.

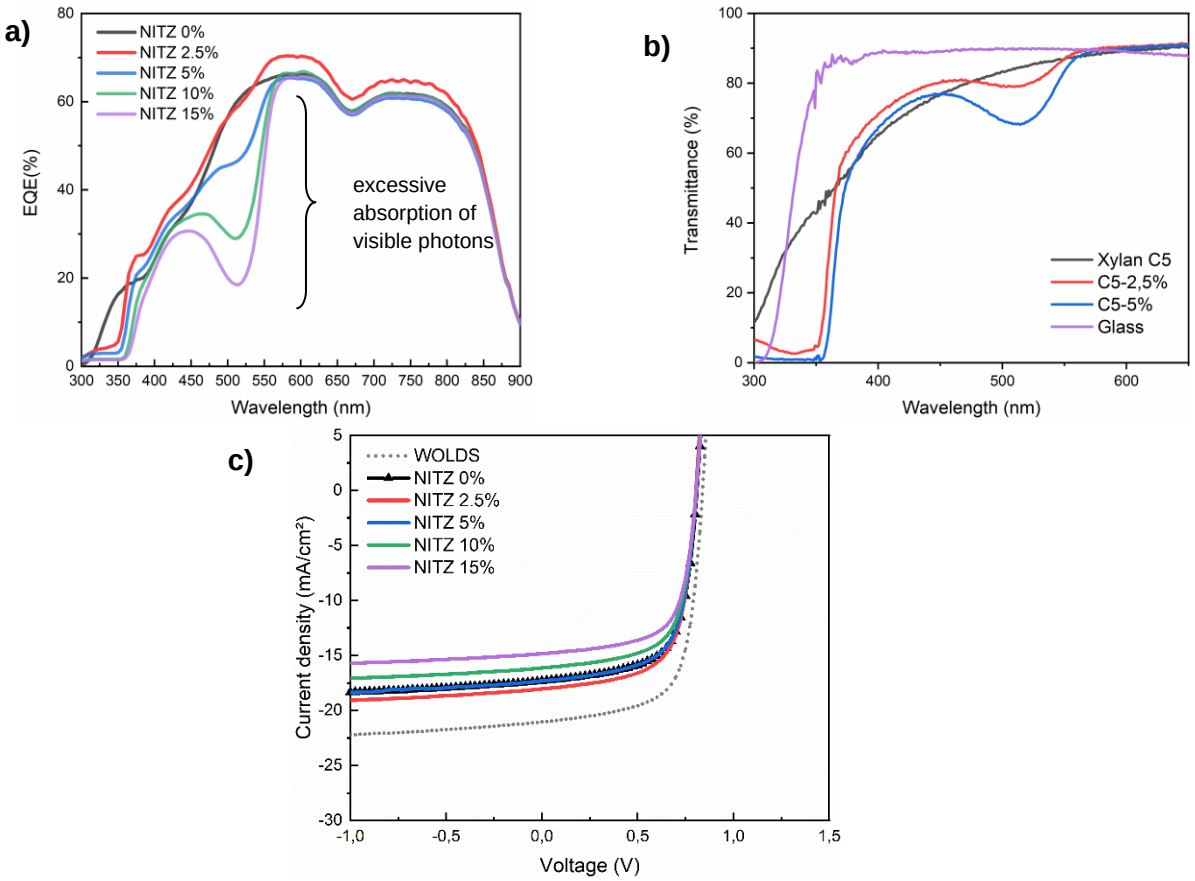

Figure 97. a) EQE of PM6:Y6 OPVs incorporating C5 xylan films with different concentrations of NITZ (0%, 2.5%, 5%, 10%, and 15%). b) Transmittance spectra of C5 xylan films with varying NITZ concentrations (0%, 2.5%, and 5%) compared to bare glass. c) JV curve of C5 xylan film with varying NITZ concentration and without DSL.

Table 32. PV performance parameters of PM6:Y6 OPVs containing C5 xylan films with different concentrations of NITZ (0%, 2.5%, 5%, 10%, and 15%) and without DSL.

Xylan C5	V_{OC} (V)	J_{SC} (mA.cm^{-2})	Jsc.eqe (mA.cm^{-2})	FF (%)	PCE (%)
without DSL	0.85	21.0	21.2	66.6	11.9
0% NITZ	0.83	17.3	17.8	67.2	9.3
2,5% NITZ	0.80	18.0	18.6	66.6	9.6
5% NITZ	0.80	17.3	17.0	66.8	9.3
10% NITZ	0.80	16.1	16.4	66.9	8.6
15% NITZ	0.80	14.9	15.6	67.1	8.0

This EQE figure (Figure 97a) shows that the use of NITZ: C5 xylan layers to improve the PCE of OPVs is not as effective as we initially expected. From 375 to 800 nm, the 2.5% NITZ film exhibits a slightly higher EQE compared to other concentrations. However, this increase is not due to the LDS effect but to the enhanced light transmittance through the film. The transmittance data (Figure 97b) show that the 2.5% NITZ film is thinner (14 ± 3 µm) than the 0% NITZ film (28 ± 6 µm) and therefore shows higher transmittance in this range. This thickness difference allows more light to reach the active layer in the 2.5% film, thereby improving the absorption and conversion of photons, as shown in the EQE results. In addition, increasing the concentration of NITZ in the LDS layer results in excessive absorption of visible

photons (10% and 15%), particularly in the 450-560 nm range. This intense absorption reduces the amount of light reaching the active layer, ultimately reducing the PCE of the device. The LDS layer did not show significant efficiency in this experiment, possibly due to the excessive thickness of the layer, which is around 20±5 µm. A thicker film may limit the efficiency of UV absorption and the subsequent re-emission of visible light by the NITZ fluorophore. This thickness could cause scattering or re-absorption of the emitted light, reducing the overall effectiveness of the LDS process. Thinner layers may allow for more efficient energy transfer and light transmission, improving the performance of the LDS effect in future studies.

Table 32 further illustrates the effect of NITZ concentration on OPV performance. Without the LDS layer, the PM6:Y6 device achieves a V_{OC} of 0.85 V, a J_{SC} of 21.0 mA/cm² and a PCE of 11.9%. When the 2.5% NITZ layer is applied, the V_{OC} drops slightly to 0.80 V, while the J_{SC} drops to 18.0 mA/cm², resulting in a reduced PCE of 9.6%. This trend continues with higher NITZ concentrations, with the 10% and 15% NITZ films showing further reductions in V_{OC} (0.80 V), J_{SC} (16.1 mA/cm² and 14.9 mA/cm²) and PCE (8.6% and 8.0% respectively). These results emphasize that, although the NITZ:C5 xylan layer has UV protection, its effectiveness as an LDS material is compromised by excessive visible light absorption and film thickness.

To enhance the LDS effect in future studies, employing thinner layers could facilitate more efficient energy and light transmission, thus improving the overall performance of LDS layers in OPV devices. To achieve this, we used a spin coater to create thinner LDS layers to minimize visible photon absorption while retaining the UV downshift functionality. CF solutions of C5 xylan containing different concentrations of NITZ were prepared and spin-coated onto glass substrates at 6000 rpm, 3000 rpm/s acceleration for 40 seconds, and then air dried at room temperature for 10 minutes. The process produced LDS films with a consistent thickness of 1.2 µm (Figure 98a), which is much thinner than typical self-filmed layers of varying thickness. The uniform thickness achieved by spin coating ensures more predictable light transmission and LDS performance. This thinner LDS film was then integrated with the PM6:Y6 OSC, as shown in Figure 99.

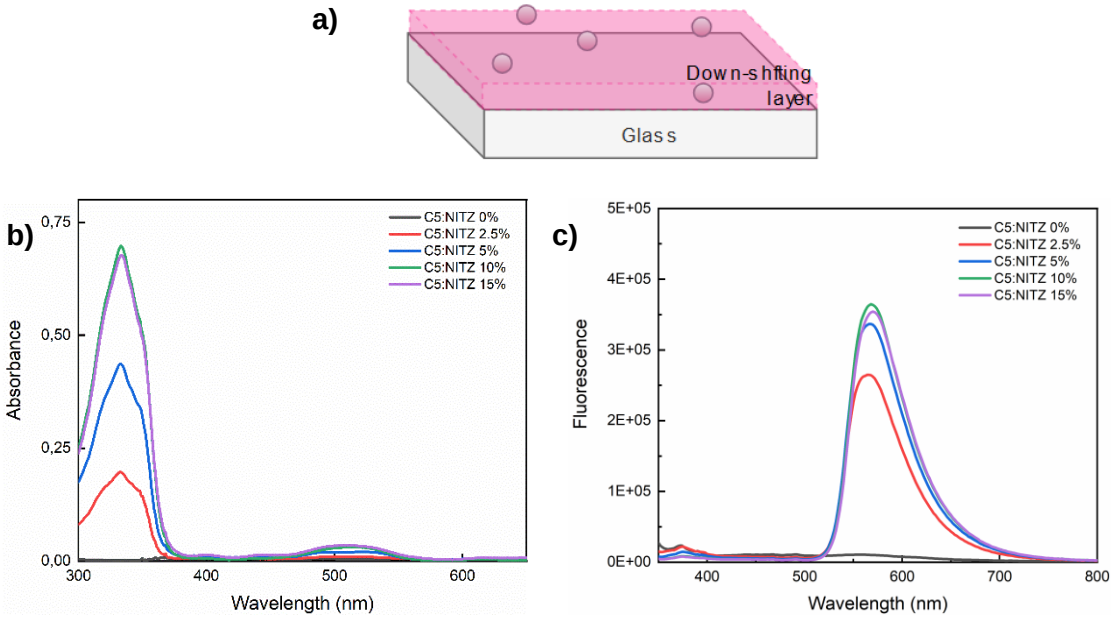

Figure 98. a) The structure of the LDS layer is deposited on glass using a spin-coater. b) Absorbance and c) fluorescence spectra of the C5 LDS layer with varying NITZ concentrations (0%, 2.5%, 5%, 10%, 15%) deposited on a glass substrate by spin-coater, with excitation at 334 nm.

Table 33. PLQY values of the C5 LDS layer with varying NITZ concentrations (2.5%, 5%, 10%, 15%) deposited on a glass substrate by spin-coater.

	PLQY (%)
2.5%NITZ:C5 xylan	43.4±2
5%NITZ:C5 xylan	42.5±2
10%NITZ:C5 xylan	40.2±3
15%NITZ:C5 xylan	37.6±4

Figure 98b and 98c show the absorption and fluorescence spectra of the spin-coated C5 xylan LDS layers, which exhibit similar behavior to the self-filming LDS layer. The primary absorption occurs between 300 and 375 nm, with a peak at 344 nm, corresponding to the strong UV absorption of NITZ. Secondary absorption bands appear between 450 and 560 nm. The absorption intensity increases with increasing NITZ concentration. The emission spectrum ranges from 530 to 700 nm, with a peak around 570 nm. The fluorescence intensity increases with increasing NITZ concentration, confirming the efficient conversion of UV photons into visible photons. Saturation of emission is observed at 10% NITZ concentration, indicating that beyond this level, additional fluorophores do not significantly increase the emission intensity, likely due to self-quenching effects. The PLQY values of both spin-coated and self-forming NITZ films remain consistent, with a value around 40% for the different NITZ concentrations (2.5%, 5%, 10%, 15%). This similarity suggests that whether the layer is deposited by spin-coating or self-forming technique, the downshift efficiency remains relatively unaffected by the deposition method, maintaining a stable photoluminescence quantum yield of around 40%.

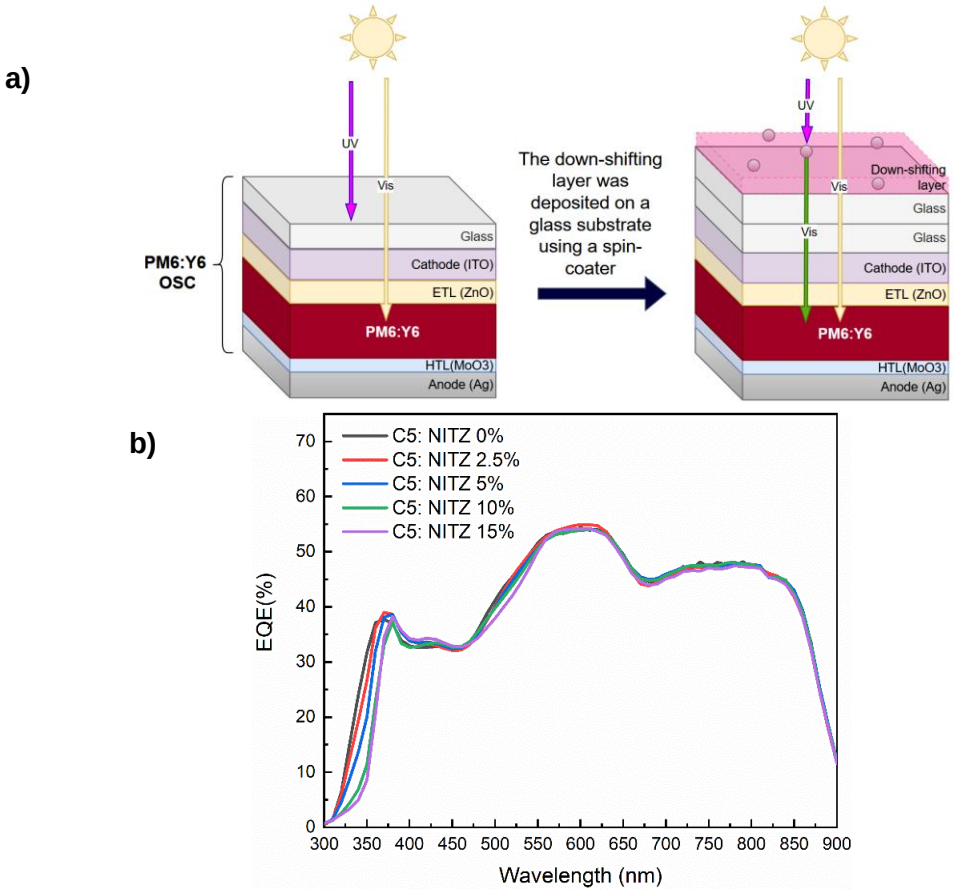

Figure 99. a) Deposition of the LDS layer onto a glass substrate using a spin-coater for integration with a PM6:Y6 OSC. b) EQE of spin-coater deposited LDS layers with varying NITZ concentrations.

Figure 99b shows that the use of a thinner down-shift layer can avoid excessive absorption of visible photons in the 450-560 nm range. However, in the excitation region of NITZ (around 334 nm), the EQE of the device with NITZ is still lower than that of the device without NITZ, which is not as effective as expected. This reduction may be due to the direct absorption of incident photons by the NITZ fluorophore molecules in the down-shift layer, thereby reducing the number of photons that reach the active layer and can be converted into charge carriers. There is a competition between the absorption of the down-shifting layer in the UV region and the absorption of these photons by the active layer and their direct conversion into photocurrent. As discussed in Alexandre Gheno's paper[205], we can summarize this problem by defining a ratio X that takes into account the PLQY of the downshifted layer and the efficiency of the OSC in the excitation and emission spectra of the downshifted molecule.

$$X = EQY \times \int_{\lambda_{exc}} R \times \frac{\int_{\lambda_{emi}} \frac{P_{elec}(\lambda)}{P_{lum}(\lambda)} d\lambda}{\int_{\lambda_{exc}} \frac{P_{elec}(\lambda)}{P_{lum}(\lambda)} d\lambda}$$

(Equation 16)

In this formula, P_{elec} (λ) represents the electric power produced by the OSC as a function of wavelength, while P_{lum} (λ) denotes the illumination power from the light source as a function of wavelength. The term λ_{emi} corresponds to the emission range of the down-shifting molecule, and λ_{exc} represents its excitation range. The factor R accounts for the fact that NITZ emits light isotropically: approximately 50% of the emitted photons are directed away from the solar cell, reducing the fraction of usable photons. Furthermore, R also considers the effect of total internal reflection at the interface between C5 xylan film and glass substrate. At this interface, photons emitted beyond a certain critical angle are internally reflected, resulting in additional losses as they are redirected within the LDS layer instead of reaching the active layer. In our calculations, we assumed a best-case scenario for R (0.5) to estimate the maximum potential benefit of the downshift strategy. When X is greater than 1, the energy produced by the OSC with the DLS exceeds that produced by the OSC alone, indicating that the use of this LDS material is beneficial. This behavior suggests that the LDS effectively converts the extra UV photons into visible photons that the OSC can utilize, thereby increasing the overall power output of the device. For our PM6:Y6 OPV, the EQE is 54% at 570 nm and 24% at 340 nm. Based on these values, the calculated X value for this system is 0.47, indicating that the strategy of using NITZ as the LDS layer for PM6:Y6 is not the best choice. Therefore, while a thinner down-shift layer can alleviate some of the visible light absorption, it still hinders the utilization of photons in the UV range, ultimately limiting its ability to improve overall device performance.

If we add a UV filter layer between the LDS layer and the OSC, we can potentially improve the overall device performance. The UV filter would block harmful high-energy UV photons that could degrade the active layer while still allowing the LDS layer to absorb UV light and re-emit it as visible light. This re-emitted visible light would pass through the UV filter and reach the active layer, enhancing photon utilization and reducing the risk of damage to the OSC, as shown in Figure 100a. The UV filter film was approximately 60 µm thick and was purchased from Film Pour Vitre. The transmittance of the system with a UV filter is shown in Figure 100b.

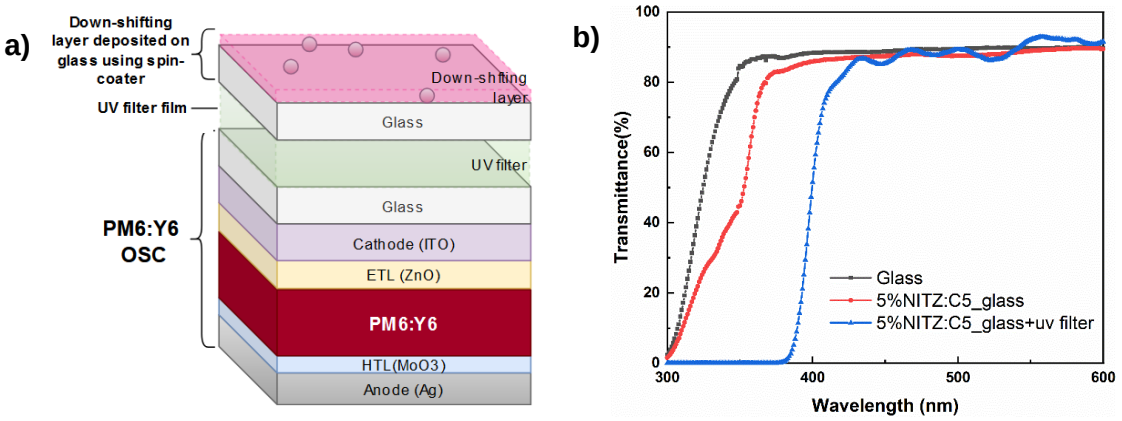

Figure 100. a) The device structure includes a UV filter positioned between the spin-coater deposited LDS layer and the OSC. b) Transmittance spectra of three different samples: bare glass (black curve), spin-coater deposited 5% NITZ:C5 LDS layer (red curve), spin-coater deposited 5% NITZ:C5 LDS layer combined with a UV filter (blue curve).

The device includes a UV filter film between the spin-coated 5% NITZ:C5 xylan down-shifting layer and the PM6:Y6-based OSC. Figure 100b shows the transmittance spectra of samples. The blue curve is the transmittance of the sample with both spin-coated 5% NITZ:C5 xylan LDS layer and a UV filter film. The transmittance is lower below 400 nm, indicating that the UV blocking effect is enhanced. The UV filter film effectively blocks the passage of ultraviolet rays. In addition, the transmittance in the visible light range is still high, similar to the red curve, ensuring the transmission of visible light.

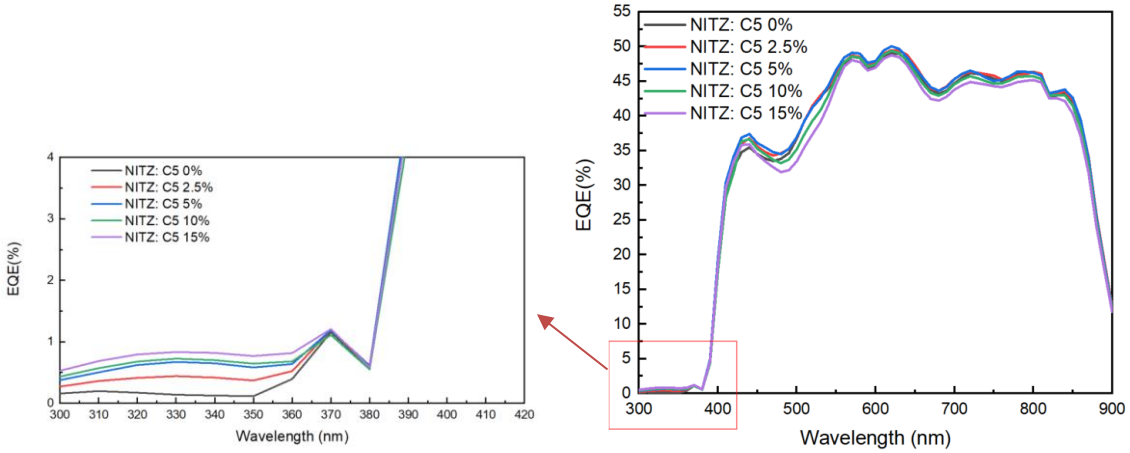

Figure 101. EQE spectra of the structure with a UV filter between the spin-coater deposited LDS layer and the OSC.

From the EQE spectra, there is a slight improvement in the UV region (300-375 nm), indicating that the UV filter successfully prevents direct UV exposure to the active layer while allowing the LDS layer to absorb UV light. However, the increase in EQE due to the LDS process is not as significant as expected due to several factors:

- Air gaps between solar cells, UV filters, and LDS layers cause optical losses. Air gaps cause additional reflection and scattering of light, which reduces the amount of light reaching the active layer of the solar cell. This reduces the effectiveness of the LDS layer in improving EQE.

- NITZ fluorophores emit light in all directions, and approximately 50% of the emitted photons may be directed away from the solar cell[205], thus reducing the number of valuable photons that can be converted into charge carriers. This non-preferential emission leads to high photon losses, as only half of the emitted photons are directed toward the solar cell. The other half is lost in the opposite direction[212,213]. To address this limitation, future work could explore photonic strategies to redirect or focus these emitted photons toward the active layer. Techniques such as embedding reflective or scattering layers or applying angle-selective filters can help direct more of the emitted photons back into the device[214].
- The refractive index mismatch between the C5 xylan LDS layer and the glass substrate can result in total internal reflection. At certain angles, photons emitted from the NITZ molecules may be trapped within the LDS layer or reflect toward it instead of passing through the solar cell. This limits the amount of light that can reach the active layer of the solar cell, further reducing efficiency.

V.4. Effects of UV protection on device stability in OSCs

The use of NITZ in our OSCs does not significantly improve the PCE. However, by converting harmful UV radiation into visible light, NITZ can potentially protect the active layer from UV-induced degradation, thereby extending the lifetime of the solar cell. Although the direct impact on the PCE is small, NITZ's protection against UV-induced degradation can improve the durability and reliability of OSCs in outdoor applications, which is a crucial requirement for widespread application of OPV outside buildings and under sunlight. To evaluate the effectiveness of the UV protection strategy, two PM6:Y6 OSCs were exposed to simulated solar irradiation for 200 minutes under the following conditions:

Without NITZ (1.2 µm, only the glass substrate with C5 xylan): This control condition includes a 1.2 µm C5 xylan layer on glass, without the incorporation of NITZ, to evaluate the performance of the OSC without any UV protection.

With 5% NITZ:C5 xylan (1.2 µm, spin-coated 5% NITZ:C5 xylan on glass): A 1.2 µm layer of 5% NITZ: C5 xylan was spin-coated onto the glass, providing UV protection by absorbing harmful UV light and shifting it down into the visible region.

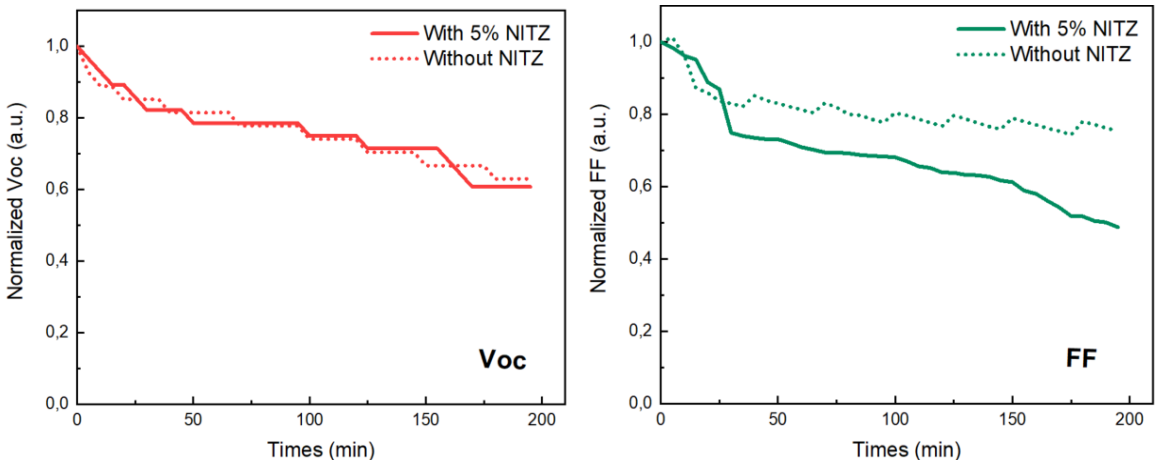

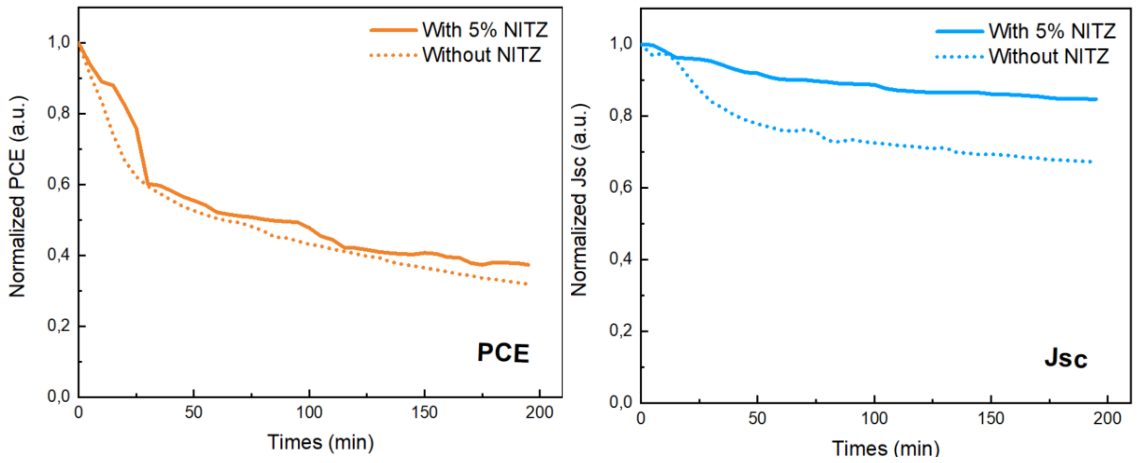

Figure 102. The evolution of normalized V_{OC}, FF, PCE and J_{SC} over time for OSCs without a UV filter, comparing without NITZ and with 5% NITZ deposited on glass.

The addition of a 1.2 µm thick 5% NITZ layer by spin coating significantly enhances the stability of PM6:Y6 OSCs under prolonged simulated solar radiation, thereby protecting the active layer from UV-induced degradation. As shown in Figure 102, this protective effect is manifested by the slower decrease in V_{OC}, PCE, and J_{SC} after 200 min of exposure. After 200 minutes, the PCE of the 5% NITZ film declines to 37% of its initial value, while the PCE of the non-NITZ film declines more dramatically, retaining only 31% of its initial PCE. Furthermore, J_{SC}, which is particularly sensitive to UV degradation due to its dependence on both light absorption and charge collection, retains 85% of the initial value of the 5% NITZ film after 200 minutes. This is important because UV irradiation generally degrades the optical properties of the active layer and the electrode interface, disrupts the generation and collection of charge carriers, and directly reduces J_{SC}. In contrast, the non-NITZ OSC retains only 67% of its initial photocurrent under the same conditions. However, the FF decreases faster in the presence of the NITZ layer, indicating a possible trade-off in charge transport. In summary, the NITZ layer improves UV stability by decreasing the degradation of the optical absorption (as shown by the stable J_{SC}) and reducing the overall degradation of PCE and V_{OC}.

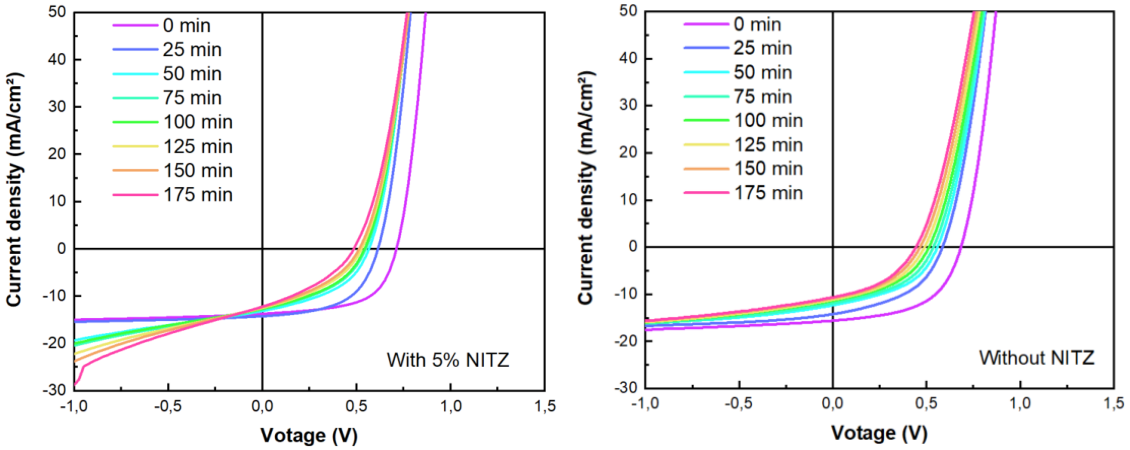

Figure 103. Changes in the JV curves of PM6:Y6 OPV devices with (left) and without (right) a 5% NITZ UV-filter layer under simulated solar irradiation over time.

As can be seen from Figure 103, after adding 5% NITZ as a UV filter, the R_{SH} unexpectedly decreased after 30 minutes of exposure and decreased more than the device without NITZ.

This result may be influenced by initial sample variability, as only one sample was measured per setup. Small differences in the fabrication or quality of the PM6:Y6 layers might have impacted the results.

The difficulty in improving the PCE with our strategy led us to investigate the stability of the NITZ molecule itself by monitoring its PLQY over time. To this end, samples containing 5% and 10% NITZ:C5 xylan (both 1.2 µm thick, spin-coated on glass) were protected in Petri dishes and stored in the dark for 20 days to prevent photodegradation by ambient light.

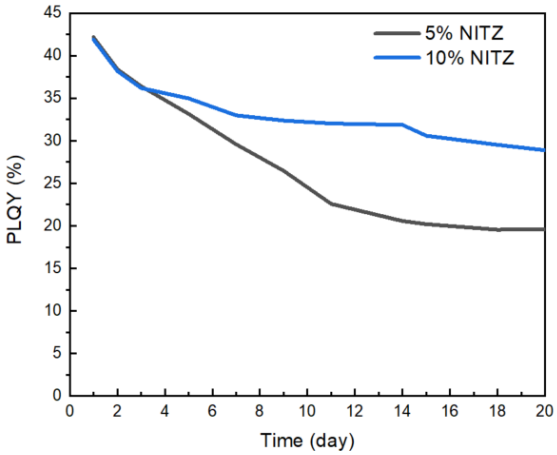

Figure 104. Degradation of PLQY over time for the NITZ molecule measured by photoluminescence spectroscopy using an integrating sphere.

As shown in Figure 104, both 5% and 10% NITZ:C5 xylan samples (1.2 µm thick, spin-coated on glass) initially exhibited a PLQY of around 42%. After 20 days of storage in the dark, the PLQY of the 5% sample decreased to about 20%, while the 10% sample decreased more slowly and stabilized at about 29%. This difference suggests that higher NITZ concentrations may provide slightly better stability, although both concentrations indicate that NITZ has an intrinsic stability limit that could affect the efficiency of the LDS layer and the overall PCE of the solar device over time. These observations are consistent with previous studies by Alexandre et al.[205], who investigated the stability of 1.5% NITZ embedded in PS films. The results show that significant photobleaching occurs in the illuminated samples exposed to simulated solar illumination (1 sun, AM1.5G, 100 mW/cm²) for 4 h, with the PLQY dropping dramatically from 30% to only 3% after exposure. The NITZ film also appears to be very sensitive to temperature, as the film not exposed to light lost 4 points of PLQY. They suggest that NITZ is sensitive not only to light but also to temperature.

V.5. Conclusion

In conclusion, our study demonstrated that NITZ has unique advantages as an LDS and UV protection layer for PM6:Y6 OSCs when embedded in a C5 xylan hemicellulose matrix. Unlike conventional polymer matrices, xylan composites can support very high NITZ concentrations (up to 15%) while maintaining relatively high PLQY. This suggests that the xylan matrix provides an environment that enhances the photoluminescence properties of NITZ, which may be due to favorable interactions between NITZ and the natural polymer or to microstructural effects that limit self-quenching.

Through JV measurements and EQE characterization, we demonstrate that NITZ, in combination with C5 xylan hemicellulose, can temporarily act as an LDS and UV protection

layer for PM6:Y6 -based OSCs. While the PLQY of this LDS material is not high enough to significantly enhance PV performance, it can effectively recycle a portion of the absorbed UV light. Notably, the choice of the correct NITZ concentration is crucial, as higher concentrations (e.g., 10% or 15%) can absorb the visible range and reduce the light available to the active layer. Our results suggest that lower concentrations (e.g., 2.5% and 5%) may provide a better balance between UV absorption and minimal interference with visible light transmission.

As PM6:Y6 OSCs already exhibit relatively high EQEs in the 300-400 nm range, the benefits of LDS are limited. However, applying this strategy to P3HT:PCBM-based OSCs, which have lower EQEs in the UV region, could lead to more significant improvements. This study highlights the importance of UV protection for specific OSC architectures. It underlines the need for LDS layers that not only protect the active materials from harmful UV radiation but also compensate for the J_{SC} loss when UV light is blocked. Further optimization of NITZ concentration and layer design could improve the stability and performance of OSCs. Additionally, our results highlight the potential of bio-based matrices, such as xylan, in LDS applications, providing not only UV protection but also high doping tolerance and enhanced PLQY.

General conclusion

To conclude, our research comprehensively explores innovative strategies for developing OSC materials and device architectures that are specifically optimized for the blue region (400-500 nm) of artificial light sources, especially white LEDs. Conventional OPV materials are primarily designed for use in outdoor sunlight, where absorption of the entire solar spectrum is critical. However, these materials typically exhibit limited absorption in the blue range, which reduces the charge generation efficiency under indoor lighting conditions dominated by blue-rich LED light. To address this gap, our work focuses on creating new photoactive materials that are highly sensitive to blue wavelengths, thereby enhancing charge carrier generation and improving overall device performance in indoor environments dominated by artificial light sources. By advancing OSCs in this way, we aim to position these technologies as efficient power sources for low-light, off-grid, and IoT applications, paving the way for sustainable energy solutions in a variety of indoor environments.

In the initial phase of this research, we focused on the integration of novel heptazine-based NFAs adapted to indoor lighting conditions. While these materials demonstrated potential for blue-region absorption, challenges in optimizing their properties for practical applications persisted. We synthesized and tested several heptazine derivatives, including TDPH, 2,4-diF-heptazine, and 2,4-dimethyl-heptazine, in combination with various donor materials. The blends exhibited promising morphological and optical characteristics but still faced limitations in current density and efficiency under indoor lighting conditions. To further address the blue absorption challenge, we introduced di-PDI as an alternative NFA, which resulted in improved photovoltaic performance. In an effort to optimize the PV performance of heptazine-based devices, we systematically explored several key experimental parameters, such as:

- Selection of p-type donor materials: We tested various donor materials, including D18, P3HT, and PCE12, to identify the most compatible donor for heptazine acceptors. PCE12 exhibited better results, achieving an impressive V_{OC} of 1.10 V when paired with 2,4-diF-heptazine.
- Donor/acceptor ratio (D/A): Fine-tuning the D/A blend ratio was critical for optimizing phase separation and charge transport, resulting in improved device performance.
- Annealing temperature and duration: We investigated the impact of thermal annealing at different temperatures and durations. The optimization of annealing conditions, such as 100°C for 10 minutes, improved the crystallinity and phase separation in di-PDI-based devices, leading to enhanced J_{SC} and overall PCE.

The optimization efforts allowed us to achieve a PCE of 0.93% with a high V_{OC} of 1.10 V for the PCE12:2,4-diF-heptazine blend under AM1.5 illumination. Under LED lighting, the J_{SC} was progressively optimized to reach13.4 µA.cm-2. The PTB7-Th:di-PDI blend achieved a PCE of 3.5% after annealing at 100°C. Furthermore, the device performance improved under LED illumination at 1000 lux, reaching a PCE of 4.7% with annealing, demonstrating its potential for indoor applications.

In the second phase of research, we investigated a medium bandgap active layer based on PF2, a fluorinated polymer donor, in combination with ITIC for indoor PV applications. The combination of chlorobenzene as a solvent and an optimized active layer thickness of 270 nm significantly improved blue-region absorption, leading to a PCE of 12.0% under 1000 lux warm

LED illumination. The device also exhibited a high V_{OC} of 0.83 V, demonstrating its suitability for low-light indoor environments.

While indoor applications were the primary focus, this thesis also addressed the challenges of UV-induced degradation in OSCs for outdoor environments. We investigated the integration of NITZ molecules with hemicellulose for LDS, which showed potential in converting harmful UV radiation into visible light, thereby enhancing the long-term stability and operational lifespan of OSCs under outdoor conditions. Unlike conventional polymer matrices, xylan composites can support very high NITZ concentrations (up to 15%) while maintaining relatively high PLQY. This suggests that the xylan matrix provides an environment that enhances the photoluminescence properties of NITZ.

Based on the findings of this thesis, there are still several promising avenues to be further explored to advance OSC technology for indoor applications. Continued optimization of heptazine derivatives and other NFAs could further improve the absorption profiles to better match the indoor lighting spectrum and increase charge generation efficiency. Advanced material combinations, such as di-PDI with various donor materials, can also improve blue light absorption and enhance device performance under low-light conditions. Furthermore, optimization of processing parameters of the PF2 system, such as solvent additives, could further improve performance and stability.

Another promising direction is the development of ternary OSC systems using PF2 in combination with other donors or acceptors. They can improve charge transport and reduce recombination losses by adding a third component that enhances exciton dissociation.

In terms of characterization, the use of advanced techniques such as grazing incidence wide-angle X-ray scattering (GIWAXS) and X-ray diffraction (XRD) can provide valuable insights into the molecular ordering, crystallinity, and phase separation of active layer materials. Furthermore, an in-depth investigation of local properties of active layers using techniques like cAFM will be conducted to gain a better understanding of nanoscale charge transport and morphology.

Bibliography

General works

1. Mathews, I., Kantareddy, S.N., Buonassisi, T., and Peters, I.M. (2019). Technology and Market Perspective for Indoor Photovoltaic Cells. Joule *3*, 1415-1426. 10.1016/j.joule.2019.03.026.
2. Xie, L., Song, W., Ge, J., Tang, B., Zhang, X., Wu, T., and Ge, Z. (2021). Recent progress of organic photovoltaics for indoor energy harvesting. Nano Energy *82*, 105770. 10.1016/j.nanoen.2021.105770.
3. Kumar, G., and Chen, F.-C. (2023). A review on recent progress in organic photovoltaic devices for indoor applications. Journal of Physics D: Applied Physics *56*. 10.1088/1361-6463/acd2e5.
4. Kim, T.H., Park, N.W., Saeed, M.A., Jeong, S.Y., Woo, H.Y., Park, J., and Shim, J.W. (2023). Record indoor performance of organic photovoltaics with long-term stability enabled by self-assembled monolayer-based interface management. Nano Energy *112*, 108429. 10.1016/j.nanoen.2023.108429.
5. Li, J., Zhang, Q., Nomura, H., Miyazaki, H., and Adachi, C. (2014). Thermally activated delayed fluorescence from 3nπ* to 1nπ* up-conversion and its application to organic light-emitting diodes. Applied Physics Letters *105*. 10.1063/1.4887346.
6. Galmiche, L., Allain, C., Le, T., Guillot, R., and Audebert, P. (2019). Renewing accessible heptazine chemistry: 2,5,8-tris(3,5-diethyl-pyrazolyl)-heptazine, a new highly soluble heptazine derivative with exchangeable groups, and examples of newly derived heptazines and their physical chemistry. Chem Sci *10*, 5513-5518. 10.1039/c9sc00665f.
7. Li, J., Nakagawa, T., MacDonald, J., Zhang, Q., Nomura, H., Miyazaki, H., and Adachi, C. (2013). Highly efficient organic light-emitting diode based on a hidden thermally activated delayed fluorescence channel in a heptazine derivative. Adv Mater *25*, 3319-3323. 10.1002/adma.201300575.
8. Ibrahim Zamkoye, I., El Gbouri, H., Antony, R., Ratier, B., Boucle, J., Galmiche, L., Trigaud, T., and Audebert, P. (2020). Characterization and Electronic Properties of Heptazine Layers: Towards Promising Interfacial Materials for Organic Optoelectronics. Materials (Basel) *13*. 10.3390/ma13173826.
9. Audebert, P., Kroke, E., Posern, C., and Lee, S.H. (2021). State of the Art in the Preparation and Properties of Molecular Monomeric s-Heptazines: Syntheses, Characteristics, and Functional Applications. Chem Rev *121*, 2515-2544. 10.1021/acs.chemrev.0c00955.
10. Ibraikulov, O.A., Ngov, C., Chávez, P., Bulut, I., Heinrich, B., Boyron, O., Gerasimov, K.L., Ivanov, D.A., Swaraj, S., Méry, S., et al. (2018). Face-on orientation of fluorinated polymers conveyed by long alkyl chains: a prerequisite for high photovoltaic performances. Journal of Materials Chemistry A *6*, 12038-12045. 10.1039/c8ta04127j.
11. Ma, X., An, Q., Ibraikulov, O.A., Lévêque, P., Heiser, T., Leclerc, N., Zhang, X., and Zhang, F. (2020). Efficient ternary organic photovoltaics with two polymer donors by minimizing energy loss. Journal of Materials Chemistry A *8*, 1265-1272. 10.1039/c9ta12025d.
12. Farinhas, J., Correia, S.F.H., Fu, L., Botas, A.M.P., André, P.S., Ferreira, R.A.S., and Charas, A. (2021). Ultraviolet-Filtering Luminescent Transparent Coatings for High-Performance PTB7-Th:ITIC–Based Organic Solar Cells. Frontiers in Nanotechnology *3*. 10.3389/fnano.2021.635929.
13. Ourahmoun, O., Trigaud, T., Ratier, B., Belkaid, M.S., Galmiche, L., and Audebert, P. (2017). An efficient tetrazine photoluminescent layer used for organic solar cells down shifting. Synthetic Metals *234*, 106-110. 10.1016/j.synthmet.2017.09.004.
14. Chiang, C.K., Fincher, C.R., Park, Y.W., Heeger, A.J., Shirakawa, H., Louis, E.J., Gau, S.C., and MacDiarmid, A.G. (1977). Electrical Conductivity in Doped Polyacetylene. Physical Review Letters *39*, 1098-1101. 10.1103/PhysRevLett.39.1098.

15. Tang, C.W. (1986). Two-layer organic photovoltaic cell. Applied Physics Letters *48*, 183-185. 10.1063/1.96937.
16. Yu, G.G., J.; Hummelen, J. C.; Wudl, F.; Heeger, A. J. (1995). Polymer Photovoltaic Cells: Enhanced Efficiencies via a Network of Internal Donor-Acceptor Heterojunctions. . 1789–1791. 10.1126/science.270.5243.1789
17. Zhang, G., Lin, F.R., Qi, F., Heumuller, T., Distler, A., Egelhaaf, H.J., Li, N., Chow, P.C.Y., Brabec, C.J., Jen, A.K., and Yip, H.L. (2022). Renewed Prospects for Organic Photovoltaics. Chem Rev *122*, 14180-14274. 10.1021/acs.chemrev.1c00955.
18. Brabec, C.J., Padinger, F., Sariciftci, N.S., and Hummelen, J.C. (1999). Photovoltaic properties of conjugated polymer/methanofullerene composites embedded in a polystyrene matrix. Journal of Applied Physics *85*, 6866-6872. 10.1063/1.370205.
19. Mühlbacher, D., Scharber, M., Morana, M., Zhu, Z., Waller, D., Gaudiana, R., and Brabec, C. (2006). High Photovoltaic Performance of a Low‐Bandgap Polymer. Advanced Materials *18*, 2884-2889. 10.1002/adma.200600160.
20. Peet, J., Kim, J.Y., Coates, N.E., Ma, W.L., Moses, D., Heeger, A.J., and Bazan, G.C. (2007). Efficiency enhancement in low-bandgap polymer solar cells by processing with alkane dithiols. Nat Mater *6*, 497-500. 10.1038/nmat1928.
21. Liang, Y., Xu, Z., Xia, J., Tsai, S.T., Wu, Y., Li, G., Ray, C., and Yu, L. (2010). For the bright future-bulk heterojunction polymer solar cells with power conversion efficiency of 7.4%. Adv Mater *22*, E135-138. 10.1002/adma.200903528.
22. Chen, J.D., Cui, C., Li, Y.Q., Zhou, L., Ou, Q.D., Li, C., Li, Y., and Tang, J.X. (2015). Single-junction polymer solar cells exceeding 10% power conversion efficiency. Adv Mater *27*, 1035-1041. 10.1002/adma.201404535.
23. He, Z., Xiao, B., Liu, F., Wu, H., Yang, Y., Xiao, S., Wang, C., Russell, T.P., and Cao, Y. (2015). Single-junction polymer solar cells with high efficiency and photovoltage. Nature Photonics *9*, 174-179. 10.1038/nphoton.2015.6.
24. Zhao, W., Qian, D., Zhang, S., Li, S., Inganas, O., Gao, F., and Hou, J. (2016). Fullerene-Free Polymer Solar Cells with over 11% Efficiency and Excellent Thermal Stability. Adv Mater *28*, 4734-4739. 10.1002/adma.201600281.
25. Liu, Y., Zhao, J., Li, Z., Mu, C., Ma, W., Hu, H., Jiang, K., Lin, H., Ade, H., and Yan, H. (2014). Aggregation and morphology control enables multiple cases of high-efficiency polymer solar cells. Nat Commun *5*, 5293. 10.1038/ncomms6293.
26. Jin, Y., Chen, Z., Xiao, M., Peng, J., Fan, B., Ying, L., Zhang, G., Jiang, X.F., Yin, Q., Liang, Z., et al. (2017). Thick Film Polymer Solar Cells Based on Naphtho[1,2‐c:5,6‐c]bis[1,2,5]thiadiazole Conjugated Polymers with Efficiency over 11%. Advanced Energy Materials *7*. 10.1002/aenm.201700944.
27. Lin, Y., Wang, J., Zhang, Z.G., Bai, H., Li, Y., Zhu, D., and Zhan, X. (2015). An electron acceptor challenging fullerenes for efficient polymer solar cells. Adv Mater *27*, 1170-1174. 10.1002/adma.201404317.
28. Wang, J.-L., Liu, K.-K., Hong, L., Ge, G.-Y., Zhang, C., and Hou, J. (2018). Selenopheno[3,2-b]thiophene-Based Narrow-Bandgap Nonfullerene Acceptor Enabling 13.3% Efficiency for Organic Solar Cells with Thickness-Insensitive Feature. ACS Energy Letters *3*, 2967-2976. 10.1021/acsenergylett.8b01808.
29. Yuan, J., Zhang, Y., Zhou, L., Zhang, G., Yip, H.-L., Lau, T.-K., Lu, X., Zhu, C., Peng, H., Johnson, P.A., et al. (2019). Single-Junction Organic Solar Cell with over 15% Efficiency Using Fused-Ring Acceptor with Electron-Deficient Core. Joule *3*, 1140-1151. 10.1016/j.joule.2019.01.004.
30. Liu, Q., Jiang, Y., Jin, K., Qin, J., Xu, J., Li, W., Xiong, J., Liu, J., Xiao, Z., Sun, K., et al. (2020). 18% Efficiency organic solar cells. Sci Bull (Beijing) *65*, 272-275. 10.1016/j.scib.2020.01.001.
31. Sperlich, A., Auth, M., and Dyakonov, V. (2021). Charge Transfer in Ternary Solar Cells Employing Two Fullerene Derivatives: Where do Electrons Go? Israel Journal of Chemistry *62*. 10.1002/ijch.202100064.
32. Singh, R., Shin, S.C., Lee, H., Kim, M., Shim, J.W., Cho, K., and Lee, J.J. (2019). Ternary Blend Strategy for Achieving High-Efficiency Organic Photovoltaic Devices for

Indoor Applications. Chemistry - A European Journal *25*, 6154-6161. 10.1002/chem.201900041.
33. Zhu, L., Zhang, M., Xu, J., Li, C., Yan, J., Zhou, G., Zhong, W., Hao, T., Song, J., Xue, X., et al. (2022). Single-junction organic solar cells with over 19% efficiency enabled by a refined double-fibril network morphology. Nat Mater *21*, 656-663. 10.1038/s41563-022-01244-y.
34. Jahandar, M., Prasetio, A., Lee, C., Kim, H., Kim, A.R., Heo, J., Kim, Y., Kim, S., and Lim, D.C. (2022). Highly efficient flexible organic photovoltaic modules for sustainable energy harvesting under low-light condition via suppressing voltage-drop by metal-mediated cross-linkable polymer interfacial layer. Chemical Engineering Journal *448*. 10.1016/j.cej.2022.137555.
35. Liu, C., Xiao, C., Xie, C., and Li, W. (2021). Flexible organic solar cells: Materials, large-area fabrication techniques and potential applications. Nano Energy *89*. 10.1016/j.nanoen.2021.106399.
36. Miranda, B.H.S., Corrêa, L.D.Q., Soares, G.A., Martins, J.L., Lopes, P.L., Vilela, M.L., Rodrigues, J.F., Cunha, T.G., Vilaça, R.D.Q., Castro-Hermosa, S., et al. (2021). Efficient fully roll-to-roll coated encapsulated organic solar module for indoor applications. Solar Energy *220*, 343-353. 10.1016/j.solener.2021.03.025.
37. Galagan, Y., Fledderus, H., Gorter, H., t Mannetje, H.H., Shanmugam, S., Mandamparambil, R., Bosman, J., Rubingh, J.E.J.M., Teunissen, J.P., Salem, A., et al. (2015). Roll‐to‐Roll Slot–Die Coated Organic Photovoltaic (OPV) Modules with High Geometrical Fill Factors. Energy Technology *3*, 834-842. 10.1002/ente.201500150.
38. Maeda, A., Liu, R., Yu, K., Lee, S., Nakano, K., Takakuwa, M., Zhang, S., Tajima, K., Fukuda, K., Umezu, S., and Someya, T. (2021). Photoactive layer formation in the dark for high performance of air-processable organic photovoltaics. Journal of Physics: Materials *4*. 10.1088/2515-7639/ac2291.
39. Ren, M., Sweelssen, J., Grossiord, N., Gorter, H., Eggenhuisen, T.M., and Andriessen, R. (2012). Inkjet Printing Technology for OPV Applications. Journal of Imaging Science and Technology *56*, 40504-40501-40504-40505. 10.2352/J.ImagingSci.Technol.2012.56.4.040504.
40. Marc Steinberger, Xie Qingguang, Olivier J.J. Ronsin, Philipp Maisch, Kai Cheong Tam, Andreas Distler, Jens Harting, Christoph J. Brabec, and Egelhaaf, H.-J. (2024). Challenges and Opportunities in Upscaling Inkjet-printing of OPV. 10.1088/2058-8585/ad7ece.
41. Mateker, W.R., Sachs-Quintana, I.T., Burkhard, G.F., Cheacharoen, R., and McGehee, M.D. (2015). Minimal Long-Term Intrinsic Degradation Observed in a Polymer Solar Cell Illuminated in an Oxygen-Free Environment. Chemistry of Materials *27*, 404-407. 10.1021/cm504650a.
42. Li, Y., Huang, X., Ding, K., Sheriff, H.K.M., Jr., Ye, L., Liu, H., Li, C.Z., Ade, H., and Forrest, S.R. (2021). Non-fullerene acceptor organic photovoltaics with intrinsic operational lifetimes over 30 years. Nat Commun *12*, 5419. 10.1038/s41467-021-25718-w.
43. https://dracula-technologies.com/.
44. https://www.infinitypv.com/.
45. Magadley, E., Kabha, R., Dakka, M., Teitel, M., Friman-Peretz, M., Kacira, M., Waller, R., and Yehia, I. (2022). Organic photovoltaic modules integrated inside and outside a polytunnel roof. Renewable Energy *182*, 163-171. 10.1016/j.renene.2021.10.012.
46. Jahandar, M., Kim, S., and Lim, D.C. (2021). Indoor Organic Photovoltaics for Self-Sustaining IoT Devices: Progress, Challenges and Practicalization. ChemSusChem *14*, 3449-3474. 10.1002/cssc.202100981.
47. Pecunia, V., Occhipinti, L.G., and Hoye, R.L.Z. (2021). Emerging Indoor Photovoltaic Technologies for Sustainable Internet of Things. Advanced Energy Materials *11*. 10.1002/aenm.202100698.
48. Hwang, S., and Yasuda, T. (2022). Indoor photovoltaic energy harvesting based on

semiconducting π-conjugated polymers and oligomeric materials toward future IoT applications. Polymer Journal *55*, 297-316. 10.1038/s41428-022-00727-8.
49. Parsons, D.E., Koutsourakis, G., and Blakesley, J.C. (2024). Performance measurements for indoor photovoltaic devices: Classification of a novel light source. APL Energy *2*. 10.1063/5.0186028.
50. Reese, M.O., Glynn, S., Kempe, M.D., McGott, D.L., Dabney, M.S., Barnes, T.M., Booth, S., Feldman, D., and Haegel, N.M. (2018). Increasing markets and decreasing package weight for high-specific-power photovoltaics. Nature Energy *3*, 1002-1012. 10.1038/s41560-018-0258-1.
51. International Electrotechnical Commission, IEC TS 62607-7-2 Part 7-2: NanoEnabled Photovoltaics—Device Evaluation Method for Indoor Light. (2023).
52. Xu, X., Liu, W., Luo, X., Chen, H., Wei, Q., Yuan, J., and Zou, Y. (2021). An Overview of High-Performance Indoor Organic Photovoltaics. ChemSusChem *14*, 3428-3448. 10.1002/cssc.202100386.
53. Freunek, M., Freunek, M., and Reindl, L.M. (2013). Maximum efficiencies of indoor photovoltaic devices. IEEE Journal of Photovoltaics *3*, 59-64. 10.1109/jphotov.2012.2225023.
54. Bouclé, J., Ribeiro Dos Santos, D., and Julien-Vergonjanne, A. (2023). Doing More with Ambient Light: Harvesting Indoor Energy and Data Using Emerging Solar Cells. Solar *3*, 161-183. 10.3390/solar3010011.
55. Mori, S., Gotanda, T., Nakano, Y., Saito, M., Todori, K., and Hosoya, M. (2015). Investigation of the organic solar cell characteristics for indoor LED light applications. Japanese Journal of Applied Physics *54*, 071602. 10.7567/JJAP.54.071602.
56. Reich, N.H., van Sark, W.G.J.H.M., and Turkenburg, W.C. (2011). Charge yield potential of indoor-operated solar cells incorporated into Product Integrated Photovoltaic (PIPV). Renewable Energy *36*, 642-647. 10.1016/j.renene.2010.07.018.
57. Li, M., Igbari, F., Wang, Z.K., and Liao, L.S. (2020). Indoor Thin‐Film Photovoltaics: Progress and Challenges. Advanced Energy Materials *10*. 10.1002/aenm.202000641.
58. Kim, G., Lim, J.W., Kim, J., Yun, S.J., and Park, M.A. (2020). Transparent Thin-Film Silicon Solar Cells for Indoor Light Harvesting with Conversion Efficiencies of 36% without Photodegradation. ACS Appl Mater Interfaces *12*, 27122-27130. 10.1021/acsami.0c04517.
59. Teran, A.S., Wong, J., Lim, W., Kim, G., Lee, Y., Blaauw, D., and Phillips, J.D. (2015). AlGaAs Photovoltaics for Indoor Energy Harvesting in mm-Scale Wireless Sensor Nodes. IEEE Transactions on Electron Devices *62*, 2170-2175. 10.1109/ted.2015.2434336.
60. Müller, D., Jiang, E., Rivas-Lazaro, P., Baretzky, C., Loukeris, G., Bogati, S., Paetel, S., Irvine, S.J.C., Oklobia, O., Jones, S., et al. (2023). Indoor Photovoltaics for the Internet-of-Things – A Comparison of State-of-the-Art Devices from Different Photovoltaic Technologies. ACS Applied Energy Materials *6*, 10404-10414. 10.1021/acsaem.3c01274.
61. Sruthi Meledath M, S.C.P., Jayadev V (2023). Asymmetric dual species copper (II/I) electrolyte dye-sensitized solar cells with 35.6% efficiency under indoor light. 10.1039/D3TA06046B.
62. Wang, Y., Yang, T., Cai, W., Mao, P., Yang, Y., Wu, N., Liu, C., Wang, S., Du, Y., Huang, W., et al. (2024). Defect Passivation Refinement in Perovskite Photovoltaics: Achieving Efficiency over 45% under Low-Light and Low-Temperature Dual Extreme Conditions. Adv Mater *36*, e2312014. 10.1002/adma.202312014.
63. David Feldman, K.D., Jarett Zuboy, Robert Margolis Spring 2023 Solar Industry Update.
64. Cheng, R., Chung, C.C., Zhang, H., Liu, F., Wang, W.T., Zhou, Z., Wang, S., Djurišić, A.B., and Feng, S.P. (2019). Tailoring Triple‐Anion Perovskite Material for Indoor Light Harvesting with Restrained Halide Segregation and Record High Efficiency Beyond 36%. Advanced Energy Materials *9*. 10.1002/aenm.201901980.
65. Dong, C., Li, X.M., Ma, C., Yang, W.F., Cao, J.J., Igbari, F., Wang, Z.K., and Liao, L.S.

(2021). Lycopene ‐ Based Bionic Membrane for Stable Perovskite Photovoltaics. Advanced Functional Materials *31*. 10.1002/adfm.202011242.
66. https://www.epishine.com/.
67. https://www.ribestech.it/.
68. Burwell, G., Sandberg, O.J., Li, W., Meredith, P., Carnie, M., and Armin, A. (2022). Scaling Considerations for Organic Photovoltaics for Indoor Applications. Solar RRL *6*, 2200315. 10.1002/solr.202200315.
69. Ylikunnari, M., Välimäki, M., Väisänen, K.L., Kraft, T.M., Sliz, R., Corso, G., Po, R., Barbieri, R., Carbonera, C., Gorni, G., and Vilkman, M. (2020). Flexible OPV modules for highly efficient indoor applications. Flexible and Printed Electronics *5*, 014008. 10.1088/2058-8585/ab6e73.
70. Lin, C.F., Zhang, M., Liu, S.W., Chiu, T.L., and Lee, J.H. (2011). High photoelectric conversion efficiency of metal phthalocyanine/fullerene heterojunction photovoltaic device. Int J Mol Sci *12*, 476-505. 10.3390/ijms12010476.
71. Singh, R., Chochos, C.L., Gregoriou, V.G., Nega, A.D., Kim, M., Kumar, M., Shin, S.C., Kim, S.H., Shim, J.W., and Lee, J.J. (2019). Highly Efficient Indoor Organic Solar Cells by Voltage Loss Minimization through Fine-Tuning of Polymer Structures. ACS Applied Materials and Interfaces *11*, 36905-36916. 10.1021/acsami.9b12018.
72. Saeed, M.A., Kim, S.H., Kim, H., Liang, J., Woo, H.Y., Kim, T.G., Yan, H., and Shim, J.W. (2021). Indoor Organic Photovoltaics: Optimal Cell Design Principles with Synergistic Parasitic Resistance and Optical Modulation Effect. Advanced Energy Materials *11*, 2003103. 10.1002/aenm.202003103.
73. Elumalai, N.K., and Uddin, A. (2016). Open circuit voltage of organic solar cells: an in-depth review. Energy & Environmental Science *9*, 391-410. 10.1039/c5ee02871j.
74. Cui, Y., Wang, Y., Bergqvist, J., Yao, H., Xu, Y., Gao, B., Yang, C., Zhang, S., Inganäs, O., Gao, F., and Hou, J. (2019). Wide-gap non-fullerene acceptor enabling high-performance organic photovoltaic cells for indoor applications. Nature Energy *4*, 768-775. 10.1038/s41560-019-0448-5.
75. Yang, Y., Chen, Z.H., Wang, T., Qiao, J.W., Cui, F.Z., Xu, L.H., Qin, C.C., Yin, H., and Hao, X.T. (2021). High performance indoor light harvesters with a wide-gap donor polymer PBDB-T. Organic Electronics *98*, 106289. 10.1016/j.orgel.2021.106289.
76. Park, S.Y., Labanti, C., Luke, J., Chin, Y.C., and Kim, J.S. (2022). Organic Bilayer Photovoltaics for Efficient Indoor Light Harvesting. Advanced Energy Materials *12*, 2103237. 10.1002/aenm.202103237.
77. Yin, H., Ho, J.K.W., Cheung, S.H., Yan, R.J., Chiu, K.L., Hao, X., and So, S.K. (2018). Designing a ternary photovoltaic cell for indoor light harvesting with a power conversion efficiency exceeding 20%. Journal of Materials Chemistry A *6*, 8579-8585. 10.1039/c8ta01728j.
78. Mola, G.T., and Abera, N. (2014). Correlation between LUMO offset of donor/acceptor molecules to an open circuit voltage in bulk heterojunction solar cell. Physica B: Condensed Matter *445*, 56-59. 10.1016/j.physb.2014.04.004.
79. Yang, C., Zhang, J., Liang, N., Yao, H., Wei, Z., He, C., Yuan, X., and Hou, J. (2019). Effects of energy-level offset between a donor and acceptor on the photovoltaic performance of non-fullerene organic solar cells. Journal of Materials Chemistry A *7*, 18889-18897. 10.1039/c9ta04789a.
80. Zheng, Z., Awartani, O.M., Gautam, B., Liu, D., Qin, Y., Li, W., Bataller, A., Gundogdu, K., Ade, H., and Hou, J. (2017). Efficient Charge Transfer and Fine-Tuned Energy Level Alignment in a THF-Processed Fullerene-Free Organic Solar Cell with 11.3% Efficiency. Adv Mater *29*. 10.1002/adma.201604241.
81. Torimtubun, A.A.A., Sánchez, J.G., Pallarès, J., and Marsal, L.F. (2020). A cathode interface engineering approach for the comprehensive study of indoor performance enhancement in organic photovoltaics. Sustainable Energy and Fuels *4*, 3378-3387. 10.1039/d0se00353k.
82. Lee, H.W., Biswas, S., Lee, Y., and Kim, H. (2023). Over 23% Efficiency under Indoor Light in Gallium-Doped Zinc Oxide Electron Transport Layer-based Inverted Organic

Solar Cell to Power IoT Devices. IEEE Internet of Things Journal, 1-1. 10.1109/JIOT.2023.3267098.
83. Lee, J.H., You, Y.J., Saeed, M.A., Kim, S.H., Choi, S.H., Kim, S., Lee, S.Y., Park, J.S., and Shim, J.W. (2021). Undoped tin dioxide transparent electrodes for efficient and cost-effective indoor organic photovoltaics (SnO2 electrode for indoor organic photovoltaics). NPG Asia Materials *13*, 43. 10.1038/s41427-021-00310-2.
84. Bin, H., Wang, J., Li, J., Wienk, M.M., and Janssen, R.A.J. (2021). Efficient Electron Transport Layer Free Small-Molecule Organic Solar Cells with Superior Device Stability. Adv Mater *33*, e2008429. 10.1002/adma.202008429.
85. Yu, R., Wu, G., and Tan, Z.a. (2021). Realization of high performance for PM6:Y6 based organic photovoltaic cells. Journal of Energy Chemistry *61*, 29-46. 10.1016/j.jechem.2021.01.027.
86. Lee, C., Lee, J.H., Lee, H.H., Nam, M., and Ko, D.H. (2022). Over 30% Efficient Indoor Organic Photovoltaics Enabled by Morphological Modification Using Two Compatible Non-Fullerene Acceptors. Advanced Energy Materials *12*, 2200275. 10.1002/aenm.202200275.
87. Singh, R., Duan, T., Kan, Z., Chochos, C.L., Kini, G.P., Kumar, M., Park, J., Lee, J., and Lee, J.J. (2020). Revealing the structural effects of non-fullerene acceptors on the performances of ternary organic photovoltaics under indoor light conditions. Nano Energy *75*, 104934. 10.1016/j.nanoen.2020.104934.
88. Lee, H.K.H., Li, Z., Durrant, J.R., and Tsoi, W.C. (2016). Is organic photovoltaics promising for indoor applications? Applied Physics Letters *108*, 253301. 10.1063/1.4954268.
89. Yang, S.S., Hsieh, Z.C., Keshtov, M.L., Sharma, G.D., and Chen, F.C. (2017). Toward High-Performance Polymer Photovoltaic Devices for Low-Power Indoor Applications. Solar RRL *1*, 1700174. 10.1002/solr.201700174.
90. Vincent, P., Shin, S.C., Goo, J.S., You, Y.J., Cho, B., Lee, S., Lee, D.W., Kwon, S.R., Chung, K.B., Lee, J.J., et al. (2018). Indoor-type photovoltaics with organic solar cells through optimal design. Dyes and Pigments *159*, 306-313. 10.1016/j.dyepig.2018.06.025.
91. Kim, S.H., Saeed, M.A., Lee, S.Y., and Shim, J.W. (2021). Investigating the Indoor Performance of Planar Heterojunction Based Organic Photovoltaics. IEEE Journal of Photovoltaics *11*, 997-1003. 10.1109/jphotov.2021.3074077.
92. You, Y.J., Song, C.E., Hoang, Q.V., Kang, Y., Goo, J.S., Ko, D.H., Lee, J.J., Shin, W.S., and Shim, J.W. (2019). Highly Efficient Indoor Organic Photovoltaics with Spectrally Matched Fluorinated Phenylene-Alkoxybenzothiadiazole-Based Wide Bandgap Polymers. Advanced Functional Materials *29*, 1901171. 10.1002/adfm.201901171.
93. Hou, X., Duan, X., Liang, M., Wang, Z., and Yan, D. (2023). Application of Bis-Adducts of Phenyl-C61 Butyric Acid Methyl Ester in Promoting the Open-Circuit Voltage of Indoor Organic Photovoltaics. Materials *16*, 2613. 10.3390/ma16072613.
94. Khan, J.I., Ashraf, R.S., Alamoudi, M.A., Nabi, M.N., Mohammed, H.N., Wadsworth, A., Firdaus, Y., Zhang, W., Anthopoulos, T.D., McCulloch, I., and Laquai, F. (2019). P3HT Molecular Weight Determines the Performance of P3HT:O‐IDTBR Solar Cells. Solar RRL *3*. 10.1002/solr.201900023.
95. Gao, M., Liu, Y., Xian, K., Peng, Z., Zhou, K., Liu, J., Li, S., Xie, F., Zhao, W., Zhang, J., et al. (2022). Thermally stable poly(3‐hexylthiophene): Nonfullerene solar cells with efficiency breaking 10%. Aggregate *3*. 10.1002/agt2.190.
96. Xian, K., Liu, Y., Liu, J., Yu, J., Xing, Y., Peng, Z., Zhou, K., Gao, M., Zhao, W., Lu, G., et al. (2022). Delicate crystallinity control enables high-efficiency P3HT organic photovoltaic cells. Journal of Materials Chemistry A *10*, 3418-3429. 10.1039/d1ta10161g.
97. Steim, R., Ameri, T., Schilinsky, P., Waldauf, C., Dennler, G., Scharber, M., and Brabec, C.J. (2011). Organic photovoltaics for low light applications. Solar Energy Materials and Solar Cells *95*, 3256-3261. 10.1016/j.solmat.2011.07.011.
98. Arai, R., Furukawa, S., Hidaka, Y., Komiyama, H., and Yasuda, T. (2019). High-

Performance Organic Energy-Harvesting Devices and Modules for Self-Sustainable Power Generation under Ambient Indoor Lighting Environments. ACS Applied Materials and Interfaces *11*, 9259-9264. 10.1021/acsami.9b00018.

99. Lee, H.K.H., Wu, J., Barbé, J., Jain, S.M., Wood, S., Speller, E.M., Li, Z., Castro, F.A., Durrant, J.R., and Tsoi, W.C. (2018). Organic photovoltaic cells – promising indoor light harvesters for self-sustainable electronics. Journal of Materials Chemistry A *6*, 5618-5626. 10.1039/c7ta10875c.
100. Arai, R., Furukawa, S., Sato, N., and Yasuda, T. (2019). Organic energy-harvesting devices achieving power conversion efficiencies over 20% under ambient indoor lighting. Journal of Materials Chemistry A *7*, 20187-20192. 10.1039/c9ta06694b.
101. Wang, C.K., Che, X., Lo, Y.C., Li, Y.Z., Wang, Y.H., Forrest, S.R., Liu, S.W., and Wong, K.T. (2020). New D-A-A'-Configured Small Molecule Donors Employing Conjugation to Red-shift the Absorption for Photovoltaics. Chemistry - An Asian Journal *15*, 2520-2531. 10.1002/asia.202000635.
102. Su, J.M., Li, Y.Z., Chang, Y.H., Li, M.Z., Qiu, W.Z., Liu, S.W., and Wong, K.T. (2021). Novel thieno[3,2-b]thiophene-embedded small-molecule donors for highly efficient and photostable vacuum-processed organic photovoltaics. Materials Today Energy *20*, 100633. 10.1016/j.mtener.2020.100633.
103. Gao, Y., Piradi, V., Zhu, X., and So, S.K. (2022). Palladium(II) and Platinum(II) Porphyrin Donors for Organic Photovoltaics. ACS Applied Energy Materials *5*, 4916-4925. 10.1021/acsaem.2c00317.
104. Ding, Z., Zhao, R., Yu, Y., and Liu, J. (2019). All-polymer indoor photovoltaics with high open-circuit voltage. Journal of Materials Chemistry A *7*, 26533-26539. 10.1039/c9ta10040g.
105. Jung, S., Oh, J., Yang, U.J., Lee, S.M., Lee, J., Jeong, M., Cho, Y., Kim, S., Baik, J.M., and Yang, C. (2020). 3D Cu ball-based hybrid triboelectric nanogenerator with non-fullerene organic photovoltaic cells for self-powering indoor electronics. Nano Energy *77*, 105271. 10.1016/j.nanoen.2020.105271.
106. Liu, J., Cui, Y., Zu, Y., An, C., Xu, B., Yao, H., Zhang, S., and Hou, J. (2020). Organic photovoltaic cells for low light applications offering new scope and orientation. Organic Electronics *85*, 105798. 10.1016/j.orgel.2020.105798.
107. Saeed, M.A., Cheng, S., Biswas, S., Kim, S.H., Kwon, S.K., Kim, H., Kim, Y.H., and Shim, J.W. (2022). Remarkably high performance of organic photovoltaic devices with 3,9-bis(2-methylene- (3-(1,1-dicyanomethylene)-indanone))-5,5,11,11-tetrakis(4-hexyl meta-phenyl)-dithieno[2,3-d:2′,3′-d']-s-indaceno[1,2-b:5,6-b']dithiophene)-ethylhexyloxy] photoactive acceptor under halogen light illumination. Journal of Power Sources *518*, 230782. 10.1016/j.jpowsour.2021.230782.
108. Radford, C.L., Mudiyanselage, P.D., Stevens, A.L., and Kelly, T.L. (2022). Heteroatoms as Rotational Blocking Groups for Non-Fullerene Acceptors in Indoor Organic Solar Cells. ACS Energy Letters, 1635-1641. 10.1021/acsenergylett.2c00515.
109. Bai, F., Zhang, J., Zeng, A., Zhao, H., Duan, K., Yu, H., Cheng, K., Chai, G., Chen, Y., Liang, J., et al. (2021). A highly crystalline non-fullerene acceptor enabling efficient indoor organic photovoltaics with high EQE and fill factor. Joule *5*, 1231-1245. 10.1016/j.joule.2021.03.020.
110. Luo, S., Bai, F., Zhang, J., Zhao, H., Angunawela, I., Zou, X., Li, X., Luo, Z., Feng, K., Yu, H., et al. (2022). Optimizing spectral and morphological match of nonfullerene acceptors toward efficient indoor organic photovoltaics with enhanced light source adaptability. Nano Energy *98*, 107281. 10.1016/j.nanoen.2022.107281.
111. Ma, L.K., Chen, Y., Chow, P.C.Y., Zhang, G., Huang, J., Ma, C., Zhang, J., Yin, H., Hong Cheung, A.M., Wong, K.S., et al. (2020). High-Efficiency Indoor Organic Photovoltaics with a Band-Aligned Interlayer. Joule *4*, 1486-1500. 10.1016/j.joule.2020.05.010.
112. Yue, Q., Liu, W., and Zhu, X. (2020). N-Type Molecular Photovoltaic Materials: Design Strategies and Device Applications. Journal of the American Chemical Society *142*, 11613-11628. 10.1021/jacs.0c04084.

113. Xu, Y., Yao, H., Ma, L., Wu, Z., Cui, Y., Hong, L., Zu, Y., Wang, J., Woo, H.Y., and Hou, J. (2021). Organic photovoltaic cells with high efficiencies for both indoor and outdoor applications. Materials Chemistry Frontiers *5*, 893-900. 10.1039/d0qm00633e.
114. Kim, S., Hong, K.P., Saeed, M.A., Kim, T.H., Ahn, H., Lee, W., Shim, J.W., and Kim, Y.H. (2023). Outer sidechain engineering of selenophene and thiophene-based Y-series acceptors to produce efficient indoor organic solar cells. Applied Surface Science *623*, 157140. 10.1016/j.apsusc.2023.157140.
115. Park, S., Ahn, H., Kim, J.Y., Park, J.B., Kim, J., Im, S.H., and Son, H.J. (2020). High-Performance and Stable Nonfullerene Acceptor-Based Organic Solar Cells for Indoor to Outdoor Light. ACS Energy Letters *5*, 170-179. 10.1021/acsenergylett.9b01819.
116. Je, H.I., Shin, E.Y., Lee, K.J., Ahn, H., Park, S., Im, S.H., Kim, Y.H., Son, H.J., and Kwon, S.K. (2020). Understanding the Performance of Organic Photovoltaics under Indoor and Outdoor Conditions: Effects of Chlorination of Donor Polymers. ACS Applied Materials and Interfaces *12*, 23181-23189. 10.1021/acsami.0c02712.
117. Qin, L., Li, X., Dong, C., Zhou, J., Guo, Q., Tang, A., Zhong, Y., and Zhou, E. (2023). Low-cost material combination based on PTQ10 and completely non-fused nonfullerene acceptor for high VOC organic photovoltaics. Chemical Engineering Journal *464*, 142743. 10.1016/j.cej.2023.142743.
118. Chen, Z., Wang, T., Wen, Z., Lu, P., Qin, W., Yin, H., and Hao, X.T. (2021). Trap State Induced Recombination Effects on Indoor Organic Photovoltaic Cells. ACS Energy Letters *6*, 3203-3211. 10.1021/acsenergylett.1c01336.
119. Wang, T., Wen, Z.C., Xu, L.H., Qin, C.C., Yin, H., Liu, J.Q., and Hao, X.T. (2021). One-micron-thick organic indoor light harvesters with low photocurrent loss and fill factors over 67%. Journal of Materials Chemistry A *9*, 13515-13521. 10.1039/d1ta02345d.
120. Lübke, D., Hartnagel, P., Hülsbeck, M., and Kirchartz, T. (2022). Understanding the Thickness and Light-Intensity Dependent Performance of Green-Solvent Processed Organic Solar Cells. ACS Materials Au. 10.1021/acsmaterialsau.2c00070.
121. Tintori, F., Laventure, A., Koenig, J.D.B., and Welch, G.C. (2020). High open-circuit voltage roll-to-roll compatible processed organic photovoltaics. Journal of Materials Chemistry C *8*, 13430-13438. 10.1039/d0tc03614e.
122. Su, Y.J., Huang, S.C., Chen, T.W., Chueh, L.C., Cui, Y., Hong, L., Yao, H., Hou, J., Chen, J.T., and Hsu, C.S. (2021). Elucidating End-Group Modifications of Carbazole-Based Nonfullerene Acceptors in Indoor Applications for Achieving a PCE of over 20%. ACS Applied Materials and Interfaces *13*, 26247-26255. 10.1021/acsami.1c06360.
123. Bi, P., An, C., Zhang, T., Chen, Z., Xu, Y., Cui, Y., Wang, J., Li, J., Wang, Y., Ren, J., et al. (2022). Achieving 31% efficiency in organic photovoltaic cells under indoor light using a low energetic disorder polymer donor. Journal of Materials Chemistry A *11*, 983-991. 10.1039/d2ta07506g.
124. Yin, H., Ma, L.K., Yan, J., Zhang, Z., Cheung, A.M.H., Zhang, J., Yan, H., and So, S.K. (2020). Thick-Film Low Driving-Force Indoor Light Harvesters. Solar RRL *4*, 2000291. 10.1002/solr.202000291.
125. Xu, Y., Cui, Y., Yao, H., Zhang, T., Zhang, J., Ma, L., Wang, J., Wei, Z., and Hou, J. (2021). A New Conjugated Polymer that Enables the Integration of Photovoltaic and Light-Emitting Functions in One Device. Adv Mater *33*, e2101090. 10.1002/adma.202101090.
126. Cui, Y., Yao, H.F., Xu, Y., Bi, P.Q., Zhang, J.Q., Zhang, T., Hong, L., Chen, Z.H., Wei, Z.X., Hao, X.T., and Hou, J.H. (2022). 100 cm2 Organic Photovoltaic Cells with 23% Efficiency under Indoor Illumination. Chinese Journal of Polymer Science (English Edition) *40*, 979-988. 10.1007/s10118-022-2761-x.
127. Wang, Z., Tang, A., Wang, H., Guo, Q., Guo, Q., Sun, X., Xiao, Z., Ding, L., and Zhou, E. (2023). Organic photovoltaic cells offer ultrahigh VOC of ~ 1.2 V under AM 1.5G light and a high efficiency of 21.2 % under indoor light. Chemical Engineering Journal *451*, 139080. 10.1016/j.cej.2022.139080.
128. Schlachter, A., Marineau-Plante, G., Fortin, D., Sharma, G.D., and Harvey, P.D. (2023). Rather Simple D-A Nonfullerene for High-Performance Indoor Photovoltaic Cells. ACS

Applied Energy Materials. 10.1021/acsaem.3c00437.
129. Bi, P., Ren, J., Zhang, S., Wang, J., Chen, Z., Gao, M., Cui, Y., Zhang, T., Qin, J., Zheng, Z., et al. (2022). Low-cost and high-performance poly(thienylene vinylene) derivative donor for efficient versatile organic photovoltaic cells. Nano Energy *100*, 107463. 10.1016/j.nanoen.2022.107463.
130. Rajagopalan, R., Shankar S, S., Balasubramaniyan, N., and Sharma, G.D. (2023). Simple and Efficient Acceptor-Donor-Acceptor-Type Non-fullerene Acceptors for a BODIPY-Thiophene-Backboned Polymer Donor for High-Performance Indoor Photovoltaics. ACS Applied Materials and Interfaces *15*, 13405-13414. 10.1021/acsami.2c23048.
131. Bi, P., Zhang, S., Chen, Z., Xu, Y., Cui, Y., Zhang, T., Ren, J., Qin, J., Hong, L., Hao, X., and Hou, J. (2021). Reduced non-radiative charge recombination enables organic photovoltaic cell approaching 19% efficiency. Joule *5*, 2408-2419. 10.1016/j.joule.2021.06.020.
132. Doumon, N.Y., Yang, L., and Rosei, F. (2022). Ternary organic solar cells: A review of the role of the third element. Nano Energy *94*. 10.1016/j.nanoen.2021.106915.
133. Nam, M., Kang, J.H., Shin, J., Na, J., Park, Y., Cho, J., Kim, B., Lee, H.H., Chang, R., and Ko, D.H. (2019). Ternary Organic Blend Approaches for High Photovoltaic Performance in Versatile Applications. Advanced Energy Materials *9*, 1901856. 10.1002/aenm.201901856.
134. Cho, Y., Kumari, T., Jeong, S., Lee, S.M., Jeong, M., Lee, B., Oh, J., Zhang, Y., Huang, B., Chen, L., and Yang, C. (2020). Guest-oriented non-fullerene acceptors for ternary organic solar cells with over 16.0% and 22.7% efficiencies under one-sun and indoor light. Nano Energy *75*, 104896. 10.1016/j.nanoen.2020.104896.
135. Kim, S., Lee, C., Lee, S., Baek, S.H., Ko, D.H., and Han, W.S. (2022). Novel perylene diimides for improved photophysical and electrochemical properties. Journal of Materials Research and Technology *17*, 2675-2683. 10.1016/j.jmrt.2022.02.026.
136. Yang, T., Liu, Y., Qiu, J., Zhang, H., Li, F., and Wang, Y. (2022). Quinacridone-based small molecule acceptor as a third component in ternary organic solar cells. Chemical Engineering Journal *432*, 134405. 10.1016/j.cej.2021.134405.
137. Wang, K., Liu, C., Meng, T., Yi, C., and Gong, X. (2016). Inverted organic photovoltaic cells. Chemical Society Reviews *45*, 2937-2975. 10.1039/c5cs00831j.
138. Paula, T., and de Fatima Marques, M. (2022). Recent advances in polymer structures for organic solar cells: A review. AIMS Energy *10*, 149-176. 10.3934/energy.2022009.
139. Mutlu, A., Can, M., and Tozlu, C. (2019). Performance improvement of organic solar cell via incorporation of donor type self-assembled interfacial monolayer. Thin Solid Films *685*, 88-96. 10.1016/j.tsf.2019.05.064.
140. Zamani-Meymian, M.-R., Sheikholeslami, S., and Fallah, M. (2020). Stability of Non-Flexible vs. Flexible Inverted Bulk-Heterojunction Organic Solar Cells with ZnO as Electron Transport Layer Prepared by a Sol-Gel Spin Coating Method. Surfaces *3*, 319-327. 10.3390/surfaces3030023.
141. Ibraikulov, O.A., Wang, J., Kamatham, N., Heinrich, B., Méry, S., Kohlstädt, M., Würfel, U., Ferry, S., Leclerc, N., Heiser, T., and Lévêque, P. (2019). ITO‐Free Organic Photovoltaic Modules Based on Fluorinated Polymers Deposited from Non‐Halogenated Solution: A Major Step Toward Large‐Scale Module Production. Solar RRL *3*. 10.1002/solr.201900273.
142. Makula, P., Pacia, M., and Macyk, W. (2018). How To Correctly Determine the Band Gap Energy of Modified Semiconductor Photocatalysts Based on UV-Vis Spectra. J Phys Chem Lett *9*, 6814-6817. 10.1021/acs.jpclett.8b02892.
143. Rubin, K.A., Yang, Y., Amster, O., Scrymgeour, D.A., Misra, S. (2019). Scanning Microwave Impedance Microscopy (sMIM) in Electronic and Quantum Materials. In: Celano, U. (eds) Electrical Atomic Force Microscopy for Nanoelectronics. 10.1007/978-3-030-15612-1_12.
144. Coq Germanicus, R., Mercier, D., Agrebi, F., M, F.E., Mariolle, D., Descamps, P., and

LeclEre, P. (2020). Quantitative mapping of high modulus materials at the nanoscale: comparative study between atomic force microscopy and nanoindentation. J Microsc. 10.1111/jmi.12935.
145. Young, T.J., Monclus, M.A., Burnett, T.L., Broughton, W.R., Ogin, S.L., and Smith, P.A. (2011). The use of the PeakForceTMquantitative nanomechanical mapping AFM-based method for high-resolution Young's modulus measurement of polymers. Measurement Science and Technology *22*. 10.1088/0957-0233/22/12/125703.
146. Zhang, S., Weng, Y., and Ma, C. (2021). Quantitative Nanomechanical Mapping of Polyolefin Elastomer at Nanoscale with Atomic Force Microscopy. Nanoscale Res Lett *16*, 113. 10.1186/s11671-021-03568-1.
147. Kwaśniewska, A., Świetlicki, M., Prószyński, A., and Gładyszewski, G. (2021). The Quantitative Nanomechanical Mapping of Starch/Kaolin Film Surfaces by Peak Force AFM. Polymers. doi.org/10.3390/polym13020244.
148. Blakesley, J.C., Castro, F.A., Kylberg, W., Dibb, G.F.A., Arantes, C., Valaski, R., Cremona, M., Kim, J.S., and Kim, J.-S. (2014). Towards reliable charge-mobility benchmark measurements for organic semiconductors. Organic Electronics *15*, 1263-1272. 10.1016/j.orgel.2014.02.008.
149. Melianas, A., Pranculis, V., Xia, Y., Felekidis, N., Inganäs, O., Gulbinas, V., and Kemerink, M. (2017). Photogenerated Carrier Mobility Significantly Exceeds Injected Carrier Mobility in Organic Solar Cells. Advanced Energy Materials *7*. 10.1002/aenm.201602143.
150. Chang, S.-W., Kettle, J., Waters, H., and Horie, M. (2015). Cyclopentadithiophene–benzothiadiazole copolymers with permutations of repeating unit length and ratios; synthesis, optical and electrochemical properties and photovoltaic characteristics. RSC Advances *5*, 107276-107284. 10.1039/c5ra22946d.
151. Chakraborty, A., Lucarelli, G., Xu, J., Skafi, Z., Castro-Hermosa, S., Kaveramma, A.B., Balakrishna, R.G., and Brown, T.M. (2024). Photovoltaics for Indoor Energy Harvesting. Nano Energy. 10.1016/j.nanoen.2024.109932.
152. Baillot, R., and Deshayes, Y. (2017). Integration of the Methodology Starting from Component Design. In Reliability Investigation of LED Devices for Public Light Applications, pp. 147-186. 10.1016/b978-1-78548-149-9.50004-3.
153. BS EN 12464-1: Light and Light - Lighting of work places - Part 1: Indoor work places. (2002).
154. Cui, Y., Hong, L., Zhang, T., Meng, H., Yan, H., Gao, F., and Hou, J. (2021). Accurate photovoltaic measurement of organic cells for indoor applications. Joule *5*, 1016-1023. 10.1016/j.joule.2021.03.029.
155. Zhu, L., Zhang, M., Zhou, G., Hao, T., Xu, J., Wang, J., Qiu, C., Prine, N., Ali, J., Feng, W., et al. (2020). Efficient Organic Solar Cell with 16.88% Efficiency Enabled by Refined Acceptor Crystallization and Morphology with Improved Charge Transfer and Transport Properties. Advanced Energy Materials *10*. 10.1002/aenm.201904234.
156. Cheng, H.W., Juan, C.Y., Mohapatra, A., Chen, C.H., Lin, Y.C., Chang, B., Cheng, P., Wang, H.C., Chu, C.W., Yang, Y., and Wei, K.H. (2021). High-Performance Organic Photovoltaics Incorporating an Active Layer with a Few Nanometer-Thick Third-Component Layer on a Binary Blend Layer. Nano Lett *21*, 2207-2215. 10.1021/acs.nanolett.0c05045.
157. Guo, Q., Guo, Q., Geng, Y., Tang, A., Zhang, M., Du, M., Sun, X., and Zhou, E. (2021). Recent advances in PM6:Y6-based organic solar cells. Materials Chemistry Frontiers *5*, 3257-3280. 10.1039/d1qm00060h.
158. He, Y., Alem, S., Lu, J., Yee, N., and Tao, Y. (2023). A new non-fullerene acceptor based on an asymmetric electron-deficient core for indoor organic photovoltaic cells. Materials Chemistry and Physics *306*. 10.1016/j.matchemphys.2023.128036.
159. Clavier, G., and Audebert, P. s-Tetrazines as Building Blocks for New Functional Molecules and Molecular Materials. Chem. Rev. 2010, 110, 3299−3314.
160. Audebert, P., and Miomandre, F. (2013). Electrofluorochromism: from molecular systems to set-up and display. Chem. Sci. *4*, 575-584. 10.1039/c2sc21503a.

161. Zambon, A., Mouesca, J.M., Gheorghiu, C., Bayle, P.A., Pecaut, J., Claeys-Bruno, M., Gambarelli, S., and Dubois, L. (2016). s-Heptazine oligomers: promising structural models for graphitic carbon nitride. Chem Sci *7*, 945-950. 10.1039/c5sc02992a.
162. Dang, Q.Q., Zhan, Y.F., Wang, X.M., and Zhang, X.M. (2015). Heptazine-Based Porous Framework for Selective CO2 Sorption and Organocatalytic Performances. ACS Appl Mater Interfaces *7*, 28452-28458. 10.1021/acsami.5b09441.
163. Liu, X., Lin, L., Ye, X., Tan, C.H., and Jiang, Z. (2016). Aerobic Oxidation of Benzylic sp3 C−H Bonds through Cooperative Visible‐Light Photoredox Catalysis of N‐Hydroxyimide and Dicyanopyrazine. Asian Journal of Organic Chemistry *6*, 422-425. 10.1002/ajoc.201600426.
164. Savateev, A., Tarakina, N.V., Strauss, V., Hussain, T., Ten Brummelhuis, K., Sanchez Vadillo, J.M., Markushyna, Y., Mazzanti, S., Tyutyunnik, A.P., Walczak, R., et al. (2020). Potassium Poly(Heptazine Imide): Transition Metal-Free Solid-State Triplet Sensitizer in Cascade Energy Transfer and [3+2]-cycloadditions. Angew Chem Int Ed Engl *59*, 15061-15068. 10.1002/anie.202004747.
165. Lau, V.W., Mesch, M.B., Duppel, V., Blum, V., Senker, J., and Lotsch, B.V. (2015). Low-molecular-weight carbon nitrides for solar hydrogen evolution. J Am Chem Soc *137*, 1064-1072. 10.1021/ja511802c.
166. Schwarzer, A., Saplinova, T., and Kroke, E. (2013). Tri-s-triazines (s-heptazines)—From a “mystery molecule” to industrially relevant carbon nitride materials. Coordination Chemistry Reviews *257*, 2032-2062. 10.1016/j.ccr.2012.12.006.
167. Mir Sayed, S., Deng, L.-L., Lin, B.-P., and Yang, H. (2017). A room-temperature heptazine core discotic liquid crystal. Liquid Crystals *44*, 2175-2183. 10.1080/02678292.2017.1371343.
168. Kailasam, K., Schmidt, J., Bildirir, H., Zhang, G., Blechert, S., Wang, X., and Thomas, A. (2013). Room temperature synthesis of heptazine-based microporous polymer networks as photocatalysts for hydrogen evolution. Macromol Rapid Commun *34*, 1008-1013. 10.1002/marc.201300227.
169. Liu, Z. (2021). Enhancing the photovoltaic performance with two similar structure polymers as donors by broadening the absorption spectrum and optimizing the molecular arrangement. Organic Electronics *93*. 10.1016/j.orgel.2021.106153.
170. Mahdy, S., Feteha, M., Soliman, M., Hussien, H., Sadat-Shafai, T., and Ebrahim, S. (2023). Effect of solvent and thermal annealing on D18/Y6 polymer solar cells. Journal of Materials Science *58*, 17543-17556. 10.1007/s10853-023-09095-x.
171. Hofinger, J., Putz, C., Mayr, F., Gugujonovic, K., Wielend, D., and Scharber, M.C. (2021). Understanding the low voltage losses in high-performance non-fullerene acceptor-based organic solar cells. Materials Advances *2*, 4291-4302. 10.1039/d1ma00293g.
172. Wang, Y., Luke, J., Privitera, A., Rolland, N., Labanti, C., Londi, G., Lemaur, V., Toolan, D.T.W., Sneyd, A.J., Jeong, S., et al. (2023). The critical role of the donor polymer in the stability of high-performance non-fullerene acceptor organic solar cells. Joule *7*, 810-829. 10.1016/j.joule.2023.03.002.
173. Kanai, K., Miyazaki, T., Suzuki, H., Inaba, M., Ouchi, Y., and Seki, K. (2010). Effect of annealing on the electronic structure of poly(3-hexylthiophene) thin film. Phys Chem Chem Phys *12*, 273-282. 10.1039/b914100f.
174. Ntwaeaborwa, O.M., Zhou, R., Qian, L., Pitale, S.S., Xue, J., Swart, H.C., and Holloway, P.H. (2012). Post-fabrication annealing effects on the performance of P3HT:PCBM solar cells with/without ZnO nanoparticles. Physica B: Condensed Matter *407*, 1631-1633. 10.1016/j.physb.2011.09.103.
175. Ye, T., Jin, S., Kang, C., Tian, C., Zhang, X., Zhan, C., Lu, S., and Kan, Z. (2018). Comparison Study of Wide Bandgap Polymer (PBDB-T) and Narrow Bandgap Polymer (PBDTTT-EFT) as Donor for Perylene Diimide Based Polymer Solar Cells. Front Chem *6*, 613. 10.3389/fchem.2018.00613.
176. Li, X., He, Z., Sun, M., Zhang, H., Guo, Z., Xu, Y., Li, H., Liang, C., and Jing, X. (2019). Exploring alkylthiol additives in PBDB-T:ITIC blended active layers for solar cell

applications*. Chinese Physics B *28*. 10.1088/1674-1056/28/8/088802.
177. Zang, Y., Li, C.Z., Chueh, C.C., Williams, S.T., Jiang, W., Wang, Z.H., Yu, J.S., and Jen, A.K. (2014). Integrated molecular, interfacial, and device engineering towards high-performance non-fullerene based organic solar cells. Adv Mater *26*, 5708-5714. 10.1002/adma.201401992.
178. Ye, L., Jiang, W., Zhao, W., Zhang, S., Qian, D., Wang, Z., and Hou, J. (2014). Selecting a donor polymer for realizing favorable morphology in efficient non-fullerene acceptor-based solar cells. Small *10*, 4658-4663. 10.1002/smll.201401082.
179. Sharma, V., Koenig, J.D.B., and Welch, G.C. (2021). Perylene diimide based non-fullerene acceptors: top performers and an emerging class featuring N-annulation. Journal of Materials Chemistry A *9*, 6775-6789. 10.1039/d0ta11197j.
180. https://www.sigmaaldrich.com/FR/fr/product/aldrich/900774.
181. Liu, S.Y., Wu, C.H., Li, C.Z., Liu, S.Q., Wei, K.H., Chen, H.Z., and Jen, A.K. (2015). A Tetraperylene Diimides Based 3D Nonfullerene Acceptor for Efficient Organic Photovoltaics. Adv Sci (Weinh) *2*, 1500014. 10.1002/advs.201500014.
182. Wang, Y., Lee, J., Hou, X., Labanti, C., Yan, J., Mazzolini, E., Parhar, A., Nelson, J., Kim, J.S., and Li, Z. (2020). Recent Progress and Challenges toward Highly Stable Nonfullerene Acceptor‐Based Organic Solar Cells. Advanced Energy Materials *11*. 10.1002/aenm.202003002.
183. Ciammaruchi, L., Zapata-Arteaga, O., Gutiérrez-Fernández, E., Martin, J., and Campoy-Quiles, M. (2020). Structure dependent photostability of ITIC and ITIC-4F. Materials Advances *1*, 2846-2861. 10.1039/d0ma00458h.
184. Wang, Y., Fan, Q., Guo, X., Li, W., Guo, B., Su, W., Ou, X., and Zhang, M. (2017). High-performance nonfullerene polymer solar cells based on a fluorinated wide bandgap copolymer with a high open-circuit voltage of 1.04 V. J. Mater. Chem. A *5*, 22180-22185. 10.1039/c7ta07785h.
185. Fan, Q., Xu, Z., Guo, X., Meng, X., Li, W., Su, W., Ou, X., Ma, W., Zhang, M., and Li, Y. (2017). High-performance nonfullerene polymer solar cells with open-circuit voltage over 1 V and energy loss as low as 0.54 eV. Nano Energy *40*, 20-26. 10.1016/j.nanoen.2017.07.047.
186. Wang, Q., Zhang, S., Xu, B., Li, S., Yang, B., Yuan, W., and Hou, J. (2017). Efficient Fullerene-Free Polymer Solar Cells Based on Alkylthio Substituted Conjugated Polymers. The Journal of Physical Chemistry C *121*, 4825-4833. 10.1021/acs.jpcc.6b11848.
187. Ibrahim Zamkoye, I., Bouclé, J., Leclerc, N., Lucas, B., and Vedraine, S. (2022). Silver Nanowire Electrodes Integrated in Organic Solar Cells with Thick Active Layer Based on a Low‐Cost Donor Polymer. Solar RRL *7*. 10.1002/solr.202200756.
188. Hansen, C.M. (2, 2007.). Hansen solubility parameters: a user's handbook, CRC Press, the United States.
189. Hansen, C.M., and Smith, A.L. (2004). Using Hansen solubility parameters to correlate solubility of C60 fullerene in organic solvents and in polymers. Carbon *42*, 1591-1597. 10.1016/j.carbon.2004.02.011.
190. Olla, T., Ibraikulov, O.A., Ferry, S., Boyron, O., Méry, S., Heinrich, B.t., Heiser, T., Lévêque, P., and Leclerc, N. (2019). Benzothiadiazole Halogenation Impact in Conjugated Polymers, a Comprehensive Study. Macromolecules *52*, 8006-8016. 10.1021/acs.macromol.9b01760.
191. Morales-Aragonés, J.I., Alonso-García, M.d.C., Gallardo-Saavedra, S., Alonso-Gómez, V., Balenzategui, J.L., Redondo-Plaza, A., and Hernández-Callejo, L. (2021). Online Distributed Measurement of Dark I-V Curves in Photovoltaic Plants. Applied Sciences *11*. 10.3390/app11041924.
192. Zhang, D., Fan, B., Ying, L., Li, N., Brabec, C.J., Huang, F., and Cao, Y. (2021). Recent progress in thick‐film organic photovoltaic devices: Materials, devices, and processing. SusMat *1*, 4-23. 10.1002/sus2.10.
193. Cheng, P., and Zhan, X. (2016). Stability of organic solar cells: challenges and

strategies. Chem Soc Rev *45*, 2544-2582. 10.1039/c5cs00593k.
194. Duan, L., and Uddin, A. (2020). Progress in Stability of Organic Solar Cells. Adv Sci (Weinh) *7*, 1903259. 10.1002/advs.201903259.
195. Zhang, Y., Samuel, I.D.W., Wang, T., and Lidzey, D.G. (2018). Current Status of Outdoor Lifetime Testing of Organic Photovoltaics. Advanced Science *5*, 1800434. 10.1002/advs.201800434.
196. Du, X., Heumueller, T., Gruber, W., Classen, A., Unruh, T., Li, N., and Brabec, C.J. (2019). Efficient Polymer Solar Cells Based on Non-fullerene Acceptors with Potential Device Lifetime Approaching 10 Years. Joule *3*, 215-226. 10.1016/j.joule.2018.09.001.
197. Bertho, S., Janssen, G., Cleij, T.J., Conings, B., Moons, W., Gadisa, A., D'Haen, J., Goovaerts, E., Lutsen, L., Manca, J., and Vanderzande, D. (2008). Effect of temperature on the morphological and photovoltaic stability of bulk heterojunction polymer:fullerene solar cells. Solar Energy Materials and Solar Cells *92*, 753-760. 10.1016/j.solmat.2008.01.006.
198. Parnell, A.J., Cadby, A.J., Dunbar, A.D.F., Roberts, G.L., Plumridge, A., Dalgliesh, R.M., Skoda, M.W.A., and Jones, R.A.L. (2015). Physical mechanisms responsible for the water‐induced degradation of PC61BM P3HT photovoltaic thin films. Journal of Polymer Science Part B: Polymer Physics *54*, 141-146. 10.1002/polb.23902.
199. Manceau, M., Bundgaard, E., Carlé, J.E., Hagemann, O., Helgesen, M., Søndergaard, R., Jørgensen, M., and Krebs, F.C. (2011). Photochemical stability of π-conjugated polymers for polymer solar cells: a rule of thumb. Journal of Materials Chemistry *21*. 10.1039/c0jm03105d.
200. Wang, N., Tong, X., Burlingame, Q., Yu, J., and Forrest, S.R. (2014). Photodegradation of small-molecule organic photovoltaics. Solar Energy Materials and Solar Cells *125*, 170-175. 10.1016/j.solmat.2014.03.005.
201. Han, J., Xu, H., Paleti, S.H.K., Sharma, A., and Baran, D. (2024). Understanding photochemical degradation mechanisms in photoactive layer materials for organic solar cells. Chem Soc Rev *53*, 7426-7454. 10.1039/d4cs00132j.
202. Liu, T., Burlingame, Q.C., Ivancevic, M.R., Liu, X., Hu, J., Rand, B.P., and Loo, Y.L. (2023). Photochemical Decomposition of Y‐Series Non‐Fullerene Acceptors Is Responsible for Degradation of High‐Efficiency Organic Solar Cells. Advanced Energy Materials *13*. 10.1002/aenm.202300046.
203. Zhao, Y., Wu, Z., Liu, X., Zhong, Z., Zhu, R., and Yu, J. (2021). Revealing the photo-degradation mechanism of PM6:Y6 based high-efficiency organic solar cells. Journal of Materials Chemistry C *9*, 13972-13980. 10.1039/d1tc03655f.
204. Jeong, J., Seo, J., Nam, S., Han, H., Kim, H., Anthopoulos, T.D., Bradley, D.D., and Kim, Y. (2016). Significant Stability Enhancement in High-Efficiency Polymer:Fullerene Bulk Heterojunction Solar Cells by Blocking Ultraviolet Photons from Solar Light. Adv Sci (Weinh) *3*, 1500269. 10.1002/advs.201500269.
205. Gheno, A., Trigaud, T., Bouclé, J., Audebert, P., Ratier, B., and Vedraine, S. (2018). Stability assessments on luminescent down-shifting molecules for UV-protection of perovskite solar cells. Optical Materials *75*, 781-786. 10.1016/j.optmat.2017.11.027.
206. Meng, L., Wu, X.-G., Ma, S., Shi, L., Zhang, M., Wang, L., Chen, Y., Chen, Q., and Zhong, H. (2020). Improving the efficiency of silicon solar cells using in situ fabricated perovskite quantum dots as luminescence downshifting materials. Nanophotonics *9*, 93-100. 10.1515/nanoph-2019-0320.
207. Fernandes, R.V., Urbano, A., Duarte, J.L., Bristow, N., Kettle, J., and Laureto, E. (2018). Tuning the optical properties of luminescent down shifting layers based on organic dyes to increase the efficiency and lifetime of P3HT: PCBM photovoltaic devices. Journal of Luminescence *203*, 165-171. 10.1016/j.jlumin.2018.06.053.
208. Kettle, J., Bristow, N., Gethin, D.T., Tehrani, Z., Moudam, O., Li, B., Katz, E.A., Dos Reis Benatto, G.A., and Krebs, F.C. (2016). Printable luminescent down shifter for enhancing efficiency and stability of organic photovoltaics. Solar Energy Materials and Solar Cells *144*, 481-487. 10.1016/j.solmat.2015.09.037.

209. Chen, J.Y., Huang, C.K., Hung, W.B., Sun, K.W., and Chen, T.M. (2014). Efficiency improvement of Si solar cells using metal-enhanced nanophosphor fluorescence. Solar Energy Materials and Solar Cells *120*, 168-174. 10.1016/j.solmat.2013.08.039.
210. Gong, Y.H., Miomandre, F., Méallet‐Renault, R., Badré, S., Galmiche, L., Tang, J., Audebert, P., and Clavier, G. (2009). Synthesis and Physical Chemistry of s‐Tetrazines: Which Ones are Fluorescent and Why? European Journal of Organic Chemistry *2009*, 6121-6128. 10.1002/ejoc.200900964.
211. Qing, Z., Audebert, P., Clavier, G., Méallet-Renault, R., Miomandre, F., and Tang, J. (2011). Bright fluorescence through activation of a low absorption fluorophore: the case of a unique naphthalimide–tetrazine dyad. New Journal of Chemistry *35*. 10.1039/c1nj20100j.
212. Charlène Crevant, Christophe Lucchesi, Myriam Paire, and Guillemoles, J.-F. (2017). Luminescent Downshifting Layers Using Organic Dyes and Quantum Dots. 10.1002/pssc.201700178.
213. Klampaftis, E., Ross, D., McIntosh, K.R., and Richards, B.S. (2009). Enhancing the performance of solar cells via luminescent down-shifting of the incident spectrum: A review. Solar Energy Materials and Solar Cells *93*, 1182-1194. 10.1016/j.solmat.2009.02.020.
214. Zakirullin, R. (2015). Creating optical filters with angular-selective light transmission. Appl Opt *54*, 6416-6419. 10.1364/AO.54.006416.
215. https://shiken.ai/chemistry/benzene-structure.

Appendices

Appendix 1. A summary of crucial molecular units known for their blue light absorption capabilities:

Molecular unit	Chemical structure		Example
Thiophene		approximately 400-500 nm	P3HT PF2
Benzothiadiazole (BT)	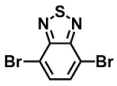	BT derivatives are used to create donor-acceptor (D-A) copolymers with tailored bandgaps for blue light absorption. They improve charge separation and transport.	PCDTBT PF2
Perylene	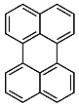	400-600	Bay-linked perylene bisimide (di-PBI)
Carbazole	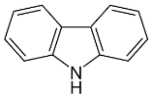		
Fluorene	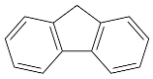		
Anthracene	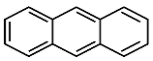		
Naphthalene Diimide (NDI)	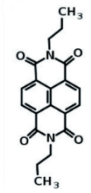	strong electron acceptors	

Appendix 2. Material properties

Appendix 2.1. Calculated the optical E_g of Heptazine derivatives using a Tauc plot

The optical E_g of the heptazine derivatives can be estimated using the Tauc plot method from their UV-Vis absorption spectra[142].

Determination of TDPH

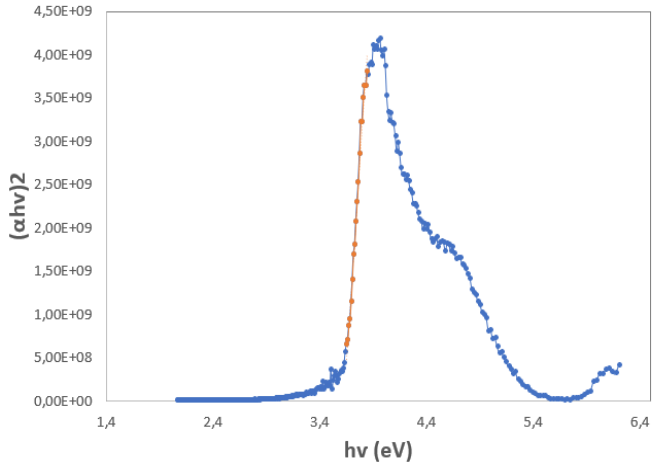

n=1/2		
$(\alpha hv)^2$	R^2	0,987
	intercept	-6,66E+10
	slope	1,84E+10
	Egap	3,62

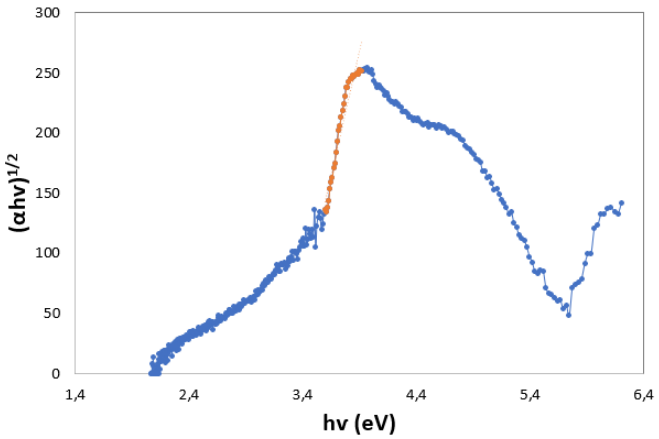

n=2		
$(\alpha hv)^{1/2}$	R^2	0,9275
	intercept	-1554,57
	slope	473,82
	Egap	3,28

The R^2 value of 0.987 indicates a good fit, and the linear area is much more visible and sharp, confirming that TDPH behaves more like a direct band gap material. The optical E_g of TDPH is around 3.62 eV.

Determination of 2,4-diF-Hep

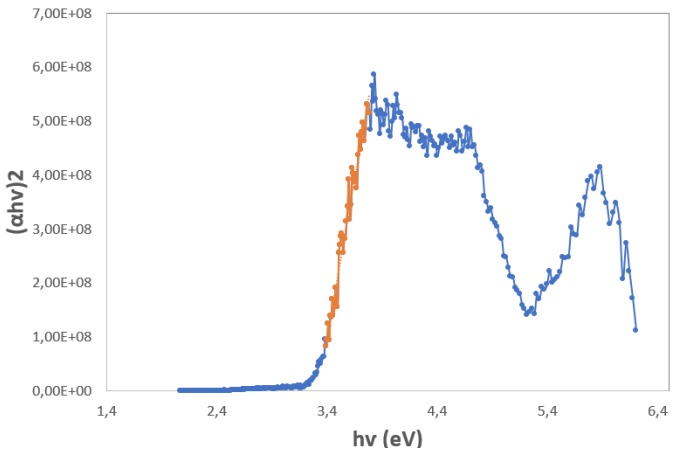

n=1/2		
$(\alpha hv)^2$	R^2	0,966
	intercept	-3,87E+09
	slope	1,17E+09
	Egap	3,31

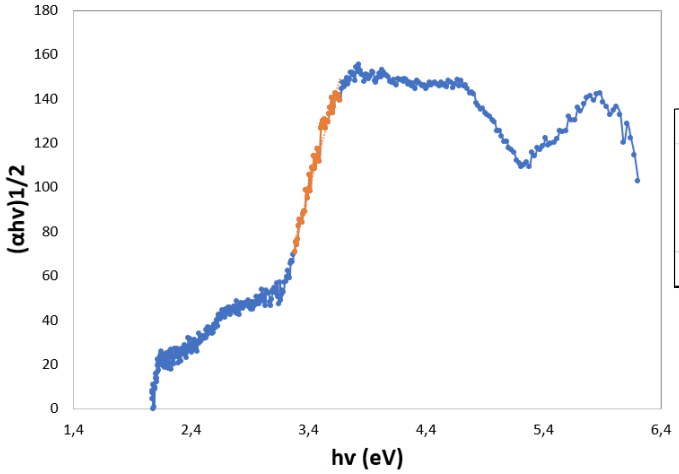

n=2		
$(\alpha hv)^{1/2}$	R^2	0,961
	intercept	-550,51
	slope	190,87
	Egap	2,88

The R² value of 0.966 indicates a good fit, and the linear area is much more visible and sharp, confirming that 2,4-diF-Hep behaves more like a direct band gap material. The optical E_g of 2,4-diF-Hep is around 3.31 eV.

Determination of 2,4-DM-Hep

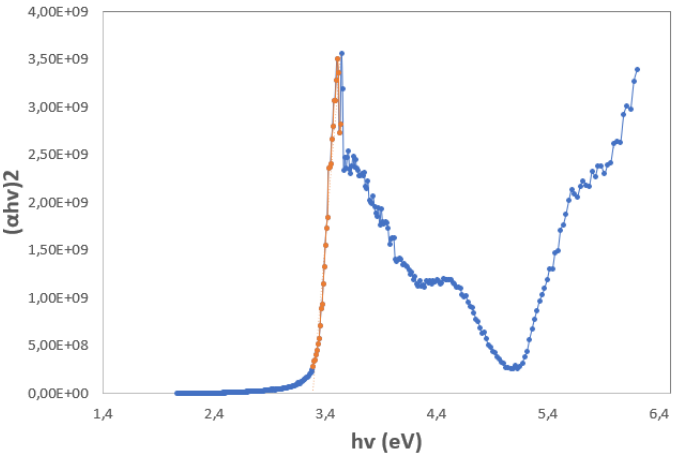

n=1/2		
$(\alpha hv)^2$	R^2	0,934
	intercept	-4,77E+10
	slope	1,45E+10
	Egap	3,29

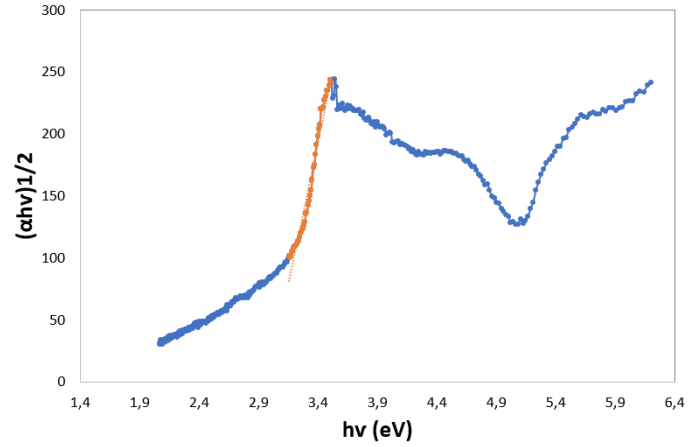

n=2		
$(\alpha hv)^{1/2}$	**R^2**	**0,963**
	intercept	**-1368,23**
	slope	**459,23**
	Egap	**2,98**

The R² value of 0.963 indicates a good fit, and the linear area is much more visible and sharp, confirming that 2,4-diF-Hep behaves more like an indirect band gap material. The optical E_g of 2,4-diF-Hep is around 2.98 eV.

Appendix 2.2. Estimate the length of the PF2 polymer chain

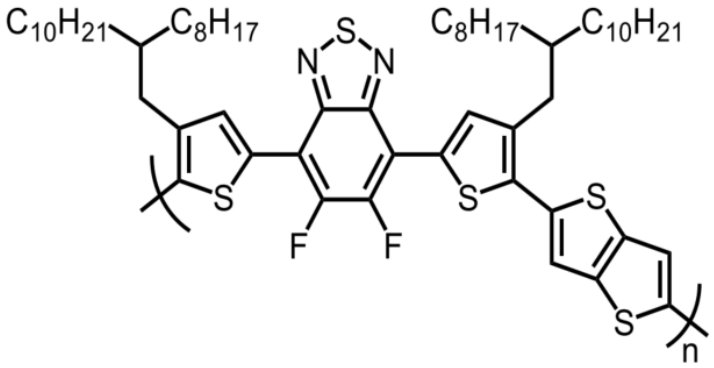

Figure 105. Chemical structure of PF2 polymer.

Molecular weight (M_W) of the PF2 Polymer = 30000 g/mol

Polydispersity index (PDI) = 3.8

Molecular weight of one monomer = 1033.66 g/mol

Estimate the length of one monomer

C-C bond : is around 0.154 nm[215]

Aromatic rings: Each benzene-like ring has a typical length of around 0.28-0.3 nm.

Alkyl side chain ($C_{10}H_{21}$ and C_8H_{17}) can be quite extended, a C_{10} chain can be roughly 1.2-1.4 nm in length if fully extended.

Assuming that the monomer has about 3 aromatic rings attached to the sulfur atom, and that the alkyl chain extends in some linear fashion, the length of one monomer unit can be estimated as follows: 0.154x3+0.28x3+1.2x2=3.528nm

Calculate the degree of polymerization (DP)

The degree of polymerization, DP, is the average number of monomer units in a polymer chain and can be calculated by:

$$DP = \frac{\text{Average molecular weight of polymer } (M_W)}{Molecular\ weight\ of\ monomer\ (M_{mono})}$$

Using the provided data:

$$DP = \frac{30000}{1033.66} = 29\ monomoer\ units$$

Length for PF2 chain

Thus, an estimated length for PF2 chain would be around:

$$Length\ of\ polymer\ chain\ (L) = DP\ \times length\ per\ monomer\ unit$$
$$= 29 \times 3.528\ = 103\ nm$$

Appendix 3. LDS molecules for UV protection of OSCs

Appendix 3.1. Calculation of NITZ fluorophore brightness (B)

Definition of Brightness (B)

The brightness (B) of a fluorophore is determined by two key parameters:

$$B = \varepsilon \Phi_F$$

Where:

ε (L mol^{-1} cm^{-1}) is the molar extinction coefficient, which indicates how strongly a molecule absorbs light at a given wavelength.

Φ_F or PLQY is the fluorescence quantum yield, which indicates the efficiency of fluorescence emission.

For NITZ, we consider two different fluorescence emission pathways:

- Direct emission from the imide moiety (378nm)
- Emission from the tetrazine moiety via Förster resonance energy transfer (FRET) (562 nm)

Table 34. Photophysical and electrochemical properties of compounds in dichloromethane[211].

Compound	λ_{max}/nm	ε/L mol^{-1} cm^{-1}	λ_{em}/nm	ϕ_F	$\varepsilon_{\lambda(ex)} \times \phi_F$	τ_F/ns	E^0_{red}/V
NITZ (tetrazine data)	517	400	562[b]	0.32[b]	130	158[c,d]	−0.86
NITZ (imide data)	334	9100 (5000 at 355 nm)	378 400[c]	0.003[c]	12	0.03[c]	−1.70

[a] λ_{ex} = 350 nm. [b] λ_{ex} = 517 nm. [c] λ_{ex} = 355 nm. [d] λ_{ex} = 495 nm.

Brightness calculation without FRET

- For NITZ (imide emission wavelength is 378/400 nm):

  Extinction coefficient at 334 nm: ε_{imide} = 9100 L mol^{-1} cm^{-1}

  Quantum yield: Φ_F = 0.003

  B_{imide} = 9100 x 0.003 = 27.3

- For NITZ (tetrazine emission wavelength is 562 nm):

  Extinction coefficient at 517 nm: $\varepsilon_{tetrazine}$ = 400 L mol^{-1} cm^{-1}

  Quantum yield: Φ_F = 0.32

  $B_{tetrazine}$ = 400 x 0.32 = 128

This indicates that direct excitation of tetrazine can produce a brightness of 128, which is higher than that of imide emission.

Brightness Calculation with FRET

Since NITZ undergoes intramolecular FRET from the imide moiety to the tetrazine moiety, brightness calculations must take into account the FRET efficiency:

$$B_{NITZ} = \varepsilon_{imide}\, \Phi_{F_{tetrazine}} \Phi_{ET}$$

Where Φ_{ET} is the efficiency of this energy transfer, which is approximately 0.95. [211]

Then: $$B_{NITZ} = 9100 \times 0.32 \times 0.95 = 2766$$

By FRET, the brightness od NITZ is much higher, about 2766.

Appendix 3.2. C4

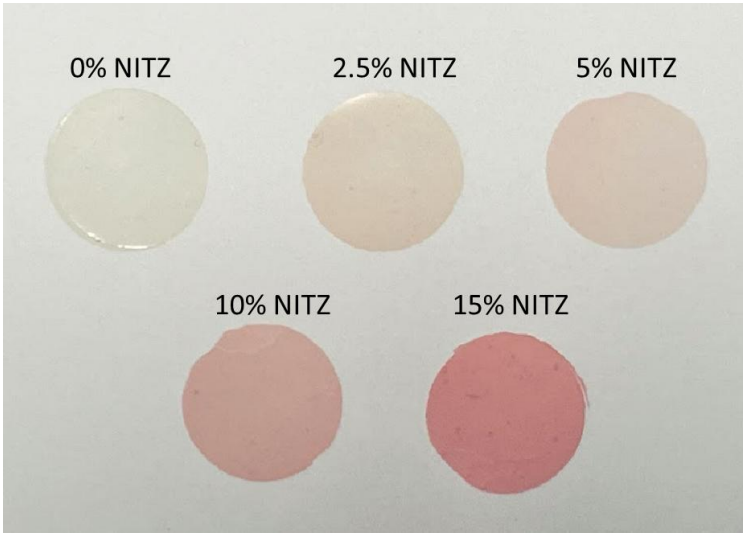

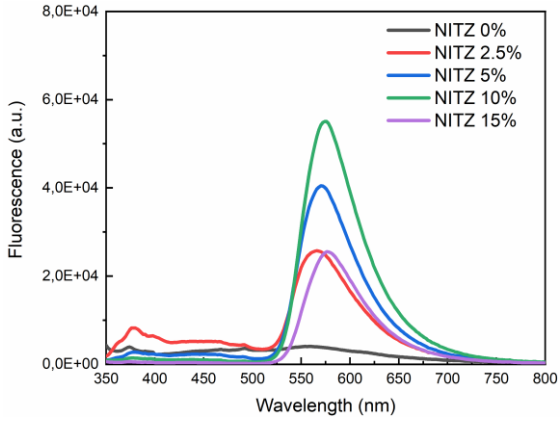

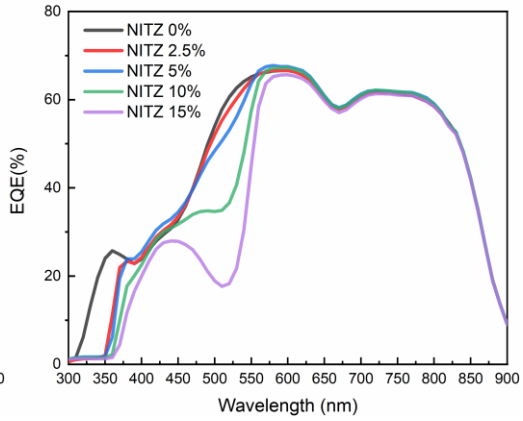

Appendix 3.3. C8

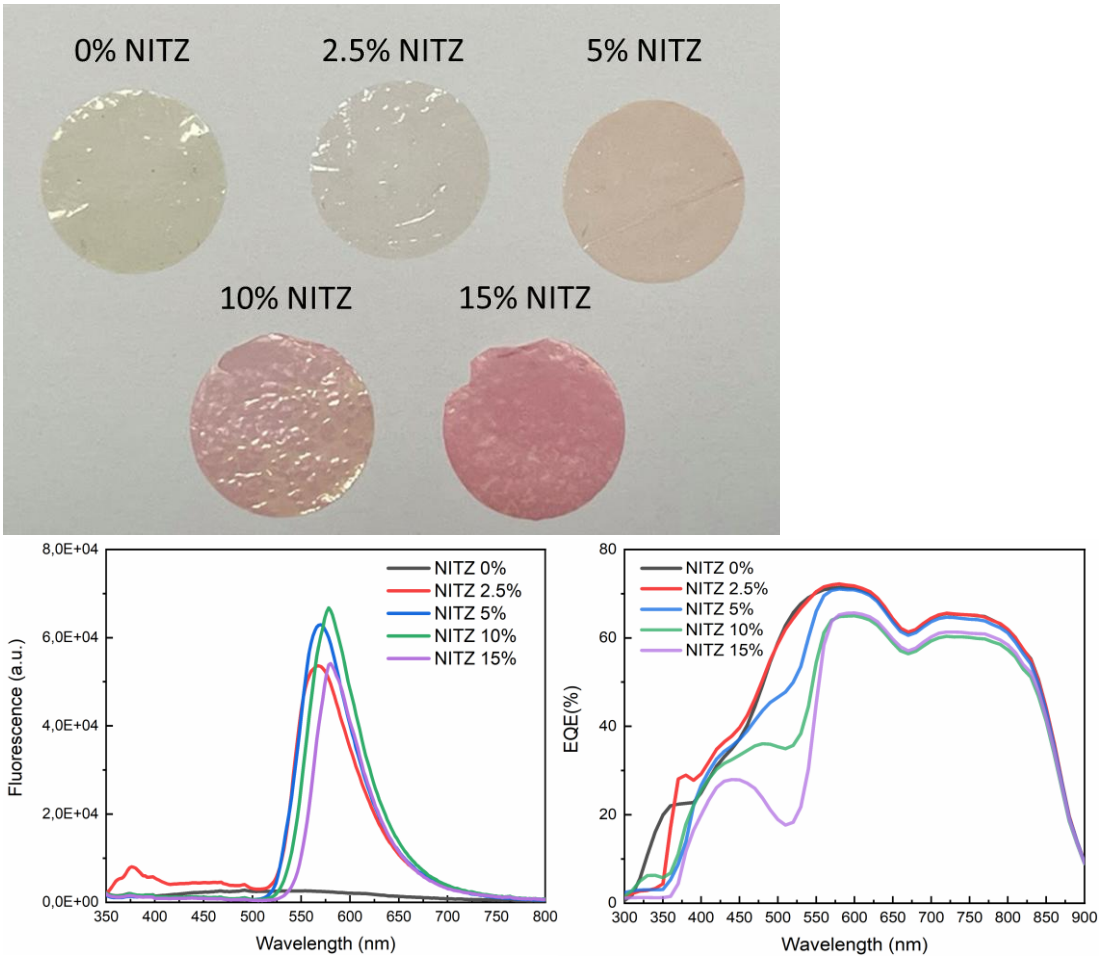

Appendix 3.4. C12

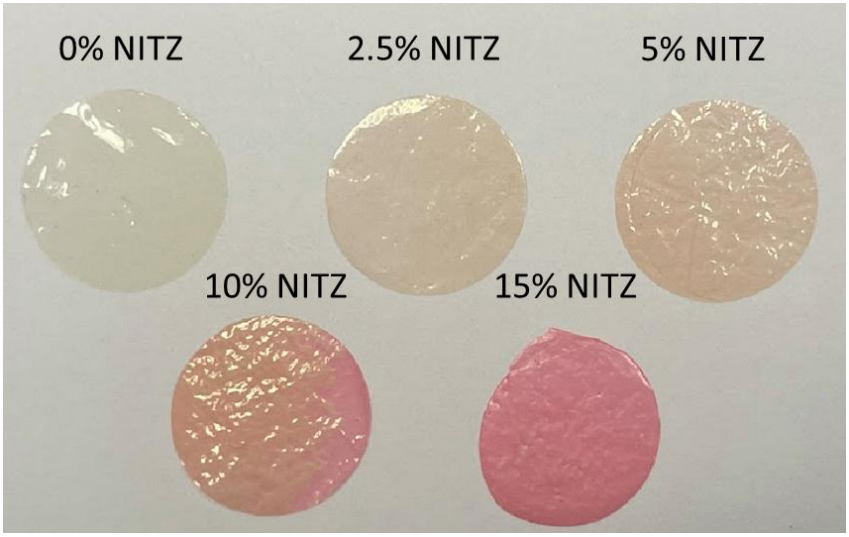

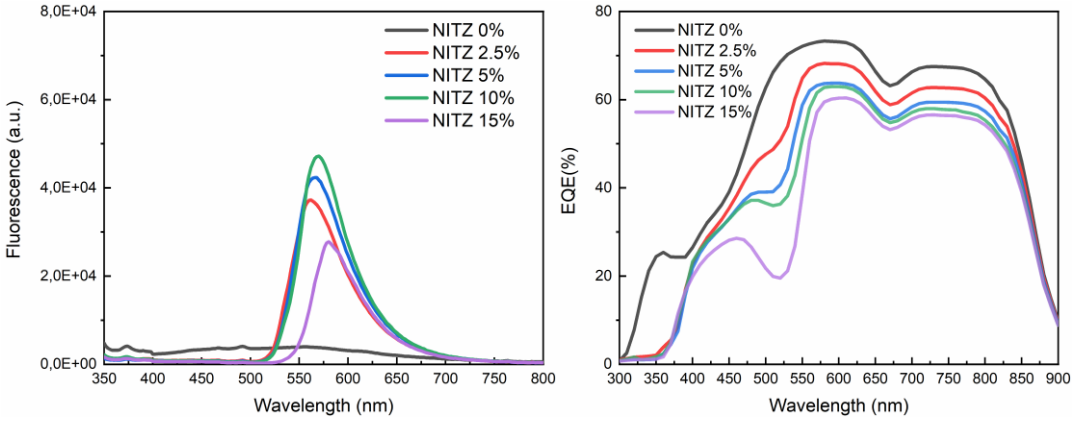

Résumé

Les cellules solaires organiques (OSC) à hétérojonction en volume (BHJ) semblent être des candidates idéales pour alimenter les appareils de l'Internet des objets (IoT) en conditions intérieures en raison de leur compatibilité avec les technologies d'impression à faible coût, leur flexibilité, et leur efficacité de conversion de puissance élevée (PCE) sous faible illumination. De plus, l'adaptabilité des matériaux organiques permet de moduler précisément leurs propriétés optiques et électroniques pour que leur absorption corresponde idéalement aux spectres d'émission des sources d'éclairage de type LED. Cependant, des améliorations supplémentaires de l'efficacité et de la stabilité sont nécessaires pour exploiter leur potentiel. Dans cette thèse, nous avons étudié plusieurs stratégies liées aux matériaux de couches actives pour améliorer les performances des OSC en conditions indoor. Le premier objectif était d'intégrer de nouveaux accepteurs non fullerènes (NFA), notamment à base d'heptazines, pour mieux exploiter la région bleue (400-500 nm) de l'émission des LED blanches, qui reste mal adressées à ce jour. Des dérivés d'heptazine innovants ont été étudiés et intégrés dans les couches actives des OSC dans ce contexte. Bien que des propriétés optiques et morphologiques appropriées aient été observées, ainsi qu'une séparation de charge prometteuse entre les matériaux donneurs et accepteurs, des limitations spécifiques de performance, telles qu'une faible génération de photocourant, ont été mises en évidence. Néanmoins, ce travail jette les bases d'une optimisation supplémentaire des NFA à base d'heptazine pour les applications OSC en intérieur. La deuxième orientation de recherche s'est concentrée sur l'optimisation de la couche active OSC à base du mélange PF2:ITIC, utilisé pour la première en intérieur.. À cette fin, nous avons exploité plusieurs paramètres cruciaux tels que la sélection du solvant, l'épaisseur de la couche active et le rapport donneur/accepteur (D:A). Grâce à des techniques spécifiques de caractérisation en champ proche, nous avons identifié le chlorobenzène (CB) comme le solvant le plus efficace pour traiter le mélange PF2:ITIC, produisant des couches actives lisses et uniformes avec d'excellentes caractéristiques morphologiques. L'augmentation de l'épaisseur de la couche active de 100 nm à 270 nm a considérablement amélioré l'absorption de la lumière dans la région bleue, ce qui a entraîné un photocourant plus élevé, permettant ainsi de démontrer des dispositifs atteignant un PCE allant jusqu'à 11,95 % avec un V_{OC} élevé de 0,73 V sous un éclairage LED chaud à 1000 lux. Ce travail démontre finalement l'importance d'une conception moléculaire innovante et de l'optimisation du système pour améliorer les performances des OSC pour les applications intérieures.

Mots-clés : Cellules solaires organiques, Récupération d'énergie indoor, Accepteurs non fullerène, Internet des objets (IoT), Photovoltaïque d'intérieur.

Abstract

Organic solar cells (OSCs) based on a bulk-heterojunction (BHJ) concept are emerging as ideal candidates for powering indoor Internet-of-things (IoT) devices due to their compatibility with low-cost printing technologies, flexible substrates, and high power conversion efficiency (PCE) under indoor lighting. Additionally, the tunability of organic materials allows for precise adjustments in their optical and electronic properties to ideally match the emission spectra of indoor sources such as LEDs. This adaptability makes OSCs particularly promising for indoor environments. However, further improvements in efficiency and stability are needed to exploit their potential. In this thesis, several strategies were explored to improve OSC performance for indoor applications. The first focus was on the integration of novel non-fullerene acceptors (NFAs), especially heptazine-based, to better address the blue region (400-500 nm) of white LED emission, which remains a specific challenge. Innovative Heptazine derivatives were studied and integrated into OSC active layers in this context. Although suitable optical and morphological properties were observed, as well as promising charge separation between donor and acceptor materials, specific limitations in performance, such as low photocurrent generation, were evidenced. Nevertheless, this work lays the foundation for further optimization of heptazine-based NFAs for indoor OSC applications. The second research direction focused on optimizing the PF2:ITIC-based OSC active layer for indoor applications. To this end, we explore several crucial parameters, such as solvent selection, active layer thickness, and donor-to-acceptor (D:A) ratio. Thanks to specific near-field characterization techniques, we identified chlorobenzene (CB) as the most effective solvent to process the PF2:ITIC blend, producing smooth, uniform active layers with excellent morphological features. Increasing the active layer thickness from 100 nm to 270 nm significantly improved light absorption in the blue region, resulting in a higher photocurrent, enabling the demonstration of devices achieving PCE up to 11.95% with a high V_{OC} of 0.73 V under warm LED illumination at 1000 lux. Finally, this work demonstrates the crucial importance of innovative molecular design and system optimization in improving the performance of OSCs for indoor applications.

Keywords: Organic solar cells, Indoor energy harvesting, Non-fullerene acceptors, Internet of things (IoT), Indoor photovoltaics, Bulk-heterojunction.